TU Delft

Delft University of Technology

Sintering Fundamentals of Nano-Metallic Particle Interconnects

Du, L.

DOI
10.4233/uuid:b28b556e-585f-446e-8649-35d225f34dda

Publication date
2025

Document Version
Final published version

Citation (APA)
Du, L. (2025). *Sintering Fundamentals of Nano-Metallic Particle Interconnects*. [Dissertation (TU Delft), Delft University of Technology]. https://doi.org/10.4233/uuid:b28b556e-585f-446e-8649-35d225f34dda

Important note
To cite this publication, please use the final published version (if applicable).
Please check the document version above.

Copyright
Other than for strictly personal use, it is not permitted to download, forward or distribute the text or part of it, without the consent of the author(s) and/or copyright holder(s), unless the work is under an open content license such as Creative Commons.

Takedown policy
Please contact us and provide details if you believe this document breaches copyrights.
We will remove access to the work immediately and investigate your claim.

This work is downloaded from Delft University of Technology.
For technical reasons the number of authors shown on this cover page is limited to a maximum of 10.

Sintering Fundamentals of Nano-Metallic Particle Interconnects

SINTERING FUNDAMENTALS OF NANO-METALLIC PARTICLE INTERCONNECTS

Dissertation

for the purpose of obtaining the degree of doctor
at Delft University of Technology
by the authority of the Rector Magnificus Prof.dr.ir. T.H.J.J. van der Hagen
chair of the Board for Doctorates
to be defended publicly on
Thursday 04 September 2025 at 10:00 o'clock

by

Leiming DU

Master of Engineering in Mechanics,
Harbin Institute of Technology, Shenzhen, China,
born in Shandong, China

This dissertation has been approved by the promotors.

Composition of the doctoral committee:

Rector Magnificus,	Chairperson
Prof. dr. G.Q. Zhang,	Delft University of Technology, promotor
Prof. dr. ir. W.D. van Driel,	Delft University of Technology, promotor
Dr. ir. R.H. Poelma,	Delft University of Technology, copromotor
Independent members:	
Prof. dr. P.J. French	Delft University of Technology
Prof. dr. S. Liu	Wuhan Unversity, China
Prof. dr. D. Kiener	Montanuniversität Leoben, Austria
Prof. dr. ir. J.B. van den Brand	TNO
Em. prof. dr. ir. P.M. Sarro,	Delft University of Technology, reserve member

Keywords: Sintered Cu nanoparticles, anisotropy, fracture toughness, micro-cantilever bending test, micro-pillar compression test, molecular dynamics simulation, cohesive zone model, phase-field fracture method, precession electron diffraction

Printed by: Ipskamp Printing

Copyright © 2025 by Leiming Du
This dissertation has an embargo period until 04 September 2027.

ISBN 978-94-6384-817-6

An electronic version of this dissertation is available at
http://repository.tudelft.nl/.

To my parents

SUMMARY

THIS thesis systematically investigated the microstructure evolution and mechanical behavior of sintered copper (Cu) nanoparticles (NPs) using an integrated approach combining multiscale simulations with micromechanical tests. The research addressed critical challenges in the design and optimization of sintered Cu for advanced electronic applications, with a focus on anisotropic fracture behavior, porosity-dependent properties, thermal effects, interfacial strength, particle morphology, and the role of ALD coatings.

Chapter 1 established the foundational context for this study by underscoring the significance of sintered Cu NPs in electronics packaging and identifying critical gaps in the existing literature. It defined the research objectives and outlined the thesis structure, emphasizing the necessity of an integrated experimental and computational approach to link microstructure evolution with mechanical performance.

Chapter 2 systematically investigated the influence of sintering pressure on the evolution of anisotropic microstructures in sintered Cu NPs. By integrating molecular dynamics (MD) simulations with micro-cantilever bending tests, the study revealed that uniaxial sintering pressure promoted preferential neck alignment along the loading direction, resulting in pronounced mechanical anisotropy. These findings underscored the critical role of processing parameters in governing microstructural orientation and, consequently, in tailoring the mechanical performance of sintered Cu NPs. This chapter established a foundational understanding of the process–structure–property relationships central to nanoparticle-based sintering.

Chapter 3 examined the influence of sintering pressure on densification and mechanical performance. Sintered Cu NPs exhibited a favorable combination of high strength and low elastic modulus, highlighting their suitability for electronic packaging. A two-stage deformation mechanism was identified, governed by the material's porous architecture and heterogeneous microstructure. Initial compressive loading compacted voids and formed dense interparticle contacts, followed by plastic deformation primarily accommodated through intragranular slip.

Chapter 4 investigated the strain rate- and temperature-dependent viscoplastic behavior of sintered Cu NPs. Micro-pillar compression tests, coupled with the Anand viscoplastic model, revealed the competing effects of strain-rate hardening and thermal softening. Phase-field fracture simulations further elucidated the influence of porosity on crack initiation and propagation, providing critical insight into fracture mechanisms under varying loading conditions.

Chapter 5 focused on the interfacial strength and fracture behavior of sintered Cu NPs bonded to Cu substrates. Micro-cantilever bending tests and cohesive zone model (CZM) demonstrated that interface-notched specimens exhibited superior fracture resistance, with a stress intensity factor (K_Q) of 2.88 ± 0.10 MPa·m$^{1/2}$, compared to 2.12 ± 0.11 MPa·m$^{1/2}$ for Cu NP-notched specimens. Simulations aligned with ex-

perimental results, showing that reduced fracture resistance in Cu NP-notched samples stemmed from porosity and stress concentration, while enhanced strength at the interface was attributed to strong bonding and minimized void formation.

Chapter 6 examined the effect of Cu particle morphology on densification and fracture toughness. Fracture resistance was found to be highly morphology-dependent: bimodal sintered Cu exhibited the greatest toughness, attributed to effective crack deflection and bridging. Monomodal Cu showed moderate resistance, while flake-shaped Cu displayed the lowest toughness, primarily due to weak interlamellar bonding and anisotropic porosity.

Chapter 7 revealed that the fracture toughness of sintered Cu NPs was strongly dependent on loading mode. Mode II (in-plane shear) exhibited the highest toughness due to shear-induced particle interlocking, followed by mode I (tensile) characterized by ductile tearing, and mode III (out-of-plane shear), which showed the lowest toughness due to triaxial stress and unstable crack propagation. The application of an Al_2O_3 coating enhanced fracture toughness across all modes, with the greatest improvement observed under shear-dominated and mixed-mode loading. The coating constrained surface deformation, delayed crack initiation, and strengthened interparticle boundaries, while preserving the intrinsic ductile fracture mechanism.

Chapter 8 concluded the thesis by synthesizing the key findings and outlining future research directions, including the mitigation of oxidation, investigation of size-dependent mechanical behavior, understanding of stiffness mismatch, and exploration of metamaterial-inspired design strategies.

SAMENVATTING

DEZE thesis onderzocht systematisch de microstructurele evolutie en het mechanisch gedrag van gesinterde koper-nanodeeltjes (Cu NPs) via een geïntegreerde benadering van multischalige simulaties en micromechanische tests. Het onderzoek behandelde cruciale uitdagingen in het ontwerp en de optimalisatie van gesinterd koper voor geavanceerde elektronische toepassingen, met de nadruk op anisotroop breukgedrag, porositeitsafhankelijke eigenschappen, temperatuureffecten, interface-sterkte, de invloed van partikelmorfologie en de rol van ALD-coatings.

Hoofdstuk 1 vormde de fundamentele context van deze studie door het belang van gesinterde Cu NPs in elektronica-verpakkingen te onderstrepen en kritieke hiaten in de bestaande literatuur te identificeren. Het formuleerde de onderzoeksdoelstellingen en gaf de structuur van de thesis weer, waarbij het belang werd benadrukt van een geïntegreerde experimentele en computationele aanpak om de relatie tussen microstructurele evolutie en mechanische prestaties te begrijpen.

Hoofdstuk 2 onderzocht systematisch de invloed van sinterdruk op de evolutie van anisotrope microstructuren in gesinterde Cu NPs. Door middel van moleculaire dynamica (MD) simulaties en micro-cantilever buigtesten werd aangetoond dat uniaxiale sinterdruk leidde tot voorkeursoriëntatie van sinternekken in de belastingsrichting, wat resulteerde in uitgesproken mechanische anisotropie. Deze bevindingen onderstreepten het cruciale belang van procesparameters bij het sturen van microstructurele oriëntatie en dus bij het afstemmen van de mechanische prestaties van gesinterde Cu NPs. Dit hoofdstuk legde een basis voor het begrijpen van het proces–structuur–eigenschappen verband bij nanopartikel-sintering.

Hoofdstuk 3 onderzocht de invloed van sinterdruk op verdichting en mechanische prestaties. Gesinterde Cu NPs vertoonden een gunstige combinatie van hoge sterkte en lage elasticiteitsmodulus, wat hun geschiktheid voor elektronische verpakkingen benadrukte. Er werd een tweefasig deformatie-mechanisme vastgesteld, bepaald door de poreuze architectuur en heterogene microstructuur van het materiaal: aanvankelijke druk leidde tot compactie van poriën en vorming van dichte interpartikelcontacten, gevolgd door plastische vervorming via intragranulaire glijmechanismen.

Hoofdstuk 4 onderzocht het viscoplastische gedrag van gesinterde Cu NPs onder variërende rek- en temperatuursnelheden. Microzuil-compressietests, gekoppeld aan het Anand-viscoplastische model, toonden het samenspel van verharding door rektempo en thermische verzachting aan. Faseveld-simulaties van breukgedrag verduidelijkten verder de invloed van porositeit op scheurinitiatie en -voortplanting, wat waardevolle inzichten bood in breukmechanismen onder verschillende belastingstoestanden.

Hoofdstuk 5 richtte zich op de interface-sterkte en het breukgedrag van gesinterde Cu NPs verbonden met Cu-substraten. Micro-cantilever buigtesten en het Cohesive Zone Model (CZM) toonden aan dat monsters met scheuren aan de interface een hogere breukweerstand vertoonden, met een spanningsintensiteitsfactor (K_Q) van 2.88 ± 0.10

$MPa{\cdot}m^{1/2}$, vergeleken met 2.12 ± 0.11 $MPa{\cdot}m^{1/2}$ voor monsters met scheuren in het Cu NP-gedeelte. Simulaties bevestigden de experimentele resultaten en wezen uit dat de lagere breukweerstand van NP-notched monsters voortkwam uit porositeit en spanningsconcentratie, terwijl de hogere sterkte van interface-notched monsters werd toegeschreven aan sterke binding en minimale poriedistributie.

Hoofdstuk 6 onderzocht het effect van Cu-partikelmorfologie op verdichting en breuktaaiheid. De breukweerstand bleek sterk afhankelijk van de morfologie: bimodale gesinterde Cu vertoonde de hoogste taaiheid dankzij effectieve scheurafbuiging en -overbrugging. Monomodale Cu vertoonde matige taaiheid, terwijl vlokvormige Cu de laagste weerstand toonde, voornamelijk door zwakke interlamellaire binding en anisotrope porositeit.

Hoofdstuk 7 toonde aan dat de breuktaaiheid van gesinterde Cu NPs sterk afhing van de belastingmodus. Mode II (in-plane schuifbelasting) vertoonde de hoogste taaiheid door partikelvergrendeling, gevolgd door mode I (trekbelasting) met ductiel scheuren, en mode III (out-of-plane schuifbelasting), die de laagste taaiheid vertoonde door triaxiale spanningen en instabiele scheurvoortplanting. Toepassing van een Al_2O_3-coating verbeterde de breuktaaiheid in alle modi, met de grootste verbetering bij schuifgedomineerde en gemengde belastingen. De coating beperkte oppervlaktevervorming, vertraagde scheurinitiatie en versterkte interpartikelbinding zonder het onderliggende ductiele breukmechanisme aan te tasten.

Hoofdstuk 8 sloot de thesis af met een synthese van de belangrijkste bevindingen en stelde toekomstig onderzoek voor, waaronder het tegengaan van oxidatie, de studie van grootte-afhankelijke mechanica, het begrijpen van stijfheidsverschillen en de verkenning van op metamaterialen geïnspireerde ontwerpstrategieën.

1

INTRODUCTION

Although sintering science has been extensively studied over the past century, a number of fundamental questions remain unresolved, particularly from a mechanical perspective. When considering the sintering of nanoparticles (NPs), issues such as size-dependent deformation, interparticle bonding, porosity evolution, and fracture behavior introduce complexities that are not adequately captured by conventional sintering theories. These challenges highlight the need for continued investigation into the mechanical aspects of nanoparticle sintering to advance both scientific understanding and technological application.

1

1.1. BACKGROUND

WIDE band gap (WBG) semiconductors, particularly silicon carbide (SiC) and gallium nitride (GaN), have emerged as critical materials in next-generation power modules due to their superior electrical and thermal performance [1–3]. These materials exhibit high breakdown electric fields, wide thermal operating windows, and excellent carrier mobility, making them ideal for high-power, high-frequency, and high-temperature environments. The continued development of WBG-based devices has enabled substantial improvements in energy efficiency and power density, thereby driving the evolution of compact and high-performance power electronic systems.

However, the advancement of WBG semiconductors necessitates corresponding improvements in interconnect bonding technologies. Conventional solder alloys, predominantly based on Sn or Pb, face significant challenges under the thermal and mechanical demands imposed by WBG devices. Their low melting points limited thermal conductivity, and insufficient resistance to creep and electromigration render them increasingly unsuitable for high-reliability applications [4–6]. Furthermore, the miniaturization trend in advanced packaging—characterized by finer pitches, higher current densities, and increasing integration complexity—further amplifies these limitations.

In response, metallic nanoparticles (NPs) have garnered increasing interest as alternative bonding materials for power electronics packaging [7–10]. Metallic NPs offer several compelling advantages, including low-temperature sintering, high intrinsic melting points, excellent electrical and thermal conductivities, and high mechanical strength [11–13]. These properties make them especially suitable for applications where traditional solders fall short. Among various candidates, silver (Ag) and copper (Cu) NPs have been most extensively explored for die-attach and interconnect applications (Fig. 1.1a). Ag NPs are particularly attractive due to their outstanding electrical conductivity and oxidation resistance [14], contributing to superior thermal and mechanical reliability under harsh conditions. Nevertheless, the widespread adoption of Ag NPs is hindered by their high cost and susceptibility to electrochemical migration, particularly in humid environments. As a result, Cu NPs have emerged as a cost-effective alternative (Fig. 1.1b). Despite their inherent tendency to oxidize, ongoing research has demonstrated that surface engineering strategies—such as organic ligand passivation, alloying, and sintering in reducing atmospheres—can effectively mitigate oxidation and enable stable bonding.

In addition, Cu NP-based sintering offers significant advantages for fine-pitch, high-density interconnects (Fig. 1.1c), particularly in 3D integration schemes [15–18]. Compared to conventional bulk Cu bonding, which requires temperatures exceeding 300°C and high mechanical pressures, nanoscale Cu sintering can be achieved at substantially lower thermal budgets (160–250°C) and reduced pressures [17, 19]. This alleviates concerns regarding thermal stress and damage to low-k dielectrics. Recent studies have demonstrated that Cu NP-bonded joints can achieve robust mechanical strength (up to 60 MPa) without the need for expensive surface planarization techniques such as chemical mechanical polishing (CMP). Moreover, Cu NP-based joints exhibit superior thermal stability and electromigration resistance, positioning them as a promising replacement for both solder- and Ag-based bonding solutions in advanced packaging.

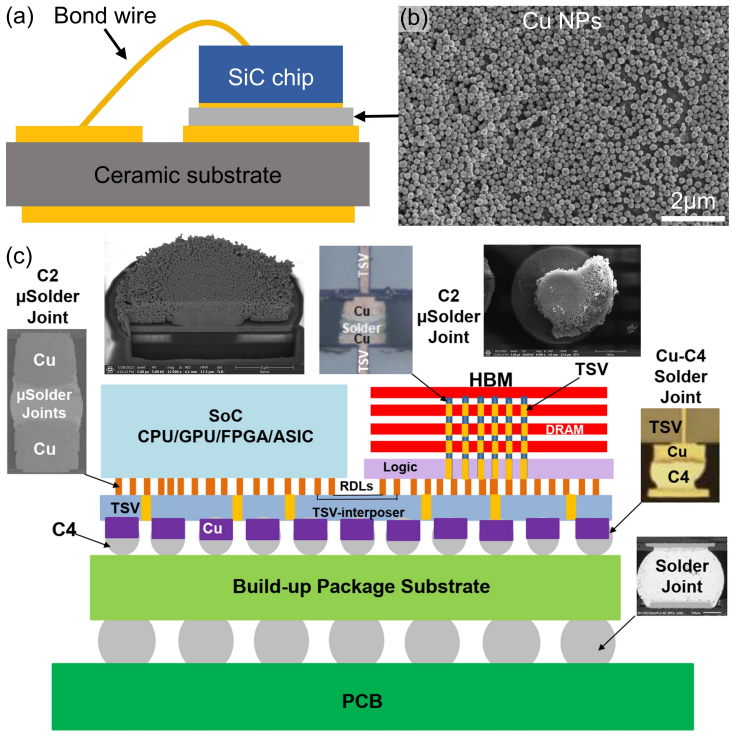


Figure 1.1: (a) Schematic of power electronic packaging; (b) SEM of Cu NPs; (c) schematic of interconnect architecture in 3D integrated systems.

1.2. OVERVIEW OF PARTICLE SINTERING DYNAMICS

1.2.1. ADVANCEMENTS IN IN-SITU CHARACTERIZATION

Understanding particle sintering dynamics is fundamental to elucidating the interplay between processing conditions (temperature, time) and microstructural evolution in NP systems. In particular, the sintering behavior of Cu NPs has garnered significant interest due to its implications for microstructure control and mechanical performance in functional materials. Recent advancements in in-situ characterization techniques have enabled direct observation of sintering processes across multiple length scales, offering unprecedented insights into both atomic-scale mechanisms and mesoscale kinetics. In-situ scanning electron microscopy (SEM) has proven instrumental in visualizing key morphological transitions during sintering, including particle rearrangement, neck formation, coalescence, and pore closure [20–23]. These studies reveal how thermally induced stresses and surface energy gradients drive densification in NP assemblies. Complementing SEM, in-situ transmission electron microscopy (TEM) provides atomic-resolution insights into fundamental diffusion mechanisms [24–27], as shown in Fig. 1.2a. For example, high-resolution TEM and high-angle annular dark-field environmental scanning TEM (HAADF-ESTEM) have been employed to track surface diffusion pathways, interfacial migration, and crystallographic reorientations at Cu/Cu_2O inter-

faces during oxidation-reduction cycles. LaGrow et al. [28], for instance, demonstrated the unidirectional propagation of oxide fronts in Cu NPs, correlating interfacial dynamics with local temperature gradients and oxygen partial pressure. Similar in-situ TEM investigations on Ag and Pt NPs have uncovered dislocation-mediated sintering, as well as the influence of particle size and surface contamination on diffusion kinetics [29].

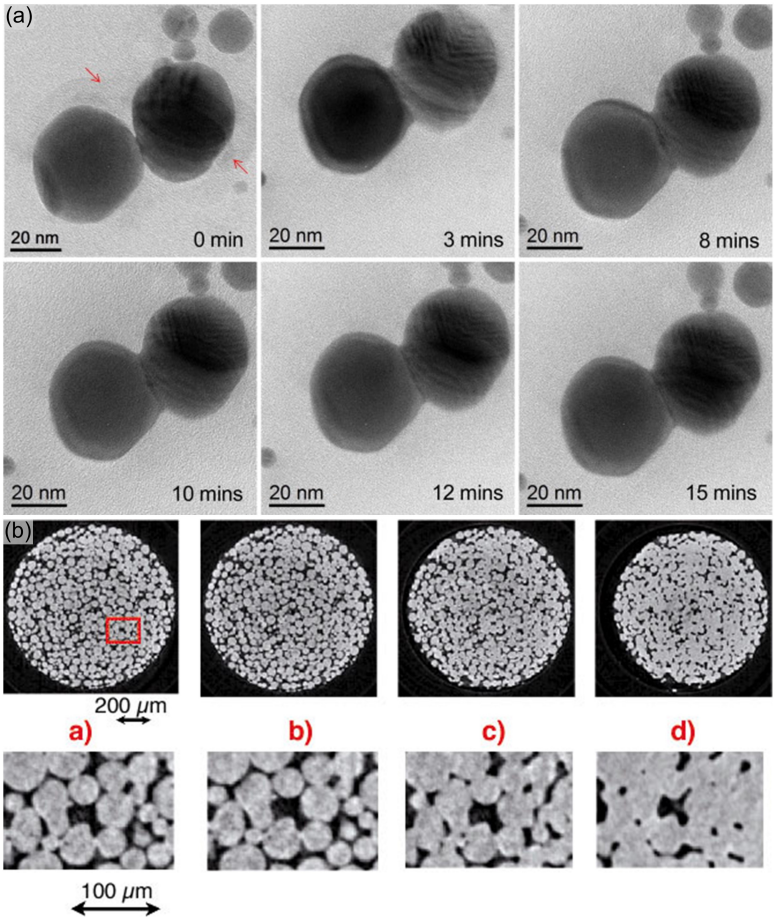


Figure 1.2: (a) In-situ TEM images showing nanoparticle sintering dynamics [24]; (b) in-situ synchrotron X-ray microtomography capturing microstructure evolution during sintering (ESRF).

Beyond electron microscopy, synchrotron-based X-ray techniques have substantially expanded the understanding of sintering dynamics at the bulk scale [30–33], as shown in Fig. 1.2b. High-energy X-ray microtomography enables non-destructive 3D imaging of powder compacts during sintering, revealing anisotropic shrinkage, pore network evolution, and the persistence of packing defects [30, 31, 34]. For example, studies by Lame et al. [30] demonstrated that prior compaction history governs the redistribution of residual porosity during sintering. Additionally, in-situ synchrotron X-ray diffraction (XRD)

has been employed to monitor real-time phase transformations, strain evolution, and redox reactions in Cu NPs, linking crystallographic changes to the thermodynamics and kinetics of sintering under reactive environments [35]. The integration of multimodal techniques combining in-situ SEM, TEM, and synchrotron data has enabled correlative analysis of microstructural evolution across spatial and temporal scales. Ultimately, these in-situ studies form a critical foundation for developing predictive models of sintering and for optimizing processing strategies in nanoparticle-based material systems.

1.2.2. MICROSTRUCTURE CHARACTERIZATION

The inherently high porosity and nanoscale feature sizes characteristic of sintered metallic NPs present significant challenges for both mechanical property evaluation and accurate microstructural characterization. Traditional two-dimensional (2D) imaging techniques, such as SEM and TEM, remain indispensable tools for initial assessments of microstructural features. These methods enable detailed visualization of surface morphology, particle-particle contact, and the formation of sintering necks, as well as pore shape and distribution. For example, Zuo et al. [36] investigated the microstructural evolution of Cu NPs under pressureless sintering conditions, employing sequence of SEM observation to capture grain growth and grain boundary migration at elevated temperatures, thereby offering valuable insights into nanoscale densification mechanisms.

However, due to the complex three-dimensional (3D) architecture of sintered NP networks—where interparticle connections and pore interconnectivity govern functional properties such as electrical conductivity, thermal transport, and mechanical integrity—2D imaging alone is often insufficient for comprehensive analysis. As a result, volumetric characterization techniques have become essential to capture the true spatial distribution of microstructural features. Two widely adopted approaches for 3D reconstruction are focused ion beam–scanning electron microscopy (FIB-SEM) serial sectioning [37–40] and synchrotron-based X-ray computed tomography (XCT) [41–43]. FIB-SEM provides nanoscale resolution and is particularly suitable for characterizing high-resolution sub-micron structures in NP sintered bodies (Fig. 1.3a), while synchrotron XCT offers non-destructive imaging capabilities with the advantage of larger volume analysis, albeit at slightly lower spatial resolution (Fig. 1.3b).

Through 3D reconstruction, critical geometric parameters, such as pore volume fraction [38], neck diameter distribution, coordination number, and mean intercept length [39], can be quantitatively extracted to describe the evolving microstructure during sintering. Moreover, metrics such as particle sphericity, connectivity, and tortuosity enable a more nuanced understanding of structure–property relationships. Recent work has also introduced the concept of areal relative density curves derived from 3D image stacks [37, 44, 45], which allow for the quantification of local density fluctuations and porosity anisotropy across different spatial planes. These analyses provide a direct link between processing parameters, microstructural heterogeneity, and the resultant macroscopic performance of the sintered structure.

Moreover, characterizing the crystallographic grain structure, specifically grain orientation, size and residual stress, is essential for understanding the mechanical and functional properties of sintered NPs. Grain orientation governs anisotropic behavior in plastic deformation and crack propagation, while residual stress influences reliabil-

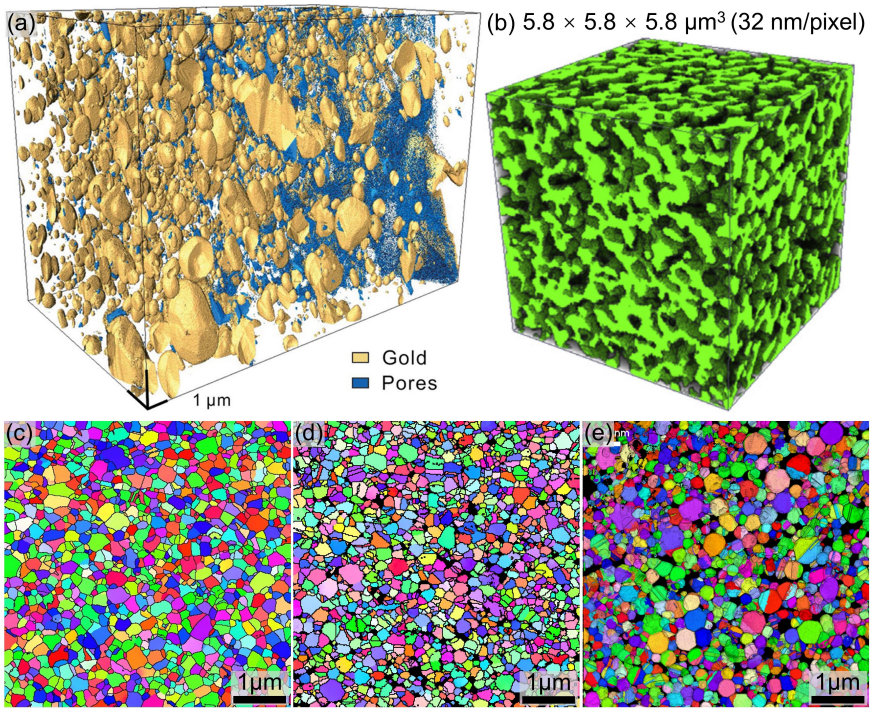


Figure 1.3: (a) FIB-SEM 3D reconstruction (Avizo); (b) synchrotron XCT reconstruction [41]; (c–e) crystallographic grain orientation maps obtained by (c) EBSD, (d) TKD, and (e) PED techniques.

ity under thermal and mechanical loading. In nanoparticle-sintered materials, where grain size often falls in the sub-micron or nanometer regime, conventional techniques like electron backscatter diffraction (EBSD) face spatial resolution limitations. EBSD (Fig. 1.3c), typically performed in a SEM, provides orientation maps and grain boundary information with a resolution down to 50 nm [46, 47], making it suitable for microcrystalline structures. However, for nanocrystalline sintered Cu or Ag structures, higher-resolution methods are required. Transmission Kikuchi Diffraction (TKD) [48, 49], an adaptation of EBSD performed in transmission mode, can achieve 10 nm resolution and is particularly effective for thin foils prepared from sintered films (Fig. 1.3d). Precession Electron Diffraction (PED), typically conducted in TEM, offers even finer spatial resolution and enables accurate orientation and strain mapping at the nanoscale [50, 51], as shown in Fig. 1.3e. These advanced diffraction techniques are critical not only for grain size quantification but also for capturing crystallographic texture, local misorientation, and strain distributions—parameters that directly impact sintering behavior, mechanical reliability, and electronic performance in advanced packaging applications.

In summary, the combined use of high-resolution 2D imaging and advanced 3D reconstruction techniques forms a comprehensive framework for characterizing the hierarchical porosity and structural complexity inherent to sintered NPs. Such multiscale characterization is indispensable for guiding process optimization and predictive mod-

eling in advanced electronic packaging and functional materials design. Complementing these approaches, crystallographic grain orientation analysis—achieved through techniques such as TKD and PED—provides critical insights into grain size, texture, and local strain at the nanoscale. These parameters significantly influence sintering kinetics, anisotropic mechanical behavior, and overall device reliability, thereby underscoring the importance of integrated structural and crystallographic characterization in understanding and engineering nanoparticle-based sintered materials.

1.2.3. MULTISCALE SINTERING SIMULATION

Multiscale modeling provides a comprehensive understanding of sintering by integrating atomic, mesoscale, and macroscopic perspectives. Molecular Dynamics (MD) simulations play a crucial role in capturing atomic-scale mechanisms such as surface diffusion and dislocation-driven densification [45, 52–54]. Liu et al. [52] used MD simulations to investigate how substrate surface roughness affects the sintering quality of Cu NPs, revealing that smaller roughness enhances sintering, whereas larger roughness negatively impacts the densification process. Kart et al. [53] explored the thermodynamic properties of Cu NPs using MD, demonstrating that nanoparticle size significantly influences melting temperatures and diffusion rates. The primary advantage of MD lies in its ability to provide detailed insights into atomic interactions and defect formation (Fig. 1.4a). However, it is severely constrained by small time and length scales, typically simulating only nanoseconds and small domains, making it unsuitable for studying large-scale sintering behavior. Phase-Field (PF) models [55–58] are widely used for mesoscale simulations of sintering, particularly in capturing microstructural evolution (Fig. 1.4b). Chockalingam et al. [55] developed a PF model for sintering of Ag NPs, incorporating tensorial mobility formulations to accurately describe diffusion along particle surfaces. Similarly, Hötzer et al. [57] applied a PF model to study solid-state sintering, implementing a grand potential approach to investigate volume, surface, and grain boundary diffusion. The advantage of PF modeling is its ability to predict complex sintering phenomena such as anisotropic pore alignment and grain coarsening with high accuracy. However, it requires significant computational resources, particularly for large-scale three-dimensional simulations, and the diffuse interface nature of the model may limit its ability to capture sharp grain boundaries accurately. Monte Carlo (MC) simulations [59–62] are effective in predicting sintering kinetics, grain growth, and pore migration, making them particularly useful for large-scale microstructure evolution studies (Fig. 1.4c). Song et al. [59] employed a kinetic Monte Carlo (KMC) model to simulate nanoparticle deposition and diffusion, highlighting its efficiency in handling large time scales compared to MD. Zhou et al. [60] extended KMC simulations to study sintering in composite electrodes, demonstrating that machine learning-assisted calibration significantly improves predictive accuracy. The key advantage of MC methods is their ability to efficiently handle large microstructures while maintaining relatively low computational costs. However, they lack detailed temporal resolution and atomic-scale accuracy, making them less effective for studying fine-grained diffusion mechanisms. Discrete Element Method (DEM) is particularly useful for modeling particle rearrangement and stress distribution in sintered powders [63–66]. Martin et al. [63] applied DEM to simulate the densification of metallic powders, incorporating coarsening effects to achieve favorable comparisons

with experimental data (Fig. 1.4d). Paredes-Goyes et al. [64] used DEM to investigate two-step sintering of alumina nanopowders, demonstrating that heating rate and grain boundary mobility significantly influence densification and grain growth suppression. The advantage of DEM is its ability to model particle-scale mechanical interactions, making it ideal for studying densification and stress evolution. However, it oversimplifies atomic-scale diffusion mechanisms and grain boundary interactions, requiring integration with other methods for a more complete sintering analysis.

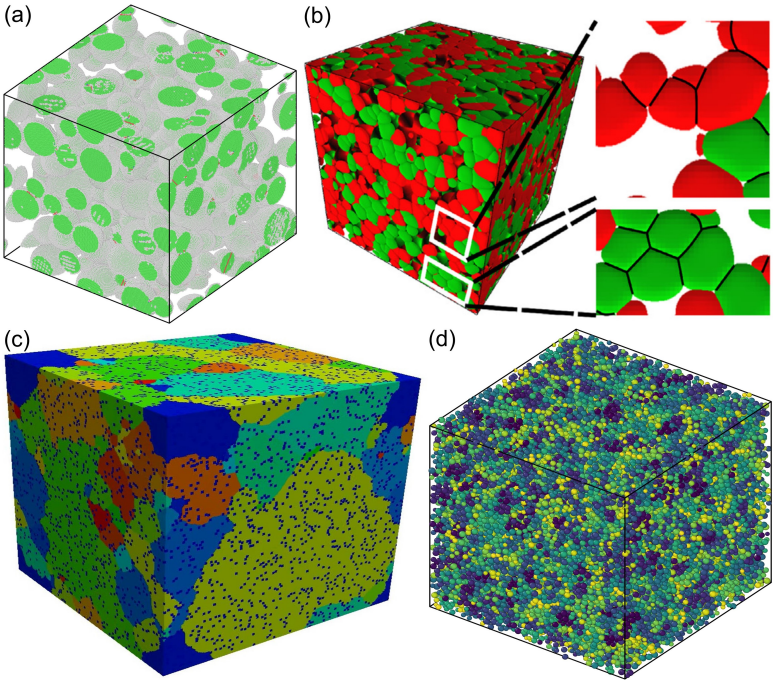


Figure 1.4: Simulations of sintering dynamics using various modeling approaches: (a) MD simulation; (b) PF modeling [56]; (c) MC simulation; (d) DEM simulation.

In summary, the integration of these multiscale modeling approaches enables a comprehensive understanding of sintering phenomena. MD offers unparalleled resolution of defect dynamics, PF modeling excels in describing continuous diffusion-driven microstructure evolution, MC provides time-efficient exploration of large-scale kinetic processes, and DEM captures the granular mechanics of particle interactions. The synergistic application of these methods allows for accurate prediction and optimization of sintering behavior across scales, ultimately supporting the rational design of nanoparticle-based materials.

1.3. OVERVIEW OF MECHANICAL BEHAVIOR

1.3.1. MACROSCALE MECHANICAL EXPERIMENTS

At the macroscale, several experimental techniques have been developed to evaluate the mechanical behavior of sintered NP materials, particularly in the context of die-attach layers for power electronics. Among these, the shear test is one of the most widely adopted methods [10, 67–69], offering critical insights into interfacial adhesion strength and porosity evolution, as shown in Fig. 1.5a. This method is especially relevant for assessing the long-term reliability of sintered joints under thermal and mechanical stresses. For example, Paknejad et al. [70] demonstrated that the shear strength of sintered Ag NPs on Ag substrates increases with aging due to grain coarsening and reduced porosity. Conversely, on Au substrates, void migration during thermal aging was found to degrade interfacial strength, highlighting substrate-dependent failure mechanisms. Tensile test has also been extensively employed to evaluate the bulk mechanical performance of sintered NP films [71–74]. Wakamoto et al. [71] investigated sintered Ag films reinforced with CuO NPs, revealing that increased reinforcement content enhances tensile strength but compromises ductility due to restricted grain boundary mobility. In addition, thermal shock and thermal cycling tests are commonly used to assess fatigue resistance by subjecting samples to repeated heating and cooling [75–77]. While these methods provide valuable information on degradation behavior, they are inherently time-consuming, limiting their practicality in accelerated reliability testing. To address these limitations, bending tests—such as the nine-point bending (NPB) test proposed by Wakamoto et al.—have been developed to induce out-of-plane deformation and accelerate failure in die-attach layers [78]. However, the macroscopic scale of these tests often fails to replicate the actual dimensions and stress states of thin bond-lines (<100 μm), limiting their applicability to real device conditions.

Overall, while these macroscale methods offer essential performance metrics, they lack the resolution to decouple intrinsic failure mechanisms from complex, integrated structures and cannot fully capture the localized mechanical behavior intrinsic to nanoscale sintered interfaces.

1.3.2. MICROSCALE MECHANICAL EXPERIMENTS

To complement macroscale test, microscale mechanical characterization techniques have emerged as essential tools for probing the intrinsic mechanical behavior of sintered NP materials with high spatial resolution. Among these, nanoindentation is widely employed to quantify localized hardness, elastic modulus, and time-dependent creep behavior [79–82]. This method enables depth controlled mechanical probing of heterogeneous microstructures, making it particularly suitable for sintered structures with grain- or pore-scale inhomogeneities (Fig. 1.5b). For instance, Long et al. [80] demonstrated that sintered Ag NPs exhibit increased hardness but reduced ductility compared to bulk counterparts, attributing these trends to grain boundary effects. Further, Zhang et al. [83] showed a notable decrease in hardness at elevated temperatures due to thermally activated vacancy formation and enhanced creep, underscoring the temperature sensitivity of sintered nanostructures. Micro-pillar compression test provides direct measurements of yield strength and plasticity at the microscale (Fig. 1.5c), with the abil-

ity to resolve size effects and deformation mechanisms in isolated micro-volumes [84–87]. Studies by Singh et al. [88] and Mayer et al. [89] revealed that smaller-diameter pillars exhibit higher flow stresses, consistent with the smaller is stronger paradigm. These tests are particularly useful for studying anisotropic mechanical behavior and the role of nanoscale reinforcements in multilayered or composite sintered materials. Additionally, micro-cantilever bending tests (Fig. 1.5d) have proven effective for quantifying fracture toughness and crack initiation behavior in sintered structures [90–93]. Csanádi et al. [94] and Tarleton et al. [95] demonstrated that failure often originates at submicron defects or weak interfacial regions, highlighting the importance of microstructural integrity in mechanical reliability.

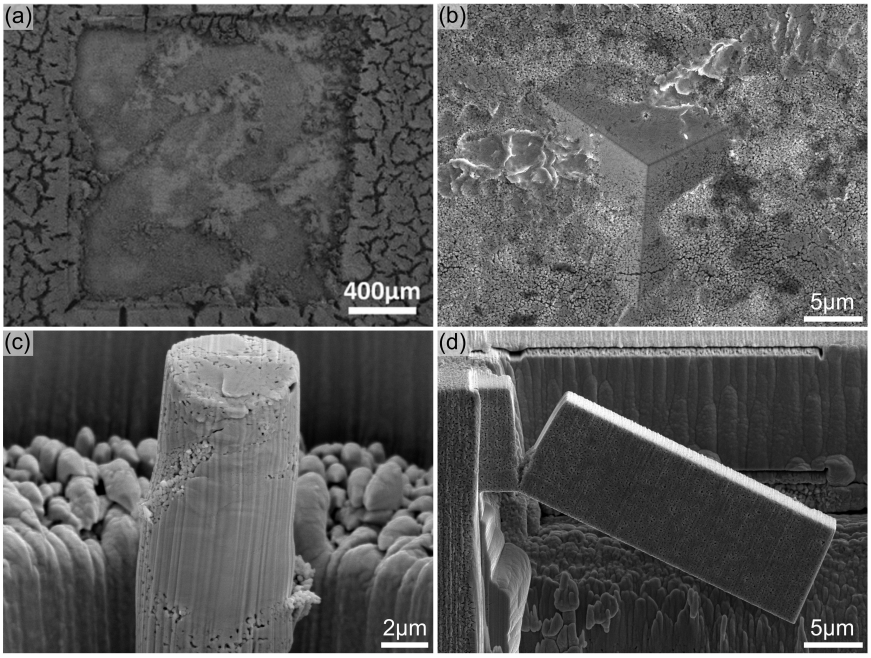


Figure 1.5: SEM images of mechanical testing techniques: (a) Shear test [69]; (b) nanoindentation test; (c) micro-pillar compression test; (d) micro-cantilever bending test.

Collectively, these microscale techniques offer significant advantages over traditional macroscale methods by enabling the quantification of true scale mechanical properties relevant to thin die-attach layers and by providing insights into localized deformation, fracture, and interface-driven failure mechanisms. This localized understanding is crucial for the design and optimization of high-reliability sintered NP-based interconnects.

1.3.3. MULTISCALE MECHANICAL SIMULATION

Multiscale simulation is essential for understanding the mechanical reliability of advanced materials, offering insights into fracture mechanisms across atomic, mesoscale and macroscopic scales. Among the computational methods employed, Molecular

Dynamics (MD) [96–98], Phase-Field (PF) modeling [99–101], Cohesive Zone Modeling (CZM) [100, 102–104], and the Extended Finite Element Method (XFEM) [105–107] provide complementary capabilities for capturing fracture behavior at different length scales. MD simulations excel in resolving atomic-scale phenomena, such as crack nucleation, void coalescence, and dislocation-mediated failure mechanisms (Fig. 1.6a). For instance, Zhan et al. [96] utilized MD to investigate sintering and fracture processes, revealing that high-temperature conditions enhance neck growth but also induce stress localization at grain boundaries, leading to premature failure. Malti et al. [97] further demonstrated the role of dislocation nucleation in influencing fracture toughness at elevated temperatures. However, MD is inherently limited by its nanoscale domain size and nanosecond time scales, making it unsuitable for modeling larger-scale fracture evolution.

At the mesoscale, PF modeling offers a robust framework for simulating crack propagation by treating fractures as diffuse interfaces (Fig. 1.6b). This approach is particularly effective for capturing the influence of microstructural features, such as grain boundaries and porosity, on crack paths. Clayton et al. [99] applied PF modeling to polycrystalline materials, demonstrating that grain boundary anisotropy significantly affects crack propagation behavior. Despite its strengths, PF modeling is computationally demanding, especially for three-dimensional simulations, which limits its application to larger systems. For interfacial failure analysis, CZM provides a discrete approach to simulating debonding and crack initiation at material interfaces (Fig. 1.6c, d). Faivre et al. [103] developed a CZM-based energy minimization model that accurately predicts fracture initiation in porous structures, leveraging experimental data from microcantilever bending tests. However, CZM requires predefined traction-separation laws, which can restrict its ability to model emergent fracture phenomena.

At the macroscopic scale, the XFEM is widely used to simulate arbitrary crack propagation without the need for remeshing. Khoei et al. [105] extended XFEM to analyze crack evolution in porous materials, demonstrating its ability to capture the influence of microstructural connectivity on fracture resistance. Their results closely aligned with experimental R-curve behavior, validating XFEM as a reliable tool for large-scale fracture analysis. Nevertheless, XFEM can become computationally intensive when applied to highly heterogeneous microstructures.

When applied to sintered Cu NPs, these multiscale methods collectively bridge the gap between atomic-scale damage mechanisms (MD), mesoscale crack nucleation and propagation (PF and CZM), and macroscopic fracture behavior (XFEM). For example, MD simulations reveal how sintering conditions influence stress localization and dislocation activity, while PF and CZM models elucidate the role of porosity and sintered neck distributions in fracture energy dissipation. XFEM, on the other hand, provides a comprehensive understanding of large-scale crack growth and its dependence on microstructural connectivity. By integrating these approaches, researchers can achieve a holistic understanding of fracture processes, enabling the design of materials with enhanced mechanical performance and reliability.

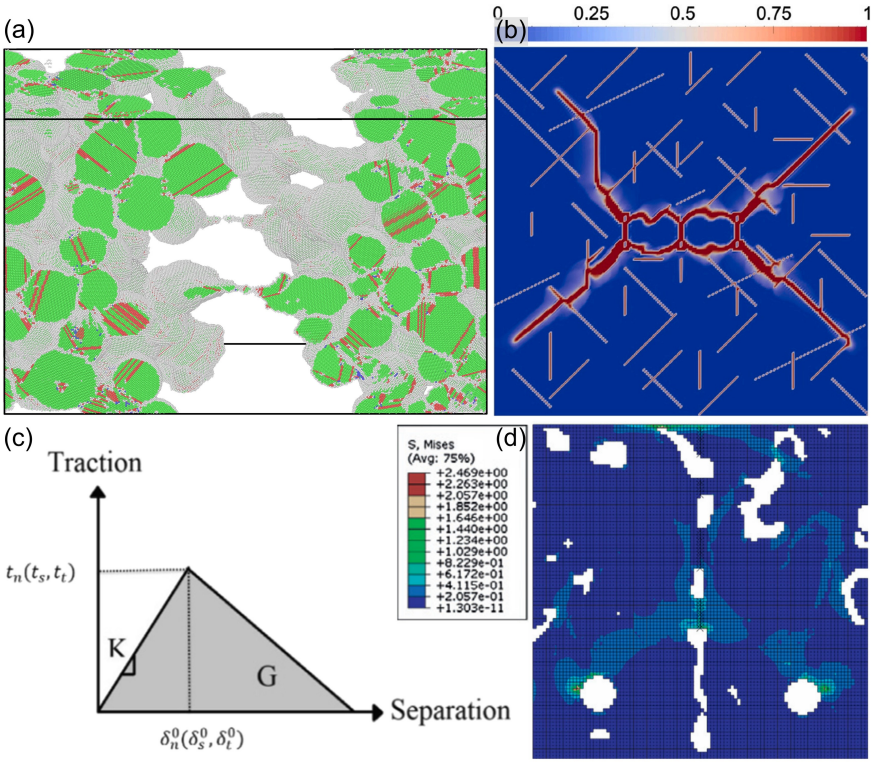


Figure 1.6: Fracture modeling using multiscale approaches: (a) MD simulation; (b) PF simulation of crack propagation [101]; (c, d) CZM illustrating traction–separation behavior and stress distribution [102].

1.4. MOTIVATION AND OUTLINE

1.4.1. MOTIVATION

Understanding the microstructure evolution and deformation mechanisms of sintered Cu NPs is essential for advancing their application in electronic packaging. While the mechanical behavior of sintered Cu has been widely studied, several critical issues, such as fracture anisotropy, interfacial reliability, and temperature-dependent degradation, remain inadequately addressed. This thesis aims to bridge these knowledge gaps by integrating microscale mechanical tests with multiscale simulation, providing a comprehensive framework to elucidate the intrinsic and extrinsic factors governing the mechanical performance of sintered Cu NPs.

A challenge lies in the anisotropic fracture behavior of sintered Cu, which is strongly influenced by porosity, grain structure, and sintering conditions. This work systematically investigates the role of sintering-induced voids in modulating strength and failure mechanisms, with particular emphasis on the evolution of porosity and its localization near interfaces. High-temperature mechanical behavior is also explored, focusing on grain boundary sliding, dislocation climb, and creep—phenomena that critically determine thermal stability in service environments. Interfacial strength between sintered

Cu NPs and Cu substrates is another focal point, as it governs the mechanical integrity of metallurgical bonds in electronic interconnects. This research further examines the influence of particle morphology (monomodal, bimodal, and flake-shape) on fracture toughness, densification kinetics, and crack path deflection. Finally, the thesis explores the use of Atomic Layer Deposition (ALD) coatings to enhance interfacial adhesion and crack resistance, offering a novel route for engineering sintered Cu materials with improved mechanical reliability.

Collectively, the insights gained from this study contribute to a deeper understanding of sintering-induced mechanical behavior and support the rational design of high-performance Cu-based interconnect materials for advanced electronic packaging.

1.4.2. OUTLINE

This thesis is structured into eight chapters, systematically investigating the microstructure evolution and mechanical behavior of sintered Cu NPs through an integrated approach combining experimental characterization and multiscale simulations. The research addresses critical aspects such as anisotropic fracture toughness, porosity-dependent mechanical properties, high-temperature deformation mechanisms, interface strength, particle morphology effects, and the role of ALD coatings.

Chapter 1 introduces the importance of sintered Cu NPs in electronic packaging, with emphasis on applications in power electronics and interconnects. It provides a critical review of existing literature on microstructure evolution and mechanical behavior, highlighting unresolved gaps in linking multiscale simulations with microscale mechanical tests.

Chapter 2 presents the fundamentals of pressure-assisted sintering, focusing on the influence of processing conditions on microstructural evolution, porosity formation, and sintered neck growth. The chapter highlights the emergence of anisotropy in sintered Cu NPs and its implications for mechanical strength, supported by micro-cantilever bending tests and tensile simulations.

Chapter 3 examines the porosity-dependent mechanical properties of sintered Cu NPs. Micro-pillar compression tests are conducted under varying sintering pressures. This chapter underscores the importance of sintering pressure in tailoring mechanical strength and deformation mechanism.

Chapter 4 investigates the viscoplastic deformation behavior of sintered Cu NPs at higher temperature. The Anand model is employed to quantitatively describe the deformation response. Phase-field fracture simulations further enhance understanding of crack propagation in porous structures, offering critical insights into the mechanical stability of sintered Cu under high-temperature conditions.

Chapter 5 explores the interface strength and fracture behavior of sintered Cu NP-Cu substrate systems, which are critical for all-Cu interconnect applications. Micro-cantilever bending tests reveal higher fracture toughness at the Cu-Cu interface due to strong interfacial bonding and reduced void density. The findings validate the feasibility of direct Cu-Cu sintering for high-performance microelectronic interconnects.

Chapter 6 investigates how particle morphology (monomodal, bimodal, flake-shaped) affects fracture toughness and crack propagation. Micro-cantilever bending tests show that bimodal Cu offers better densification and mechanical stability, while

flake-shaped Cu displays anisotropic porosity and weak interlamellar bonding. The J-integral method quantifies crack initiation and growth, linking morphology to microstructure and mechanical performance.

Chapter 7 examines modes I–III fracture toughness and the effect of ALD coatings on the fracture resistance of sintered Cu NPs. Micro-cantilever bending tests reveal anisotropic toughness under varying loading modes, with ALD coatings enhancing interparticle bonding and limiting plastic deformation. The findings inform design strategies for ALD-coated Cu in power electronics and interconnect applications.

Chapter 8 summarizes the key findings of this thesis and outlines future research directions for sintered Cu NPs. By integrating multiscale simulations (MD, PF, CZM) and micro-mechanical tests (micro-cantilever bending, micro-pillar compression, nanoindentation), this research establishes a comprehensive framework for understanding and enhancing the mechanical reliability of sintered Cu NPs.

REFERENCES

[1] C. Eddy Jr and D. Gaskill, "Silicon carbide as a platform for power electronics", *Science*, vol. 324, no. 5933, pp. 1398–1400, 2009.

[2] C. Buttay *et al.*, "State of the art of high temperature power electronics", *Materials Science and Engineering: B*, vol. 176, no. 4, pp. 283–288, 2011.

[3] Y. Gao *et al.*, "Reliability analysis of sintered cu joints for sic power devices under thermal shock condition", *Microelectronics Reliability*, vol. 100, p. 113 456, 2019.

[4] M. Sadiq, M. Khan, A. Mateen, M. Shahzad, K. Akhtar, J. Khan, *et al.*, "Thermal aging impact on microstructure, creep and corrosion behavior of lead-free solder alloy (sac387) use in electronics", *Microelectronics Reliability*, vol. 122, p. 114 180, 2021.

[5] W. Zhang *et al.*, "A supersaturated cu-ag nanoalloy joint with ultrahigh shear strength and ultrafine nanoprecipitates for power electronic packaging", *Journal of Materials Science & Technology*, vol. 145, pp. 56–65, 2023.

[6] J. Wang *et al.*, "Nucleation and growth of cu6sn5 during the aging process of cu/sn interface in electronic packaging-by in-situ tem", *Acta Materialia*, vol. 264, p. 119 581, 2024.

[7] Z. Wu *et al.*, "Novel cu@ ag micro/nanoparticle hybrid paste and its rapid sintering technique via electromagnetic induction for high-power electronics", *ACS omega*, vol. 8, no. 34, pp. 31 021–31 029, 2023.

[8] B. H. Lee, M. Z. Ng, A. A. Zinn, and C. L. Gan, "Application of copper nanoparticles as die attachment for high power led", in *2015 IEEE 17th Electronics Packaging and Technology Conference (EPTC)*, IEEE, 2015, pp. 1–5.

[9] H.-J. Huang, X. Wu, M.-B. Zhou, and X.-P. Zhang, "A highly reliable die bonding approach for high power devices by low temperature pressureless sintering using a novel Cu nanoparticle paste", in *2020 IEEE 70th Electronic Components and Technology Conference (ECTC)*, IEEE, 2020, pp. 1697–1702.

[10] D. Dai *et al.*, "A rapid-sintering cu-cu joints with ultrahigh shear strength and super reliability for power electronics package", *Materials Science in Semiconductor Processing*, vol. 178, p. 108 405, 2024.

[11] J. Liu, H. Chen, H. Ji, and M. Li, "Highly conductive cu–cu joint formation by low-temperature sintering of formic acid-treated cu nanoparticles", *ACS applied materials & interfaces*, vol. 8, no. 48, pp. 33 289–33 298, 2016.

[12] A. Bouafia *et al.*, "The recent progress on silver nanoparticles: Synthesis and electronic applications", *Nanomaterials*, vol. 11, no. 9, p. 2318, 2021.

[13] H. W. Tan, J. An, C. K. Chua, and T. Tran, "Metallic nanoparticle inks for 3d printing of electronics", *Advanced Electronic Materials*, vol. 5, no. 5, p. 1 800 831, 2019.

[14] L. Liu, T. Chen, L. Han, Z. Qian, J. Li, and G. Gan, "Thermally conductive silver adhesive enhanced by mxene@ agnps with excellent thermal conductivity for thermal management applications", *Applied Surface Science*, vol. 672, p. 160 787, 2024.

[15] Z. Zeng, J. Zhang, and P. Liu, "Review of copper-silver core-shell sintering pastes: Technology and future trends", in *2021 22nd International Conference on Electronic Packaging Technology (ICEPT)*, IEEE, 2021, pp. 1–6.

[16] Z. Cui *et al.*, "Review on shear strength and reliability of nanoparticle sintered joints for power electronics packaging", *Journal of Electronic Materials*, vol. 53, no. 6, pp. 2703–2726, 2024.

[17] L. Del Carro, J. Zürcher, U. Drechsler, I. E. Clark, G. Ramos, and T. Brunschwiler, "Low-temperature dip-based all-copper interconnects formed by pressure-assisted sintering of copper nanoparticles", *IEEE Transactions on Components, Packaging and Manufacturing Technology*, vol. 9, no. 8, pp. 1613–1622, 2019.

[18] S. Wang, G. Zou, Y. Wu, Z. Deng, R. Du, and L. Liu, "Patterned Cu nanoparticle film for all-Cu interconnection without chemical mechanical polishing pretreatment", *IEEE Transactions on Components, Packaging and Manufacturing Technology*, vol. 13, no. 5, pp. 604–614, 2023.

[19] J. Zürcher *et al.*, "Nanoparticle assembly and sintering towards all-copper flip chip interconnects", in *2015 IEEE 65th Electronic Components and Technology Conference (ECTC)*, IEEE, 2015, pp. 1115–1121.

[20] H. Alarifi, "Ag nanoparticles and their application in low-temperature bonding of cu", 2014.

[21] F. Orsini *et al.*, "In situ scanning electron microscopy (sem) observation of interfaces within plastic lithium batteries", *Journal of power sources*, vol. 76, no. 1, pp. 19–29, 1998.

[22] X. Hu *et al.*, "Investigating sintering mechanism of 100 nm ag nanoparticles via in-situ sem observation and phase field simulation", in *2024 IEEE 74th Electronic Components and Technology Conference (ECTC)*, IEEE, 2024, pp. 1236–1240.

[23] Y. Zuo, S. Carter-Searjeant, M. Green, L. Mills, and S. H. Mannan, "Low temperature cu joining by in situ reduction-sintering of cuo nanoparticle for high power electronics", *Advanced Powder Technology*, vol. 31, no. 10, pp. 4135–4144, 2020.

[24] M. Asoro, P. Ferreira, and D Kovar, "In situ transmission electron microscopy and scanning transmission electron microscopy studies of sintering of ag and pt nanoparticles", *Acta Materialia*, vol. 81, pp. 173–183, 2014.

[25] T. B. Holland, A. M. Thron, C. S. Bonifacio, A. K. Mukherjee, and K. van Benthem, "Field assisted sintering of nickel nanoparticles during in situ transmission electron microscopy", *Applied Physics Letters*, vol. 96, no. 24, 2010.

[26] C. S. Bonifacio, J. F. Rufner, T. B. Holland, and K. Van Benthem, "In situ transmission electron microscopy study of dielectric breakdown of surface oxides during electric field-assisted sintering of nickel nanoparticles", *Applied Physics Letters*, vol. 101, no. 9, 2012.

[27] J. Mittal and K.-L. Lin, "Exothermic low temperature sintering of cu nanoparticles", *Materials Characterization*, vol. 109, pp. 19–24, 2015.

[28] A. P. LaGrow, D. C. Lloyd, P. L. Gai, and E. D. Boyes, "In situ scanning transmission electron microscopy of ni nanoparticle redispersion via the reduction of hollow nio", *Chemistry of Materials*, vol. 30, no. 1, pp. 197–203, 2018.

[29] C. Chen, Z. Hu, Y. Li, L. Liu, H. Mori, and Z. Wang, "In-situ high-resolution transmission electron microscopy investigation of overheating of cu nanoparticles", *Scientific reports*, vol. 6, no. 1, p. 19 545, 2016.

[30] O. Lame, D. Bellet, M. Di Michiel, and D. Bouvard, "In situ microtomography investigation of metal powder compacts during sintering", *Nuclear Instruments and Methods in Physics Research Section B: Beam Interactions with Materials and Atoms*, vol. 200, pp. 287–294, 2003.

[31] O Lame, D Bellet, M Di Michiel, and D Bouvard, "Bulk observation of metal powder sintering by x-ray synchrotron microtomography", *Acta materialia*, vol. 52, no. 4, pp. 977–984, 2004.

[32] A. M. Venkatesh, "In-situ x-ray nano-tomography analysis of ceramic powder sintering", Ph.D. dissertation, Université Grenoble Alpes [2020-....], 2023.

[33] A. Y. Khodakov *et al.*, "Assessment of metal sintering in the copper-zeolite hybrid catalyst for direct dimethyl ether synthesis using synchrotron-based x-ray absorption and diffraction", *Catalysis today*, vol. 343, pp. 199–205, 2020.

[34] L. Olmos *et al.*, "Analysing the sintering of heterogeneous powder structures by in situ microtomography", *Philosophical Magazine*, vol. 89, no. 32, pp. 2949–2965, 2009.

[35] J. Feijóo *et al.*, "Operando high-energy-resolution x-ray spectroscopy of evolving cu nanoparticle electrocatalysts for co2 reduction", *Journal of the American Chemical Society*, vol. 145, no. 37, pp. 20 208–20 213, 2023.

[36] Y. Zuo, C. Zhao, A. Robador, M. Wickham, and S. H. Mannan, "Quasi-in-situ observation of the grain growth and grain boundary movement in sintered cu nanoparticle interconnects", *Acta Materialia*, vol. 236, p. 118 135, 2022.

[37] T. Youssef *et al.*, "Power modules die attach: A comprehensive evolution of the nanosilver sintering physical properties versus its porosity", *Microelectronics Reliability*, vol. 55, no. 9-10, pp. 1997–2002, 2015.

[38] B. Chen, Z. Xia, and K. Lu, "Understanding sintering characteristics of zno nanoparticles by fib-sem three-dimensional analysis", *Journal of the European Ceramic Society*, vol. 33, no. 13-14, pp. 2499–2507, 2013.

[39] G. Okuma *et al.*, "Anisotropic microstructural evolution and coarsening in free sintering and constrained sintering of metal film by using fib-sem tomography", *Acta Materialia*, vol. 215, p. 117 087, 2021.

[40] X. Hu *et al.*, "Exploring the process-microstructure-thermal properties relationship of resin-reinforced ag sintering material for high-power applications via 3d fib-sem nanotomography", *Materials & Design*, vol. 244, p. 113 185, 2024.

[41] E. Wargo, T Kotaka, Y Tabuchi, and E. Kumbur, "Comparison of focused ion beam versus nano-scale x-ray computed tomography for resolving 3-d microstructures of porous fuel cell materials", *Journal of Power Sources*, vol. 241, pp. 608–618, 2013.

[42] A. M. Venkatesh, D. Bouvard, P. Lhuissier, J. Villanova, and C. Rajon, "In-situ 3d x-ray investigation of ceramic powder sintering at the particle length-scale", *Ceramics International*, vol. 50, no. 3, pp. 4715–4728, 2024.

[43] A. M. Venkatesh, D. Bouvard, P. Lhuissier, and J. Villanova, "3d analysis of ceramic powder sintering by synchrotron x-ray nano-tomography", *Journal of the European Ceramic Society*, vol. 43, no. 6, pp. 2553–2563, 2023.

[44] P. Gadaud, V. Caccuri, D. Bertheau, J. Carr, and X. Milhet, "Ageing sintered silver: Relationship between tensile behavior, mechanical properties and the nanoporous structure evolution", *Materials Science and Engineering: A*, vol. 669, pp. 379–386, 2016.

[45] L. Du *et al.*, "Microstructural and mechanical anisotropy in pressure-assisted sintered copper nanoparticles", *Acta Materialia*, vol. 287, p. 120 772, 2025.

[46] S. Gamanov, A Dlouhy, D Bürger, G Eggeler, and P Thome, "Evolution of local misorientations in the γ/γ'-microstructure of single crystal superalloys during creep studied with the rotation vector baseline (rvb) ebsd method", *Microscopy research and technique*, vol. 87, no. 3, pp. 516–533, 2024.

[47] A. Mandal, B. Beausir, J. Guyon, V. Taupin, and A. Guitton, "Estimation of dislocation densities with nondestructive scanning electron microscope techniques: Application to gallium nitride", *Microscopy and Microanalysis*, vol. 31, no. 1, ozae124, 2025.

[48] G. C. Sneddon, P. W. Trimby, L. Tegg, and J. M. Cairney, "Parameter dependence of depth and lateral resolution of transmission kikuchi diffraction", *Ultramicroscopy*, vol. 267, p. 114 062, 2024.

[49] L. Crouzier, N. Feltin, and B. Jablon, "A new metrology tool: Using transmission kikuchi diffraction (tkd) to identify and separate nanoparticles for regulatory purposes", *Measurement Science and Technology*, vol. 36, no. 1, p. 015 038, 2024.

[50] L. Du, X. Pan, and Y. Hong, "New insights into microstructure refinement in crack initiation region of very-high-cycle fatigue for slm ti-6al-4v via precession electron diffraction", *Materialia*, vol. 33, p. 102 008, 2024.

[51] P Favia *et al.*, "Unveiling strain in future generation transistor technology by bessel beam electron diffraction method", *Microelectronic Engineering*, vol. 299, p. 112 334, 2025.

[52] G. Liu, H. Li, J. Cao, and J. Shen, "Effect of substrate surface roughness and parameters on the behavior of cu nanoparticles sintering: A study by molecular dynamics simulation", *Applied Surface Science*, p. 162 744, 2025.

[53] H. H. Kart, H Yildirim, S. O. Kart, and T Çağin, "Physical properties of cu nanoparticles: A molecular dynamics study", *Materials Chemistry and Physics*, vol. 147, no. 1-2, pp. 204–212, 2014.

[54] B. Cheng and A. H. Ngan, "The sintering and densification behaviour of many copper nanoparticles: A molecular dynamics study", *Computational materials science*, vol. 74, pp. 1–11, 2013.

[55] K Chockalingam, V. G. Kouznetsova, O. van der Sluis, and M. G. Geers, "2d phase field modeling of sintering of silver nanoparticles", *Computer Methods in Applied Mechanics and Engineering*, vol. 312, pp. 492–508, 2016.

[56] Y. Lei, T.-L. Cheng, and Y.-H. Wen, "Phase field modeling of microstructure evolution and concomitant effective conductivity change in solid oxide fuel cell electrodes", *Journal of Power Sources*, vol. 345, pp. 275–289, 2017.

[57] J. Hötzer, M. Seiz, M. Kellner, W. Rheinheimer, and B. Nestler, "Phase-field simulation of solid state sintering", *Acta Materialia*, vol. 164, pp. 184–195, 2019.

[58] A. Ishii *et al.*, "High-fidelity phase-field simulation of solid-state sintering enabled by bayesian data assimilation using in situ electron tomography data", *Acta Materialia*, vol. 278, p. 120 251, 2024.

[59] J.-H. Song, K.-H. Choi, R. Dai, J.-O. Choi, S.-H. Ahn, and Y. Wang, "Controlled kinetic monte carlo simulation of laser improved nano particle deposition process", *Powder Technology*, vol. 325, pp. 651–658, 2018.

[60] S. Zhou, X. Liu, Z. Yan, S. Hara, N. Shikazono, and Z. Zhong, "Kinetic monte carlo (kmc) simulation of sintering of nickel oxide-yttria stabilized zirconia composites: Model, parameter calibration and validation", *Materials & Design*, vol. 232, p. 112 094, 2023.

[61] N. Sdobnyakov *et al.*, "Solution combustion synthesis and monte carlo simulation of the formation of cuni integrated nanoparticles", *Computational Materials Science*, vol. 184, p. 109 936, 2020.

[62] F. B. Sweidan and H. J. Ryu, "Kinetic monte carlo simulations of the sintering microstructural evolution in density graded stainless steel fabricated by sps", *Materials Today Communications*, vol. 26, p. 101 863, 2021.

[63] C. Martin, L. Schneider, L Olmos, and D Bouvard, "Discrete element modeling of metallic powder sintering", *Scripta materialia*, vol. 55, no. 5, pp. 425–428, 2006.

[64] B. Paredes-Goyes, A. M. Venkatesh, D. Jauffres, and C. L. Martin, "Two-step sintering of alumina nano-powders: A discrete element study", *Journal of the European Ceramic Society*, vol. 43, no. 2, pp. 501–509, 2023.

[65] B. Paredes-Goyes, D. Jauffres, J.-M. Missiaen, and C. L. Martin, "Grain growth in sintering: A discrete element model on large packings", *Acta Materialia*, vol. 218, p. 117 182, 2021.

[66] T. Yu, Z. Zhao, and J. Li, "Effects of refined grains and doped nanoparticles on fabricating al2o3 ceramics using binder jetting", *Ceramics International*, vol. 50, no. 17, pp. 30 533–30 540, 2024.

[67] Z. Pešina, V. Vykoukal, M. Palcut, and J. Sopoušek, "Shear strength of copper joints prepared by low temperature sintering of silver nanoparticles", *Electronic Materials Letters*, vol. 10, pp. 293–298, 2014.

[68] J.-W. Yoon and J.-H. Back, "Effect of sintering conditions on the mechanical strength of cu-sintered joints for high-power applications", *Materials*, vol. 11, no. 11, p. 2105, 2018.

[69] Q. Zhang *et al.*, "Mechanical property and reliability of bimodal nano-silver paste with ag-coated sic particles", *Soldering & Surface Mount Technology*, vol. 31, no. 4, pp. 193–202, 2019.

[70] S. Paknejad, G Dumas, G West, G Lewis, and S. Mannan, "Microstructure evolution during 300 c storage of sintered ag nanoparticles on ag and au substrates", *Journal of Alloys and Compounds*, vol. 617, pp. 994–1001, 2014.

[71] K. Wakamoto, Y. Kumakiri, and T. Namazu, "Mechanical property changes in sintered silver films by including copper oxide nanoparticles", *Microelectronics Reliability*, vol. 153, p. 115 322, 2024.

[72] T. Matsuda *et al.*, "Fracture behavior of thermally aged ag–cu composite sinter joint through microscale tensile test coupled with nano x-ray computed tomography", *Materials & Design*, vol. 206, p. 109 818, 2021.

[73] T. Ogura, T. Yagishita, S. Takata, T. Fujimoto, and A. Hirose, "Bondability of copper joints formed using a mixed paste of ag2o and cuo for low-temperature sinter bonding", *Materials Transactions*, vol. 54, no. 6, pp. 860–865, 2013.

[74] Y. Tang, R. Zhou, H. Li, W. Yuan, and L. Lu, "Experimental study on the tensile strength of a sintered porous metal composite", *Materials Science and Engineering: A*, vol. 607, pp. 536–541, 2014.

[75] L. Wang, Y. Ji, S. Li, and P. Mei, "Effect of particle shapes on thermal shock reliability of sintered ag joints under low-temperature pressureless sintering", *Journal of Materials Engineering and Performance*, vol. 32, no. 10, pp. 4427–4436, 2023.

[76] K. Son, A. Oh, E. Park, and H.-C. Bae, "Thermal shock reliability of micro–nano bimodal cu–ag sintered joints", *Journal of Materials Science: Materials in Electronics*, vol. 33, no. 22, pp. 17 493–17 501, 2022.

[77] J. Son, D.-Y. Yu, Y.-C. Kim, S.-I. Kim, D. Byun, and J. Bang, "Thermal reliability of cu sintering joints for high-temperature die attach", *Microelectronics Reliability*, vol. 147, p. 115 002, 2023.

[78] K Wakamoto, K Fuji, T Otsuka, K Nakahara, and T Namazu, "Nine point bending test technique for understanding of sintered silver die bonding failure mechanism", *Experimental Techniques*, vol. 48, no. 3, pp. 399–408, 2024.

[79] J. Fan *et al.*, "High-temperature nanoindentation characterization of sintered nano-copper particles used in high power electronics packaging", *Results in Physics*, vol. 33, p. 105 168, 2022.

[80] X. Long, B. Hu, Y. Feng, C. Chang, and M. Li, "Correlation of microstructure and constitutive behaviour of sintered silver particles via nanoindentation", *International Journal of Mechanical Sciences*, vol. 161, p. 105 020, 2019.

[81] T. Ishizaki, D Miura, A Kuno, K Hasegawa, M. Usui, and Y Yamada, "Young's modulus of a sintered cu joint and its influence on thermal stress", *Microelectronics Reliability*, vol. 76, pp. 405–408, 2017.

[82] X. Ji, L. Du, S. He, H. van Zeijl, and G. Zhang, "Microstructural and micromechanical characterization of sintered nano-copper bump for flip-chip heterogeneous integration", *Microelectronics Reliability*, vol. 150, p. 115 180, 2023.

[83] H. Zhang, Y. Liu, L. Wang, F. Sun, X. Fan, and G. Zhang, "Indentation hardness, plasticity and initial creep properties of nanosilver sintered joint", *Results in Physics*, vol. 12, pp. 712–717, 2019.

[84] K. Nur *et al.*, "Mechanical properties of cold sintered zno investigated by nanoindentation and micro-pillar testing", *Journal of the European Ceramic Society*, vol. 42, no. 2, pp. 512–524, 2022.

[85] M. S. Saleh, M. HamidVishkasougheh, H. Zbib, and R. Panat, "Polycrystalline micropillars by a novel 3-d printing method and their behavior under compressive loads", *Scripta Materialia*, vol. 149, pp. 144–149, 2018.

[86] C. Chen and K. Suganuma, "Microstructure and mechanical properties of sintered ag particles with flake and spherical shape from nano to micro size", *Materials & Design*, vol. 162, pp. 311–321, 2019.

[87] Q.-G. Jiang, C. Cao, T.-C. Lin, S. Wu, and X. Li, "Strong and tough glass with self-dispersed nanoparticles via solidification", *Advanced Materials*, vol. 31, no. 33, p. 1 901 803, 2019.

[88] S. Singh, *Deformation Behavior of Co-Sputtered and Nanolaminated Metal/Ceramic Composites*. Arizona State University, 2018.

[89] C. R. Mayer, *Mechanical Behavior of Al-SiC Nanolaminate Composites Using Micro-Scale Testing Methods*. Arizona State University, 2016.

[90] D. Hu, L. Du, M. Alfreider, J. Fan, D. Kiener, and G. Zhang, "Microscopic fracture toughness of notched porous sintered cu micro-cantilevers for power electronics packaging", *Materials Science and Engineering: A*, vol. 897, p. 146 316, 2024.

[91] J. Tatami, Y. Imoto, T. Yahagi, T. Takahashi, and M. Iijima, "Relationship between bending strength of bulk porous silicon carbide ceramics and grain boundary strength measured using microcantilever beam specimens", *Journal of the European Ceramic Society*, vol. 40, no. 7, pp. 2634–2641, 2020.

[92] C. Chen *et al.*, "Macroscale and microscale fracture toughness of microporous sintered ag for applications in power electronic devices", *Acta Materialia*, vol. 129, pp. 41–51, 2017.

[93] R. Henry, H. Saad, A. Doitrand, S. Deville, and S. Meille, "Interface failure in nacre-like alumina", *Journal of the European Ceramic Society*, vol. 40, no. 13, pp. 4694–4699, 2020.

[94] T. Csanádi, M. Vojtko, Z. Dankházi, M. J. Reece, and J. Dusza, "Small scale fracture and strength of high-entropy carbide grains during microcantilever bending experiments", *Journal of the European Ceramic Society*, vol. 40, no. 14, pp. 4774–4782, 2020.

[95] E Tarleton, D. Balint, J Gong, and A. Wilkinson, "A discrete dislocation plasticity study of the micro-cantilever size effect", *Acta Materialia*, vol. 88, pp. 271–282, 2015.

[96] L. Zhan, X. Zhu, X. Qin, M. Wu, and X. Li, "Sintering mechanism of copper nanoparticle sphere-plate of crystal misalignment: A study by molecular dynamics simulations", *Journal of Materials Research and Technology*, vol. 12, pp. 668–678, 2021.

[97] A. Malti, A. Kardani, and A. Montazeri, "An insight into the temperature-dependent sintering mechanisms of metal nanoparticles through md-based microstructural analysis", *Powder Technology*, vol. 386, pp. 30–39, 2021.

[98] A Abedini, A Malti, A Kardani, and A Montazeri, "Probing neck growth mechanisms and tensile properties of sintered multi-nanoparticle al-cu systems via md simulation", *Advanced Powder Technology*, vol. 34, no. 8, p. 104 084, 2023.

[99] J. Clayton, J Knap, and R. Leavy, "On rate dependence and anisotropy in phase field modeling of polycrystalline fracture", *Mechanics of Materials*, vol. 180, p. 104 606, 2023.

[100] P. Li *et al.*, "A review on phase field models for fracture and fatigue", *Engineering Fracture Mechanics*, vol. 289, p. 109 419, 2023.

[101] S. Kar, A. Chaudhuri, A. Singh, and S. Pal, "Phase field method to model hydraulic fracturing in saturated porous reservoir with natural fractures", *Engineering Fracture Mechanics*, vol. 286, p. 109 289, 2023.

[102] Q. Dai and K. Ng, "2d cohesive zone modeling of crack development in cementitious digital samples with microstructure characterization", *Construction and Building Materials*, vol. 54, pp. 584–595, 2014.

[103] M Faivre, B. Paul, F. Golfier, R. Giot, P. Massin, and D Colombo, "2d coupled hm-xfem modeling with cohesive zone model and applications to fluid-driven fracture network", *Engineering Fracture Mechanics*, vol. 159, pp. 115–143, 2016.

[104] A. D. Taleghani, M. Gonzalez-Chavez, H. Yu, and H. Asala, "Numerical simulation of hydraulic fracture propagation in naturally fractured formations using the cohesive zone model", *Journal of Petroleum Science and Engineering*, vol. 165, pp. 42–57, 2018.

[105] A. Khoei and M Nikbakht, "Contact friction modeling with the extended finite element method (x-fem)", *Journal of materials processing technology*, vol. 177, no. 1-3, pp. 58–62, 2006.

[106] A. R. Khoei, T. Ahmadpour, and Y. Navidtehrani, "An x–fem technique for modeling the frp strengthening of concrete arches with a plastic–damage model; numerical and experimental investigations", *European Journal of Computational Mechanics*, vol. 30, no. 1, pp. 1–50, 2021.

[107] A. Khoei and M Nikbakht, "An enriched finite element algorithm for numerical computation of contact friction problems", *International Journal of Mechanical Sciences*, vol. 49, no. 2, pp. 183–199, 2007.

2

Microstructural and Mechanical Anisotropy in Pressure-Assisted Sintered Copper Nanoparticles

The mechanical strength of sintered nanoparticles (NPs) limits their application in advanced electronics packaging. In this study, we explore the anisotropy in the microstructure and mechanical properties of sintered copper (Cu) NPs by combining experimental techniques with molecular dynamics (MD) simulations. We establish a clear relationship between processing conditions, microstructural evolution, and resulting properties in pressure-assisted sintering of Cu NPs. Our findings reveal that pressure-assisted sintering induces significant anisotropy in the microstructure, as evidenced by variations in areal relative density and the orientation distribution of necks formed during sintering. Specifically, along the direction of applied pressure, the microstructure exhibits reduced variation in areal relative density and a higher prevalence of necks with favorable orientations. The resulting anisotropic mechanical properties, with significantly higher strength along the pressure direction compared to other directions, are demonstrated through microcantilever bending tests and tensile simulations. This anisotropy is further explained by the combined effects of strain localization (influenced by areal relative density) and the failure modes of necks (determined by their orientation relative to the loading direction). This work provides valuable insights into the analysis of sintered NPs microstructures and offers guidance for optimizing the sintering process.

Parts of this chapter have been published in Acta Materialia, 2025 [1].

2.1. INTRODUCTION

WIDE band gap (WBG) materials like silicon carbide (SiC) and gallium nitride (GaN) have been widely used in power modules owing to their excellent electric and thermal properties and performance [2–4], especially when operated at high breakdown voltages and high temperatures (< 200 ^{o}C). Traditional interconnect bonding materials like Sn- or Pb-based solder alloys face limitations in power devices due to the low melting point, limited thermal conductivity and insufficient creep resistance [5–8]. In recent years, sintered silver (Ag) and copper (Cu) nanoparticles (NPs) interconnects are proposed as an alternative to solder alloys in the die-attachment of WBG semiconductors because of their low sintering temperature, high melting temperature and high electrical and thermal conductivity [9–11].

Despite these advantages, the anisotropy of the microstructure and mechanical properties of sintered Cu NPs poses a critical challenge for the bonding quality and long-term reliability of joints. NPs sintering is characterized by low sintering temperatures (less than 300 ^{o}C), short sintering times, and the assistance of uniaxial compressive stress [12]. This process, while efficient, inherently induces anisotropy in the sintered microstructure. Many experiments have highlighted the anisotropy in micrometer-sized particles, such as alumina and Cu, when sintered with uniaxial compressive stress [13–15]. The sintered bodies exhibit greater shrinkage in the direction of the applied stress. At the microscale, this anisotropy originates from the evolution and orientation change of the pores [13]. The aspect ratio of the pores increases after sintering, and the orientation of the long axis tends to align parallel to the stress direction [16, 17]. Additionally, the constraints imposed by the substrate on particle merging affect the shape of the pores [18]. For Cu NPs, the sintered microstructure is highly porous, and the anisotropy is even more pronounced under these conditions. From a bonding quality perspective, this anisotropy can lead to uneven stress distribution within the joint, particularly during thermal cycling or mechanical loading [15], potentially compromising the structural integrity. Furthermore, from a reliability viewpoint, local variations in mechanical properties can influence crack initiation and propagation pathways [19], significantly affecting the long-term performance. These concerns are especially critical for SiC devices, which often operate under extreme conditions, including high temperatures and power densities. Addressing the anisotropy in the microstructure and mechanical properties of sintered Cu NPs is therefore essential. Given the sintering conditions for NPs, the resulting microstructure after sintering is highly porous, and severe anisotropy is expected [14].

The high porosity and small feature sizes of sintered NPs pose challenges for mechanical property testing and microstructure characterization. Scanning electron microscopy (SEM) and transmission electron microscopy (TEM) are widely used for microstructure observation, such as examining pore shapes and necks formed during sintering. Zuo et al. [20] studied the microstructure evolution of Cu NPs during pressureless sintering. The grain growth and grain boundary movement were clearly observed using TEM at elevated temperature. Since the spatial features of particle packing and pore distribution strongly influence the electrical, thermal, and elastic properties of sintered NPs, three-dimensional (3D) characterization of the microstructure is crucial. Two methods for 3D reconstruction have been reported: focused ion beam combined with scanning electron microscopy (FIB-SEM) [21–23], and synchrotron X-ray computed to-

mography [24, 25]. Through 3D reconstruction, the inter-particle necks can be identified, and the evolution of the microstructure can be described using metrics such as pore numbers [22], mean intercept length [23], and particle shape [24]. Areal relative density curves have also been proposed to illustrate variations in local microstructure [21, 26].

The mechanical properties of sintered NPs are typically measured with micro-pillar compression tests [27] and micro-cantilever bending tests [28–30]. Chen et al. [28] studied the effect of micro-cantilever size (20, 10 and 5 μm in width) on fracture toughness of sintered Ag NPs by micro-cantilever bending tests, revealing that fracture toughness decreases as specimen size decreases. Recently, we studied the effect of depth of pre-crack on the fracture toughness of sintered Cu NPs by micro-cantilever bending tests [30]. Results show that microscopic fracture toughness presents a limited relationship with notch depth.

Due to difficulties in experiments, simulation methods spanning multiple length and time scales are applied to investigate various aspects of NPs sintering. Discrete element modelling (DEM) primarily focuses on the particle packing [18] and neck formation during sintering [31]. Specifically, Wonisch et al. [32] analyzed the anisotropic microstructure of sintered micro-sized particles induced by external stress using both experiments and DEM, identifying the size of contact areas in different directions as a crucial factor. The grain growth and evolution of pores during sintering process are also studied using phase field simulation in both two-dimensional (2D) [33] and 3D [34, 35] models. The relationship between microstructure and properties is modeled using finite element method (FEM) [36, 37] and phase field methods [38]. The porous structure for the simulation are from SEM images [36] and stochastic modeling [37, 38].

Molecular dynamics (MD) simulations have been used to study the NPs sintering process and subsequent mechanical tests. Two-particle models are extensively utilized to examine atom diffusion and neck formation during sintering [39–41]. Multi-particle sintering has also been explored with MD [42–44]. Guo et al. simulated the densification process of a high-entropy alloy to show the influence of initial particle packing [43]. The accuracy and effectiveness of the multiple particles sintering model were verified using a phase-field model. This method was also applied to investigate the influence of initial particle morphology on the sintering of gold NPs [44]. Due to the limited timescale of MD simulations, the contributions of diffusion mechanisms, such as surface diffusion and bulk diffusion, are underestimated, and densification in these simulations is mainly caused by plastic flow under stress. However, MD simulations are expected to yield physically meaningful results considering the short sintering time and low temperature characteristic of NP sintering. Additionally, Zuo et al. [20] demonstrated that without external stress, grain growth and grain boundary mobility are insignificant at 220^{o}C.

This paper aims to elucidate the relationship between sintering methods and microstructural anisotropy, as well as the anisotropy of mechanical properties, through a combination of experiments and simulations. Section 2 details the experimental and simulation methods. In Section 3, the microstructure of sintered Cu NPs from FIB-SEM reconstruction, precession electron diffraction and MD simulations are analyzed based on areal relative density and neck formation during sintering. The origin of microstructural anisotropy is discussed. In Section 4, the strength of sintered NPs is measured by

micro-cantilever bending tests and tensile simulations, and the anisotropic strength of sintered Cu NPs is connected with their microstructure.

2.2. EXPERIMENTAL AND SIMULATION PROCEDURE

2.2.1. CU NPS AND SINTERED SAMPLE PREPARATION

The Cu paste used in this study was prepared by a reductive pretreatment method [45]. Fig. 2.1a presents an SEM image of the Cu NPs, showing them as quasi-spherical and uniformly distributed with an average size (diameter) of 150 nm (Fig. 2.1b). Energy dispersive spectroscopy (EDS) was conducted on the cross-section, confirming the sintered Cu NPs is almost pure with minimal oxidation, as shown in Fig. 2.1c. A die-attach structure (Cu dummy die, sintered Cu NPs layer, and Cu substrate) was prepared using pressure-assisted sintering technology. As illustrated in Fig. 2.1d, the Cu paste was firstly transferred onto the Cu substrate with a stencil thickness of 100 μm using a screen printer and a flat scraper. Second, the substrate was heated to 120^{o}C for 5 minutes to evaporate the organic solvent after removing the stencil. Then, the Cu dummy dies were attached to the substrates using a vacuum pick-up pen. Pressure-assisted sintering was conducted in a nitrogen atmosphere (Applied Microengineering Ltd., UK). The Cu paste was sintered for 10 minutes at 250^{o}C under 25 MPa uniaxial stress in a reducing atmosphere (5% H_2/N_2). Finally, the sintered sample (Fig. 2.1e) was removed from the furnace after cooling down. The schematic diagram of the die-attach structure in power electronics is shown in Fig. 2.1f.

2.2.2. FIB-SEM TOMOGRAPHY

FIB-SEM tomography, an SEM-based technique, enables advanced characterization and improved understanding of 2D results. Here, we used FIB-SEM tomography to characterize the void distribution in sintered Cu NPs. The methodology involved using a dual-beam FEI Helios G4 CX FIB-SEM system for imaging and slicing to reconstruct 3D structures. Before ion milling, a platinum protective layer, approximately 1 µm thick, was deposited on the region of interest to prevent damage during ion milling. Subsequently, fiducial markers were strategically placed on the samples, allowing for real-time drift correction between successive milling operations. To facilitate FIB-SEM tomography, the sample was tilted at 52°, enabling milling perpendicular to the surface. Additionally, a U-shaped trench was milled alongside the area of interest to create space for redepositing material removed during tomography. The FIB slicing was conducted at an accelerating voltage of 30 kV and 40 pA, and SEM images were taken at 10 kV using an SE detector. The Auto Slice and View software (ASV4) was utilized to automate the tomography process by estimating the next slice position based on the top view image.

2.2.3. PRECESSION ELECTRON DIFFRACTION

To characterize the grain orientation of sintered Cu NPs, precession electron diffraction (PED) [46–50], a state-of-the-art transmission electron microscopy (TEM)-based technique was employed in this study. PED was performed using a JEM-2200FS (JEOL) transmission electron microscope (TEM) operating at 200 kV and equipped with the ASTAR system (Nanomegas) [49]. The microscope was operated in nanobeam diffraction (NBD)

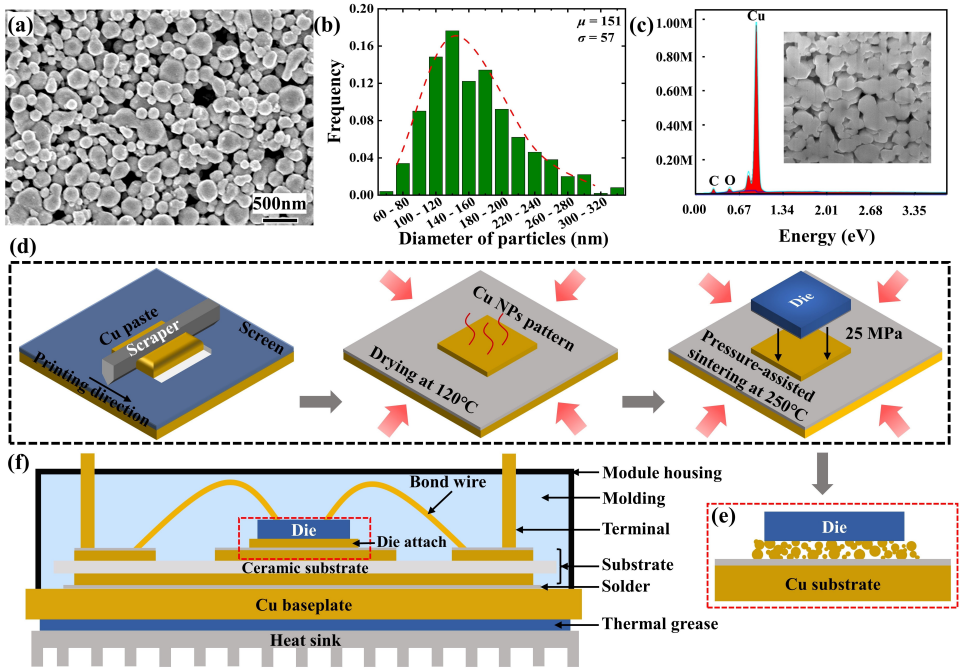


Figure 2.1: (a) SEM image of the Cu NPs; (b) size (diameter) distribution; (c) EDS Spectrum of the sintered Cu NPs; (d) pressure-assisted sintering technique; (e) schematic diagram of sintered die-attach structure; (f) schematic diagram of the die-attach structure in power electronics.

mode with the smallest spot size and a condenser aperture of 10 µm. The probe diameter was approximately 1 nm with a convergence angle of 2 mrad. A precession frequency of 100 Hz and a precession angle of 0.5° were applied during nanobeam scanning. This configuration reduces dynamical diffraction effects and enables reliable orientation and phase identification by integrating intensities over multiple diffraction conditions. By tilting the incident electron beam in a conical motion, PED reduces dynamical diffraction effects and enhances the reliability of orientation and phase identification. Compared to conventional techniques such as electron backscatter diffraction (EBSD) with 50-100 nm [51] and transmission Kikuchi diffraction (TKD) with 10-20 nm [50], PED offers superior resolution down to 1 nm, sensitivity to weak reflections, and the ability to analyze thin samples, making it particularly suitable for nanocrystalline materials. These advantages establish PED as a critical tool for detailed microstructural analysis and phase fingerprinting in advanced materials research.

2.2.4. MICRO-CANTILEVER BENDING TESTS

Micro-cantilever bending test is an effective technique for probing the mechanical properties of microscale samples [52, 53]. As shown in Fig. 2.2a, three kinds of micro-cantilevers with different orientations with respect to the direction of external pressure during sintering were fabricated, i.e. 0^o (perpendicular), 45^o, and 90^o (parallel). For each

orientation, six specimens were prepared to ensure the reliability of the data. Fig. 2.2b illustrates that the fabrication process involved five steps: milling a notch with a low ion current (10 pA), creating U-shaped trenches with a large beam current (20 nA), tilting and milling the base with 3 nA, rotating and repeating on the other side, and forming the micro-cantilever by undercutting. The micro-cantilever was then polished with 1 nA to ensure symmetry and cleaned with 100 pA to minimize damage. A precise marking was made on the free end to establish a well-defined loading point. Fig. 2.2c shows a typical SEM image of the micro-cantilever. The micro-cantilevers were fabricated at the middle position of the die-attach layer. This choice was deliberate to ensure consistency in the microstructure and minimize variations caused by non-uniformities during sintering [54]. The middle region is more representative of the average sintering degree and microstructure, as the edges may experience different thermal and pressure conditions [55]. By focusing on this central position, the influence of local non-uniformity was reduced [56], leading to more reliable and reproducible mechanical property measurements. The micro-cantilever has a pentagonal cross-section. We chose this shape for two reasons: it provides more flexibility in selecting the location compared to a rectangular shape, and the stress distribution in a pentagonal cross-section is less affected by preparation inaccuracies, leading to more reliable mechanical property measurements [57, 58].

An in-situ nanoindenter setup from Alemnis AG (Switzerland) was utilized to perform micro-cantilever bending tests in a Zeiss Ultra55 FEG SEM chamber. Before conducting the bending tests, the SEM carefully positioned the indenter tip to the fiducial mark on the top surface of the micro-cantilever, as shown in Fig. 2.2c. The quasi-static bending test is controlled by displacement. A constant load rate of 10 nm s^{-1} was applied for all micro-cantilevers until fracture occurred. The bending load was applied with a conospherical diamond tip (radius = 1 µm). Compared with the sharp-tipped indenter, such as the Berkovich indenter, the conospherical indenter with a spherical tip exhibited minimal indentation on the surface of the micro-cantilever [59].

2.2.5. MD SIMULATIONS OF THE SINTERING PROCESS AND TENSILE TESTS

The sintering and tensile process were simulated by the MD method using Large-scale Atomic/Molecular Massively Parallel Simulator (LAMMPS) software [60]. The atomic configurations were visualized and analyzed with the Open Visualization Tool (OVITO) [61]. The Cu embedded atom method (EAM) interatomic potential proposed by Mishin et al. [62] is employed to describe the atomic interaction, which has been successfully applied in simulating various mechanical properties and microscopic phenomena in Cu, such as diffusion and grain boundary migration [63–65]. The melting point of bulk Cu within this potential is 1273 ± 30 K, which matches well with the experimentally observed value of 1358 K. The initial Cu particle model has the following characteristics: spherical shape, non-contact or point-contact interactions between particles, a total volume fraction of about 45%, random spatial orientation of each particle, and a particle size distribution that is comparable to experimental observation. To enhance computational efficiency, the particle diameter in the simulation was 3-12 nm, as shown in Fig. 2.3b. Similar values (2-15 nm) have been used in previous MD simulations of the sintering process of Cu NPs [40]. Moreover, since Fig. 2.1c shows that the organic sub-

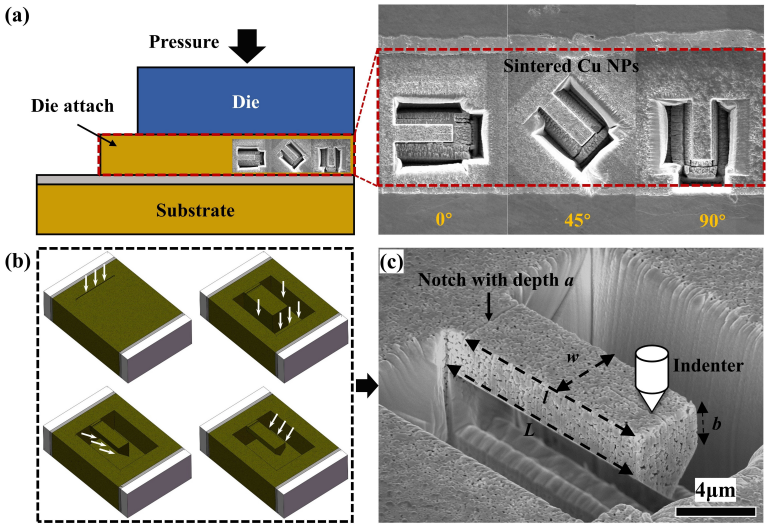


Figure 2.2: (a) Relationship of micro-cantilever orientations with pressure during sintering process; (b) FIB process for micro-cantilever fabrication; (c) SEM image of a micro-cantilever.

stances evaporated during the sintering process, the influence of the organic binder in the sintering process is ignored.

The procedure for generating 3D models of Cu NPs is as follows:

1. Select a point in 3D space randomly to be the center of the Cu NPs. The particle radius is determined by a randomly generated number that follows a normal distribution
2. Validate the new particle by making sure it does not overlap with existing spheres considering the periodic boundary condition (PBC).
3. Assign a random orientation to the particle.
4. Repeat the procedure until the acceptance rate is very low.
5. Select particles randomly and expand them until they meet each other.
6. Execute energy minimization by employing the conjugate gradient (CG) algorithm.

Fig. 2.3a shows the resulting particle model of Cu NPs, which is color-coded with Adaptive Common Neighbor Analysis and has dimensions of roughly $450 \times 450 \times 450$ Å^3, consisting of around 240 particles and 3.6 million atoms. The initial relative density of the model is approximately 45%. Two types of external stresses (uniaxial and hydrostatic) during the sintering process are considered in MD simulation. The models sintered under uniaxial and hydrostatic stress are labeled as US and HS, respectively. The sintering method employed in US model is similar to sintering process in Section 2.1, while the HS model shares similarities with a constrained sintering method reported in [66].

The sintering process in the MD simulation includes three stages. Initially, the temperature increases to 523 K (in consistent to the experiments) with a Nose-Hoover thermostat at a speed of 2 K/ps. Subsequently, a uniaxial strain is applied to the US model, with strain rate of 1×10^9 s^{-1}. The pressure in the non-compressed direction is main-

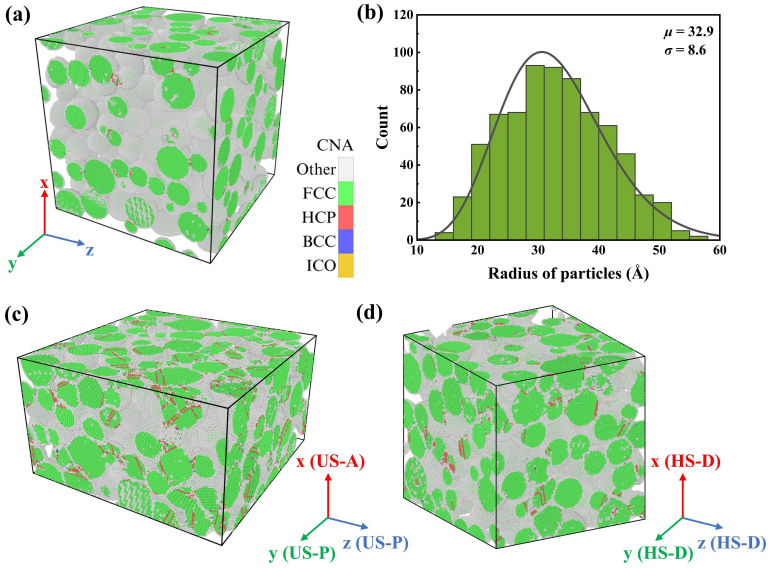


Figure 2.3: 3D Cu NPs model (a) before and after (c, d) sintering. (b) radius value distribution of Cu NPs; (c) after uniaxial stress sintering along the X-axis; (d) after hydrostatic stress sintering.

tained at 0, corresponding to the sintering process in experiments which is unconstrained in the non-loading direction. The overall deformation along strain direction is 40%, according to the height changes of the powder during sintering in experiments (roughly from 1.8 μm to 1.3 μm). For the HS model, a hydrostatic stress is applied on all surfaces during the sintering process until the relative density reaches the same level as the US model. The loading rate is 0.2 MPa/ps. The sintering process finishes after approximately 800 ps. Finally, the temperature is kept at 523 K, the volume remains constant, and a relaxation period of 100 ps is applied to eliminate the additional stress caused by the high strain rate in the previous loading step. The US and HS models after sintering are shown in Figs. 2.3c and d, respectively.

Due to the significant anisotropy of models after sintering on both microstructure and mechanical performance, directional terminology is introduced for convenience of description. The direction aligned with the stress direction during sintering is labeled as US-A, while the direction perpendicular to the stress direction during sintering is denoted as US-P, as shown in Fig. 2.3c. Note that US-A and US-P represent the loading and observation directions. However, such distinction is not necessary for HS models, and all three orientations are labeled as HS-D, as shown in Fig. 2.3d. Given the impact of the initial particle distribution on sintering and mechanical performance, three independent models with random initial particle packing are employed. Before simulating the tensile process, a relaxation procedure with variable box dimensions is implemented to ensure that the model has no residual internal stresses. The tensile simulation is under fully periodic boundary conditions using the NPT ensemble (constant number of particles, pressure, and temperature) and the temperature is maintained at 300 K (room tempera-

ture). The maximum tensile strain is 45% in this study, and the loading rate for the tensile simulation is set at 5×10^8 s^{-1}. This loading rate is commonly employed in literature [67]. The stress values in directions other than the tensile direction are maintained at 0.

2.3. ANISOTROPY IN STRUCTURAL EVOLUTION DURING SINTERING

2.3.1. AREAL RELATIVE DENSITY BY FIB-SEM

Fig. 2.4a presents the image of the slicing and imaging area under FIB-SEM tomography. The dimension of the imaging area is around 10×8 μm^2 and the depth is around 4.5 µm. To obtain reliable and representative results, it is crucial to estimate the minimum volume size that must be reconstructed. The critical volume size, which is commonly called a representative volume element (RVE) or stochastic equivalent representative volume element (SERVE), has been extensively discussed in [68–70]. Given that the width and thickness of the micro-cantilevers are near 4 µm, the reconstructed volume of $4 \times 4 \times 4$ μm^3 is large enough to depict the real microstructure of sintered Cu NPs. 3D reconstruction was carried out by Avizo (Thermo Scientific) after serial image acquisition, which entailed alignment, image processing, and segmentation. Fig. 2.4b shows the image sequence generated via FIB-SEM. Once imaging is done, FIB milling can remove another layer of material using the same parameters to obtain a second image with SEM. By repeatedly performing this milling and imaging process, a 3D dataset of SEM images is created, with each image depicting a 25 nm thick section of the sintered Cu NPs. 200 images were obtained, and around 160 high-resolution images were used to finish the 3D construction. The 'thresholding' method was applied in this study [71, 72]. The optimal thresholds for the reconstruction were selected by comparing reconstructed models with the morphology of voids in SEM. Figs. 2.4c and d represent the sintered Cu NPs and the void volume, respectively.

Here, we define areal relative density as

$$D_{\mathrm{r}}^{\mathrm{areal}} = \frac{A^{\mathrm{matter}}}{A^{\mathrm{cross\text{-}section}}} \times 100\% \tag{2.1}$$

where A^{matter} and $A^{\mathrm{cross\text{-}section}}$ are the area of the sintered Cu NPs domain and the cross-section, respectively. The areal relative density and its mean (μ) and standard deviation (SD, σ) of the 3D reconstructed model along different directions are measured, as shown in Fig. 2.4e. The XY plane is perpendicular to the pressure, while the YZ and XZ planes are parallel to the pressure. For the SD of areal relative density, a significantly lower SD (0.8%) is obtained on XY cross-section, compared with 1.5% of YZ and XZ cross-sections. Meanwhile, the XY cross-section has a minimum areal relative density of 78%, which is greater than that of the YZ (73%) and XZ (74%) cross-sections. It is evident that the areal relative density of the porous structure is anisotropic. Therefore, pressure direction leads to a more uniform distribution of areal relative density, with a relatively high minimum area of cross-section compared to the other two directions.

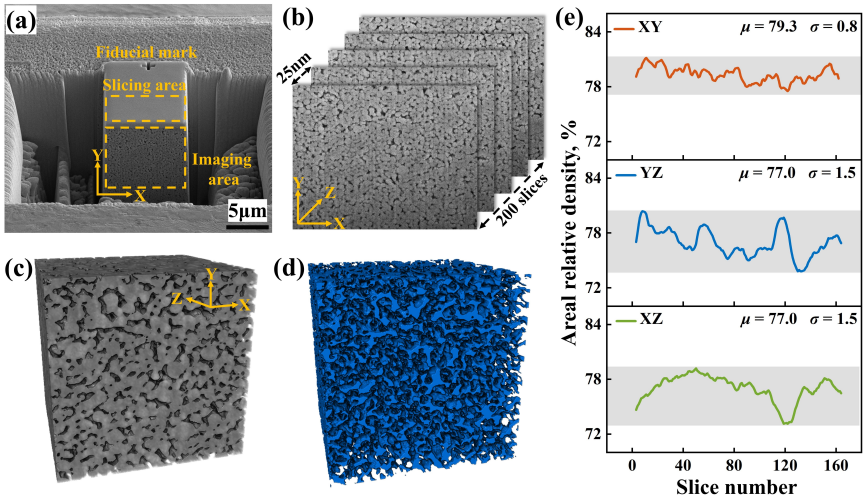


Figure 2.4: (a) FIB-SEM tomography image showing the slicing and imaging areas; (b) stacked SEM slices illustrating the consecutive slicing process; (c) sintered Cu NPs domain; (d) porous domain; (e) areal relative density in different directions

2.3.2. AREAL RELATIVE DENSITY BY SIMULATION

The sintered structures obtained from the MD simulation are referred to Figs. 2.3c and d. The final volumetric relative densities for models after simulated sintering is 67.4 ± 0.7% (under HS), and 68.3 ± 1.7% (under US). The density is slightly lower than that for experiments because of the limitations of MD simulations on time scales. As for the microstructure, the spherical shape of the particles is preserved after sintering and numerous sintering necks are formed. The majority of pores remain interconnected and the growth and merging of grains are not significant (as evidenced by the minimal change in grain count before and after sintering). The simulated structures are very similar to those reconstructed with FIB-SEM, as shown in Fig. 2.4c, illustrating the reliability of this modeling approach. Since the atomic position in the model is discrete, the model is divided into slices with a thickness of 2 Å (about 1/30 of the average particle diameter) along the observation direction to calculate areal relative density. Within each slice, the ratio of the number of atoms to the volume of the slice is calculated, and this ratio is then scaled by the atomic density in a dense cubic Cu. Therefore, the areal relative density is defined as

$$D_{\mathrm{r}}^{\mathrm{areal}} = \frac{N^{\mathrm{slice}} V^{\mathrm{atom}}}{V^{\mathrm{slice}}} \times 100\% \tag{2.2}$$

where $N^{\mathrm{slice}} V^{\mathrm{atom}}$ is the number of atoms inside the slice of the model. V^{slice} and V^{atom} is the volume of the slice and a single Cu atom in FCC crystal (a = 3.615 Å), respectively. Our tests show that this slice thickness can capture structural variations without being excessively sensitive, for example, to the influence of grain orientation.

To investigate the effect of the sintering method on the areal relative density distribution, we calculated the areal relative density distribution along different directions for

sintered models obtained from the same particle model by different sintering methods. Fig. 2.5a is the schematic diagram of the view direction for measuring the areal relative density.

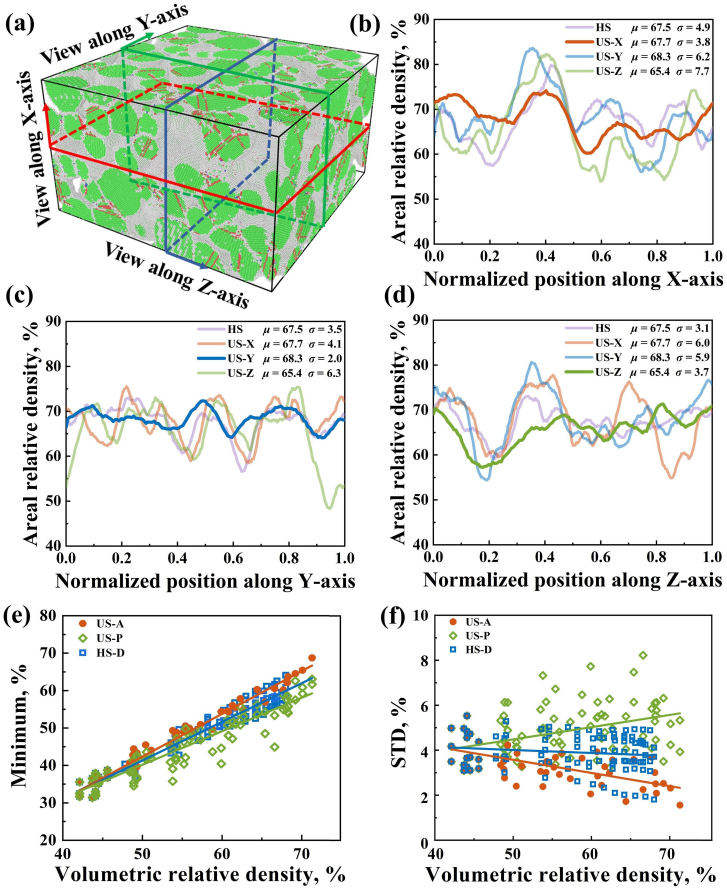


Figure 2.5: (a) Sintered model showing the orientations of cross-sections for measuring the areal relative density; (b-d) the changes of areal relative density with position along (b) X-axis, (c) Y-axis and (d) Z-axis under four different sintering conditions, namely, hydrostatic stress (HS) and uniaxial stress (US-X, US-Y, US-Z); (e) the minimum areal relative density versus volumetric relative density; (f) the SD of areal relative density versus volumetric relative density.

Figs. 2.5b-d show the changes of areal relative density along three directions, i.e. X, Y, and Z-axis. Each figure contains four curves corresponding to four sintering methods, i.e. under hydrostatic stress (HS) and uniaxial stress along the X-, Y-, and Z-axis (US-X, US-Y, and US-Z, respectively). Curves corresponding to US-A, which means for the model the observation direction is consistent with the direction of the stress during sintering, are with deeper color. The normalized coordinates are used as the horizontal axis due to the inconsistent dimensions of the sintered models. Three findings can be drawn from Figs. 2.5b-d.

First, a certain degree of heritability in the location of the peaks and troughs of the curves is observed in areal relative density. That means for the same particle model sintered using different methods, when observing along the same direction, the positions of the peaks and valleys of areal relative density curves still exhibit a certain correspondence (although the relative height changes are different), showing the influence of the particle initial packing.

Second, the cross-sections in the US-A direction consistently exhibit a smaller SD and a higher minimum areal relative density value than those of cross-sections in the US-P direction for US models. That means during the sintering process, along the stress direction, the low-density regions caused by the random packing of particles are effectively filled. Surprisingly, US-A curves show lower peaks than US-P curves, indicating particles in high-density regions become more dispersed in the sintering direction. Close inspection of the atomic displacement reveals that due to higher strain and stress in the loading direction, particles require greater displacement along this axis to connect with other particles and bear the load, while along other directions particles have lower driven force for movement.

Third, the cross-sections in HS models generally show intermediate values between those of US-A and US-P for both areal relative density SD and minimum areal relative density. The deviation from the general trend, where the cross-sections of HS model exhibit a lower SD of areal relative density than US-A along the Z-direction, can be attributed to the low areal relative density of the US model compared to the HS model.

In order to quantitatively characterize the changes in these structures during sintering, we calculated the minimum values and SD of areal relative density of cross-sections along different directions for each model at various time points during the sintering process, as depicted in Figs. 2.5e, f.

We found that as the bulk density rises during sintering, the minimum value of the areal relative density rises linearly. The slope of the fitted line for US-A in minimum areal relative density is slightly higher than that for US-P. The case of HS-D is between US-A and US-P. However, for SD of the areal relative density, the tendency is distinctly different for different sintering conditions and observation directions. For the US-A direction, the SD decreases with the increase in bulk density. In contrast, the SD of cross-sections in the US-P direction increases with the rise in bulk density, indicating amplification of structural fluctuations along the direction perpendicular to the applied stress during the sintering process. For HS-D, SD remains nearly constant, implying that the fluctuations in the structure across different directions are at the same magnitude during sintering. Both the two properties along the US-P direction exhibit larger fluctuations than those for US-A, suggesting a more significant influence from the initial particle packing. The fluctuation range for HS-D falls between these two cases.

2.3.3. GRAIN ORIENTATION CHARACTERIZATION

To investigate the effect of sintering pressure on grain orientation and void distribution, two TEM samples were fabricated from the sintered Cu NPs layer. One TEM sample was extracted perpendicular to the sintering pressure direction, aligning with the orientation of the 90^o micro-cantilevers. The other one was extracted parallel to the sintering pressure direction, corresponding to the 0^o micro-cantilever orientation. Preces-

sion electron diffraction (PED) was subsequently performed to characterize the grain orientation maps and void distributions of the two samples. The results are presented in Fig. 2.6. Figs. 2.6a and b depict the grain orientation maps for the perpendicular and parallel directions, respectively. The PED analysis demonstrates that the grain orientation shows no significant dependence on the applied sintering pressure. However, clear anisotropy is observed in the void morphology and particle deformation. In the perpendicular direction (Figs. 2.6c, e), the voids appear irregular and smaller, reflecting localized densification with minimal particle elongation. Conversely, in the parallel direction (Figs. 2.6d, f), the voids are larger and elongated, which can be attributed to the deformation of particles under uniaxial stress during sintering. The external pressure facilitates particle flattening and void coalescence along the loading direction, leading to an anisotropic void structure. These observations align with the findings discussed in Sections 3.1 and 3.2, where the pressure direction enhances the uniformity of areal relative density while reducing structural fluctuations. Specifically, the lower standard deviation of relative density along the pressure direction indicates a more stable and homogeneous microstructure. In contrast, the larger density fluctuations in the perpendicular direction reflect the significant influence of initial particle packing and localized void formation.

2.3.4. FORMATION OF NECKS DURING SINTERING

The fusion between the particles plays an important role in the densification process. According to Ref. [73], the contact area between two particles is considered the sintering neck. In MD models, if atom A, belonging to particle P_A, is within the cutoff distance of atom B, which belongs to particle P_B, then both atom A and B are considered part of the sintering neck between P_A and P_B. The cutoff distance is set to 3.5 Å to ensure that all sintering necks are sufficiently large for meaningful measurement. Using this method, the shape of the necks before and after sintering under stress along the X-axis is shown in red in Figs. 2.7a and b, respectively. Different particles are distinguished by different shades of gray. The shrinkage along the X-axis after sintering is about 40%. A significant rise in the number and volume of neck regions can be observed. After sintering, the fractions of atoms that were labeled as neck increased from 4.6% to 14.8%. Moreover, the necks are interconnected to form a 3D network after sintering is completed, which is beyond the 2D model used in previous simulations of sintering.

To further determine the orientation of each sintering neck, the positions of the atoms for a single sintering neck are extracted, as shown in Fig. 2.7c. We consider the neck to be a thin sheet with a significant difference between thickness and area, with the thickness direction representing the orientation of the neck. Using principal component analysis (PCA), the three orthogonal principal component (PC) vectors for the atomic positions are determined. The plane defined by PC1 and PC2 is the plane with the most dispersed atomic coordinates. PC3, which is perpendicular to this plane, is the direction with the least atomic dispersion, indicating the orientation of the sintering neck. Fig. 2.7d is a schematic diagram for calculating the angle θ between the neck orientation (PC3) and the X-axis. It is clear that when θ approaches 0, the neck is perpendicular to the given axis, while θ near 90^o means the neck is parallel to the given axis.

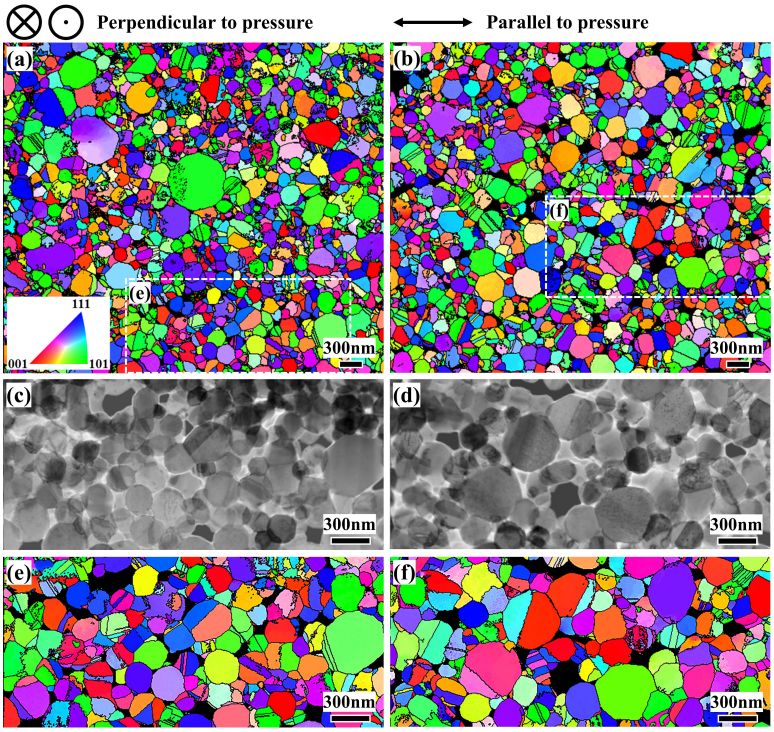


Figure 2.6: PED analysis of sintered Cu NPs under external pressure. (a) Grain orientation map of the the TEM sample aligned perpendicular to the sintering pressure, corresponding to the 90^o micro-cantilevers. (b) Grain orientation map of the TEM sample aligned parallel to the sintering pressure, corresponding to the 0^o micro-cantilevers. (c, d) Virtual bright-field images of the dashed regions in (a) and (b), respectively, revealing local grain morphology. (e, f) Corresponding orientation maps of the local regions shown in (c) and (d), respectively.

It is important to note that, mathematically, the distribution of the angle of a random vector in 3D space with a specific vector is not uniform. It is trivial to prove that for angle θ ranging in 0 to 90^o, the probability density function $F(\theta)$ of the angle between a random vector and a fixed vector is

$$F(\theta) \propto sin(\theta) \tag{2.3}$$

Thus there is a much higher possibility for a vector to be perpendicular to a specific axis, rather than parallel to that.

A DEM study of ceramic sintering showed that the anisotropy flattening under stress has a substantial contribution to structure anisotropy [32]. Since the sintering of metal NPs is featured by low sintering temperature and short sintering time, the anisotropy induced by particle deformation is expected to be more significant. Here we use a 2D schematic to illustrate the effect of deformation caused by the uniaxial stress on the orientation of the neck formed during sintering. Fig. 2.8a shows two particles before sintering. θ is the angle between the normal of the initial contact surface and the stress

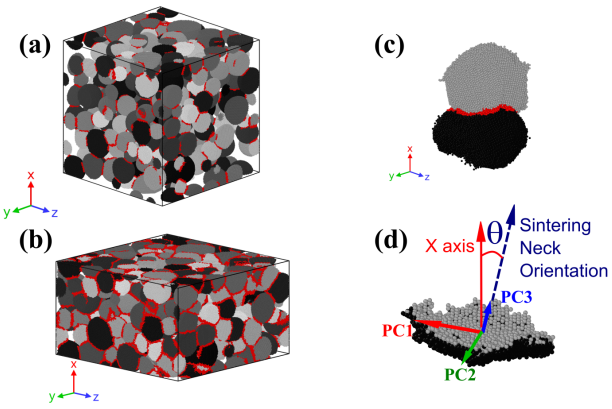


Figure 2.7: Neck regions in MD simulation for (a) model before sintering and (b) model sintered under stress along X-axis. (c) A neck between two particles after sintering. (d) Principal component analysis for atoms location in a neck. The orientation is quantitatively calculated as the angle between the third principal component and X-axis.

direction. Here,

$$\tan\theta = \frac{a}{b} \tag{2.4}$$

where a and b are the dimensions of the initial sintering neck in the parallel and perpendicular directions to the loading, respectively. After uniaxial stress-assisted sintering, the particle shape significantly contracts along the direction of the uniaxial stress with a strain of ε, while Poisson expansion occurs in the other directions, as shown in Fig. 2.8b. The neck also grows during sintering. Then θ' can be estimated as

$$\tan\theta' = \frac{k \cdot a(1-\varepsilon)}{k \cdot b(1+\nu\varepsilon)} \tag{2.5}$$

where k describes the uniform growth of the sintering neck dimensions in all directions, and ν is the Poisson's ratio of the bulk material. It should be noted that the strain during sintering should be smaller than the shrinkage deformation along the stress direction, as both particle deformation and densification contribute to the shrinkage. Using this method, the orientation distributions of necks considering particle deformation are calculated, as shown in Fig. 2.8c. The black curve, which is for particles before deformation, corresponding to the distribution described by Eq. 2.3. The peak of angle distribution significantly shifts to low angle region as particle strain increases, meaning that after large deformation, necks tend to be perpendicular to the stress direction geometrically.

The orientations of the necks in the MD models sintered under stress along the X-axis are analyzed. The US-X with deformation of 40% (Figs. 2.9a-c) and 50% (Figs. 2.9d-f) contain 742 and 883 necks, respectively. The model with 50% deformation is analyzed here to better show the effect of uniaxial compression during sintering on the microstructure. Figs. 2.9(a, d), (b, e), and (c, f) are for the neck orientations with respect to X-, Y-, and Z-axis, respectively. In each figure, the histogram counts the number of

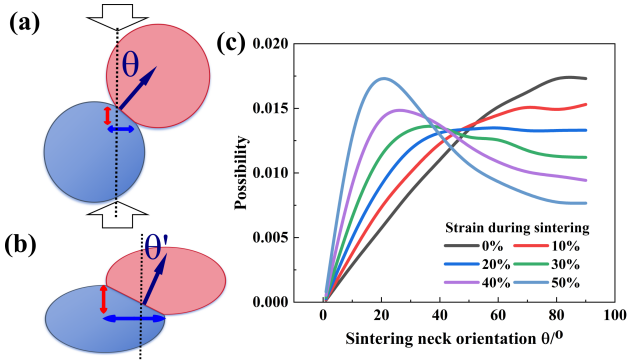


Figure 2.8: Schematic illustration of the effect of particle deformation on sintered neck orientation. (a) Two particles with initial contact before sintering. (b) A neck formed between two deformed particles. (c) Distribution of θ for particles with various strain derived from the 2D model.

necks with different angles to the axis. The scatter plot shows the number of atoms contained in the necks with different orientations. The size of marks in scatter plots is also adjusted according to the number of atoms. The distribution curves for the angles between randomly oriented vectors to the axis (Eq. 2.3) are shown with a red solid line in each histogram for reference. In Figs. 2.9a and d, the distribution of the neck orientations derived from Eq.2.5 are shown in blue curves. In the calculation, the strain of each particle is considered as half of the deformation along the X-axis and $\mu = 0.3$. Three points

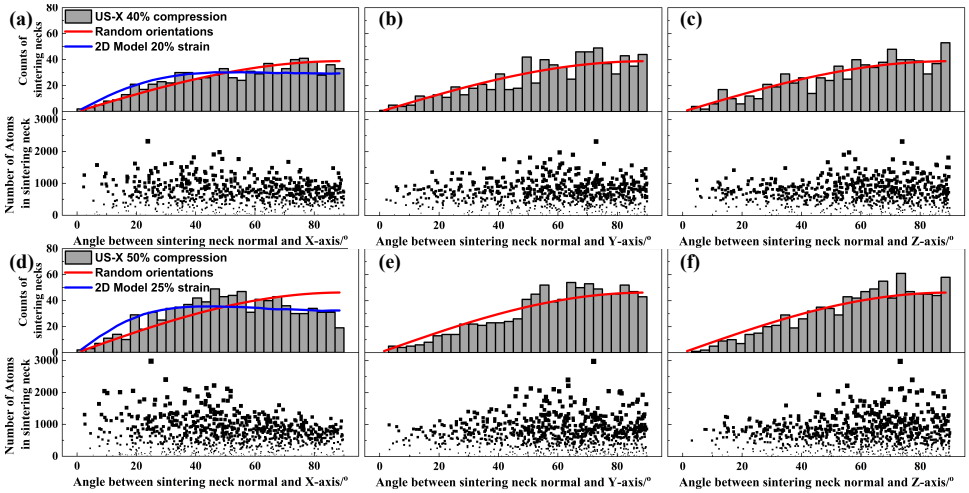


Figure 2.9: Statistics on sintering necks orientation (histograms) and size (scatter plots). (a-c) are for model with 40% deformation and (d-f) are for model with 50% deformation along X-axis during sintering. The angle shown in (a,d), (b,e), and (c,f) are between neck normals and X-, Y-, and Z-axis, respectively. Red reference curves show the angle distribution for randomly oriented vectors. Blue lines are derived from Eq. 2.5.

can be drawn from the figure.

1. For the orientation of necks concerning the direction of the uniaxial stress, here X-axis, the histogram shows that the number is higher between 0 and 50^o than the reference line. For the orientation of the sintered neck along the Y and Z axes, the number is higher near 90^o. This indicates that along the X-axis, more sintered necks are present perpendicular to the X-axis or at an angle of less than 50^o, while in the other two orientations, most of the sintered necks are close to parallel to this orientation.

2. Large dots in the scatter plots corresponding to the X-axis are clustered in the angle range of 10 to 45^o, while for the plots of the Y- and Z-axis, the dots representing a larger number of atoms are clustered in the range of 60 to 90^o. This suggests that sintered necks oriented close to perpendicular to the stress direction (here the X-axis) grow larger (compared to those parallel to the X-axis).

3. By comparing models experiencing 40% versus 50% deformation, the effect of deformation strain on the formation and growth of necks is revealed. With extra 10% compression, both the number and size of necks at an angle of 20 to 50^o to the X-axis rise significantly, while there is no such tendency for the Y- and Z-axes.

The orientation of the sintered necks mainly originates from the flattening of the particle shape under uniaxial stress. In Ref. [32], the authors state that the particle flattening induced by uniaxial stress is anisotropic, with particles having a larger size and surface area perpendicular to the stress direction. The trend can be seen by comparing Fig. 2.7a and b. The difference between the solid blue line and the actual distribution is mainly caused by the non-uniform strain distribution during sintering. Another reason for the distribution of neck orientations is the high body shrinkage along the direction of the sintering stress. Along the direction of the stress, the particles have more opportunities to contact each other thus more necks form.

2.4. MECHANICAL PROPERTIES OF SINTERED NPS AND DISCUSSION

2.4.1. MICRO-CANTILEVER BENDING TESTS

Due to the limitations of FIB in preparing specimens with different orientations, the cross-section of the cantilever beam in this study is not rectangle. In our previous work, the fracture toughness of sintered Cu NPs was measured with standard micro-cantilevers as 3.2 MPa·m$^{1/2}$ [30], which aligns well with other reports [28]. Figs. 2.10a-c show the load-displacement curves obtained from micro-cantilever bending tests. The initial elastic loading parts matched well across specimens, but some scatter appeared at larger displacements due to slight differences in sample dimensions. The maximum load values F_{max} were retrieved from the peak points of the load-displacement curves. As depicted in Fig. 2.10d, the maximum load and SD of 0^o, 45^o, and 90^o micro-cantilevers are 203 ± 20 μN, 266 ± 68 μN, and 286 ± 36 μN, respectively. Since the specimens are essentially the same size, F_{max} is proportional to the fracture strength. The 90^o micro-cantilevers, in which the prefabricated notch is perpendicular to the uniaxial stress during sintering, show 41% higher strength than 0^o micro-cantilevers. The 45^o micro-cantilevers exhibit slightly lower strength than the 90^o micro-cantilevers, and the values are dispersed in a large range. The slopes of the load-displacement curves indicate the degree of densification of the specimen in the loaded direction, so we also calculated

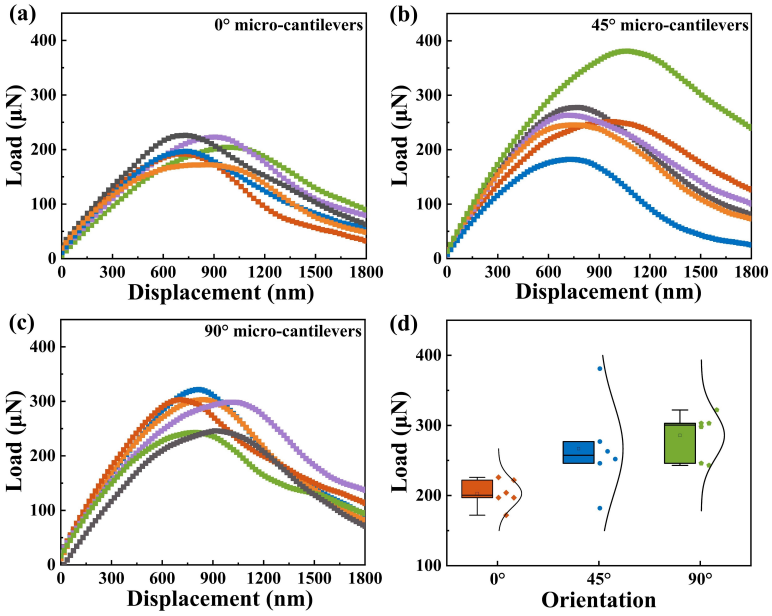


Figure 2.10: Load-displacement curves of (a) 0°; (b) 45°, (c) 90° micro-cantilevers; (d) maximum loads of micro-cantilevers with different orientations.

the slopes as the effective modulus. For 0°, 45°, and 90° micro-cantilevers, the modulus are 0.32 ± 0.04 $\mu N \cdot nm^{-1}$, 0.42 ± 0.06 $\mu N \cdot nm^{-1}$, and 0.45 ± 0.05 $\mu N \cdot nm^{-1}$, respectively. The value for 90° micro-cantilevers is slightly higher than that for 45° micro-cantilevers, and significantly higher than that for 0° micro-cantilevers. Intuitively, we expect the mechanical property of 45° micro-cantilevers to be between those of 0° and 90°, following the rule of mixtures. The high toughness measured on 45° micro-cantilevers which is beyond expectation will be discussed in Section 4.3.

2.4.2. TOUGHNESS FROM MD SIMULATION

Three independent sintering models were used for the simulations, resulting in nine MD models subjected to uniaxial stress and three models to hydrostatic stress. Tensile simulations were then conducted in the X, Y, and Z directions for the nine sintered models, generating 27 stress-strain curves. For the three models sintered under hydrostatic stress, the tensile tests produced nine stress-strain curves.

To characterize the microstructure and mechanical behavior, we use a model sintered under a stress along the X-axis as an illustrative example, shown in Fig. 2.11c. The models under 40% tensile deformation along the X, Y, and Z axes are depicted in Figs. 2.11a-c, respectively. Fracture is observed in the models stretched along the Y and Z axes, which is also reflected in the stress-strain curves (Fig. 2.11d). The curve corresponding to tensile stress along the X-direction shows higher tensile strength than those for the Y and Z directions, matching well with experimental results. The toughness of the sintered Cu NPs models is related to the areas under the stress-strain curves, calculated

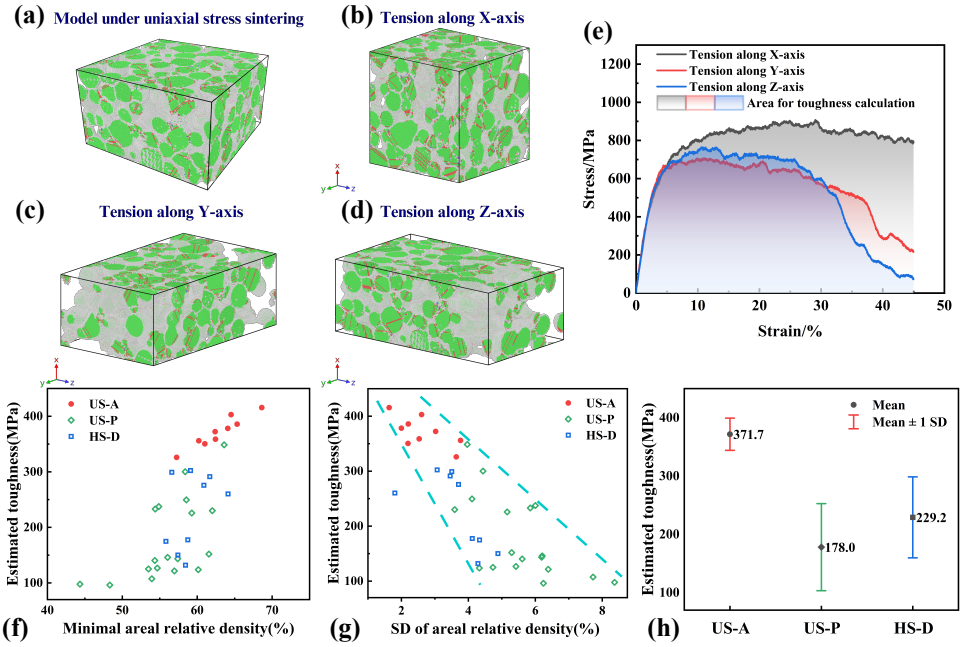


Figure 2.11: (a) Cu NPs model sintered under uniaxial stress along the X-axis. Atoms are colored according to its local structure. (b-d) Sintered model after 45% tensile deformation along (b) X-axis, (c) Y-axis and (d) Z-axis. (e) Stress-strain curves for tensile deformation along the three axes. The shaded area under each curve was used to calculate the tensile toughness. Two features describing the microstructure are connected with the estimated toughness: (f) minimum and (g) standard deviation of areal relative density. (h) Toughness for tensile along different directions. US-A(US-P) refer to the direction along(perpendicular) to the stress direction during sintering. HS-D refers to models sintered under hydrostatic stress. The dash lines in (g) are guide to eyes.

as follows:

$$G_f = \int_0^{\varepsilon_f} \sigma d\varepsilon \tag{2.6}$$

where ε_f is the strain corresponding to failure and σ is the tensile stress [74]. The toughness here indicates the capacity for energy absorption during plastic deformation, not the fracture toughness. The unit for toughness is MPa or $MJ \cdot m^{-3}$.

The fracture toughness estimated from the 36 stress-strain curves is connected to features of areal relative density. Fig. 2.11f illustrates that toughness increases rapidly when the minimal areal relative density exceeds 60%. Even with similar minimal areal relative density, the toughness for tensile stress along the sintering direction (US-A) is much higher than that for US-P and HS-D. In Fig. 2.11g, directions with smaller SD exhibit higher toughness. Moreover, a small SD value indicates a small variance in toughness. A direct comparison of toughness for US-A, US-P, and HS-D is shown in Fig. 2.11h. Along the direction of sintering stress (US-A), the toughness is twice that of US-P. The toughness of HS-D is close to the average values in the three directions of the model sintered under uniaxial stress.

2.4.3. EFFECT OF MICROSTRUCTURAL ANISOTROPY ON MECHANICAL PERFORMANCE

Experimental and MD simulations reveal the anisotropy of the sintered structure in terms of surface density distribution and sintering neck orientation. The influence of the minimal areal relative density on mechanical properties is evident. Under uniform deformation, locations with small cross-sections are prone to stress concentrations, akin to the necking observed in general tensile deformation. Moreover, since Cu NPs are at the nanoscale, dislocation generation and multiplication are suppressed, and work hardening can hardly contribute to the strength of regions with high strain. Thus, strain localization at cross-sections with small areas is self-promoting, limiting mechanical performance. Long et al. [75] proved the effect of strain localization on the mechanical properties of sintered NPs.

For a homogeneous dense structure, stress concentration is bound to occur at the minimum areal relative density. For sintered Cu NPs, however, the stress distribution under uniform strain is strongly dependent on the porous structure and the position with minimal area is not necessarily the most dangerous region. SD is not sensitive to extreme values but describes the homogeneity of the material distribution for porous structures, complementing the minimal areal relative density. For structures with similar bulk relative densities, those with smaller SD have a lower possibility for strain localization and thus better mechanical properties. This conclusion is also supported by FEM [76] and phase field [77] simulations of tensile deformation of porous structures.

In other studies, it has been observed that the aspect ratio of pores increases after sintering and pores mainly align along the direction of the stress. The presence of elongated pores along the stress direction leads to smaller fluctuations in areal relative density in that direction compared to larger fluctuations in other directions. Therefore the anisotropy of pore shape reported before is consistent with the differences in directional SD of areal relative density we observed. For 3D interconnected pores, as shown by the 3D reconstruction, 2D interface observation is insufficient to fully display their characteristics. Here, we point out that SD of areal relative density is a reliable indicator for the quantitative description of 3D porous structures. Additionally, using SD as a measurement provides an alternative explanation for the size effect of porous structures [78]. For the same pore distribution, the areal relative density of smaller samples is more significantly affected by the pores, resulting in a higher SD. Multiple reports indicate that after high-temperature aging, accompanied by an increase in pore size, the mechanical properties of sintered Ag decline even if the relative density remains unchanged or increases. This is also consistent with the conclusions drawn here.

From another perspective, the anisotropy of sintered NPs can be explained by difference of failure mode. In the experiments conducted in [79], two primary failure modes were observed: tensile fracture and shear fracture. Since the necks are the weakest regions in the material, it can be inferred that the failure mode is related to the orientation of these necks. Due to the good plasticity of Cu, the fracture surfaces in the microcantilever bending tests did not completely separate, allowing only the observation of the fracture surfaces.

In MD simulations, these two fracture modes are also observed. For the model sintered under stress along the X-axis, the typical fracture surfaces during tensile deforma-

tion along X-axis (US-A) and Y-axis (US-P) are shown in Figs. 2.12a and b, respectively. Atoms from different particles are color-coded, and the overall deformation of the model is indicated below each image. The total deformation along the tensile direction at 30% strain is marked on each particle. On the right side, the atomic structures before and after 30% deformation are shown, analyzed using CNA, with the surface amorphous layer removed for clarity. Red indicates the hexagonal closest packed (HCP) structure, corresponding to stacking faults in Cu.

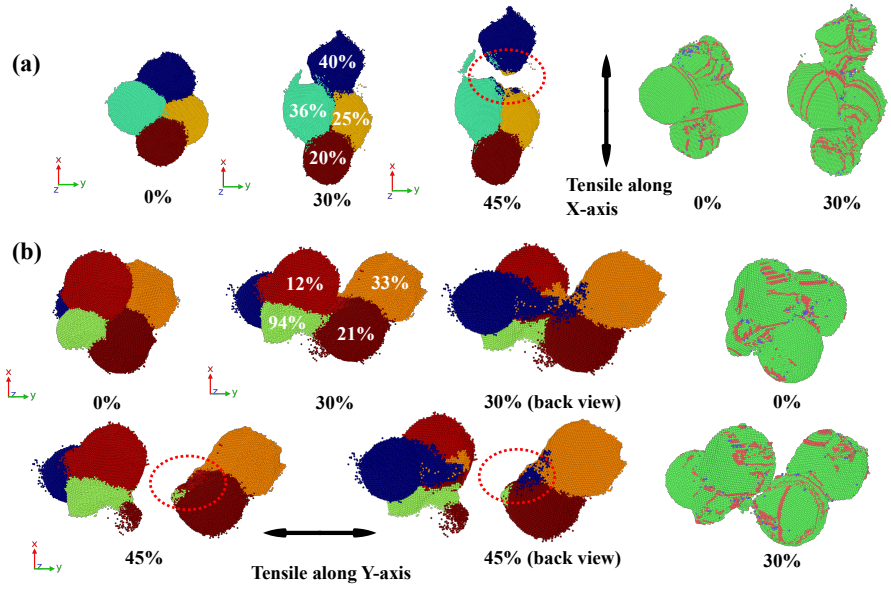


Figure 2.12: The fracture process during tensile deformation along (a) X-axis and (b) Y-axis. The model is sintered under stress along X-axis. Atoms are colored according to the particle they belong to. Left side shows the atomic structure with common neighbour analysis(CNA).

In Fig. 2.12a, the sintering neck is almost perpendicular to the tensile direction, resulting in uniform deformation across the particles (each particle contains many stacking faults), indicating tensile fracture. In Fig. 2.12b, the sintering neck is nearly parallel to the tensile direction, resulting in significantly higher deformation in the green particle compared to the overall deformation value, while the red particle shows less deformation. At the fracture site, many atoms adhere to other particles, suggesting the fracture is by shearing at the neck.

Considering a sintering neck with an orientation angle θ and area A, as shown in Fig. 2.8, when stretched along the direction of sintering stress, its effective bearing area is $A\cos\theta$. When stretched in the vertical direction, the effective bearing area is $A\sin\theta$. Moreover, for necks with θ varying from 0 to 90^0, the stress state on the neck plane changes from pure tension to pure shear, which lead to a transition in fracture mode. Thus, geometrically, sintering necks with a smaller angle between the normal and tensile direction are more advantageous. Given the observed anisotropy in the orientation

of sintering necks after sintering, θ angles of sintering necks observed along the X-axis are more likely to be smaller, leading to better mechanical performance when stretched along the X-axis.

In the micro-cantilever bending tests, the 45° specimens exhibited strength close to that of the 90° specimens. Considering that the orientation distribution of sintering necks has a peak at 45°, it can be inferred that when stretched at a 45° angle to the sintering stress direction, many necks align favorably, resulting in better performance.

Due to the complexity of the sintered particle structure, the effects of areal relative density fluctuations, sintering neck orientation, and other factors not considered (such as grain boundary types and grain orientations) are superimposed.

2.5. CONCLUSION

The mechanical strength of sintered NPs limits their application in advanced electronics packaging. In this work, we reveal the anisotropy in the microstructure and mechanical properties of sintered Cu NPs by combining experimental methods with MD simulations. We clearly explain the processing-microstructure-property relationship of pressure-assisted sintered Cu NPs. The main findings are as follows:

1. The evolution of the microstructure during sintering is quantitatively described by areal relative density, which shows distinct differences in each direction during stress-assisted sintering. Directions along the stress exhibit a quick decrease in the minimum and SD of areal relative density, while directions perpendicular to the stress show an increase in SD. For sintering under hydrostatic stress, changes in all directions are similar.

2. MD simulations reveal that the necks formed during sintering are anisotropic. Necks tend to attain a smaller angle between their normal and the stress direction. Additionally, necks with such favorable orientation can achieve larger sizes.

3. The anisotropy in the mechanical properties of Cu NPs sintered under uniaxial stress is demonstrated by both micro-cantilever tests and tensile simulations. Along the direction of the sintering stress, the strength (load in experiments and toughness in simulations) is significantly higher (41% in experiments and 108% in simulations) than that along the perpendicular directions.

4. The mechanical anisotropy is induced by the microstructure through two aspects: variations in areal relative density affect the tendency for strain localization, and the size and orientation of necks affect the fracture mode. Along the direction of the sintering stress, the structure is more uniform, and more necks are in favorable orientations, resulting in higher strength compared to other directions.

We expect this study to provide new insights for nanoscale experimental design and performance analysis, as well as inform the design of NPs sintering processes.

REFERENCES

[1] L. Du *et al.*, "Microstructural and mechanical anisotropy in pressure-assisted sintered copper nanoparticles", *Acta Materialia*, vol. 287, p. 120 772, 2025.

[2] C. Eddy Jr and D. Gaskill, "Silicon carbide as a platform for power electronics", *Science*, vol. 324, no. 5933, pp. 1398–1400, 2009.

[3] C. Buttay *et al.*, "State of the art of high temperature power electronics", *Materials Science and Engineering: B*, vol. 176, no. 4, pp. 283–288, 2011.

[4] Y. Gao *et al.*, "Reliability analysis of sintered cu joints for sic power devices under thermal shock condition", *Microelectronics Reliability*, vol. 100, p. 113 456, 2019.

[5] A. Telang, T. Bieler, A Zamiri, and F Pourboghrat, "Incremental recrystallization/grain growth driven by elastic strain energy release in a thermomechanically fatigued lead-free solder joint", *Acta Materialia*, vol. 55, no. 7, pp. 2265–2277, 2007.

[6] M. Sadiq, M. Khan, A. Mateen, M. Shahzad, K. Akhtar, J. Khan, *et al.*, "Thermal aging impact on microstructure, creep and corrosion behavior of lead-free solder alloy (sac387) use in electronics", *Microelectronics Reliability*, vol. 122, p. 114 180, 2021.

[7] W. Zhang *et al.*, "A supersaturated cu-ag nanoalloy joint with ultrahigh shear strength and ultrafine nanoprecipitates for power electronic packaging", *Journal of Materials Science & Technology*, vol. 145, pp. 56–65, 2023.

[8] J. Wang *et al.*, "Nucleation and growth of cu6sn5 during the aging process of cu/sn interface in electronic packaging-by in-situ tem", *Acta Materialia*, vol. 264, p. 119 581, 2024.

[9] M. Asoro, P. Ferreira, and D Kovar, "In situ transmission electron microscopy and scanning transmission electron microscopy studies of sintering of ag and pt nanoparticles", *Acta Materialia*, vol. 81, pp. 173–183, 2014.

[10] S. Zhao, X. Li, Y. Mei, and G. Lu, "Study on high temperature bonding reliability of sintered nano-silver joint on bare copper plate", *Microelectronics Reliability*, vol. 55, no. 12, pp. 2524–2531, 2015.

[11] X. Long *et al.*, "Mechanical behaviour of sintered silver nanoparticles reinforced by sic microparticles", *Materials Science and Engineering: A*, vol. 744, pp. 406–414, 2019.

[12] S. K. Kurapati, N Mahendar Reddy, R Sujithra, R. Kola, G. V. Ramesh, and D Saritha, "Nanomaterials and nanostructures in additive manufacturing: Properties, applications, and technological challenges", *Nanotechnology-Based Additive Manufacturing: Product Design, Properties and Applications*, vol. 1, pp. 53–102, 2023.

[13] O Lame, D Bellet, M Di Michiel, and D Bouvard, "Bulk observation of metal powder sintering by x-ray synchrotron microtomography", *Acta materialia*, vol. 52, no. 4, pp. 977–984, 2004.

[14] R. Zuo, E. Aulbach, R. K. Bordia, and J. Rödel, "Critical evaluation of hot forging experiments: Case study in alumina", *Journal of the American Ceramic Society*, vol. 86, no. 7, pp. 1099–1105, 2003.

[15] D. J. Green, O. Guillon, and J. Rödel, "Constrained sintering: A delicate balance of scales", *Journal of the European Ceramic Society*, vol. 28, no. 7, pp. 1451–1466, 2008.

[16] H. Shang, A. Mohanram, E. Olevsky, and R. K. Bordia, "Evolution of anisotropy in hierarchical porous ceramics during sinter-forging", *Journal of the European Ceramic Society*, vol. 36, no. 12, pp. 2937–2945, 2016.

[17] O. Guillon, L. Weiler, and J. Rödel, "Anisotropic microstructural development during the constrained sintering of dip-coated alumina thin films", *Journal of the American Ceramic Society*, vol. 90, no. 5, pp. 1394–1400, 2007.

[18] C. Martin and R. Bordia, "The effect of a substrate on the sintering of constrained films", *Acta Materialia*, vol. 57, no. 2, pp. 549–558, 2009.

[19] T. F. Chen and K. S. Siow, "Comparing the mechanical and thermal-electrical properties of sintered copper (cu) and sintered silver (ag) joints", *Journal of alloys and Compounds*, vol. 866, p. 158 783, 2021.

[20] Y. Zuo, C. Zhao, A. Robador, M. Wickham, and S. H. Mannan, "Quasi-in-situ observation of the grain growth and grain boundary movement in sintered cu nanoparticle interconnects", *Acta Materialia*, vol. 236, p. 118 135, 2022.

[21] T. Youssef *et al.*, "Power modules die attach: A comprehensive evolution of the nanosilver sintering physical properties versus its porosity", *Microelectronics Reliability*, vol. 55, no. 9-10, pp. 1997–2002, 2015.

[22] B. Chen, Z. Xia, and K. Lu, "Understanding sintering characteristics of zno nanoparticles by fib-sem three-dimensional analysis", *Journal of the European Ceramic Society*, vol. 33, no. 13-14, pp. 2499–2507, 2013.

[23] G. Okuma *et al.*, "Anisotropic microstructural evolution and coarsening in free sintering and constrained sintering of metal film by using fib-sem tomography", *Acta Materialia*, vol. 215, p. 117 087, 2021.

[24] A. M. Venkatesh, D. Bouvard, P. Lhuissier, J. Villanova, and C. Rajon, "In-situ 3d x-ray investigation of ceramic powder sintering at the particle length-scale", *Ceramics International*, vol. 50, no. 3, pp. 4715–4728, 2024.

[25] A. M. Venkatesh, D. Bouvard, P. Lhuissier, and J. Villanova, "3d analysis of ceramic powder sintering by synchrotron x-ray nano-tomography", *Journal of the European Ceramic Society*, vol. 43, no. 6, pp. 2553–2563, 2023.

[26] P. Gadaud, V. Caccuri, D. Bertheau, J. Carr, and X. Milhet, "Ageing sintered silver: Relationship between tensile behavior, mechanical properties and the nanoporous structure evolution", *Materials Science and Engineering: A*, vol. 669, pp. 379–386, 2016.

[27] C. Chen and K. Suganuma, "Microstructure and mechanical properties of sintered ag particles with flake and spherical shape from nano to micro size", *Materials & Design*, vol. 162, pp. 311–321, 2019.

[28] C. Chen *et al.*, "Macroscale and microscale fracture toughness of microporous sintered ag for applications in power electronic devices", *Acta Materialia*, vol. 129, pp. 41–51, 2017.

[29] L. Du, D. Hu, R. Poelm, W. Van Driel, and K. Zhang, "Micro-cantilever bending test of sintered cu nanoparticles for power electronic devices", in *2023 24th International Conference on Thermal, Mechanical and Multi-Physics Simulation and Experiments in Microelectronics and Microsystems (EuroSimE)*, IEEE, 2023, pp. 1–4.

[30] D. Hu, L. Du, M. Alfreider, J. Fan, D. Kiener, and G. Zhang, "Microscopic fracture toughness of notched porous sintered cu micro-cantilevers for power electronics packaging", *Materials Science and Engineering: A*, vol. 897, p. 146 316, 2024.

[31] B. Paredes-Goyes, D. Jauffres, J.-M. Missiaen, and C. L. Martin, "Grain growth in sintering: A discrete element model on large packings", *Acta Materialia*, vol. 218, p. 117 182, 2021.

[32] A Wonisch, O Guillon, T Kraft, M Moseler, H Riedel, and J Rödel, "Stress-induced anisotropy of sintering alumina: Discrete element modelling and experiments", *Acta Materialia*, vol. 55, no. 15, pp. 5187–5199, 2007.

[33] B. Dzepina, D. Balint, and D. Dini, "A phase field model of pressure-assisted sintering", *Journal of the European Ceramic Society*, vol. 39, no. 2-3, pp. 173–182, 2019.

[34] J. Hötzer, M. Seiz, M. Kellner, W. Rheinheimer, and B. Nestler, "Phase-field simulation of solid state sintering", *Acta Materialia*, vol. 164, pp. 184–195, 2019.

[35] R. Termuhlen, X. Chatzistavrou, J. D. Nicholas, and H.-C. Yu, "Three-dimensional phase field sintering simulations accounting for the rigid-body motion of individual grains", *Computational Materials Science*, vol. 186, p. 109 963, 2021.

[36] S. Okuno, Q. Yu, and Y. Nakata, "Influence of sintering conditions on mechanical properties of ag-nano sintered material", in *2016 IEEE 18th Electronics Packaging Technology Conference (EPTC)*, IEEE, 2016, pp. 488–491.

[37] G. He, G. Hongcun, L. Shujin, Z. Junwen, and Y. Yao, "Compressive failure mechanism of sintered nano-silver", *Journal of Materials Research*, vol. 38, no. 18, pp. 4201–4213, 2023.

[38] Y. Su *et al.*, "Thermo-elasto-plastic phase-field modelling of mechanical behaviours of sintered nano-silver with randomly distributed micro-pores", *Computer Methods in Applied Mechanics and Engineering*, vol. 378, p. 113 729, 2021.

[39] L. Ding, R. L. Davidchack, and J. Pan, "A molecular dynamics study of sintering between nanoparticles", *Computational Materials Science*, vol. 45, no. 2, pp. 247–256, 2009.

[40] D. Hu, Z. Cui, J. Fan, X. Fan, and G. Zhang, "Thermal kinetic and mechanical behaviors of pressure-assisted cu nanoparticles sintering: A molecular dynamics study", *Results in Physics*, vol. 19, p. 103 486, 2020.

[41] Y. Hu, Y. Wang, and Y. Yao, "Molecular dynamics on the sintering mechanism and mechanical feature of the silver nanoparticles at different temperatures", *Materials Today Communications*, vol. 34, p. 105 292, 2023.

[42] J. Xu, Y. Higuchi, N. Ozawa, K. Sato, T. Hashida, and M. Kubo, "Parallel large-scale molecular dynamics simulation opens new perspective to clarify the effect of a porous structure on the sintering process of ni/ysz multiparticles", *ACS applied materials & interfaces*, vol. 9, no. 37, pp. 31 816–31 824, 2017.

[43] Q. Guo, H. Hou, K. Wang, M. Li, P. K. Liaw, and Y. Zhao, "Coalescence of al0. 3cocrfeni polycrystalline high-entropy alloy in hot-pressed sintering: A molecular dynamics and phase-field study", *npj Computational Materials*, vol. 9, no. 1, p. 185, 2023.

[44] Y. O. Yildiz, "Morphological evolution of irregularly shaped au nanoparticles during the sintering process and their mechanical performance", *Computational Particle Mechanics*, vol. 10, no. 6, pp. 1659–1667, 2023.

[45] X. Liu *et al.*, "Microstructural evolution, fracture behavior and bonding mechanisms study of copper sintering on bare dbc substrate for sic power electronics packaging", *Journal of Materials Research and Technology*, vol. 19, pp. 1407–1421, 2022.

[46] L. Du, X. Pan, and Y. Hong, "New insights into microstructure refinement in crack initiation region of very-high-cycle fatigue for slm ti-6al-4v via precession electron diffraction", *Materialia*, vol. 33, p. 102 008, 2024.

[47] L. Qi *et al.*, "Diffusional-displacive transformation in a metastable β titanium alloy and its strengthening effect", *Acta Materialia*, vol. 195, pp. 151–162, 2020.

[48] H. Xiao *et al.*, "Precipitation and crystallographic relationships of nanosized η/η'precipitates at s-al interface in al-zn-mg-cu alloy", *Scripta Materialia*, vol. 214, p. 114 643, 2022.

[49] J. Jeong, N. Cautaerts, G. Dehm, and C. H. Liebscher, "Automated crystal orientation mapping by precession electron diffraction-assisted four-dimensional scanning transmission electron microscopy using a scintillator-based cmos detector", *Microscopy and Microanalysis*, vol. 27, no. 5, pp. 1102–1112, 2021.

[50] M. F. Heinig *et al.*, "High resolution crystal orientation mapping of ultrathin films in sem and tem", *Materials Characterization*, vol. 189, p. 111 931, 2022.

[51] X. Liu, Y. Zhou, X. Zhu, D. Wang, and Q. Fan, "The failure mechanism at adiabatic shear bands of titanium alloy: High-precision survey using precession electron diffraction and geometrically necessary dislocation density calculation", *Materials Science and Engineering: A*, vol. 746, pp. 322–331, 2019.

[52] R. Henry *et al.*, "Local fracture toughness measurements in polycrystalline cubic zirconia using micro-cantilever bending tests", *Mechanics of Materials*, vol. 136, p. 103 086, 2019.

[53] D. Sorensen *et al.*, "Intrinsic toughness of the bulk-metallic glass vitreloy 105 measured using micro-cantilever beams", *Acta Materialia*, vol. 183, pp. 242–248, 2020.

[54] H. Zhang, C. Chen, J. Jiu, S. Nagao, and K. Suganuma, "Microstructural homogeneity of sintered ag joint after pressureless sintering process", in *2017 International Conference on Electronics Packaging (ICEP)*, IEEE, 2017, pp. 122–124.

[55] C. Chen *et al.*, "Interface reaction and evolution of micron-sized ag particles paste joining on electroless ni-/pd-/au-finished dba and dbc substrates during extreme thermal shock test", *Journal of Alloys and Compounds*, vol. 862, p. 158 596, 2021.

[56] F. Yang, W. Zhu, W. Wu, H. Ji, C. Hang, and M. Li, "Microstructural evolution and degradation mechanism of sic–cu chip attachment using sintered nano-ag paste during high-temperature ageing", *Journal of Alloys and Compounds*, vol. 846, p. 156 442, 2020.

[57] T. Csanádi, A. Azizpour, M. Vojtko, and W. G. Fahrenholtz, "The effect of crystal anisotropy on fracture toughness and strength of zrb2 microcantilevers", *Journal of the American Ceramic Society*, vol. 107, no. 3, pp. 1669–1681, 2024.

[58] J. Gong and A. J. Wilkinson, "Anisotropy in the plastic flow properties of single-crystal α titanium determined from micro-cantilever beams", *Acta Materialia*, vol. 57, no. 19, pp. 5693–5705, 2009.

[59] G. Dehm, B. N. Jaya, R. Raghavan, and C. Kirchlechner, "Overview on micro-and nanomechanical testing: New insights in interface plasticity and fracture at small length scales", *Acta Materialia*, vol. 142, pp. 248–282, 2018.

[60] A. P. Thompson *et al.*, "Lammps-a flexible simulation tool for particle-based materials modeling at the atomic, meso, and continuum scales", *Computer Physics Communications*, vol. 271, p. 108 171, 2022.

[61] A. Stukowski, "Visualization and analysis of atomistic simulation data with ovito–the open visualization tool", *Modelling and simulation in materials science and engineering*, vol. 18, no. 1, p. 015 012, 2009.

[62] Y. Mishin, M. Mehl, D. Papaconstantopoulos, A. Voter, and J. Kress, "Structural stability and lattice defects in copper: Ab initio, tight-binding, and embedded-atom calculations", *Physical Review B*, vol. 63, no. 22, p. 224 106, 2001.

[63] Y. Mishin, M Asta, and J. Li, "Atomistic modeling of interfaces and their impact on microstructure and properties", *Acta Materialia*, vol. 58, no. 4, pp. 1117–1151, 2010.

[64] T. Frolov, D. L. Olmsted, M. Asta, and Y. Mishin, "Structural phase transformations in metallic grain boundaries", *Nature communications*, vol. 4, no. 1, p. 1899, 2013.

[65] J. Han, S. L. Thomas, and D. J. Srolovitz, "Grain-boundary kinetics: A unified approach", *Progress in Materials Science*, vol. 98, pp. 386–476, 2018.

[66] B Henrich, A Wonisch, T Kraft, M Moseler, and H Riedel, "Simulations of the influence of rearrangement during sintering", *Acta Materialia*, vol. 55, no. 2, pp. 753–762, 2007.

[67] D. E. Spearot, M. A. Tschopp, K. I. Jacob, and D. L. McDowell, "Tensile strength of< 1 0 0> and< 1 1 0> tilt bicrystal copper interfaces", *Acta materialia*, vol. 55, no. 2, pp. 705–714, 2007.

[68] S. Bargmann *et al.*, "Generation of 3d representative volume elements for heterogeneous materials: A review", *Progress in Materials Science*, vol. 96, pp. 322–384, 2018.

[69] X. Tu, A. Shahba, J. Shen, and S. Ghosh, "Microstructure and property based statistically equivalent rves for polycrystalline-polyphase aluminum alloys", *International Journal of Plasticity*, vol. 115, pp. 268–292, 2019.

[70] R. Vieira, H Sehitoglu, and J Lambros, "Representative volume elements for plasticity and creep measured from high-resolution microscale strain fields", *Acta Materialia*, vol. 214, p. 117 021, 2021.

[71] J. Lifton and T. Liu, "An adaptive thresholding algorithm for porosity measurement of additively manufactured metal test samples via x-ray computed tomography", *Additive Manufacturing*, vol. 39, p. 101 899, 2021.

[72] M. Makowska *et al.*, "Cracks, porosity and microstructure of ti modified polymer-derived sioc revealed by absorption-, xrd-and xrf-contrast 2d and 3d imaging", *Acta Materialia*, vol. 198, pp. 134–144, 2020.

[73] H. E. Exner and E. Arzt, "Sintering processes", *Sintering Key Papers*, pp. 157–184, 1990.

[74] W. Soboyejo, *Mechanical properties of engineered materials*. CRC press, 2002.

[75] X. Long *et al.*, "Finite element analysis to the constitutive behavior of sintered silver nanoparticles under nanoindentation", *International Journal of Applied Mechanics*, vol. 10, no. 10, p. 1 850 110, 2018.

[76] Y. Su, Z. Shen, X. Long, C. Chen, L. Qi, and X. Chao, "Gaussian filtering method of evaluating the elastic/elasto-plastic properties of sintered nanocomposites with quasi-continuous volume distribution", *Materials Science and Engineering: A*, vol. 872, p. 145 001, 2023.

[77] Y. Su, J. Zhu, X. Long, L. Zhao, C. Chen, and C. Liu, "Statistical effects of pore features on mechanical properties and fracture behaviors of heterogeneous random porous materials by phase-field modeling", *International Journal of Solids and Structures*, vol. 264, p. 112 098, 2023.

[78] J. Hohe and V. Hardenacke, "Analysis of uncertainty effects due to microstructural disorder in cellular or porous materials", *International Journal of Solids and Structures*, vol. 49, no. 7-8, pp. 1009–1021, 2012.

[79] G. He, Y. Yao, and Y. Yuting, "Size effect on the fracture of sintered porous nano-silver joints: Experiments and weibull analysis", *Journal of Alloys and Compounds*, vol. 863, p. 158 611, 2021.

3

Tailoring Microstructure and Mechanical Properties of Sintered Copper Nanoparticles

This study investigates the microstructure evolution and mechanical behavior of sintered copper (Cu) nanoparticles (NPs) under varying sintering pressures. Micro-pillar compression tests reveal a transition from collapse-dominated to compaction-driven deformation as sintering pressure increases. Transmission electron microscopy (TEM) and transmission Kikuchi diffraction (TKD) analyses identify a two-stage deformation mechanism—initial pore compaction followed by intragranular slip—fundamentally distinct from bulk Cu. Molecular dynamics (MD) simulations further reveal that large particles promote dislocation-mediated plasticity by accommodating intragranular slip, while small particles enhance load transfer through localized shear-compaction, together enabling uniform strain distribution and supporting the experimentally observed strain accommodation. The resulting microstructure achieves a combination of high yield strength (up to 320 MPa) and low elastic modulus (20 GPa), offering a compliant yet robust response. These findings elucidate a unique processing–structure–property relationship and provide a rational basis for designing porous metal interconnects capable of withstanding thermomechanical stresses in advanced electronic packaging.

Parts of this chapter have been submitted to Acta Materialia.

3.1. INTRODUCTION

PRESSURE-assisted sintering enables the rapid densification of metallic nanoparticles (NPs) at relatively low temperatures, significantly reducing processing time compared to conventional pressureless sintering [1, 2]. Copper (Cu) NPs consolidated via this method exhibit superior electrical, thermal, and mechanical properties [3, 4], making them highly attractive for high-throughput and reliable electronic packaging. However, the resulting microstructure—particularly porosity and neck formation—is highly sensitive to sintering pressure, directly influencing mechanical performance [5, 6]. While previous studies have extensively investigated the relationship between sintering parameters, microstructure and mechanical behavior, the focus has largely remained at the macroscale [7–14]. The microscale mechanical response, especially the roles of porosity and sintered necks, remains inadequately understood. Therefore, establishing a clear correlation among sintering pressure, microstructural features and mechanical properties is critical for optimizing the reliability of sintered Cu NPs in advanced engineering applications.

Previous studies have explored the microscale mechanical behavior of sintered NPs using in-situ scanning electron microscopy (SEM) tensile tests [15–17] and microcantilever bending tests [17–20], however, investigations focusing on micro-pillar compression tests, particularly for sintered Cu NPs, remain limited. Micro-pillar compression test has emerged as a powerful technique for characterizing the microscale mechanical properties of materials [21–30]. Its ability to isolate small, representative material volumes reduces geometric and size-related artifacts, enabling precise analysis of key features such as porosity and sintered necks. This makes it particularly effective for studying localized deformation mechanisms that govern the mechanical response of sintered NPs [26, 27]. For instance, Chen et al. [26] demonstrated through micro-pillar compression tests that the mechanical performance of sintered silver (Ag) particles is strongly influenced by porosity and necking growth, with Ag flakes achieving superior bonding strength above 30 MPa due to enhanced neck formation from self-generated NPs. Inspired by such findings, this study employs micro-pillar compression tests to systematically investigate the influence of sintering pressure on the mechanical properties of sintered Cu NPs.

Investigating microstructure evolution during sintering is crucial for optimizing material performance, particularly mechanical properties. However, experimental methods face limitations in capturing the dynamic evolution of sintered Cu NPs, prompting the development of various computational models, including Molecular Dynamics (MD) [31, 32], phase-field modeling [33–36], Monte Carlo (MC) simulations [37–39], finite element methods (FEM) [40–42], and the Discrete Element Method (DEM) [34, 43–46]. Among these, the phase-field approach offers a key advantage by naturally simulating the evolution of complex microstructures without explicitly tracking interfaces or imposing predefined assumptions. Notably, Dzepina et al. [35] introduced a phase-field sintering model incorporating an efficient contact mechanics algorithm, enabling the simulation of pressure-assisted sintering. DEM, on the other hand, excels in modelling large-scale particle packing and neck formation [45], providing insights into the structural development of sintered materials. Due to the computational challenges associated with representing particle shapes and capturing sintering physics, most ap-

proaches—except for DEM—are typically restricted to a limited number of particles, often within a 2D framework. MC simulations, in contrast, have demonstrated the ability to model relatively large particle ensembles, effectively capturing the microstructure evolution and kinetic processes of solid-state sintering [39]. However, a key drawback of the MC method is the lack of direct physical interpretation for model parameters and time steps (Monte Carlo steps). Additionally, MC models are generally constrained to free sintering [47], limiting their applicability to pressure-assisted sintering scenarios.

MD simulations are powerful tools for investigating atomic-scale sintering mechanisms, such as neck formation and atomic diffusion [48–53]. Although their limited timescales lead to an underestimation of diffusion-driven densification—particularly surface and bulk diffusion—MD provides precise control over sintering conditions, enabling systematic analysis of the effects of pressure on mass transport, dislocation generation, and sintered neck stability. Compared to other computational approaches, MD excels in capturing real-time atomic diffusion and neck evolution during sintering. For instance, Wang et al. [31] demonstrated the temperature-dependent sintering behavior of Cu NPs, showing that enhanced surface diffusion and atomic motion at sintering necks facilitate bonding under elevated pressures. Moreover, MD allows direct observation of dislocation activity and stacking fault accumulation during both sintering and deformation, providing critical insights into localized plastic deformation. Given these advantages, MD simulations were employed in this study to examine the sintering dynamics and mechanical deformation of sintered Cu NPs.

The aim of this study is to investigate the influence of sintering pressure on the microstructure evolution and mechanical properties of sintered Cu NPs. To achieve this, sintered Cu NPs were fabricated with increasing sintering pressure from 0 to 30 MPa, and their mechanical behavior was systematically examined through micro-pillar compression tests. Post-deformation microstructural analysis was performed using SEM, transmission electron microscopy (TEM) and transmission Kikuchi diffraction (TKD) analyses to reveal the deformation mechanisms and crystallographic orientations. Additionally, MD simulations were employed to reveal atomic-scale sintering dynamics and mechanical deformation. By integrating experimental and computational approaches, this study provides comprehensive insights into sintering and deformation mechanisms of sintered Cu NPs.

3.2. EXPERIMENTAL AND SIMULATION METHOD

3.2.1. SAMPLE PREPARATION

To fabricate sintered Cu samples, a layer of Cu paste was initially printed onto an Active Metal Brazing (AMB) substrate with dimensions of 3 mm × 3 mm and a thickness of 200 µm. The AMB substrate consists of a silicon nitride (Si_3N_4) ceramic core bonded to finished Cu layers. The sintering process was carried out under a nitrogen atmosphere at 250^{o}C for 5 minutes using a sintering system (Sinterstar, Boschman Technologies BV), with simultaneous application of external pressure to enhance densification of the Cu NPs (Fig. 3.1a). After sintering, the applied aluminum (Al) film was carefully removed, leaving a consolidated Cu layer firmly adhered to the substrate (Fig. 3.1b). Subsequently, the sintered Cu layer was sectioned from the AMB substrate to isolate specific regions

for further mechanical characterization (Fig. 3.1c).

Micro-pillar fabrication was performed using focused ion beam (FIB) milling (Fig. 3.1d) with a dual-beam FEI Helios G4 CX FIB-SEM system. This technique enabled the precise removal of material surrounding the target region, producing cylindrical micro-pillars with well-defined geometries. The fabricated micro-pillars exhibited a diameter of approximately 6 µm and a height of 20 µm, as confirmed by the SEM image in Fig. 3.1e. This gives an aspect ratio (height to diameter) of around 3:1, ensuring mechanical stability during compression tests [26].

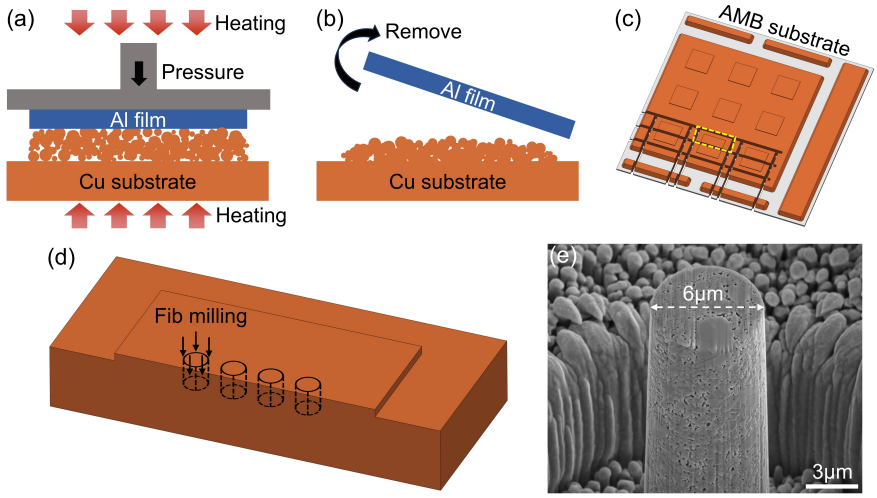


Figure 3.1: (a) Diagram of sintering process (250°C, 5min); (b) Al film removal; (c) sintered Cu pattern on AMB substrate; (d) FIB milling process; (e) a typical SEM image of the micro-pillar.

3.2.2. MICRO-PILLAR COMPRESSION TESTS

The micro-pillar compression tests were conducted using an InSEM HT System (KLA Corporation, Milpitas, CA, USA), equipped with an InForce 50 actuator capable of applying a maximum load of 50 mN [54]. A flat punch tip, acquired from Synton-MDP (Nidau, Switzerland), was employed for precise load application. The boron carbide tip used in the tests has a Young's modulus of 461 GPa and a Poisson's ratio of 0.21. To ensure reproducibility and statistical significance, five micro-pillars were tested under each experimental condition. The tests were performed in displacement control mode, with continuous load-displacement data acquisition to monitor the mechanical response of the micro-pillars. Prior to testing, samples were meticulously aligned to ensure axial loading and minimize bending effects. Additionally, a pre-conditioning load was applied to establish consistent contact and eliminate surface irregularities. Post-compression, the deformation behavior of the sintered Cu micro-pillars was analyzed, focusing on key mechanical properties such as yield strength, strain hardening and failure mechanisms.

3.2.3. SEM AND TEM CHARACTERIZATION

To investigate the internal microstructure of the sintered Cu NPs, a focused ion beam scanning electron microscopy (FIB-SEM) three-dimensional (3D) reconstruction technique was employed. This method enables high-resolution imaging of subsurface features through a sequential milling and imaging process. The procedure began with the identification of the region of interest (ROI), as highlighted in Fig. 3.2a, where the imaging area was demarcated. To ensure precise alignment and accurate relocation throughout the milling process, a fiducial marker was fabricated on the sample surface (Fig. 3.2b). Material removal was performed systematically using the FIB along the designated milling direction, and each newly exposed cross-sectional surface was imaged using SEM. The resulting two-dimensional (2D) SEM images were sequentially collected and stacked to generate a high-resolution 3D reconstruction of the microstructure (Fig. 3.2c) by using a commercial software Avizo. Despite the protective deposition of a Pt layer over the ROI prior to milling, minor damage to the Pt layer was observed due to the ion beam, as illustrated in Fig. 3.2d. This highlights a common challenge in FIB-based sample preparation, particularly for sensitive surface layers, but did not significantly affect the overall integrity of the 3D dataset.

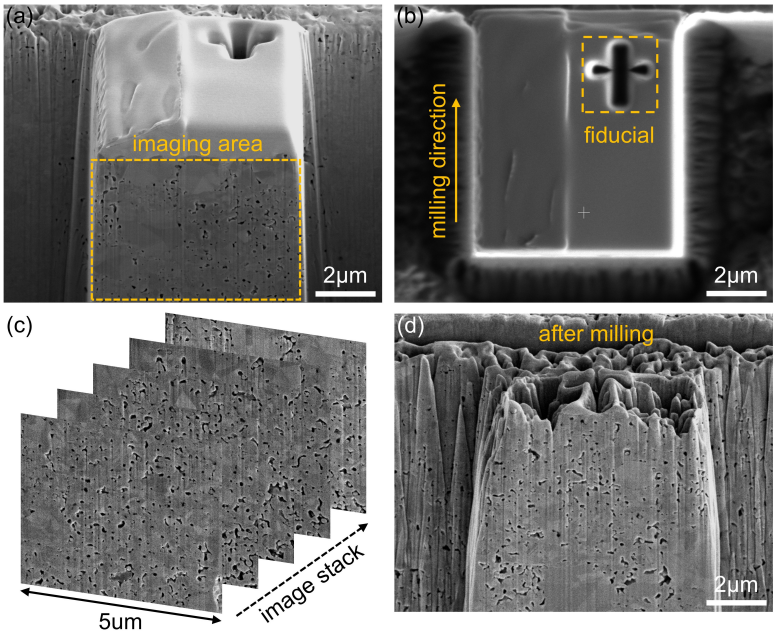


Figure 3.2: FIB-SEM slice-and-view procedure: (a) Deposition of Pt layer and imaging area; (b) fiducial marking for milling; (c) stacked SEM slices; (d) reconstructed region after milling.

Following 3D reconstruction, compression-tested micro-pillars were analyzed to investigate the failure mechanisms. The post-compression morphology was examined using SEM, enabling the identification and comparison of typical failure modes across samples prepared under different sintering pressures. To further elucidate the defor-

mation mechanisms, TEM (Cs-corrected Titan) was employed for a detailed microstructure analysis of the deformed micro-pillars at the nanoscale. Moreover, TKD was employed to characterize the crystallographic orientation of sintered Cu NP micro-pillars after deformation. Although electron backscatter diffraction (EBSD) is widely used in micromechanical studies [55, 56], its spatial resolution (50–100 nm) is insufficient for resolving the submicron grain structure and porosity typical of sintered Cu NPs. In contrast, TKD offers spatial resolutions below 10 nm [57, 58], enabling statistically meaningful microstructural characterization critical for understanding microscale deformation mechanisms.

3.2.4. MOLECULAR DYNAMICS SIMULATION

The sintering and mechanical behavior of bimodal Cu NP models were investigated using MD simulations with the Large-scale Atomic/Molecular Massively Parallel Simulator (LAMMPS) [59]. The atomic configurations, dislocations and local crystallographic environments during sintering and deformation were visualized and analyzed using the Open Visualization Tool (OVITO) [60]. The Cu-Cu atomic interactions were modeled using the Embedded Atom Method (EAM) potential proposed by Mishin et al. [61], which has been widely validated for simulating diffusion, grain boundary migration and mechanical responses in Cu systems. A 3D bimodal particle model was constructed within a simulation box measuring 800 × 800 × 100 $Å^3$, as shown in Fig. 3.3. Large cylindrical particles (diameter: 25 nm; height: 10 nm along the z-axis) were initially positioned in the simulation domain, and 1500 smaller spherical particles (average diameter: 2.5 nm) were randomly introduced to fill the voids around the cylinders, ensuring a high packing density of approximately 55%. The final model consisted of 3.1 million atoms. The sintering process was simulated in three stages. First, the system temperature was gradually increased to 523 K using a Nosé-Hoover thermostat to facilitate NP diffusion and sintering. Next, uniaxial strains of 30%, 40% and 50% were applied sequentially along the X- and Y-axes to simulate pressure-assisted sintering and replicate the height reduction observed in experiments. During this step, lateral pressures in the non-loading directions were maintained at zero, and a strain rate of 1×10^9 s^{-1} was employed. The system was then equilibrated at 523 K for 100 ps to relax residual stresses from the high strain rate, resulting in a sintered model.

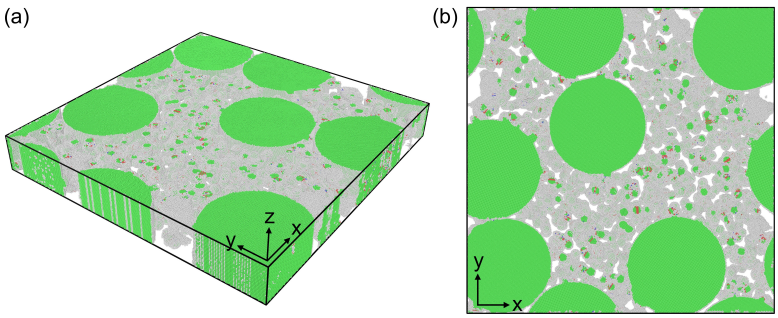


Figure 3.3: Sintered Cu NPs with bimodal size distribution and periodic boundary conditions for MD simulation: (a) 3D perspective model; (b) orthogonal view of (a).

To evaluate the mechanical response of the sintered Cu NPs, tensile and compression simulations were performed along the X- and Y-directions (the long axes of the model), based on the previously sintered configurations. This resulted in 12 distinct stress-strain curves corresponding to the sintered models under three different applied strains (30%, 40%, and 50%) and two loading directions (tensile along X and Y, compression along X and Y). Tensile and compression simulations were performed under fully periodic boundary conditions using the NPT ensemble, with the temperature maintained at 300 K. A maximum tensile strain of 30% was applied at a strain rate of 5×10^8 s^{-1}, a value consistent with prior studies [62]. Compressive strains, on the other hand, were applied up to approximately 16%, aligning with experimental results. Stresses in the non-loading directions were maintained at zero during both tensile and compressive simulations to replicate uniaxial loading conditions.

3.3. RESULTS

3.3.1. EFFECT OF SINTERING PRESSURE ON POROSITY

The influence of sintering pressure on the porosity and microstructure of sintered Cu NPs was investigated using a combination of 2D cross-sectional imaging and 3D FIB-SEM reconstruction. Fig. 3.4 presents 2D cross-sectional images of samples sintered under different pressures, providing a detailed characterization of porosity evolution and void morphology. Before sintering (Fig. 3.4a), the Cu NPs exhibit a significant bimodal size distribution. At 0 MPa (Fig. 3.4b), the Cu NPs retain their distinct morphology with clear and well-defined particle boundaries, indicating that significant sintering has not yet occurred. Increasing the pressure to 5 MPa (Fig. 3.4c) enhances neck growth but leads to the formation of larger, more irregular voids. This can be attributed to particle coalescence, where larger particles consume smaller ones, resulting in isolated and irregularly shaped voids. Moreover, the distribution of voids is not uniform. In some regions, void concentration is higher. At 10 MPa (Fig. 3.4d), the structure becomes noticeably more compact, with voids that are smaller, more rounded and less interconnected. The neck growth between particles becomes more pronounced, although isolated voids persist, indicating incomplete densification. At 20 MPa (Fig. 3.4e), the microstructure demonstrates significant densification with tightly packed particles and well-defined sintered necks. The voids are smaller, more uniform and exhibit a more spherical shape, suggesting that higher pressure promotes void collapse and improved particle rearrangement. Beyond 20 MPa, further increasing the pressure to 30 MPa (Fig. 3.4f) results in only a slight improvement in densification. The voids stabilize in size and shape, becoming uniformly distributed and more spherical.

To quantitively measure the porosity, FIB-SEM 3D reconstruction technique were applied on the five groups of sintered samples. The 3D reconstruction results of 5 MPa sintered Cu NPs, shown in Fig. 3.5a, provide a clear visualization of the internal porosity of the sintered samples, with the voids represented in blue. Quantitative analysis of the 3D volume porosity extracted from the software as a function of sintering pressure is presented in Fig. 3.5b. It is evident that porosity decreases with increasing sintering pressure. At 0 MPa, the porosity is approximately 10%, while further increasing the pressure to 30 MPa reduces the porosity to a stable value of 7%. Two key observations arise

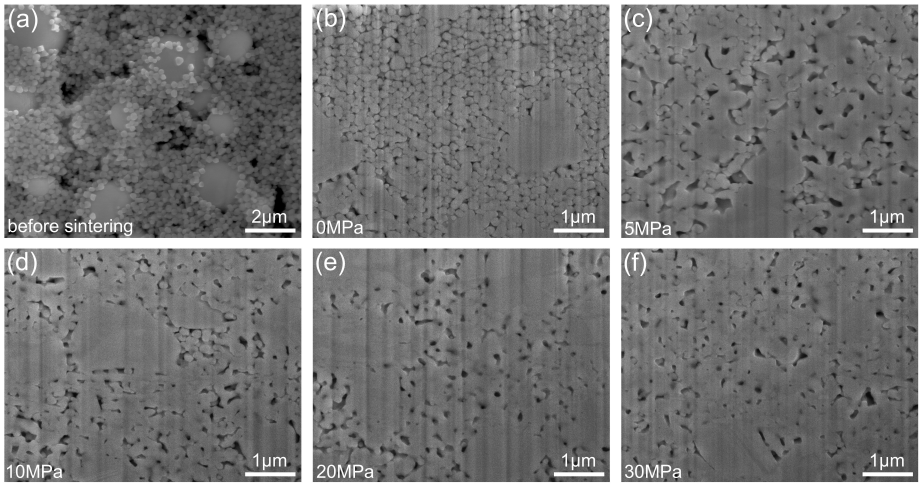


Figure 3.4: Microstructure evolution of Cu NPs: (a) Before sintering; (b) sintered at 0MPa; (c) sintered at 5MPa; (d) sintered at 10MPa; (e) sintered at 20MPa; (f) sintered at 30MPa.

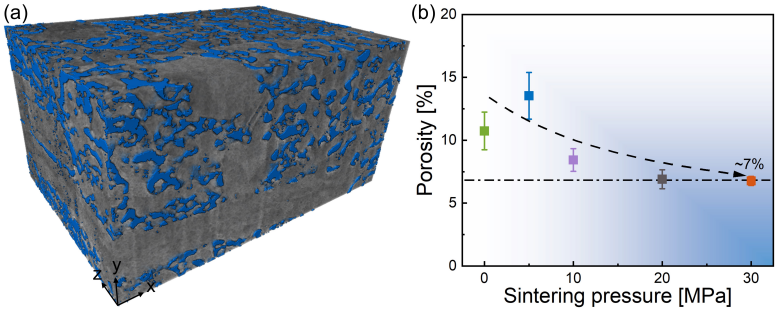


Figure 3.5: (a) A 3D reconstructed structure of 5 MPa sintered sample; (b) relationship between the porosity and the sintering pressure.

from this trend. First, the reduction in porosity with increasing pressure is attributed to enhanced particle rearrangement, melting at contact points and sintered neck formation, which are facilitated by the applied pressure. Second, despite increasing the sintering pressure from 20 MPa to 30 MPa, the porosity stabilizes around 7%, indicating a threshold where further densification is limited by residual nanoscale voids and geometric constraints. Interestingly, the porosity of the sample sintered without pressure (0 MPa) is slightly lower than that of the sample sintered with pressure of 5 MPa. This anomaly can be attributed to the sintering dynamics: at 5 MPa, particle rearrangement initiates, and larger particles grow at the expense of smaller ones (Ostwald ripening [40]), leading to the formation of larger and resolvable voids. In contrast, at 0 MPa, sintering barely progresses, and the particles remain loosely packed with minimal neck growth. The resulting voids are small and difficult to resolve using FIB-SEM, which could lead to an underestimation of porosity.

In summary, the sintering pressure not only reduces porosity but also significantly influences void shape and distribution. Higher pressures transform voids from irregular and interconnected at low pressures to smaller, more spherical and evenly distributed at pressures beyond 20 MPa. Importantly, the non-uniform void distribution observed under lower pressures highlights localized sintering effects around large particles. To elucidate these mechanisms further, sintering dynamics based on MD simulations will be presented in the next section.

3.3.2. STRESS-STRAIN CURVES

The mechanical properties of sintered Cu NPs, evaluated through micro-pillar compression tests, show a strong dependence on sintering pressure and porosity (Fig. 3.6). The stress-strain curves for samples sintered under pressures ranging from 0 MPa to 30 MPa are presented in Fig. 3.6a. A clear enhancement in mechanical properties, including yield stress and elastic modulus, is observed with increasing sintering pressure. The yield strength of the sintered Cu micro-pillars was determined using the 0.2% offset yield criterion [63], a widely adopted method for defining the onset of plastic deformation in metallic materials. At 0 MPa, the stress-strain curve reveals a low yield stress of approximately 120 MPa and an ultimate strength of 150 MPa, reflecting poor interparticle bonding and high porosity that limit load transfer and lead to premature failure. Increasing the sintering pressure to 5 MPa results in an improvement in yield stress to 210 MPa and ultimate strength to 260 MPa, attributed to initial densification and neck formation between particles. At 10 MPa, further enhancement is observed, with yield stress reaching 230 MPa and ultimate strength rising to 320 MPa, indicating better particle rearrangement, reduced voids and stronger neck growth. A significant improvement occurs at 20 MPa, where the yield stress exceeds 300 MPa and the ultimate strength approaches 470 MPa. The stress-strain curve exhibits a steeper slope in the elastic region, corresponding to a notable increase in stiffness, which reflects a more optimized microstructure with fewer voids and enhanced neck formation. At 30 MPa, the yield stress increases slightly to 320 MPa, and the ultimate strength is close to 510 MPa; however, the improvement relative to 20 MPa is less pronounced.

The relationship between sintering pressure, yield stress and elastic modulus is quantified in Fig. 3.6b. The elastic modulus increases significantly with sintering pressure, rising from 4.8 GPa at 0 MPa to 20 GPa at 20 MPa, with only a marginal gain at 30 MPa. This plateauing behavior indicates that the microstructure reaches near-optimal densification and sintered neck growth at 20 MPa, beyond which additional pressure provides diminishing returns. Fig. 3.6c further illustrates the correlation between mechanical properties and porosity. A clear trend emerges where decreasing porosity leads to significant improvements in both yield stress and elastic modulus. Specifically, at porosities exceeding 10%, the mechanical performance is severely limited due to insufficient neck formation and void concentration, whereas samples with porosities below 7–8% exhibit significantly enhanced strength and stiffness.

The mechanical properties of sintered Cu NPs differ significantly from those of bulk Cu in its various forms. Notably, the yield strength of sintered Cu NPs exceeds that of bulk single-crystalline Cu (40–70 MPa) [21, 64–67] and bicrystalline Cu (80–120 MPa) [68–70], and is comparable to that of polycrystalline Cu (250–350 MPa) [29, 71], although

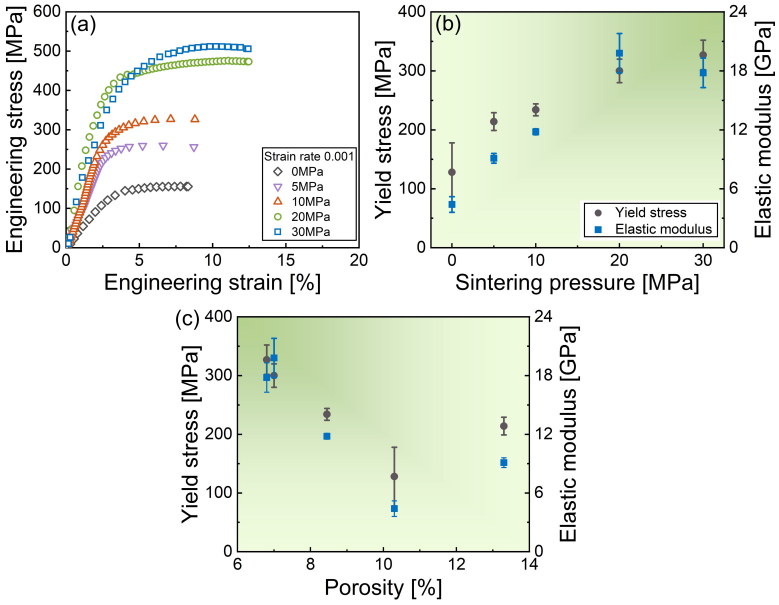


Figure 3.6: Mechanical properties of sintered Cu NPs: (a) Stress-strain curves of samples sintered under pressures of 0 MPa, 5 MPa, 10 MPa, 20 MPa and 30 MPa; (b) relationship between yield stress, elastic modulus and sintering pressure; (c) relationship between yield stress, elastic modulus and porosity.

it remains lower than that of nanocrystalline Cu (500–800 MPa) [29, 72, 73]. This enhanced strength, despite the intrinsic porosity of the sintered network, highlights the effectiveness of nanoscale sintering in generating strong interparticle bonds. In contrast, the elastic modulus of sintered Cu NPs is significantly reduced (20 GPa) compared to bulk Cu (75–130 GPa across all microstructures). In electronic packaging, this combination of high yield strength and low elastic modulus provides critical advantages: the reduced stiffness accommodates thermomechanical deformation mismatches between the die, substrate, and interconnect during thermal cycling, mitigating stress-induced failure while retaining mechanical integrity.

3.3.3. FAILURE MODES ANALYSIS

Fig. 3.7 illustrates the post-compression morphologies of sintered Cu micro-pillars under varying sintering pressures (0, 10, and 20 MPa), highlighting the evolution of deformation and failure mechanisms. At 0 MPa (Figs. 3.7a, d), failure is dominated by structural collapse, primarily due to weak inter-particle adhesion and insufficient neck formation. These poorly bonded particles lack the cohesion necessary to sustain shear or tensile stresses. With the application of 10 MPa (Figs. 3.7b, e), sintering is enhanced through the initiation of neck formation and localized particle coalescence, where larger particles partially engulf smaller ones. This improves bonding strength but still results in heterogeneous microstructures with significant unsintered regions due to limited particle rearrangement. Collapse failure is suppressed, and the failure mechanism transitions

to compaction-dominated deformation. At 20 MPa (Figs. 3.7c, f), the pillars exhibit well-developed sintering necks and reduced porosity. The cross-sectional view reveals uniform densification and continuous bonding pathways, which alleviate stress concentrations and enable distributed plastic deformation. Clear evidence of slip traces in Fig. 3.7c indicates that the fully sintered structure can accommodate higher mechanical loads, marking a transition to ductile, stress-bearing behavior.

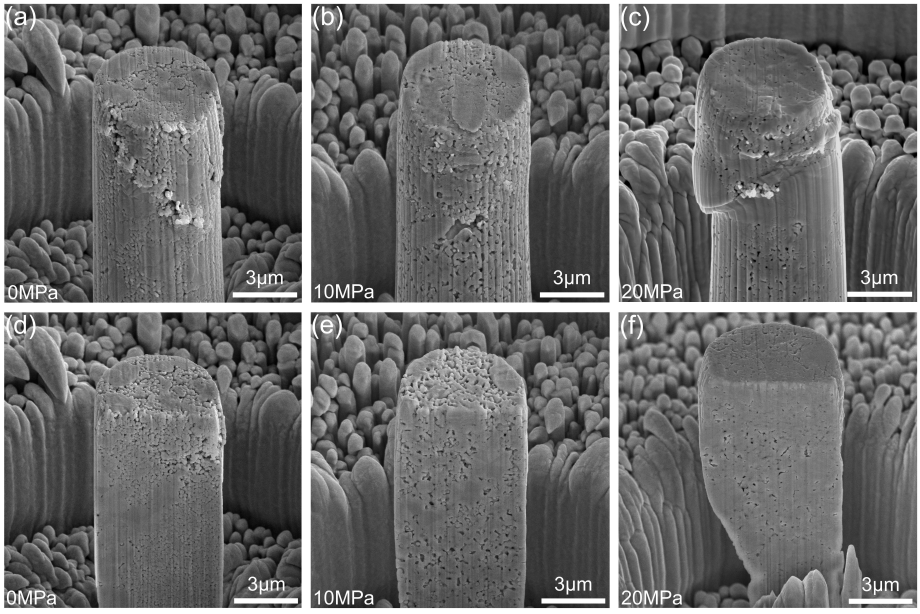


Figure 3.7: Typical morphologies of micro-pillar after compression tests: (a) 0 MPa; (b) 10 MPa; (c) 20 MPa; (d) cross-section of (a); (e) cross-section of (b); (f) a typical cross-section of a 20 MPa sintered micro-pillar.

3.4. DISCUSSION

3.4.1. DEFORMATION MECHANISMS

Fig. 3.8 presents TEM images of the 20 MPa sintered Cu micro-pillar after compression (corresponding to Fig. 3.7c), revealing a heterogeneous microstructure composed of both nano- and microparticles. As shown in Fig. 3.8a, the upper region and the vicinity of larger particles exhibit pronounced densification, indicative of localized compaction under compressive stress. High-magnification observations (Figs. 3.8b, c) reveal that initially porous regions have undergone significant pore compaction, resulting in a more continuous matrix with reduced void volume. Plastic deformation is highly localized and governed by particle size and distribution. Large particles accommodate deformation primarily through intergranular slip, as evidenced by the distinct slip bands shown in Fig. 3.8d, demonstrating their ability to sustain and dissipate stress. Simultaneously, smaller particles—particularly those situated at particle boundaries—undergo severe shear and compression-induced deformation, leading to localized densification

(Figs. 3.8d, e). In addition, the oxygen distribution in the sintered Cu NPs was characterized via energy-dispersive X-ray spectroscopy (EDX) in TEM. The measured oxygen content was approximately 0.07 wt%, which lies within the typical range for commercial-grade Cu [74]. This low level of oxidation is critical for preserving interparticle metallic bonding during sintering and promoting the formation of continuous, well-developed necks, thereby enhancing mechanical integrity.

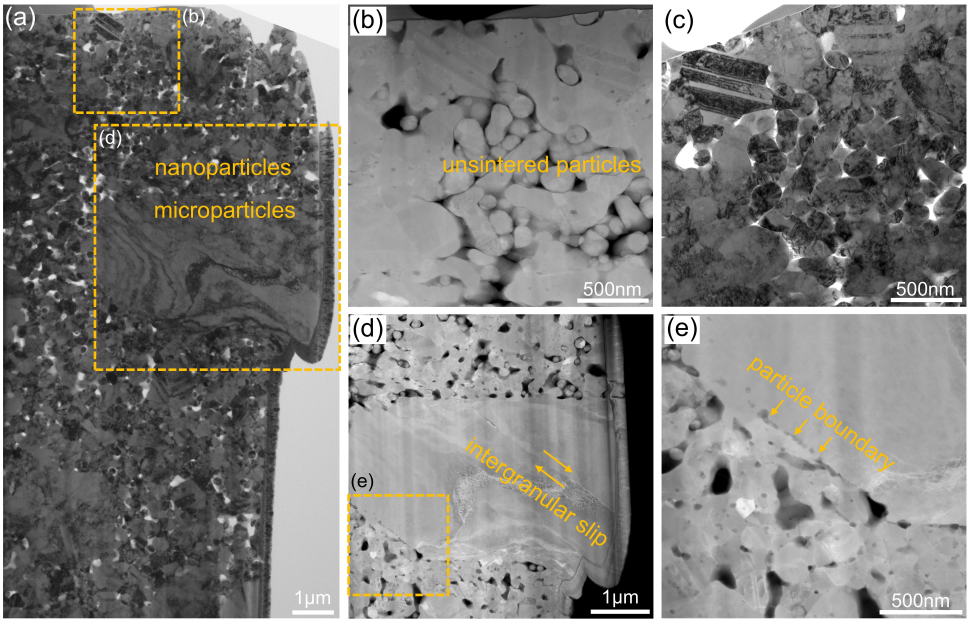


Figure 3.8: TEM images of the extracted micro-pillar sintered under 20 MPa after compression test: (a) A bright-field TEM overview shows the coexistence of large and small particles; (b) scanning transmission electron microscopy (STEM) image reveals the presence of unsintered NPs; (c) bright-field image highlights dislocation structures induced by compression; (d) intergranular slip deformation observed in a large particle, indicative of plastic flow under applied stress; (e) a enlarged area marked in (d).

To elucidate the localized deformation mechanisms underlying the mechanical behavior of sintered Cu NP micro-pillars, TKD analysis was performed on TEM lamellae extracted post-compression. Fig. 3.9a displays a representative STEM image of a micro-pillar composed predominantly of NPs. The upper region undergoes severe plastic deformation, characterized by particle flattening and void compaction under compressive loading. In contrast, the lower region retains porous morphology, reflecting strain localization in the upper zone. The corresponding orientation map (Fig. 3.9b) confirms that the particles possess a random crystallographic orientation distribution, which inherently promotes the activation of multiple, non-collinear slip systems under compression [75]. This random texture increases the likelihood of slip transmission barriers at grain boundaries, thereby contributing to strength enhancement through grain boundary hardening [76]. The geometrically necessary dislocations (GNDs) distribution in Fig. 3.9c further reveals a dense dislocation network throughout the nanoparticle matrix.

The widespread GNDs suggest significant plastic strain gradients and interparticle misorientation accumulation [77]. Such a dense, interconnected dislocation structure resembles dislocation forest hardening [78, 79], where tangled dislocations impede further slip, enhancing strain hardening and contributing to the observed mechanical robustness. Moreover, the Schmid factor map (Fig. 3.9d) displays a broad spectrum of values across the microstructure, confirming that slip activity is spatially heterogeneous, consistent with the observed complex deformation behavior. Fig. 3.10 presents TKD analysis from a second micro-pillar containing both nano- and microparticles. The STEM image (Fig. 3.10a) reveals a large embedded particle within a matrix of smaller grains. Orientation mapping (Fig. 3.10b) shows that while smaller grains remain randomly oriented, the large particle maintains a distinct crystallographic domain. This particle likely accommodates deformation via intragranular slip [80], as supported by the high local GND density observed within and around it (Fig. 3.10c). The corresponding Schmid factor map (Fig. 3.10d) indicates that the large particle lies near a high-Schmid factor orientation, favoring slip activation.

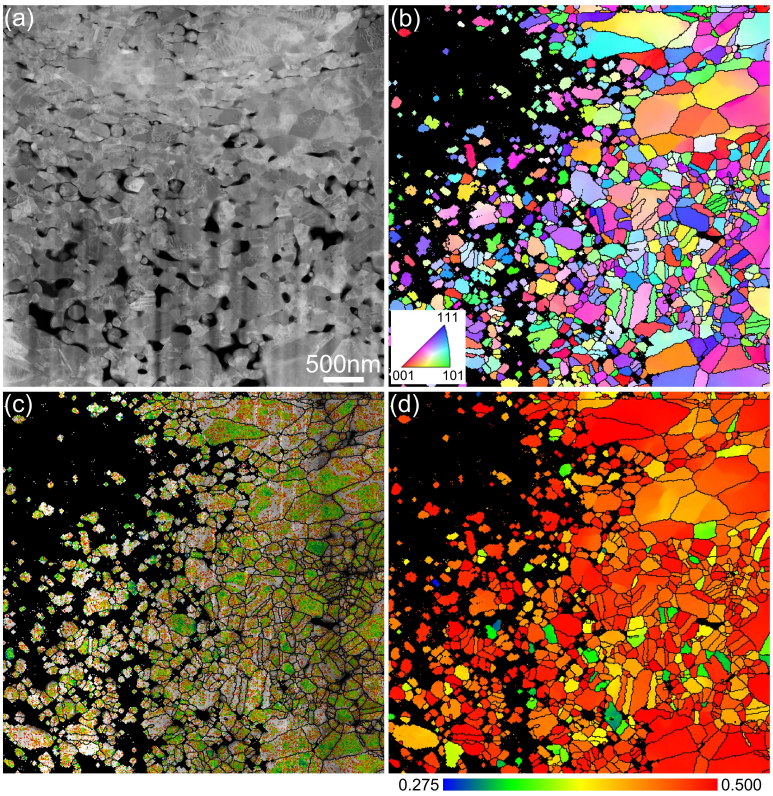


Figure 3.9: Deformation mechanism of sintered Cu NP micro-pillar after compression: (a) STEM image showing severely deformed particles in the top region; (b) inverse pole figure (IPF) map revealing a random distribution of crystallographic orientations; (c) GNDs density map; (d) Schmid factor map.

The deformation mechanism of sintered Cu NPs exhibits fundamental differences

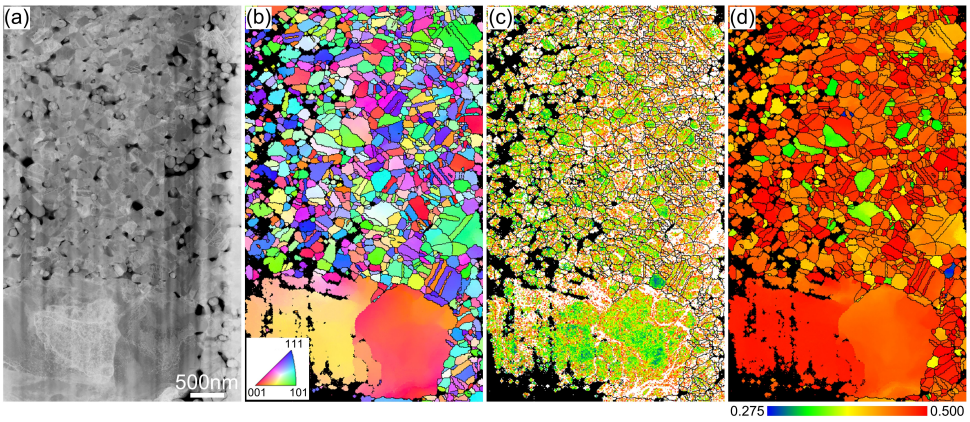


Figure 3.10: Deformation mechanism of sintered Cu NP micro-pillar after compression: (a) STEM image showing both nano- and microparticles; (b) inverse pole figure (IPF) map; (c) GNDs density map; (d) Schmid factor map.

from that of fully dense bulk Cu, including single-crystalline [21, 66], bicrystalline [69, 70], polycrystalline [29], and nanocrystalline counterparts [72, 73]. Unlike bulk Cu, where plasticity is typically governed by well-defined slip along specific crystallographic planes, the sintered Cu NPs undergo a two-stage deformation process driven by their porous architecture and heterogeneous grain structure. Initially, compressive stress leads to the compaction of the porous network, forming dense particle-particle contacts. This process reduces the effective stiffness (elastic modulus) of the material, a characteristic beneficial for applications such as electronic packaging where compliance with thermal expansion mismatch is critical [81]. Following the initial compaction stage, plastic deformation in sintered Cu NPs is primarily accommodated through intragranular slip within individual particles. The randomly distributed crystallographic orientations, as revealed by TKD analysis, lead to independent activation of multiple slip systems across different grains. This crystallographic heterogeneity promotes distributed plasticity and suppresses the formation of localized shear bands typically observed in textured or single-slip dominated structures, thereby enhancing ductility and delaying catastrophic failure [82]. The dislocations accumulate at particle interfaces and form entangled networks that obstruct further dislocation motion, effectively increasing resistance to continued plastic flow [83]. This dislocation-based interaction acts as a secondary hardening mechanism, sustaining strain hardening throughout the deformation process and contributing to the overall mechanical robustness of the porous sintered structure.

Crucially, the deformation behavior is governed not only by differences in crystallographic orientation but also by particle size heterogeneity. Large particles, owing to their extended slip paths and reduced boundary confinement, more readily accommodate intragranular plasticity and sustain significant plastic strain [84]. In contrast, smaller particles—typically situated at particle junctions or constrained interstitial sites—exhibit limited plasticity due to geometric confinement and high grain boundary density. These

features enhance their mechanical rigidity, enabling them to pin dislocations and act as local load-bearing units that resist premature yielding [85].

The tri-level interplay—between particle size, orientation, and porosity—produces a synergistic energy dissipation framework. It not only enhances load transfer and impedes crack propagation but also suppresses strain localization by activating diverse deformation pathways [86]. As a result, sintered Cu NPs achieve an exceptional combination of high strength (250–350 MPa) and low elastic modulus (20 GPa). In contrast, fully dense nanocrystalline Cu often exhibits limited strain hardening due to grain boundary-mediated softening mechanisms such as sliding and rotation [87]. The distinctive processing–structure–property relationship of sintered Cu NPs underscores the dual role of porosity and particle heterogeneity in simultaneously enhancing compliance and mechanical robustness, offering a scalable design paradigm for advanced metallic systems subjected to complex loading and thermal cycling conditions.

3.4.2. MICROSTRUCTURE EVOLUTION DURING SINTERING BY MD SIMULATION

To further reveal the evolution of the hierarchical microstructure, MD simulation for the sintering process of bimodal particle models is presented in Fig. 3.11. In the initial stage after heating to 250°C (Fig. 3.11a1), small particles coalesce significantly, and the large particles attract smaller particles due to localized capillary forces [88]. This early-stage sintering shows minimal dislocation activity, as seen in Fig. 3.11a2, since thermal effects dominate and mechanical deformation is negligible. However, as strain increases to 20% (Fig. 3.11b1), stress-induced diffusion becomes dominant, particularly near large particles. The denser structure near these earlier contact regions reflects enhanced atomic diffusion facilitated by localized stress and thermal activation. At 40% strain (Fig. 3.11c1), the sintering process accelerates further, leading to enhanced densification and reduced porosity, particularly in regions between large particles where small particles form significant sintered necks. This mechanism aligns with the experimental findings (Fig. 3.4 and Fig. 3.5), where reduced porosity and enhanced densification were observed near large particles under applied pressure. With increasing strain, dislocation density rises significantly and stacking faults begin to form, particularly within large particles (Figs. 3.11b2, c2). This reflects localized stress redistribution and strain accumulation during deformation [89]. The resulting dislocation structures and planar defects enhance interfacial contact and promote particle interlocking, thereby facilitating sintering neck growth and improving structural cohesion.

To investigate the effect of the relative positioning of large and small particles on the sintered microstructure, the sintering process was simulated using the same initial particle model under X- and Y-directional pressures at 30% and 40% strain, enabling a comparative analysis of the compaction behavior (Fig. 3.12). At 40% strain, the microstructure becomes denser, with smaller and more uniformly distributed voids compared to 30% strain, indicating that higher strain promotes enhanced particle rearrangement and densification. The stacking fault distributions (second column in Fig. 3.12) increase with strain and are primarily localized near large particles and sintered necks. This reflects stress-induced plasticity, where localized slip contributes to stress relaxation and interparticle accommodation [90]. Likewise, the dislocation density (third col-

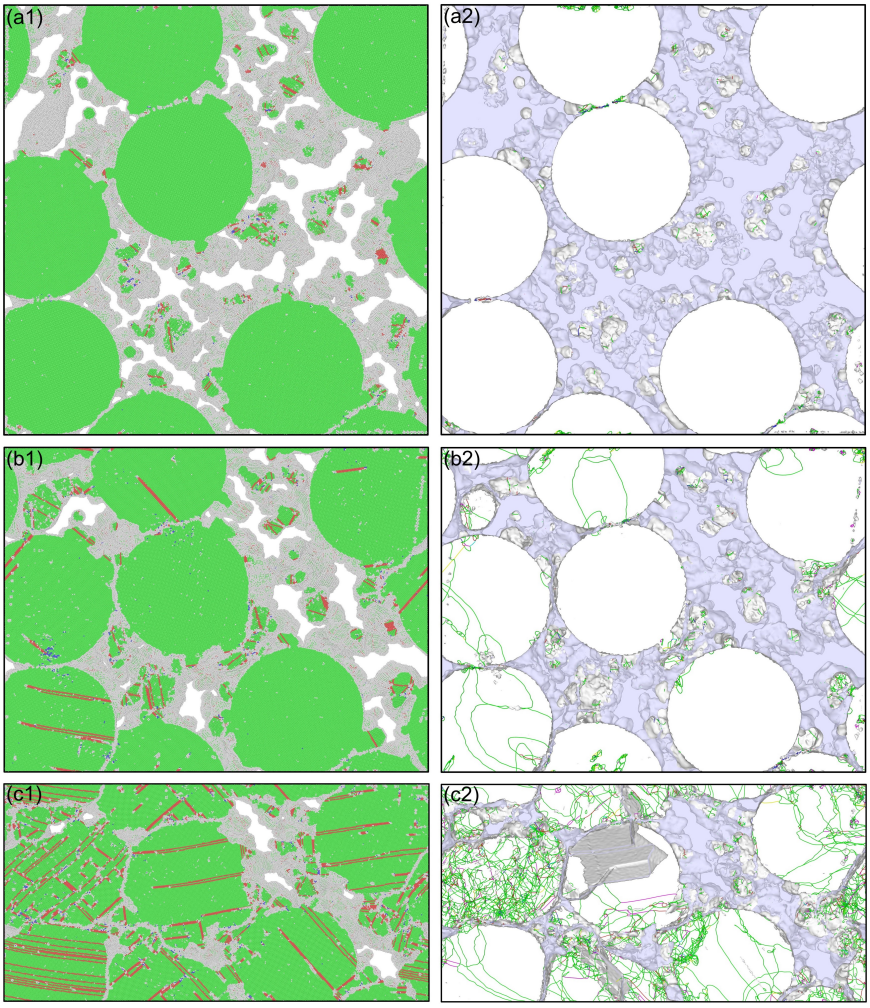


Figure 3.11: Evolution of the microstructure and dislocation distribution during the sintering process: (a1, a2) Initial particle morphology after the temperature rises to 250°C; (b1, b2) microstructure at 20% strain during sintering; (c1, c2) microstructure at 40% strain during sintering.

umn in Fig. 3.12) rises progressively with strain, with pronounced accumulation around large particles and neck regions. This dislocation activity signifies ongoing plastic deformation, which aids in relieving local stress and enabling atomic rearrangement at interfaces [91]. Moreover, the observed anisotropy in defect distributions between the X and Y directions underscores the role of initial particle configuration in shaping the local stress field and guiding microstructural evolution during deformation.

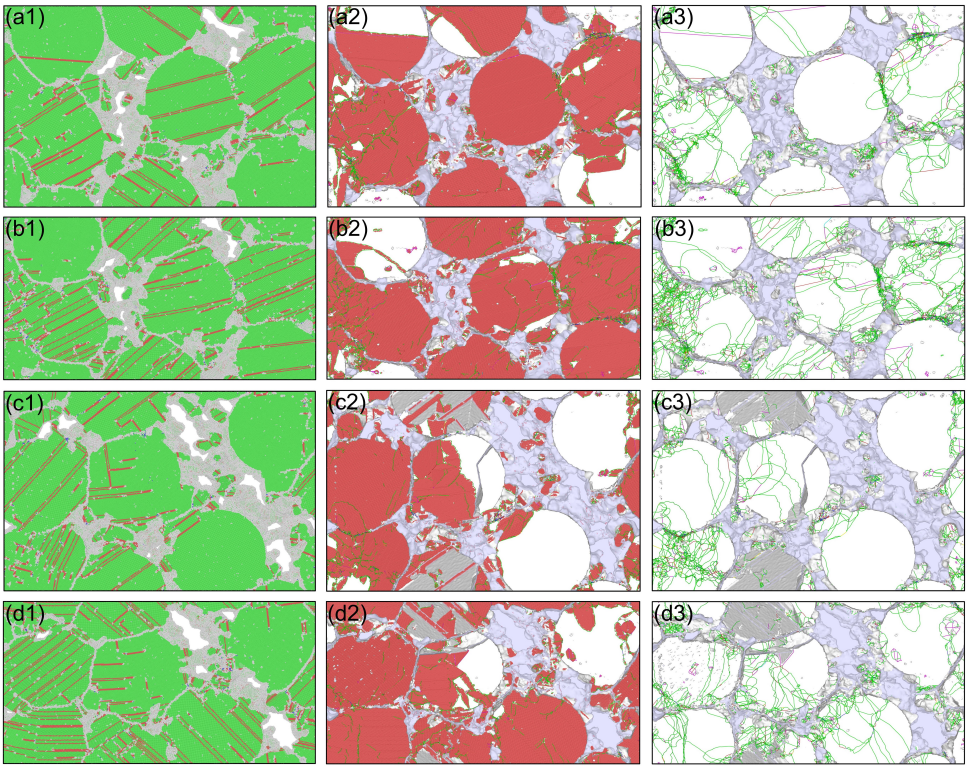


Figure 3.12: Evolution of microstructure, stacking faults and dislocations in particle models sintered under pressure along the X and Y directions: (a1–b1) Microstructure morphology at 30% and 40% strain along the X direction; (c1–d1) microstructure morphology at 30% and 40% strain along the Y direction; (a2–d2) corresponding stacking fault distributions, indicating increased fault activity with strain; (a3–d3) corresponding dislocation distributions, showing progressive accumulation and concentration of dislocations around particle boundaries and sintered necks during sintering.

3.4.3. TENSILE AND COMPRESSIVE BEHAVIOR BY MD SIMULATION

The mechanical response of sintered particle models under tensile and compressive conditions, along with the corresponding fracture morphologies, is presented in Fig. 3.13. This figure highlights the influence of sintering strain (30%, 40% and 50%) and sintering direction on both tensile and compressive behavior, revealing critical insights into the interplay between microstructure and mechanical properties. The stress-strain curves under tensile loading (Fig. 3.13a) show that tensile strength strongly depends

on the sintering strain. As the sintering strain increases from 30% to 50%, the tensile strength improves significantly, reflecting the progressive densification and enhanced interparticle bonding. This improvement is attributed to the formation of stronger sintered necks and reduced porosity, which enhance load transfer across particles. However, the fracture morphology (Figs. 3.13c1, c2, d1, d2) reveals that failure predominantly occurs in regions where small particles are accumulated. This observation confirms the insufficient sintering of small particles, which can be attributed to a stress shielding effect induced by large particles [92]. Notably, as the sintering strain increases, the fracture surface location changes. For example, Figs. 3.13d1 and d2 show that at higher sintering strain (50%), the fracture surface shifts compared to 40%. This shift suggests that the most vulnerable regions evolve with increasing densification, as stress redistribution occurs within the microstructure. The local stress concentration around partially sintered small particles may lead to a transition in fracture pathways.

Fig. 3.13b shows that the stress-strain curves under compressive loading also exhibit a strong dependence on the sintering strain. At lower sintering strains (30%), the stress-strain curves exhibit a progressive increase in stress with strain, but without a clear yield stage. This behavior can be attributed to the initial high porosity and incomplete sintering, where the applied stress primarily compacts the porous structure, resulting in densification and a corresponding increase in strength. The lack of a well-defined yield stage indicates that deformation in this regime is dominated by porosity compaction. At higher sintering strains (40% and 50%), the stress-strain curves exhibit a more pronounced yield stage. The higher sintering strain produces a denser microstructure with reduced porosity and well-formed sintered necks, which can better sustain compressive loads. The simulation results align well with the experimental findings. Under compressive loading, large particles accommodate intragranular slip and serve as initial sites for plastic deformation, absorbing early strain energy. Meanwhile, small particles—often located at interstitial or constrained sites—undergo densification and shear-compression, effectively enhancing load transfer, bridging particle interfaces, and restricting excessive localized deformation. This size-dependent synergy between large and small particles facilitates uniform strain distribution and promotes structural integrity during sintering and deformation. The compressive morphologies shown in Figs. 3.13e1, e2, f1, f2 further support this observation.

3.5. CONCLUSION

This study establishes a clear relationship between sintering pressure, microstructure evolution and the resulting mechanical strength of sintered Cu NPs, providing a fundamental understanding of the underlying mechanisms. The main findings are as follows:

1. The applied sintering pressure significantly promotes sintered neck formation and reduces porosity in Cu NPs. Under constrained temperature (250 ^{o}C), time (5 minutes) and pressure conditions (0-30 MPa), the sintered structure reaches a densification plateau. In this study, optimal densification was achieved at 20 MPa, resulting in a reduction in porosity to 7% and the formation of robust sintering necks.

2. Sintered Cu NPs exhibit a desirable combination of high strength and low elastic modulus, making them well-suited for electronic packaging applications. As sintering pressure increases from 0 to 30 MPa, the yield strength improves significantly, rising

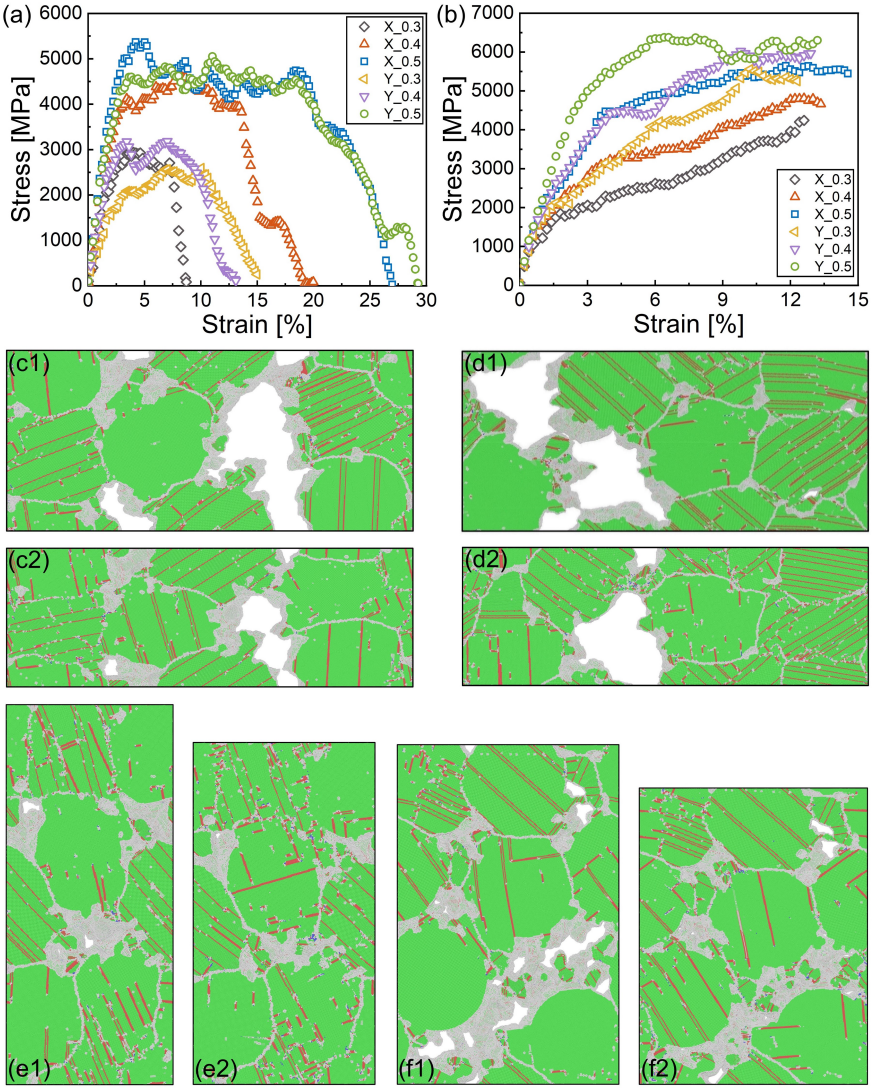


Figure 3.13: Stress-strain curves and corresponding deformed morphologies of sintered particle models under tensile and compressive conditions obtained from MD simulations: (a) Tensile stress-strain curves; (b) compressive stress-strain curves; (c1, c2) fracture morphologies after tensile loading along the X direction for models sintered under 40% and 50% strain along the Y direction, respectively; (d1, d2) fracture morphologies after tensile loading along the Y direction for models sintered under 40% and 50% strain along the X direction, respectively; (e1, e2) compressive morphologies along the X direction for the model sintered with 50% strain; (f1, f2) compressive morphologies along the Y direction for the model sintered with 30% strain.

from 120 MPa to over 320 MPa. Concurrently, the elastic modulus increases from 4.8 GPa to 20 GPa. Moreover, the failure mode transitions from collapse driven by weak interparticle adhesion and poor neck formation to compaction-dominated deformation characterized by well-developed necks and reduced porosity.

3. Sintered Cu NPs exhibit a two-stage deformation mechanism governed by their porous architecture and heterogeneous microstructure. Initially, compressive loading induces voids compaction, and establishing dense interparticle contacts. Subsequently, plastic deformation is accommodated primarily through intragranular slip. A synergistic interplay among particle size, crystallographic orientation, and porosity enables efficient energy dissipation, enhancing load transfer, suppressing strain localization, and impeding crack propagation through the activation of multiple deformation pathways.

4. MD simulations demonstrate that the mechanical behavior of sintered Cu nanoparticle assemblies is governed by a size-dependent synergy between large and small particles, modulated by sintering strain. Under tension, increased sintering strain enhances strength through densification and improved bonding, but fracture preferentially initiates in small-particle-rich regions due to stress shielding and incomplete sintering. In compression, deformation involves intragranular slip in large particles and densification in small particles, enabling effective load transfer and suppressing strain localization. This cooperative mechanism underpins the enhanced structural integrity of the sintered porous architecture, highlighting the critical role of particle size distribution and local bonding in governing mechanical performance.

In summary, this study elucidates the deformation mechanisms underlying the unique combination of high strength and low elastic modulus in sintered Cu NPs, arising from their hierarchical microstructure. The findings highlight a distinctive processing–structure–property relationship, wherein porosity and particle heterogeneity jointly enhance mechanical compliance and robustness. This dual functionality offers a scalable design strategy for advanced metallic systems operating under complex mechanical and thermal loading conditions.

REFERENCES

[1] J. Liu, H. Chen, H. Ji, and M. Li, "Highly conductive cu–cu joint formation by low-temperature sintering of formic acid-treated cu nanoparticles", *ACS applied materials & interfaces*, vol. 8, no. 48, pp. 33 289–33 298, 2016.

[2] Y. Dai *et al.*, "Enhanced copper micro/nano-particle mixed paste sintered at low temperature for 3d interconnects", *Applied Physics Letters*, vol. 108, no. 26, 2016.

[3] J. E. Morris, *Nanopackaging: Nanotechnologies and electronics packaging*. Springer, 2018.

[4] Y. Wang, D. Xu, H. Yan, C.-F. Li, C. Chen, and W. Li, "Low-temperature copper sinter-joining technology for power electronics packaging: A review", *Journal of Materials Processing Technology*, p. 118 526, 2024.

[5] Y. Zuo, C. Zhao, A. Robador, M. Wickham, and S. H. Mannan, "Quasi-in-situ observation of the grain growth and grain boundary movement in sintered cu nanoparticle interconnects", *Acta Materialia*, vol. 236, p. 118 135, 2022.

[6] M. R. Akbarpour *et al.*, "Recent advances in processing, and mechanical, thermal and electrical properties of cu-sic metal matrix composites prepared by powder metallurgy", *Progress in Materials Science*, p. 101 191, 2023.

[7] N. K. Roy, C. S. Foong, and M. A. Cullinan, "Effect of size, morphology, and synthesis method on the thermal and sintering properties of copper nanoparticles for use in microscale additive manufacturing processes", *Additive Manufacturing*, vol. 21, pp. 17–29, 2018.

[8] Z. Cui *et al.*, "Enhanced shear strength and microstructure of cu–cu interconnection by low-temperature sintering of cu nanoparticles", *Journal of Materials Science: Materials in Electronics*, vol. 35, no. 11, pp. 1–13, 2024.

[9] H. Lyu *et al.*, "Sintering and optimization of copper nanopaste-connected copper array conical microstructures", *Materials Science in Semiconductor Processing*, vol. 186, p. 109 081, 2025.

[10] A. Malti, A. Kardani, and A. Montazeri, "An insight into the temperature-dependent sintering mechanisms of metal nanoparticles through md-based microstructural analysis", *Powder Technology*, vol. 386, pp. 30–39, 2021.

[11] B. Hou, H.-J. Huang, C.-M. Wang, M.-B. Zhou, and X.-P. Zhang, "Superb sinterability of the cu paste consisting of bimodal size distribution cu nanoparticles for low-temperature and pressureless sintering of large-area die attachment and the sintering mechanism", in *2022 IEEE 72nd Electronic Components and Technology Conference (ECTC)*, IEEE, 2022, pp. 2064–2070.

[12] Z. Ni, Y Liu, and F. Ye, "Formation of ultrasonic spot welded cu/cu nps/cu joints and the mechanical properties and electrical resistance", *Materials Science and Engineering: A*, vol. 845, p. 143 251, 2022.

[13] X. Liu *et al.*, "Microstructural evolution, fracture behavior and bonding mechanisms study of copper sintering on bare dbc substrate for sic power electronics packaging", *Journal of Materials Research and Technology*, vol. 19, pp. 1407–1421, 2022.

[14] D. Dai *et al.*, "A rapid-sintering cu-cu joints with ultrahigh shear strength and super reliability for power electronics package", *Materials Science in Semiconductor Processing*, vol. 178, p. 108 405, 2024.

[15] K. Wakamoto, D. Yasugi, T. Otsuka, K. Nakahara, and T. Namazu, "Fracture mechanism of sintered silver film revealed by in-situ sem uniaxial tensile loading", *IEEE Transactions on Components, Packaging and Manufacturing Technology*, 2024.

[16] B. Li, J. Wang, and Y. Yao, "Creep behavior of sintered nano-silver at high temperature: Experimental and theoretical analysis", *Materials Today Communications*, vol. 37, p. 106 956, 2023.

[17] D. Kiener and A. Misra, "Nanomechanical characterization", *MRS Bulletin*, vol. 49, no. 3, pp. 214–223, 2024.

[18] C. Chen *et al.*, "Macroscale and microscale fracture toughness of microporous sintered ag for applications in power electronic devices", *Acta Materialia*, vol. 129, pp. 41–51, 2017.

[19] D. Kiener, M. Wurmshuber, M. Alfreider, G. J. Schaffar, and V. Maier-Kiener, "Recent advances in nanomechanical and in situ testing techniques: Towards extreme conditions", *Current Opinion in Solid State and Materials Science*, vol. 27, no. 6, p. 101 108, 2023.

[20] D. Hu, L. Du, M. Alfreider, J. Fan, D. Kiener, and G. Zhang, "Microscopic fracture toughness of notched porous sintered cu micro-cantilevers for power electronics packaging", *Materials Science and Engineering: A*, vol. 897, p. 146 316, 2024.

[21] D. Kiener, P. Guruprasad, S. M. Keralavarma, G. Dehm, and A. A. Benzerga, "Work hardening in micropillar compression: In situ experiments and modeling", *Acta Materialia*, vol. 59, no. 10, pp. 3825–3840, 2011.

[22] R. H. Poelma *et al.*, "Tailoring the mechanical properties of high-aspect-ratio carbon nanotube arrays using amorphous silicon carbide coatings", *Advanced Functional Materials*, vol. 24, no. 36, pp. 5737–5744, 2014.

[23] R. H. Poelma, X. Fan, Z.-Y. Hu, G. Van Tendeloo, H. W. van Zeijl, and G. Q. Zhang, "Effects of nanostructure and coating on the mechanics of carbon nanotube arrays", *Advanced Functional Materials*, vol. 26, no. 8, pp. 1233–1242, 2016.

[24] X Milhet *et al.*, "Evolution of the nanoporous microstructure of sintered ag at high temperature using in-situ x-ray nanotomography", *Acta Materialia*, vol. 156, pp. 310–317, 2018.

[25] J. Wu, Y. Chiu, Y. Wang, and C. Kao, "Mechanical characterizations of single-crystalline (cu, ni) 6sn5 through uniaxial micro-compression", *Materials Science and Engineering: A*, vol. 753, pp. 22–30, 2019.

[26] C. Chen and K. Suganuma, "Microstructure and mechanical properties of sintered ag particles with flake and spherical shape from nano to micro size", *Materials & Design*, vol. 162, pp. 311–321, 2019.

[27] M. Zhang, X. Wang, A. D. Dupuy, J. M. Schoenung, and X. Li, "Study on strain rate–dependent deformation mechanism of wc–10 wt% ni3al cemented carbide by micropillar compression", *Advanced Engineering Materials*, vol. 22, no. 3, p. 1 900 953, 2020.

[28] M. Hamid, M. S. Saleh, A. Afrouzian, R. Panat, and H. M. Zbib, "Modeling of porosity and grain size effects on mechanical behavior of additively manufactured structures", *Additive Manufacturing*, vol. 38, p. 101 833, 2021.

[29] R. Ramachandramoorthy *et al.*, "Anomalous high strain rate compressive behavior of additively manufactured copper micropillars", *Applied Materials Today*, vol. 27, p. 101 415, 2022.

[30] S.-H. Li, Y. Zhao, J. Radhakrishnan, and U. Ramamurty, "A micropillar compression investigation into the plastic flow properties of additively manufactured alloys", *Acta Materialia*, vol. 240, p. 118 290, 2022.

[31] Z. Wang *et al.*, "The effect of temperature on the mechanisms of cu nanoparticle sintering: A molecular dynamic study", *Powder Technology*, vol. 440, p. 119 802, 2024.

[32] J. Liu, W. Lv, C. Chen, and Y. Kang, "Atomic insight in fusion mechanism of heterogeneous and homogeneous sintering: Cu and ag nanoparticles", *Results in Physics*, vol. 57, p. 107 411, 2024.

[33] Y. U. Wang, "Computer modeling and simulation of solid-state sintering: A phase field approach", *Acta materialia*, vol. 54, no. 4, pp. 953–961, 2006.

[34] K. Shinagawa, "Simulation of grain growth and sintering process by combined phase-field/discrete-element method", *Acta materialia*, vol. 66, pp. 360–369, 2014.

[35] B. Dzepina, D. Balint, and D. Dini, "A phase field model of pressure-assisted sintering", *Journal of the European Ceramic Society*, vol. 39, no. 2-3, pp. 173–182, 2019.

[36] J. Hötzer, M. Seiz, M. Kellner, W. Rheinheimer, and B. Nestler, "Phase-field simulation of solid state sintering", *Acta Materialia*, vol. 164, pp. 184–195, 2019.

[37] S. Hara, A. Ohi, and N. Shikazono, "Sintering analysis of sub-micron-sized nickel powders: Kinetic monte carlo simulation verified by fib–sem reconstruction", *Journal of Power Sources*, vol. 276, pp. 105–112, 2015.

[38] Y. Zhang, X. Xiao, and J. Zhang, "Kinetic monte carlo simulation of sintering behavior of additively manufactured stainless steel powder particles using reconstructed microstructures from synchrotron x-ray microtomography", *Results in Physics*, vol. 13, p. 102 336, 2019.

[39] S. Zhou, X. Liu, Z. Yan, S. Hara, N. Shikazono, and Z. Zhong, "Kinetic monte carlo (kmc) simulation of sintering of nickel oxide-yttria stabilized zirconia composites: Model, parameter calibration and validation", *Materials & Design*, vol. 232, p. 112 094, 2023.

[40] F Wakai, M Yoshida, Y Shinoda, and T Akatsu, "Coarsening and grain growth in sintering of two particles of different sizes", *Acta materialia*, vol. 53, no. 5, pp. 1361–1371, 2005.

[41] K.-i. Mori, "Finite element simulation of powder forming and sintering", *Computer methods in applied mechanics and engineering*, vol. 195, no. 48-49, pp. 6737–6749, 2006.

[42] H. Ch'ng and J. Pan, "Sintering of particles of different sizes", *Acta Materialia*, vol. 55, no. 3, pp. 813–824, 2007.

[43] C. Martin, L. Schneider, L Olmos, and D Bouvard, "Discrete element modeling of metallic powder sintering", *Scripta materialia*, vol. 55, no. 5, pp. 425–428, 2006.

[44] B Henrich, A Wonisch, T Kraft, M Moseler, and H Riedel, "Simulations of the influence of rearrangement during sintering", *Acta Materialia*, vol. 55, no. 2, pp. 753–762, 2007.

[45] B. Paredes-Goyes, D. Jauffres, J.-M. Missiaen, and C. L. Martin, "Grain growth in sintering: A discrete element model on large packings", *Acta Materialia*, vol. 218, p. 117 182, 2021.

[46] B. Paredes-Goyes, A. M. Venkatesh, D. Jauffres, and C. L. Martin, "Two-step sintering of alumina nano-powders: A discrete element study", *Journal of the European Ceramic Society*, vol. 43, no. 2, pp. 501–509, 2023.

[47] M. W. Reiterer and K. G. Ewsuk, "An analysis of four different approaches to predict and control sintering", *Journal of the American Ceramic Society*, vol. 92, no. 7, pp. 1419–1427, 2009.

[48] J. Liu, W. Lv, Y. Mou, C. Chen, and Y. Kang, "Coalescence behavior of cu nanoparticles during sintering: Based on atomic scale to macro scale", *Journal of Materials Research and Technology*, vol. 27, pp. 2490–2507, 2023.

[49] A. Averardi, C. Cola, S. E. Zeltmann, and N. Gupta, "Effect of particle size distribution on the packing of powder beds: A critical discussion relevant to additive manufacturing", *Materials today communications*, vol. 24, p. 100 964, 2020.

[50] M. R. Mazlan *et al.*, "Necking mechanism under various sintering process parameters–a review", *journal of materials research and technology*, vol. 23, pp. 2189–2201, 2023.

[51] L. Ma *et al.*, "Sintering mechanism of bimodal-sized cu nanoparticle paste for power electronics packaging", *Journal of Electronic Materials*, vol. 53, no. 6, pp. 2988–2998, 2024.

[52] X. Jingxiang, H. Yuji, O. Nobuki, S. Kazuhisa, H. Toshiyuki, and K. Momoji, "Parallel large-scale molecular dynamics simulation opens new perspective to clarify the effect of a porous structure on the sintering process of ni/ysz multiparticles", 2017.

[53] P. Liang *et al.*, "Molecular dynamics simulation of sintering densification of multi-scale silver layer", *Materials*, vol. 15, no. 6, p. 2232, 2022.

[54] G. J. Schaffar, D. Tscharnuter, and V. Maier-Kiener, "Exploring the high-temperature deformation behavior of monocrystalline silicon–an advanced nanoindentation study", *Materials & Design*, vol. 233, p. 112 198, 2023.

[55] A. J. Leide, R. I. Todd, and D. E. Armstrong, "Measurement of swelling-induced residual stress in ion implanted sic, and its effect on micromechanical properties", *Acta Materialia*, vol. 196, pp. 78–87, 2020.

[56] S. Huang *et al.*, "In-situ investigation of tensile behaviors of ti–6al alloy with extra low interstitial", *Materials Science and Engineering: A*, vol. 809, p. 140 958, 2021.

[57] A. A. Saleh, G. Casillas, E. V. Pereloma, K. R. Carpenter, C. R. Killmore, and A. A. Gazder, "A transmission kikuchi diffraction study of cementite in a quenched and tempered steel", *Materials Characterization*, vol. 114, pp. 146–150, 2016.

[58] B. M. Jenkins *et al.*, "A more holistic characterisation of internal interfaces in a variety of materials via complementary use of transmission kikuchi diffraction and atom probe tomography", *Applied Surface Science*, vol. 528, p. 147 011, 2020.

[59] A. P. Thompson *et al.*, "Lammps-a flexible simulation tool for particle-based materials modeling at the atomic, meso, and continuum scales", *Computer Physics Communications*, vol. 271, p. 108 171, 2022.

[60] A. Stukowski, "Visualization and analysis of atomistic simulation data with ovito–the open visualization tool", *Modelling and simulation in materials science and engineering*, vol. 18, no. 1, p. 015 012, 2009.

[61] Y. Mishin, M. Mehl, D. Papaconstantopoulos, A. Voter, and J. Kress, "Structural stability and lattice defects in copper: Ab initio, tight-binding, and embedded-atom calculations", *Physical Review B*, vol. 63, no. 22, p. 224 106, 2001.

[62] D. E. Spearot, M. A. Tschopp, K. I. Jacob, and D. L. McDowell, "Tensile strength of< 1 0 0> and< 1 1 0> tilt bicrystal copper interfaces", *Acta materialia*, vol. 55, no. 2, pp. 705–714, 2007.

[63] J. Suryawanshi, G. Singh, S. Msolli, M. H. Jhon, and U. Ramamurty, "Tension-compression asymmetry and shear strength of titanium alloys", *Acta Materialia*, vol. 221, p. 117 392, 2021.

[64] J. Zhang, G. Liu, and J Sun, "Strain rate effects on the mechanical response in multi-and single-crystalline cu micropillars: Grain boundary effects", *International Journal of Plasticity*, vol. 50, pp. 1–17, 2013.

[65] X. Zhao, J Wu, Y. Chiu, I. Jones, R Gu, and A. Ngan, "Critical dimension for the dislocation structure in deformed copper micropillars", *Scripta Materialia*, vol. 163, pp. 137–141, 2019.

[66] S. Kalácska *et al.*, "Investigation of geometrically necessary dislocation structures in compressed cu micropillars by 3-dimensional hr-ebsd", *Materials Science and Engineering: A*, vol. 770, p. 138 499, 2020.

[67] D. Xie *et al.*, "A fundamental understanding of how dislocation densities affect strain hardening behavior in copper single crystalline micropillars", *Mechanics of materials*, vol. 184, p. 104 731, 2023.

[68] T. Hirouchi and Y. Shibutani, "Mechanical responses of copper bicrystalline micro pillars with $\sigma 3$ coherent twin boundaries by uniaxial compression tests", *Materials Transactions*, vol. 55, no. 1, pp. 52–57, 2014.

[69] P. J. Imrich, C. Kirchlechner, C. Motz, and G. Dehm, "Differences in deformation behavior of bicrystalline cu micropillars containing a twin boundary or a large-angle grain boundary", *Acta materialia*, vol. 73, pp. 240–250, 2014.

[70] C. Kirchlechner, F. Toth, F. G. Rammerstorfer, F. D. Fischer, and G. Dehm, "Pre-and post-buckling behavior of bi-crystalline micropillars: Origin and consequences", *Acta materialia*, vol. 124, pp. 195–203, 2017.

[71] C Howard *et al.*, "Investigation of specimen size effects by in-situ microcompression of equal channel angular pressed copper", *Materials Science and Engineering: A*, vol. 649, pp. 104–113, 2016.

[72] J. Zhang, G Liu, and J Sun, "Comparisons between homogeneous boundaries and heterophase interfaces in plastic deformation: Nanostructured cu micropillars vs. nanolayered cu-based micropillars", *Acta materialia*, vol. 61, no. 18, pp. 6868–6881, 2013.

[73] N. L. Okamoto, D. Kashioka, T. Hirato, and H. Inui, "Specimen-and grain-size dependence of compression deformation behavior in nanocrystalline copper", *International Journal of Plasticity*, vol. 56, pp. 173–183, 2014.

[74] M. Mutoh, T. Nagoshi, T.-F. M. Chang, T. Sato, and M. Sone, "Micro-compression test using non-tapered micro-pillar of electrodeposited cu", *Microelectronic engineering*, vol. 111, pp. 118–121, 2013.

[75] X. Zhang, H. Wang, F. Ye, C. Zou, and Z. Wei, "Cooperative effect of mg and si contents on the microstructural evolution, mechanical performance, and deformation behavior of cast al–li–mg–si alloys", *Materials Science and Engineering: A*, vol. 841, p. 142 976, 2022.

[76] M. D. Sangid, T. Ezaz, H. Sehitoglu, and I. M. Robertson, "Energy of slip transmission and nucleation at grain boundaries", *Acta materialia*, vol. 59, no. 1, pp. 283–296, 2011.

[77] T. Zhang, J. Jiang, B. A. Shollock, T. B. Britton, and F. P. Dunne, "Slip localization and fatigue crack nucleation near a non-metallic inclusion in polycrystalline nickel-based superalloy", *Materials Science and Engineering: A*, vol. 641, pp. 328–339, 2015.

[78] D. Norfleet, D. Dimiduk, S. Polasik, M. Uchic, and M. Mills, "Dislocation structures and their relationship to strength in deformed nickel microcrystals", *Acta Materialia*, vol. 56, no. 13, pp. 2988–3001, 2008.

[79] S. Queyreau, G. Monnet, and B. Devincre, "Orowan strengthening and forest hardening superposition examined by dislocation dynamics simulations", *Acta Materialia*, vol. 58, no. 17, pp. 5586–5595, 2010.

[80] H. Zhong *et al.*, "Resolving localized geometrically necessary dislocation densities in al-mg polycrystal via in situ ebsd", *Acta Materialia*, vol. 279, p. 120 290, 2024.

[81] M. Amagai, "Mechanical reliability in electronic packaging", *Microelectronics Reliability*, vol. 42, no. 4-5, pp. 607–627, 2002.

[82] S. Lavenstein, Y. Gu, D. Madisetti, and J. A. El-Awady, "The heterogeneity of persistent slip band nucleation and evolution in metals at the micrometer scale", *Science*, vol. 370, no. 6513, eabb2690, 2020.

[83] Y. Cui, G. Po, and N. Ghoniem, "Suppression of localized plastic flow in irradiated materials", *Scripta Materialia*, vol. 154, pp. 34–39, 2018.

[84] T. Bieler *et al.*, "The role of heterogeneous deformation on damage nucleation at grain boundaries in single phase metals", *International Journal of Plasticity*, vol. 25, no. 9, pp. 1655–1683, 2009.

[85] H. Wu, S. Huang, H. Zhu, and Z. Xie, "Strengthening fecrnicu high entropy alloys via combining v additions with in-situ tic particles", *Scripta Materialia*, vol. 195, p. 113 724, 2021.

[86] H. Wu *et al.*, "Manipulating the plastic strain delocalization through ultra-thinned hierarchical design for strength-ductility synergy", *Scripta Materialia*, vol. 172, pp. 165–170, 2019.

[87] A. Hua and J. Zhao, "Shear direction induced transition mechanism from grain boundary migration to sliding in a cylindrical copper bicrystal", *International Journal of Plasticity*, vol. 156, p. 103 370, 2022.

[88] S. K. Bhogaraju *et al.*, "Die-attach bonding with etched micro brass metal pigment flakes for high-power electronics packaging", *ACS Applied Electronic Materials*, vol. 3, no. 10, pp. 4587–4603, 2021.

[89] A. D. Albert, M. F. Becker, J. W. Keto, and D. Kovar, "Low temperature, pressure-assisted sintering of nanoparticulate silver films", *Acta Materialia*, vol. 56, no. 8, pp. 1820–1829, 2008.

[90] Z. Zhang, D. Lunt, H. Abdolvand, A. J. Wilkinson, M. Preuss, and F. P. Dunne, "Quantitative investigation of micro slip and localization in polycrystalline materials under uniaxial tension", *International Journal of Plasticity*, vol. 108, pp. 88–106, 2018.

[91] L. Zou *et al.*, "Dislocation nucleation facilitated by atomic segregation", *Nature materials*, vol. 17, no. 1, pp. 56–63, 2018.

[92] M Thieme *et al.*, "Titanium powder sintering for preparation of a porous functionally graded material destined for orthopaedic implants", *Journal of materials science: materials in medicine*, vol. 12, pp. 225–231, 2001.

4

Strain Rate and Temperature Dependent Viscoplasticity of Sintered Copper Nanoparticles

Sintered copper (Cu) nanoparticles (NPs) are promising for high-performance electronics due to their excellent thermal and electrical conductivity, as well as mechanical reliability. This study investigates the microscale mechanical behavior of sintered Cu NPs with a bimodal particle size distribution, focusing on strain rate and temperature effects. Micro-pillar compression tests were performed across strain rates of 0.0001 s^{-1} to 0.01 s^{-1} and temperatures from 25°C to 350°C. Results show that higher strain rates enhance yield strength through strain-rate hardening, while elevated temperatures lead to thermal softening and reduced mechanical stability. The Anand viscoplastic model accurately predicts these deformation behaviors. Microstructural analysis via scanning electron microscopy (SEM) and transmission electron microscopy (TEM) reveals localized deformation at 175°C, with dislocations concentrated near the top surface and persistent porosity below, whereas at 350°C, re-sintering and grain boundary diffusion create a denser microstructure. Phase-field fracture modeling further elucidates crack propagation, emphasizing the role of pore size and temperature. This combined experimental and modeling approach enhances understanding of viscoplastic deformation and fracture mechanisms in sintered Cu NPs, informing their use in interconnects, power electronics and thermal management systems.

Parts of this chapter have been published in Materials & Design, 2025 [1].

4.1. INTRODUCTION

THE increasing demand for high-power and high-temperature electronic applications, such as power modules based on wide-band-gap semiconductors such as SiC and GaN, requires die-attachment materials with exceptional thermal stability, mechanical reliability and cost effectiveness [2, 3]. Sintered copper (Cu) nanoparticles (NPs) have emerged as a promising alternative of solder materials due to their high melting point, excellent thermal conductivity and compatibility with power electronics packaging [4]. However, extreme operating conditions, characterized by elevated temperatures and dynamic loading, significantly influence the viscoplastic behavior and mechanical integrity of these materials [5, 6]. Although nanoindentation and tensile tests have revealed temperature- and strain-rate-dependent deformation characteristics of sintered Ag [7, 8] and Cu [9, 10] NPs, microscale investigations under compression, particularly at elevated temperatures, remain scarce. Addressing this gap is essential for a comprehensive understanding of the interplay of strain rate and temperature on the mechanical performance and failure mechanisms of sintered Cu NPs, ensuring their reliability in next-generation power electronics.

Micro-pillar compression test has emerged as a powerful technique for investigating viscoplastic properties at the microscale, particularly under varying strain-rate conditions [11–13] and high temperatures [14–16]. By isolating the effects of nanoscale microstructural features such as grain boundaries, dislocations and porosity, this method provides critical insights into strain-rate- and temperature-dependent deformation mechanisms. In bulk Cu, high-temperature micro-pillar compression tests have revealed size-dependent plasticity, where strain rate influences dislocation pile-up and recovery mechanisms [17]. However, the viscoplastic behavior of sintered Cu NPs remains largely unexplored, particularly regarding the interplay between strain rate, temperature and microstructure evolution, leaving critical gaps in understanding their thermomechanical reliability for high-power electronic packaging applications [10]. Moreover, previous studies on viscoplastic deformation in sintered nanoparticle (NP) systems have primarily relied on in-situ scanning electron microscopy (SEM) tensile tests [10, 18, 19], which consistently reveals significant tension-compression asymmetry in sintered Cu NPs. This asymmetry stems from fundamental microstructural mechanisms: under tension, inherent sintering voids/pores act as stress concentrators that accelerate void growth and intergranular fracture, reducing ductility and strength, whereas under compression, these voids partially close while hydrostatic stress suppresses cracking, enabling higher strength through grain boundary-mediated plasticity and dislocation activity [20]. While conventional tensile test provides valuable deformation insights, its stringent sample preparation requirements and limited scalability constrain broader applicability. Most critically for viscoplastic model fitting, tensile tests typically fracture before reaching substantial plastic strains [21], preventing robust characterization of full hardening/softening behavior across essential strain-rate regimes. Consequently, micro-pillar compression test offers distinct advantages for constitutive modeling: it achieves stable plastic deformation beyond 20% strain without catastrophic failure [22], enabling complete stress-strain curve acquisition for accurate parameter calibration while facilitating in situ strain-rate jump tests on individual specimens to directly quantify rate sensitivity and activation volumes with minimal artifact interference.

Therefore, this study employs micro-pillar compression test to systematically investigate the viscoplastic properties of sintered Cu NPs, addressing these limitations and providing a more comprehensive understanding of their mechanical response.

Predicting local deformation and crack propagation in porous structures is challenging due to their heterogeneity and complex microstructure. Various computational methods, including Molecular Dynamics (MD) [23, 24], the extended finite element method (XFEM) [25–27], Monte Carlo (MC) simulations [28], peridynamics [29, 30], and phase-field fracture modeling [31–33], have been developed to study crack evolution. Among these, phase-field fracture modeling has emerged as a particularly robust and versatile approach, as it models fractures as diffuse interfaces, eliminating the need for explicit crack tracking in XFEM. While MD provides atomic-scale insights, it is computationally prohibitive for large-scale porous structures, and MC simulations lack a direct physical basis for mechanical deformation. In contrast, phase-field fracture modeling ensures a thermodynamically consistent and computationally efficient framework, making it well-suited for simulating fracture in sintered NP networks. Despite its advantages, crack propagation in sintered NPs remains highly dependent on pore distribution. Phase-field fracture modeling has been successfully applied to sintered Ag NPs [34–36], however, studies on sintered Cu NPs remain limited. Thus, a deeper understanding of their fracture behavior is essential. To address this, this study integrates phase-field fracture modeling with Gaussian random field methods to provide a more comprehensive analysis of crack propagation in sintered Cu NPs.

In this study, we examines the mechanical properties of sintered Cu NPs under varying strain rates (0.0001 s^{-1}, 0.0005 s^{-1}, 0.001 s^{-1}, 0.005 s^{-1} and 0.01 s^{-1}) and temperatures (25°C, 175°C, 250°C and 350°C) through a combination of high-temperature micro-pillar compression test. Results show that the Anand viscoplastic constitutive model captures the material's deformation response under these conditions. Detailed microstructural characterization, conducted using SEM and transmission electron microscopy (TEM), provides critical insights into grain morphology, sintered neck formation and deformation mechanisms. In addition, phase-field fracture modeling is utilized to predict crack propagation and failure modes, enabling a quantitative assessment of damage evolution.

4.2. EXPERIMENTAL AND SIMULATION METHOD

4.2.1. SINTERED SAMPLE PREPARATION

To fabricate sintered Cu NPs, Cu NP paste was firstly transferred onto an Active Metal Brazing (AMB) substrate (3 mm × 3 mm, 200 µm thick) using screen printing, where a scraper spread the paste uniformly over a patterned screen (Fig. 4.1a). The AMB substrate consists of a silicon nitride (Si_3N_4) ceramic core bonded to Cu layers, providing mechanical stability and thermal conductivity. Next, the printed Cu paste underwent pressure-assisted sintering at 20 MPa, 250°C for 5 minutes under a nitrogen atmosphere using a Boschman Sinterstar system. Simultaneous application of heat and external pressure enhanced the densification of the Cu NPs, promoting strong neck formation between particles (Fig. 4.1b). After sintering, the aluminum (Al) film used to facilitate uniform pressure distribution was carefully removed, leaving a well-adhered, consoli-

dated Cu layer on the substrate. The sintered Cu layer was then sectioned to isolate specific regions for mechanical characterization (Fig. 4.1c).

In this study, Cu NPs were synthesized via physical vapor deposition (PVD) [37]. Prior to mixing with organic compounds, the Cu NPs underwent pretreatment involving acid washing with a formic acid solution, followed by centrifugation and drying, which effectively suppressed oxidation. Subsequently, two distinct Cu particle sizes were mixed with organic compounds. SEM analysis (Fig. 4.1d) revealed an average particle size of 100 nm for the smaller Cu NPs and 2.5 µm for the larger particles.

The sintered Cu layer was sectioned to isolate specific regions for microstructural and mechanical characterization. As shown in Fig. 4.1e, SEM imaging revealed the porous structure of the as-sintered Cu NPs. A TEM sample was subsequently prepared via focused ion beam (FIB) milling using an FEI Helios G4 CX dual-beam FIB-SEM system, which highlighted the heterogeneous microstructure, including well-formed sintered necks between particles (Fig. 4.1f). Porosity quantification was performed using 3D FIB-SEM reconstruction, yielding a measured porosity of 7% (Fig. 4.1g). For mechanical test, micro-pillars with a diameter of 6 µm and a height of 20 µm (aspect ratio 3:1) were fabricated via FIB (Figs. 4.1h, i). This geometry ensured mechanical stability during in-situ compression tests [38].

4.2.2. MICRO-PILLAR COMPRESSION TESTS

High-temperature micro-pillar compression tests were conducted using an in-situ high-temperature SEM (HT-SEM) nanoindenter (KLA Corporation, Milpitas, CA, USA) as shown in Fig. 4.2a, equipped with a continuous stiffness measurement (CSM) unit [39]. The CSM system applied a 100 Hz sinusoidal force signal with a 2 nm displacement amplitude, enabling continuous determination of hardness and Young's modulus as a function of indentation depth [40]. A flat punch tip made of boron carbide (Synton-MDP, Nidau, Switzerland) was employed for precise load application. The sample is firmly clamped onto a resistance-heated sample holder (Fig. 4.2b), with the thermocouple positioned within a spacer. In this study, a flat-ended indenter with a 10 µm diameter, larger than the micro-pillars (Fig. 4.2c), was used to ensure uniform stress distribution during loading, enabling accurate assessment of the mechanical response of the sintered Cu NPs. The nanoindenter was integrated within a Tescan Vega3 SEM (Tescan, Brno, Czech Republic) under high vacuum conditions ($<10^{-4}$ mbar) to ensure accurate indent positioning and prevent high-temperature oxidation of both the tip and sample. Tip temperature calibration was performed via direct indentation into a thermocouple, following the method described by Wheeler and Michler [41]. Prior to the test, a thermal stabilization period of 1–2 hours was maintained to minimize thermal drift and ensure data reliability. The area function and frame stiffness were calibrated at room temperature using fused quartz, following the procedure outlined by Oliver and Pharr [42].

In this study, micro-pillar compression tests under varying strain rates (0.0001 s^{-1}, 0.0005 s^{-1}, 0.001 s^{-1}, 0.005 s^{-1} and 0.01 s^{-1}) and temperatures (25°C, 175°C, 250°C and 350°C) were performed. To ensure experimental reproducibility and statistical robustness, five micro-pillars were tested for each condition. Post-compression analyses involved field emission scanning electron microscopy (FE-SEM, Helios G4Cx) to examine failure modes of micro-pillars. Additionally, TEM (Cs-corrected Titan) characterization

was performed to provide detailed insights into microstructure evolution and deformation mechanisms, such as dislocation activity and grain boundary interactions at elevated temperatures.

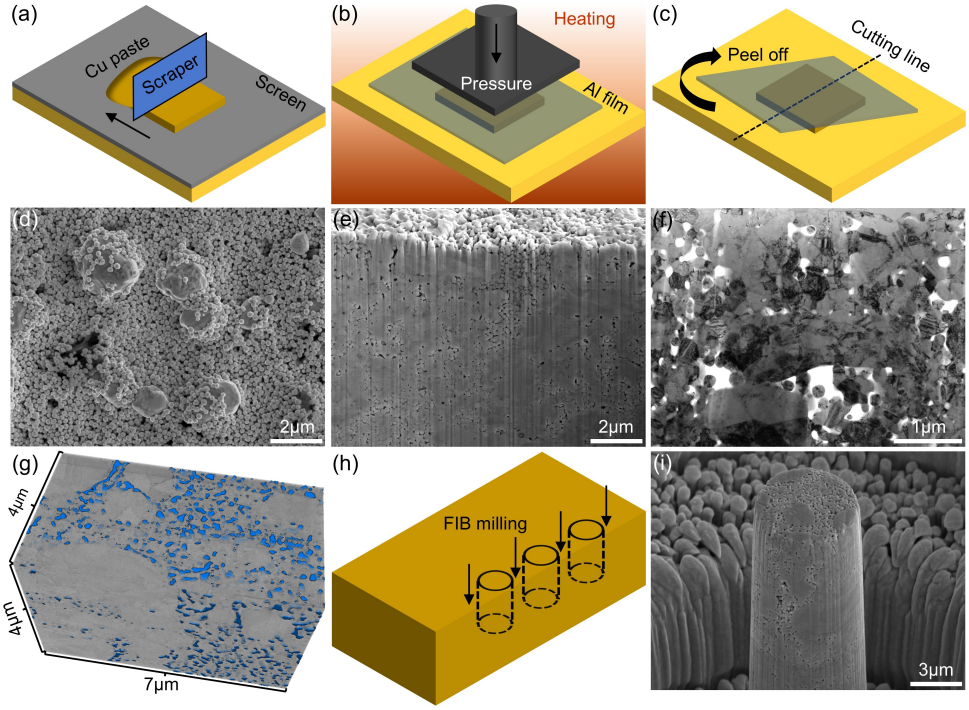


Figure 4.1: Fabrication and characterization of sintered Cu NPs: (a) Screen printing of Cu NP paste onto an AMB substrate; (b) pressure-assisted sintering process under heating with an Al film cover; (c) removal of the Al film post-sintering; (d) SEM image of as-printed Cu NPs; (e) cross-sectional SEM image of sintered Cu NPs; (f) TEM image of the sintered Cu NPs; (g) 3D reconstruction of the sintered structure showing porosity; (h) schematic of FIB milling for micro-pillar fabrication; (i) SEM image of a fabricated Cu micro-pillar.

4.2.3. ANAND CONSTITUTIVE MODEL

To quantify the strain-rate and temperature-dependent behaviour of the sintered Cu NPs, the Anand model is employed to fit the stress-strain data. The Anand model is a viscoplastic constitutive model widely used to describe the deformation behaviour of materials, particularly under varying strain rates and temperatures [43]. The model assumes that the inelastic strain rate is related to the stress through a set of material-specific constants, which account for time-dependent plasticity and temperature effects.

$$\tilde{\sigma} = cs \tag{4.1}$$

here $c = g(T, \dot{\epsilon}_p)$ and $s = h(T, \dot{\epsilon}_p)$ represent the material parameter and the internal variable, respectively. Both are functions of the absolute temperature and the inelastic strain rate. Under a constant strain rate, the specific expressions for these parameters

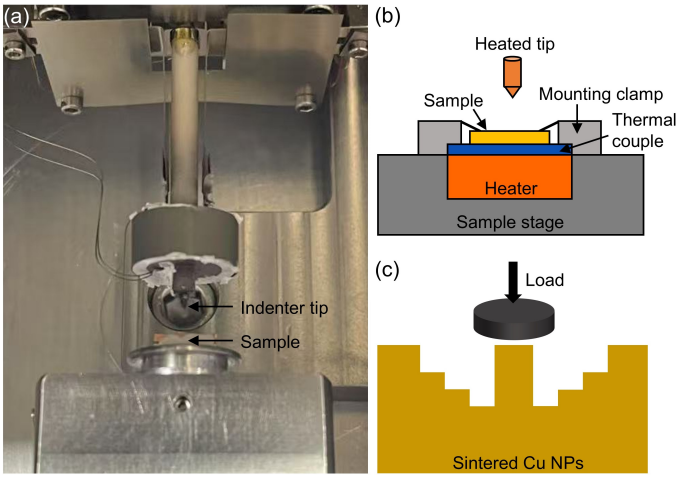


Figure 4.2: (a) HT-SEM setup with nanoindenter; (b) schematic of the heating stage with sample mounting; (c) schematic of the micro-pillar compression test.

are as follows:

$$c = \frac{1}{\xi}\sinh^{-1}\left(\left(\frac{\dot{\epsilon}_p}{A}\exp\left(\frac{Q}{RT}\right)\right)^m\right), \quad c < 1 \tag{4.2}$$

where ξ represents the multiplier of stress, $\dot{\epsilon}_p$ denotes the inelastic strain rate, A is the pre-exponential factor, Q is the activation energy, R refers to the universal gas constant, T is the absolute temperature and m indicates the strain rate sensitivity.

Mathematically, the Anand model can also be expressed as follows,

$$\dot{\epsilon}_p = A\exp\left(-\frac{Q}{RT}\right)\left[\sinh\left(\frac{\xi\tilde{\sigma}}{s}\right)\right]^{\frac{1}{m}} \tag{4.3}$$

and the internal variable s was proposed by Anand [44] and Brown et al. [43] as follows:

$$\dot{s} = \left[h_0\left(1-\frac{s}{s^*}\right)^a \operatorname{sign}\left(1-\frac{s}{s^*}\right)\right]\dot{\epsilon}_p, \quad a \geq 1 \tag{4.4}$$

$$s^* = \hat{s}\left(\frac{\dot{\epsilon}_p}{A}\exp\left(\frac{Q}{RT}\right)\right)^n \tag{4.5}$$

where s^* represents a saturation value of s associated with a set of given temperature and strain rates, h_0 is the hardening/softening constant, a is the strain rate sensitivity of hardening/softening, $\hat{s}$ and n are the coefficient and strain rate sensitivity of the saturation value of deformation resistance, respectively.

To determine the above parameters, Eq. 5.6 can be written as:

$$\dot{s} = h(\sigma, s, T)\dot{\epsilon}_p \tag{4.6}$$

where h is dynamic hardening and recovery function. Combining Eqs. 4.1 and 4.6 can lead to the following formula:

$$\frac{\mathrm{d}\tilde{\sigma}}{\mathrm{d}\dot{\epsilon}_p} = ch \tag{4.7}$$

For the case $s < s^*$, Eqs. 5.6, 4.6 and 4.7 will lead to

$$\frac{d\tilde{\sigma}}{d\dot{\epsilon}_p} = ch_0\left(1 - \frac{\tilde{\sigma}}{\tilde{\sigma}^*}\right)^a \tag{4.8}$$

where $\sigma^* = cs^*$ is the saturation or steady state stress. The integration form of Eq. 4.8 is

$$\tilde{\sigma} = \tilde{\sigma}^* - \left\{(\tilde{\sigma}^* - \tilde{\sigma}_0) + (a-1)\left[ch_0(\tilde{\sigma}^*)^{-a}\dot{\epsilon}_p\right]^{\frac{1}{1-a}}\right\} \tag{4.9}$$

where $\tilde{\sigma}_0 = cs_0$. s_0, the initial deformation resistance, representing the initial value of s. For a=1, Eq. 4.8 can be integrated as shown below:

$$\tilde{\sigma} = \tilde{\sigma}^* - (\tilde{\sigma}^* - \tilde{\sigma}_0)\exp\left\{-\left(\frac{ch_0}{\tilde{\sigma}^*}\right)\dot{\epsilon}^p\right\} \tag{4.10}$$

In the compression test, $\tilde{\sigma} = |\sigma|$, where σ is the compressive stress measured in the compression experiments. Moreover, when the plastic flow is fully developed at a certain temperature T and strain rate $\dot{\epsilon}$, it can be assumed that $\dot{\epsilon}^p \approx [\dot{\epsilon}]$. Since a constant true strain rate is considered in this manuscript, the combination of Eqs. 5.4 and 4.5 can be expressed as follows:

$$\sigma^* = \frac{\hat{s}}{\xi}\left(\frac{z}{A}\right)^n \sinh^{-1}\left[\left(\frac{z}{A}\right)^m\right] \tag{4.11}$$

where

$$z = \dot{\epsilon}\exp\left(\frac{Q}{RT}\right) \tag{4.12}$$

Therefore, nine parameters (s_0, Q, A, ξ, m, h_0, a, $\hat{s}$, and n) are required in the Anand model. Steps of fitting the nine parameters are as follows [43]:

1. Determining the saturation stress σ^* for each test based on the steady-state value of the stress-strain data.

2. Determining a, ch_0 and $\tilde{\sigma}$ by fitting Eq. 4.9 or 4.10 using the least squares method.

3. Determining A, Q, m, n and the combined term $\xi/\tilde{s}$ by fitting Eq. 4.11 using least squares method.

4. Determining ξ by substituting the above parameter values into Eq. 4.2 and ensuring that c is less than 1 for each test. Then, $\hat{s}$ can be calculated from ξ and $\xi/\tilde{s}$.

5. Determining h_0 by using the following equation:

$$h_0 = \frac{\sum_{i=1}^{n}\frac{(ch_0)_i}{c_i}}{n} \tag{4.13}$$

where i refers to the i-th test, n represents the total number of tests. Finally, s_0 is determined from σ_0 and c obtained from each test.

4.2.4. GENERATION OF RANDOM POROUS STRUCTURES

The microstructures of sintered Cu NPs are characterized by random variations in pore geometry, including size, shape and spatial distribution, which arise from particle migration, deformation and coalescence during the sintering process. To effectively capture

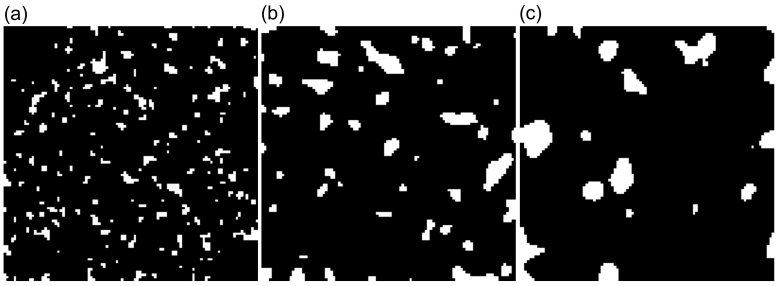


Figure 4.3: 2D random porous structures: (a) λ_x=λ_y=2; (b) λ_x=λ_y=4; (c) λ_x=λ_y=6.

these characteristics, a Gaussian Random Field (GRF)-based approach was employed to generate two-dimensional (2D) microstructures [35, 36, 45]. This method models spatial randomness through a random field $Z(x)$ characterized by a mean function $m(x)$ and a covariance function $C(x_1, x_2)$. The mean function was set to zero ($m(x) = 0$) to preserve spatial neutrality, while the covariance function controlled the spatial correlation and was expressed as:

$$C(x_1, x_2) = \sigma^2 \exp\left(-\frac{(x_1 - x_2)^2}{\lambda_x^2} - \frac{(y_1 - y_2)^2}{\lambda_y^2}\right) \tag{4.14}$$

where σ^2 represents the variance, and λ_x and λ_y are the correlation lengths in the x- and y-directions, respectively. By adjusting λ_x and λ_y, both isotropic and anisotropic structures can be generated, enabling control over pore aspect ratios and orientations [35, 36, 46]. This flexibility allows the method to simulate flattened pore shapes typically observed under directional pressure or temperature gradients.

To discretize the GRF into solid and pore phases, a threshold function was employed. The indicator function, defined as:

$$\Psi(x) = \begin{cases} 1, & Z(x) \geq F_0, \\ 0, & Z(x) < F_0, \end{cases} \tag{4.15}$$

This threshold (F_0) was optimized using quantile functions to ensure the target porosity level was met. The Gaussian width (σ) controlled the smoothing of the field, influencing the connectivity and size of the pores. Larger values of σ resulted in larger, less numerous pores, whereas smaller values generated finer, denser pore distributions.

The computational domain, a 2D grid of size 100×100, was constructed, and Gaussian filtering was applied to generate the random fields. The spatial correlations in the generated microstructures were validated by comparing statistical features, including pore size distributions, aspect ratios, and shape factors, to experimental results obtained from SEM imaging. By varying λ_x and λ_y, pores size and distribution aligned with the observed experimental morphology were reproduced. Therefore, the 2D models established in this study have the porosity of 7%. Fig. 4.3 shows the 2D random porous structure and different λ_x and λ_y, in which the black area represent the Cu domain and the white area represent the voids.

4.2.5. PHASE-FIELD FRACTURE MODEL

The phase-field fracture method, based on Griffith's fracture theory [47], regularizes cracks using a diffusive scalar damage variable $\phi \in [0,1]$. Here, $\phi = 0$ represents undamaged material, $\phi = 1$ indicates complete fracture, and intermediate values ($0 < \phi < 1$) describe the transition zone [48]. The damage zone width is controlled by the phase-field length scale parameter l. This approach formulates fracture as a minimization problem of the total potential energy functional. For the AT1 model [49], the total potential energy is expressed as:

$$\Pi = \int_{\Omega} \left[(1-\phi)^2 + k\right] \psi_0(\boldsymbol{\varepsilon}(\mathbf{u}))\, \mathrm{d}\Omega + \int_{\Omega} G_c \gamma(\phi, \nabla\phi)\, \mathrm{d}\Omega \tag{4.16}$$

where $\Psi(\mathbf{u},\phi) = [(1-\phi)^2 + \mathrm{k}]\Psi_0(\epsilon)$ is the degradation function associated with the AT1 and AT2 models, $\psi_0(\boldsymbol{\varepsilon}) = \frac{1}{2}\boldsymbol{\varepsilon}^T \mathbf{C}_0 \boldsymbol{\varepsilon}$ is the internal strain energy under the conditions of small deformations with $\boldsymbol{\varepsilon} = \frac{1}{2}\left(\nabla\mathbf{u} + \nabla^T\mathbf{u}\right)$, $\mathbf{u}$ is the displacement and G_c is the critical energy release rate. As depicted in Fig. 4.4, this equation is provided in a 2D arbitrary solid domain Ω with a discontinuous boundary Γ.

The crack surface area density function is expressed as [50]:

$$\gamma(\phi; \nabla\phi) = \frac{\phi^2}{2l} + \frac{l}{2}|\nabla\phi|^2 \tag{4.17}$$

Within this framework, crack growth can be predicted along any trajectory without arbitrary criteria, driven by global energy minimization and the conversion of stored energy into fracture energy. The displacement and phase fields are obtained by minimizing the functional, where the functional derivatives with respect to each field are set to zero. This process yields the strong form of the problem, expressed through the following Euler–Lagrange equations [48]:

$$\frac{\delta\Pi}{\delta\mathbf{u}} = \nabla\cdot\boldsymbol{\sigma} = 0, \tag{4.18}$$

$$\frac{\delta\Pi}{\delta\phi} = G_c\left(\frac{\phi}{l} - l\nabla^2\phi\right) - 2(1-\phi)\psi_0(\boldsymbol{\varepsilon}) = 0 \tag{4.19}$$

To prevent crack nucleation under compressive loading, the strain energy in the intact body is partitioned into active (ψ_0^+) and inactive (ψ_0^-) components. This decomposition distinguishes tensile and compressive contributions, addressing the tension–compression symmetry inherent in damage evolution within the phase-field framework. Such symmetry can lead to unphysical crack growth under compressive stress states, which contradicts the observed resistance to cracking in materials like metals. There are several methods for strain energy decomposition designed to prevent crack growth under compressive loading. These include the volumetric–deviatoric split proposed by Amor et al. [51], the spectral decomposition introduced by Miehe and coworkers [50], and the purely tensile splits, often referred to as no-tension models, developed by Freddi and Royer-Carfagni [52, 53] and Lo et al. [54]. This study employs a volumetric–deviatoric split of the strain tensor, coupling only the deviatoric component with phase-field evolution, ensuring that compressive energy does not drive crack

propagation [51]. The split strain energy contributions (ψ_0^+, ψ_0^-) are functions of their respective strain tensors, as shown below:

$$\psi_0^+ = \frac{1}{2}\lambda\langle \mathrm{tr}(\boldsymbol{\varepsilon}^+)\rangle^2 + \mu \mathrm{tr}\left[(\boldsymbol{\varepsilon}^+)^2\right] \tag{4.20}$$

$$\psi_0^- = \frac{1}{2}\lambda\langle \mathrm{tr}(\boldsymbol{\varepsilon}^-)\rangle^2 + \mu \mathrm{tr}\left[(\boldsymbol{\varepsilon}^-)^2\right] \tag{4.21}$$

where λ and μ are the Lamé constant, $\boldsymbol{\varepsilon}^+$ and $\boldsymbol{\varepsilon}^-$ are the positive and negative counterparts of the strain tensor.

Moreover, to prevent damage from self-healing over time τ, H (fracture driving force) is introduced as a history variable since it is an irreversible process [50].

$$H = max_{t\in[0,\mathrm{t}]}\Psi^+(t) \tag{4.22}$$

This expression represents the peak tensile elastic energy attained during the loading history, serving as the primary driving force for crack propagation. This leads to the following formulation of the strong form:

$$G_c\left(\frac{\phi}{l_0} - l_0\nabla^2\phi\right) - 2(1-\phi)H = 0 \tag{4.23}$$

The model is implemented in the implicit finite element solver Abaqus using a user-defined material subroutine (UMAT). To simplify the analysis, the phase-field parameter is represented as a temperature-like field by utilizing coupled temperature–displacement elements. This formulation exploits the mathematical analogy between the phase-field governing equations and the steady-state heat transfer equation (Eq. 6.3), as described in [55], where k is the thermal conductivity, T is temperature and r is the heat source term.

$$k\nabla^2 T = -r \tag{4.24}$$

$$\nabla^2\phi = \frac{\phi}{l^2} - 2(1-\phi)\frac{H}{f(\alpha)G_c l} \tag{4.25}$$

Specifically, the UMAT developed by Navidtehrani et al.[55–57] is employed, which incorporates both the heat transfer law and phase-field equations. Taking k as 1, a heat source is introduced in the model through the user-defined heat generation subroutine as:

$$r = -\left(\frac{\phi}{l^2} - 2(1-\phi)\frac{H}{f(\alpha)G_c l}\right) \tag{4.26}$$

This approach ensures computational efficiency and enables seamless integration within the Abaqus framework [58]. By representing the phase field through the temperature field, it leverages Abaqus's built-in features to effectively simulate fracture.

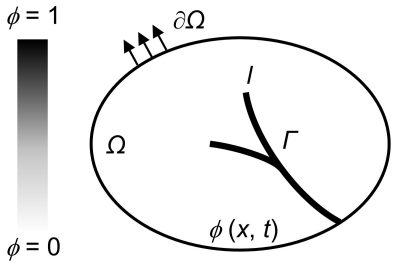


Figure 4.4: Illustration of a solid body with a distinct internal discontinuity, using the phase field method to approximate the discontinuity.

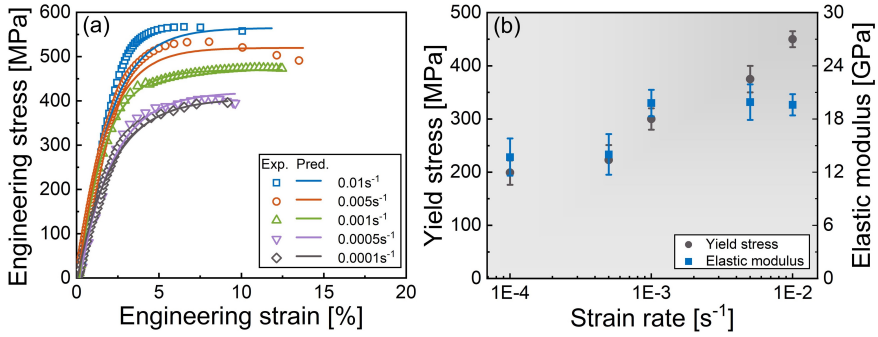


Figure 4.5: (a) Stress-strain curves versus strain rates; (b) elastic modulus and yield stress versus strain rates.

Table 4.1: Material parameters of Anand model for the sintered Cu NPs

Parameter	A (s^{-1})	Q (J/mol)	m	n	ξ	$\hat{s}$ (MPa)	h_0 (MPa)	s_0 (MPa)	a
Value	298	71013	0.477	0.0179	10	421	213	12.22	1

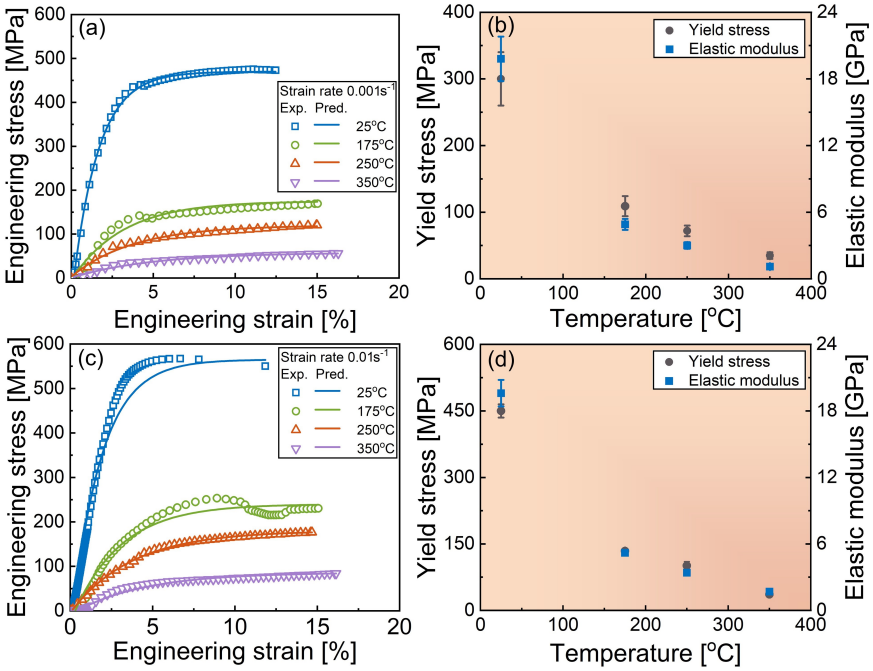


Figure 4.6: Stress-strain curves versus temperature at the strain rate of (a) 0.001 s^{-1} and (c) 0.01 s^{-1}; elastic modulus and yield stress versus temperature at the strain rate of (b) 0.001 s^{-1} and (d) 0.01 s^{-1}.

4.3. RESULTS AND DISCUSSION

4.3.1. STRESS-STRAIN CURVES UNDER DIFFERENT STRAIN RATES

The stress-strain curves of micro-pillars tested under five different strain rates (0.0001 s^{-1} to 0.01 s^{-1}) are shown in Fig. 4.5a. The results demonstrate a clear strain-rate-hardening characteristics in the mechanical properties of sintered Cu NPs. The yield strength was determined according to 0.2% offset yield criterion [59]. As the strain rate increases, both yield stress and ultimate strength rise significantly. For instance, the yield stress exceeds 450 MPa at 0.01 s^{-1}, while it falls below 200 MPa at 0.0001 s^{-1}. This trend indicates that higher strain rates enhance resistance to deformation due to limited time for dislocation motion and rearrangement, leading to dislocation accumulation and increased strength. Conversely, lower strain rates provide more time for dislocations to rearrange, reducing yield stress but improving ductility. Fig. 4.5b further reveals that the elastic modulus also increases with strain rate, rising from approximately 14 GPa at 0.0001 s^{-1} to nearly 20 GPa at 0.01 s^{-1}. The observed step-like increase in elastic modulus near a strain rate of 0.001 s^{-1} can be attributed to rate-dependent deformation mechanisms in the sintered Cu NP structure. At lower strain rates, localized deformation at inter-particle necks and void growth dominate, resulting in reduced stiffness due to heterogeneous stress distribution. In contrast, higher strain rates enhance interparticle load transfer and suppress localized damage, promoting more uniform stress fields and effective cohesion across the structure. This transition leads to a measurable increase in

apparent stiffness. Similar behavior has been reported in prior studies [60], where high strain rates were shown to induce more homogeneous deformation through concurrent activation of both favorable and less favorable sites. These findings highlight the role of strain rate in strengthening and stiffening sintered Cu NPs through microstructure confinement and stress redistribution.

4.3.2. STRESS-STRAIN CURVES UNDER DIFFERENT TEMPERATURES

The mechanical behavior of sintered Cu NPs under compression is strongly influenced by temperature, as shown in Fig. 4.6. Stress-strain curves in Figs. 4.6a and c demonstrate significant mechanical degradation with increasing temperature (25°C to 350°C) at strain rates of 0.001 s^{-1} and 0.01 s^{-1}. At room temperature, micro-pillars exhibit the highest yield strength and elastic modulus, exceeding 300 MPa and 20 GPa, respectively. However, both properties decline sharply at elevated temperatures. For instance, the yield stress drops to approximately 110 MPa at 175°C and further reduces to below 50 MPa at 350°C, accompanied by a corresponding decrease in elastic modulus to less than 2 GPa. This temperature-induced softening is attributed to thermally activated processes such as enhanced dislocation motion [61], grain boundary sliding and atomic diffusion [62, 63], which collectively reduce structural integrity. At lower temperatures, deformation resistance is dominated by dislocation pile-ups and particle necking, preserving mechanical strength. However, as temperature increases, diffusion-assisted grain boundary migration promotes plastic flow and weakening the material. Similar behavior has been observed in other nanostructured materials [64], where high-temperature deformation is linked to grain boundary effects and interfacial weakening. Additionally, strain-rate hardening effects mitigate softening to some extent. As shown in Figs. 4.6b and d, higher strain rates (0.01 s^{-1}) result in consistently higher yield stress and elastic modulus compared to lower rates (0.001 s^{-1}) across all temperatures. This rate-dependent strengthening arises from restricted dislocation motion and reduced time for diffusion, limiting void growth and enhancing load transfer within the sintered structure. The overall trend highlights the challenges of using sintered Cu NPs in high-temperature applications, where thermal degradation of mechanical properties may lead to premature failure under elevated thermal and mechanical loads.

The material parameters of Anand model for the sintered Cu NPs are presented in Table 1. It can be observed from Fig. 4.5a and Figs. 4.6a, c that the Anand model provides a good fit to the experimental data, as indicated by the close alignment between the scatter points (experimental data) and the lines (fitted results). The fitting is particularly accurate at lower temperatures and for higher strain rates, where the plastic behaviour of the material dominates. However, some discrepancies can be noticed at higher temperatures, especially in the early stages of deformation, where the model slightly underestimates the yield point. This may be due to the fact that the Anand model is primarily designed to capture plastic deformation and is less effective in modelling the initial elastic response. Despite these minor deviations, the model demonstrates a robust capability to predict the overall stress-strain behaviour across different strain rates and temperatures, making it a reliable tool for predicting the mechanical response of sintered Cu NPs under varying conditions.

4.3.3. SEM ANALYSIS

The SEM micrographs in Fig. 4.7 and Fig. 4.8 reveal the deformation mechanisms of sintered Cu NP micro-pillars under varying strain rates and temperatures. Figs. 4.7a and b show micro-pillars deformed at 25°C under strain rates of 0.0001 s^{-1} and 0.01 s^{-1}, respectively. Despite the differences in strain rate (Fig. 4.5a), both SEM micrographs (Figs. 4.7a and b) exhibit similar macroscopic deformation features, characterized by surface extrusions on the sidewalls of the compressed micro-pillars. These extrusions indicate localized plastic deformation, which likely originates from particle rearrangement and interfacial sliding—a common mechanism in sintered NP systems [65–67]. Given the absence of visible slip bands, twinning, or grain boundary migration at this resolution, the deformation is inferred to be dominated by interfacial plasticity and densification through pore collapse rather than crystallographic slip. The role of larger particles as load-bearing elements is also evident, suggesting heterogeneous stress distribution and localized deformation pathways within the pillar. Thus, the observed behavior reflects the unique mechanical response of porous sintered structures, where deformation is governed more by interparticle dynamics than by traditional intragranular mechanisms [68].

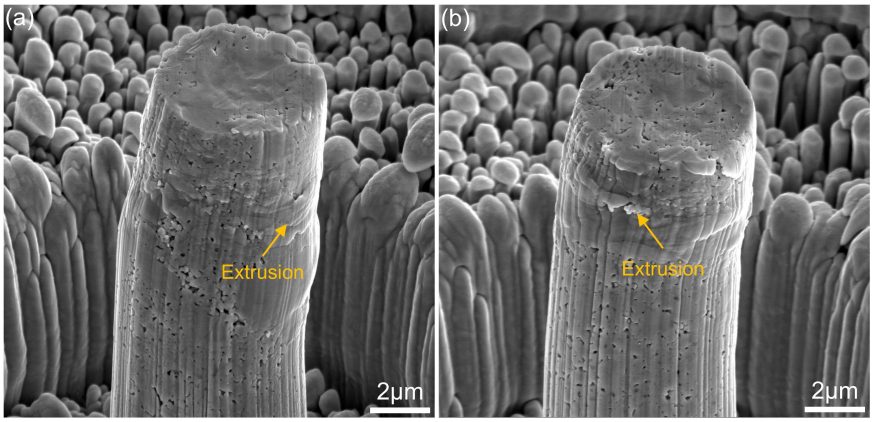


Figure 4.7: Typical morphologies of micro-pillars compressed at (a) $0.001 s^{-1}$ and (b) $0.01 s^{-1}$

Figs. 4.8a–f provide high-resolution SEM micrographs of sintered Cu NP micro-pillars compressed at elevated temperatures of 175°C and 350°C. At both temperatures, distinct thermally activated deformation mechanisms are observed. Notably, surface extrusions and lateral shear steps (Figs. 4.8b, c, e, and f) suggest the onset of localized shear deformation, likely facilitated by reduced yield strength and increased particle mobility. These features are indicative of surface flow and interfacial sliding due to the fine-grained, porous microstructure of the sintered NP pillars. The reduction in visible porosity, especially at 350°C (Figs. 4.8d–f), supports a densification mechanism akin to pressure-assisted sintering, where elevated temperature enhances atomic diffusion and facilitates void closure [69]. This is further supported by smoother surface morphologies and fewer discrete interparticle voids. The contrast between deformation at room temperature (Fig. 4.7) and elevated temperatures (Fig. 4.8) underscores a transition in dom-

inant mechanisms: from rigid-body particle interactions and force chain formation at 25°C to thermally activated interparticle sliding, shear localization, and pore collapse at 175°C and 350°C. These observations suggest that deformation at elevated temperatures is governed by a combination of viscous flow, interface sliding and diffusion-assisted particle rearrangement [70].

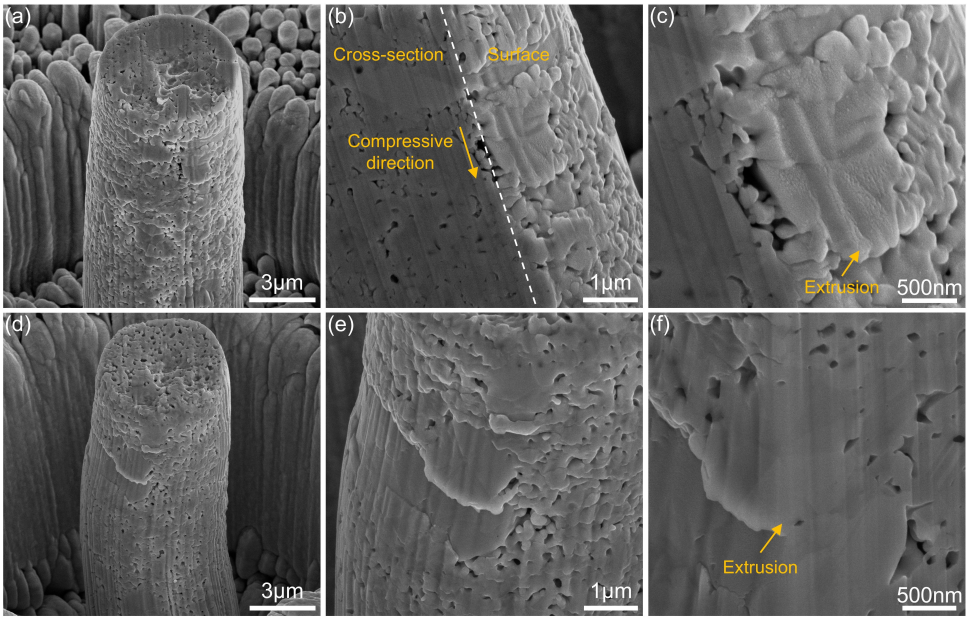


Figure 4.8: SEM images of micro-pillars compressed at a strain rate of 0.001 s^{-1}. (a–c) Deformation behavior at 175°C: (a) overall pillar morphology; (b, c) high-magnification views highlighting shear banding and surface extrusion features. (d–f) Deformation behavior at 350°C: (d) overall pillar morphology; (e, f) high-magnification views showing enhanced shear and extrusion deformation.

4.3.4. TEM CHARACTERIZATION

To further investigate the effect of high temperature on microstructure evolution of micro-pillars, two TEM samples were extracted from the compressed micro-pillars tested at 175°C and 350°C, respectively. Fig. 4.9 presents TEM bright-field (BF) images of a micro-pillar compressed at 175°C, highlighting the effect of moderate thermal activation on microstructure evolution as the re-sintering were found based on the more sphere voids compared with the initial microstructure shown in Fig. 4.1f. As shown in Fig. 4.9a, the overall morphology retains clear particle boundaries and exhibits a heterogeneous structure with regions of localized deformation. Near the top surface (Fig. 4.9b), where the indenter applied load, deformation is more concentrated due to localized stress, promoting dislocation motion and compaction, especially within larger particles. These larger particles serve as primary load carriers, forming force chains that sustain deformation and redistribute stress. In contrast, the lower region (Fig. 4.9c) shows less deformation, with more evident voids and distinct particle boundaries, indicative of in-

complete densification. While partial re-sintering has occurred, as evidenced by reduced porosity compared to room-temperature samples, the residual voids within the NP regions suggest that densification at 175°C is not yet sufficient to form a fully compact structure. Instead, the deformation is predominantly accommodated through particle rearrangement and localized sliding, with plasticity concentrated at particle necks rather than across the entire structure. This highlights the critical role of particle size and arrangement in governing deformation behavior under moderate thermal conditions.

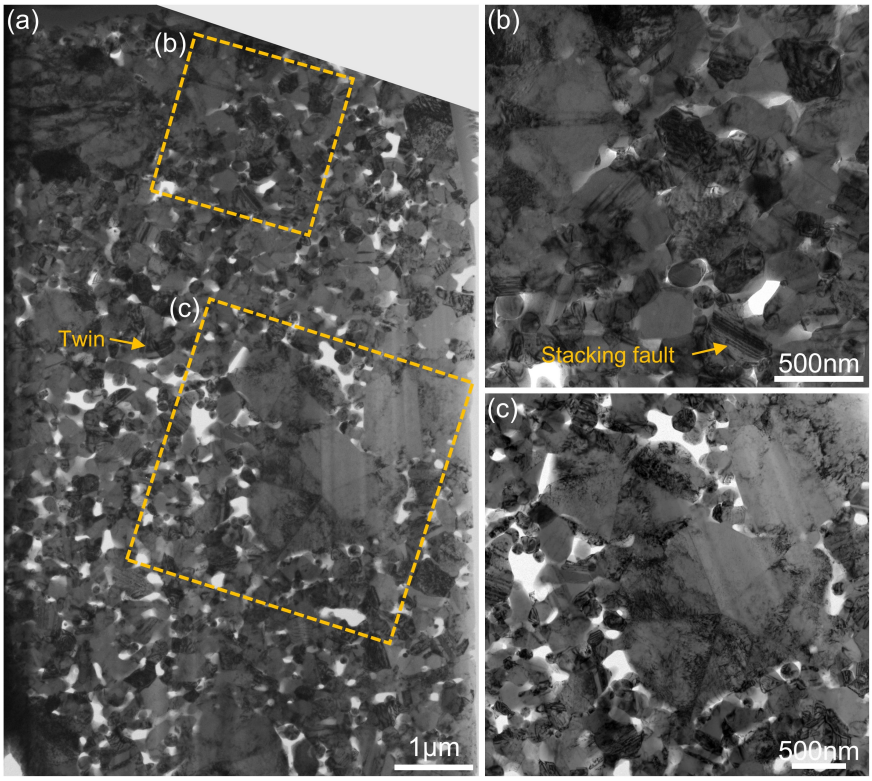


Figure 4.9: TEM images of a sintered Cu NP micro-pillar compressed at 175°C to 15% strain (strain rate: 0.001 s^{-1}). (a) Low-magnification overview of the deformed pillar; (b, c) high-magnification views of the regions indicated in (a), highlighting local microstructural features.

Fig. 4.10 illustrates microstructure changes in a micro-pillar compressed at 350°C, where higher thermal activation significantly enhances densification through re-sintering. Due to the re-sintering, the voids present a more sphere shape compared with the initial microstructure (Fig. 4.1f). The BF images (Figs. 4.10a, b) show that the micro-pillar develops a more compact and homogeneous structure, with pronounced reductions in void size and clearer evidence of particle bonding. This densification is driven by increased dislocation activity, grain boundary sliding and diffusion-assisted particle rearrangement at elevated temperatures. The stronger sintering necks between particles further improve mechanical integrity, enabling more uniform stress distribu-

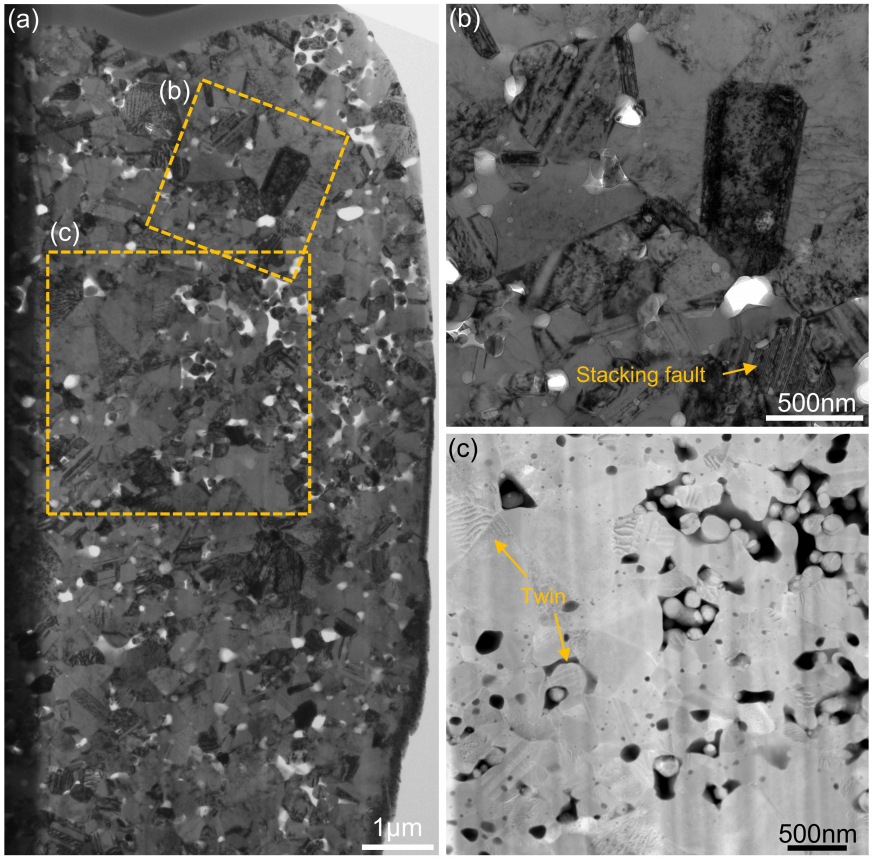


Figure 4.10: TEM images of a sintered Cu NP micro-pillar compressed at 350°C to 17% strain (strain rate: 0.001 s^{-1}). (a) Low-magnification overview of the deformed pillar; (b, c) high-magnification views of the regions indicated in (a), highlighting local microstructural features.

tion throughout the structure. Notably, the scanning transmission electron microscopy (STEM) image in Fig. 4.10c provides additional insights into the microstructure. It reveals finer voids distributed along grain boundaries, indicating that re-sintering processes are concentrated at particle interfaces, further reducing porosity. The blurred particle boundaries observed in Fig. 4.10c suggest enhanced bonding due to thermal diffusion, which promotes better stress transfer between particles. Compared to the sample deformed at 175°C, the micro-pillar compressed at 350°C exhibits not only higher compaction but also a more homogeneous deformation pattern throughout the entire volume (Fig. 4.10). This transition from localized deformation in a porous network to uniform plastic flow in a denser structure highlights the increasing influence of temperature-activated mechanisms. In particular, signs of dynamic recrystallization (DRX) can be inferred from the microstructural evolution observed in the high-temperature sample. The presence of finer, equiaxed grains and reduced dislocation density in certain regions (Fig. 4.10c) suggests the occurrence of DRX, likely facilitated

by grain boundary migration and dislocation rearrangement [71, 72]. These features are indicative of thermally activated recovery and recrystallization processes, which are known to enhance plastic deformability and structural stability under elevated temperatures. Therefore, we believe that DRX plays a significant role in accommodating strain and promoting densification during high-temperature deformation of sintered Cu NP micro-pillars.

Moreover, TEM observations reveal the presence of stacking faults and deformation twins, as shown in Fig. 4.9 and Fig. 4.10. These features are indicative of partial dislocation activity and twinning—both intragranular mechanisms that accommodate plastic strain under elevated temperatures [73, 74]. Their presence suggests that, in addition to interfacial sliding and particle rearrangement, thermally activated dislocation processes contribute significantly to the overall deformation behavior. While direct grain boundary sliding is not explicitly resolved, the heterogeneous contrast and local misorientations near grain interfaces imply its potential contribution, particularly at higher temperatures where boundary mobility increases. Overall, these deformation products play a crucial role in enhancing the ductility and energy dissipation capacity of the sintered Cu NP micro-pillars, supporting a transition from rigid interparticle force networks at room temperature to more distributed, defect-mediated plasticity at elevated temperatures.

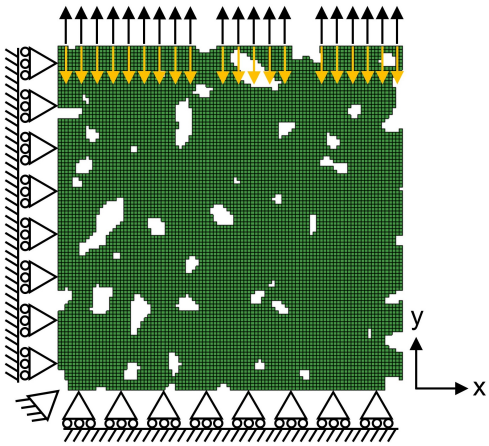


Figure 4.11: Meshed 2D model with boundary conditions.

4.3.5. PHASE-FIELD FRACTURE MODELING

In this section, 2D models with randomly distributed pores are used to simulate the mechanical properties and fracture behaviour. The dimension of the model is 5 μm × 5 μm with quadrilateral elements of 0.05 μm × 0.05 μm. Fig. 4.11 shows the corresponding finite element mesh (4 nodes CPS4) of the structure and the boundary conditions. The compressive and tensile loading is applied along the top edge (as indicated by the arrows), which is designed to simulate compressive and tensile stress, allowing for the investigation of how the porous microstructure influences mechanical behaviour, par-

ticularly crack initiation and propagation.

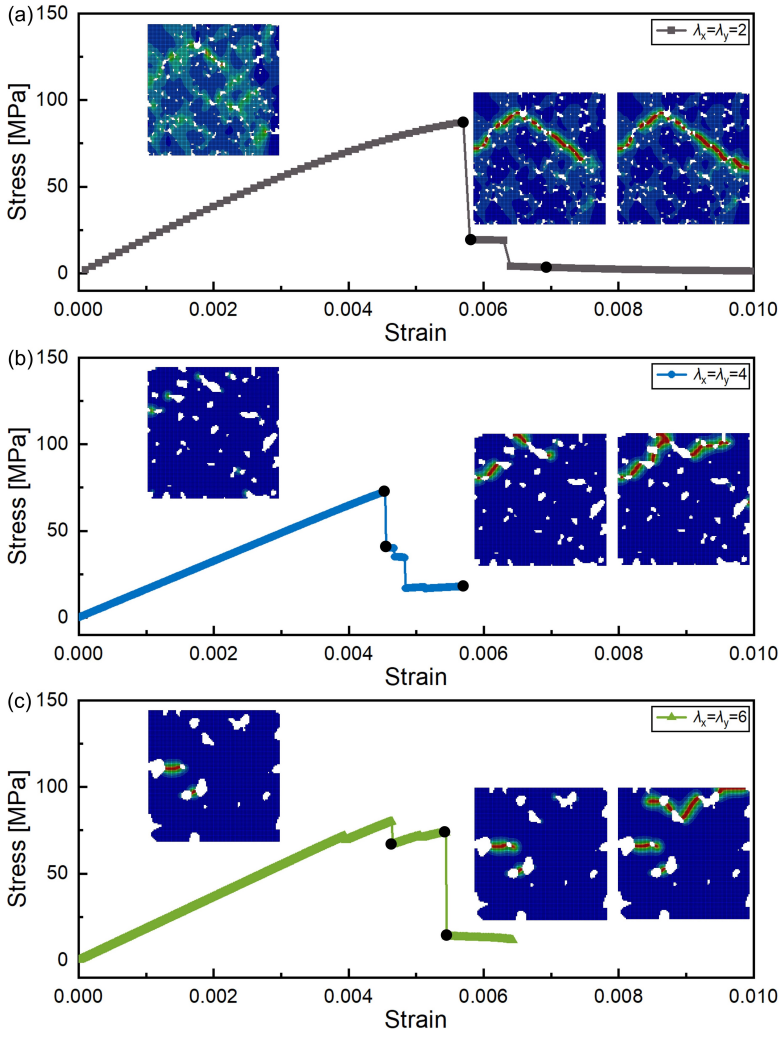


Figure 4.12: Stress–strain responses with crack evolutions under compressive load: (a) λ_x=λ_y=2; (b) λ_x=λ_y=4; (c) λ_x=λ_y=6.

The phase-field modeling results presented in Figs. 4.12-4.15 highlight the significant influence of void size and distribution on the mechanical behavior and crack evolution of sintered Cu NPs under compressive and tensile loading. The microstructures, controlled by the correlation lengths λ_x and λ_y, demonstrate that increasing these parameters leads to larger voids and fewer voids at a fixed porosity (7%). Stress–strain responses under compressive loading (Fig. 4.12) reveal that smaller voids (λ_x= λ_y=2) sustain higher stress levels due to more uniform stress distributions, which delay crack initiation and promote sudden brittle-like fracture. In contrast, larger voids (λ_x= λ_y=4, λ_x=λ_y=6) expe-

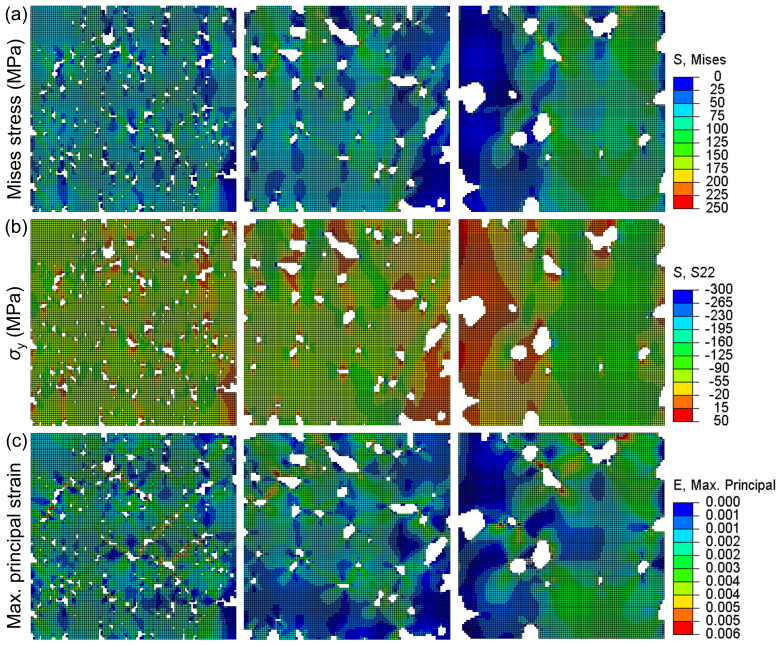


Figure 4.13: The distributions of Mises stress, stress in y direction, and maximum principal strain under compressive load: (a) λ_x=λ_y=2; (b) λ_x=λ_y=4; (c) λ_x=λ_y=6.

rience localized stress concentrations at void edges and tips, causing gradual crack propagation along interconnected voids. The stress and strain distributions (Fig. 4.13) further confirm that larger voids induce higher strain localization, weakening load transfer and accelerating failure. Moreover, the simulated crack propagation path agrees well with the experimental results in Fig. 4.8. Under tensile loading (Fig. 4.14), smaller voids also exhibit higher tensile strength and slower crack propagation compared to larger voids, which promote rapid crack extension along stress concentration regions. Unlike compression, tensile cracks result in complete void opening, leading to a sharp reduction in load-bearing capacity, as illustrated by the stress and strain fields in Fig. 4.15.

These results underscore the critical role of void morphology in governing the mechanical performance of sintered Cu NPs. Smaller voids effectively distribute stress, offering higher structural integrity and resistance to deformation, while larger voids act as stress concentrators, amplifying localized deformation and accelerating fracture propagation. The asymmetric crack evolution between compressive and tensile loading highlights distinct failure mechanisms, where compression-induced cracks are dominated by slip and void coalescence, while tensile cracks propagate through void opening [75]. The findings are consistent with experimental observations and previous studies on porous materials, demonstrating the importance of void geometry in mechanical responses and fracture paths [35]. Furthermore, the observed void evolution represents high-temperature effects, such as re-sintering and void growth, which alter stress pathways and mechanical stability. These insights provide a foundation for optimizing mi-

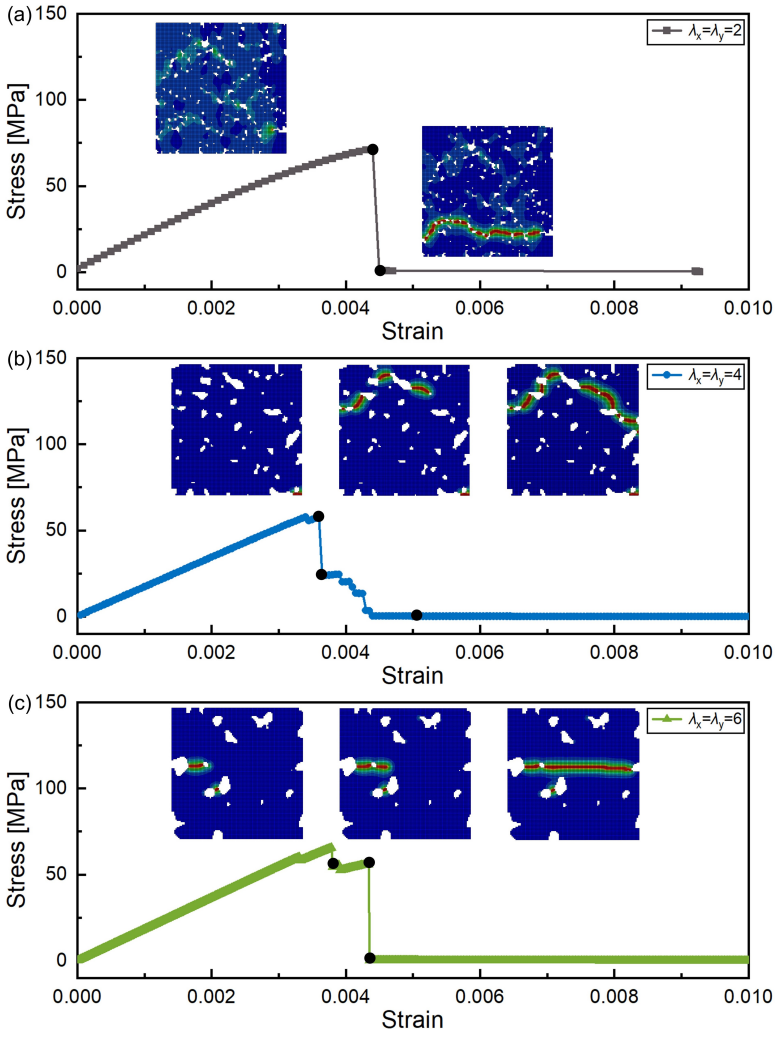


Figure 4.14: Stress–strain responses with crack evolutions under tensile load: (a) λ_x=λ_y=2; (b) λ_x=λ_y=4; (c) λ_x=λ_y=6.

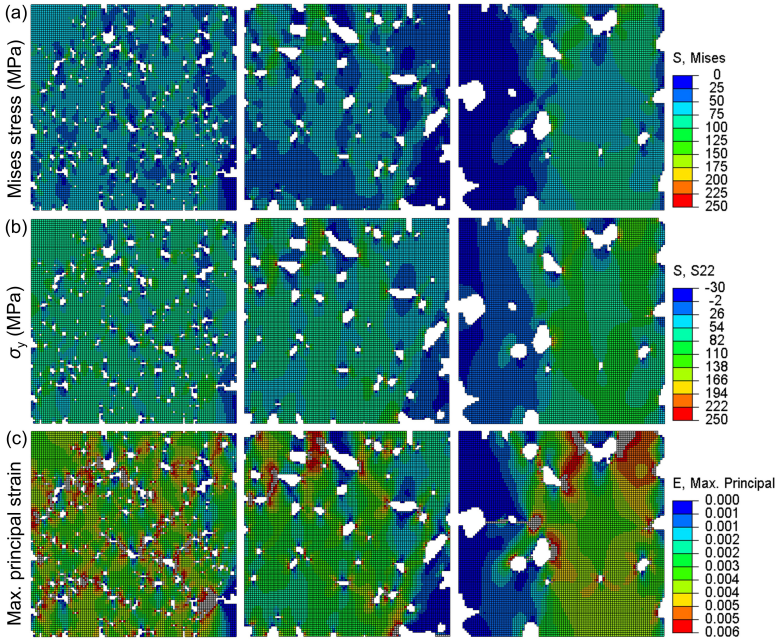


Figure 4.15: The distributions of Mises stress, stress in y direction, and maximum principal strain under tensile load: (a) λ_x=λ_y=2; (b) λ_x=λ_y=4; (c) λ_x=λ_y=6.

crostructures in sintered Cu NPs to enhance thermal and mechanical performance, particularly for high-temperature applications in electronics packaging.

Fig. 4.16 presents the stress–strain responses of sintered Cu NPs, demonstrating the influence of temperature (25°C, 175°C, 250°C and 350°C) on mechanical behavior and crack propagation under compressive and tensile loading. The results reveal a substantial reduction in strength with increasing temperature, primarily attributed to thermally induced softening. Notably, only the elastic modulus was adjusted in the present simulations to capture temperature-dependent effects, focusing on mechanical responses without explicitly modeling temperature-induced plasticity. While the phase-field fracture modeling effectively simulates crack initiation and propagation under various loading conditions, the real deformation mechanisms in sintered Cu NPs are inherently more complex, involving significant elastic–plastic interactions and time-dependent processes such as creep and stress relaxation. The simplified elastic modeling may underestimate the role of plastic deformation, which is critical for accurately predicting failure behavior under elevated temperatures. Future efforts should incorporate elastic–plastic formulations into the phase-field framework to better capture the interplay between plastic flow, void growth and crack evolution. Such enhancements will provide deeper insights into temperature-driven microstructural transformations and improve the predictive capabilities for applications requiring thermal and mechanical stability.

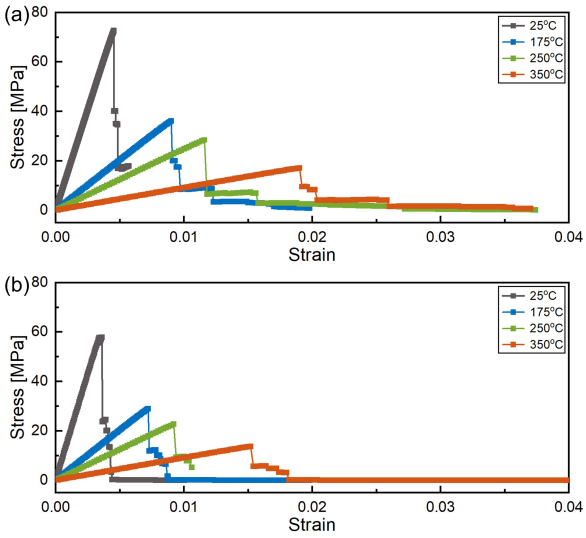


Figure 4.16: Stress–strain responses of structures with different temperatures under (a) compressive load and (b) tensile load.

4.4. CONCLUSION

In this study, the microscale mechanical properties of sintered Cu NPs were comprehensively analyzed through micro-pillar compression tests, SEM, TEM and phase-field fracture modelling. This multi-faceted approach enabled a detailed exploration of the effects of strain rate and temperature on the mechanical behaviour of sintered Cu NPs. The main conclusions are as follows:

1. The results reveal that the mechanical response of sintered Cu NPs is significantly influenced by strain rate and temperature. Higher strain rates enhance yield strength due to strain-rate hardening, whereas elevated temperatures induce thermal softening, leading to reduced strength and stiffness. These effects are effectively captured by the Anand viscoplastic model, which demonstrates excellent agreement with experimental stress-strain data across a range of strain rates (0.0001 s^{-1} to 0.01 s^{-1} and temperatures (25°C to 350°C).

2. Microstructural analyses using SEM and TEM further elucidate temperature-driven deformation mechanisms. At moderate temperatures (175°C), deformation remains localized, with dislocation activities concentrated near particle interfaces, while at higher temperatures (350°C), diffusion-assisted grain boundary migration promotes re-sintering and densification, resulting in a more compact structure with reduced porosity.

3. Phase-field fracture modeling reveals that void size and number significantly influence crack initiation and propagation, even at constant porosity levels. Structures with smaller, more numerous voids exhibit higher stiffness and delayed crack initiation due to more uniform stress distribution, while larger voids lead to localized stress concentrations, rapid crack coalescence and accelerated fracture propagation.

REFERENCES

[1] L. Du *et al.*, "Strain rate and temperature dependent viscoplasticity of sintered cu nanoparticles", *Materials & Design*, p. 114 319, 2025.

[2] A. Hutzler, A. Tokarski, S. Kraft, S. Zischler, and A. Schletz, "Increasing the lifetime of electronic packaging by higher temperatures: Solders vs. silver sintering", in *2014 IEEE 64th Electronic Components and Technology Conference (ECTC)*, IEEE, 2014, pp. 1700–1706.

[3] K. Sugiura *et al.*, "Reliability evaluation of sic power module with sintered ag die attach and stress-relaxation structure", *IEEE Transactions on Components, Packaging and Manufacturing Technology*, vol. 9, no. 4, pp. 609–615, 2019.

[4] R. Kimura, Y. Kariya, N. Mizumura, and K. Sasaki, "Effect of sintering temperature on fatigue crack propagation rate of sintered ag nanoparticles", *Materials Transactions*, vol. 59, no. 4, pp. 612–619, 2018.

[5] G. Chen *et al.*, "Applying viscoplastic constitutive models to predict ratcheting behavior of sintered nanosilver lap-shear joint", *Mechanics of Materials*, vol. 72, pp. 61–71, 2014.

[6] G. Chen, L. Yu, Y. Mei, X. Li, X. Chen, and G.-Q. Lu, "Uniaxial ratcheting behavior of sintered nanosilver joint for electronic packaging", *Materials Science and Engineering: A*, vol. 591, pp. 121–129, 2014.

[7] X. Long *et al.*, "Mechanical behaviour of sintered silver nanoparticles reinforced by sic microparticles", *Materials Science and Engineering: A*, vol. 744, pp. 406–414, 2019.

[8] X. Long, Q. Jia, Z. Shen, M. Liu, and C. Guan, "Strain rate shift for constitutive behaviour of sintered silver nanoparticles under nanoindentation", *Mechanics of Materials*, vol. 158, p. 103 881, 2021.

[9] J. Fan *et al.*, "High-temperature nanoindentation characterization of sintered nano-copper particles used in high power electronics packaging", *Results in Physics*, vol. 33, p. 105 168, 2022.

[10] D. Hu *et al.*, "High temperature viscoplastic deformation behavior of sintered nanocopper paste used in power electronics packaging: Insights from constitutive and multi-scale modelling", *Journal of Materials Research and Technology*, vol. 26, pp. 3183–3200, 2023.

[11] L. Zhao *et al.*, "Strain-rate dependent deformation mechanism of graphene-al nanolaminated composites studied using micro-pillar compression", *International Journal of Plasticity*, vol. 105, pp. 128–140, 2018.

[12] J. Carpenter, A Misra, M. Uchic, and P. Anderson, "Strain rate sensitivity and activation volume of cu/ni metallic multilayer thin films measured via micropillar compression", *Applied Physics Letters*, vol. 101, no. 5, 2012.

[13] S Breumier, S Sao-Joao, A Villani, M. Lévesque, and G Kermouche, "High strain rate micro-compression for crystal plasticity constitutive law parameters identification", *Materials & Design*, vol. 193, p. 108 789, 2020.

[14] O. T. Abad, J. M. Wheeler, J. Michler, A. S. Schneider, and E. Arzt, "Temperature-dependent size effects on the strength of ta and w micropillars", *Acta Materialia*, vol. 103, pp. 483–494, 2016.

[15] J. Cho *et al.*, "Temperature effect on mechanical response of flash-sintered zno by in-situ compression tests", *Acta Materialia*, vol. 200, pp. 699–709, 2020.

[16] A Abaza *et al.*, "Fracture properties of porous yttria-stabilized zirconia under micro-compression testing", *Journal of the European Ceramic Society*, vol. 42, no. 4, pp. 1656–1669, 2022.

[17] S. Yuan, Y. Zhu, S. Liang, M. Huang, and Z. Li, "Dislocation-density based size-dependent crystal plasticity framework accounting for climb of piled up dislocations at elevated temperature", *Mechanics of Materials*, vol. 134, pp. 85–97, 2019.

[18] B. Li, J. Wang, and Y. Yao, "Creep behavior of sintered nano-silver at high temperature: Experimental and theoretical analysis", *Materials Today Communications*, vol. 37, p. 106 956, 2023.

[19] K. Wakamoto, D. Yasugi, T. Otsuka, K. Nakahara, and T. Namazu, "Fracture mechanism of sintered silver film revealed by in-situ sem uniaxial tensile loading", *IEEE Transactions on Components, Packaging and Manufacturing Technology*, 2024.

[20] H.-Y. Jeong, "A new yield function and a hydrostatic stress-controlled void nucleation model for porous solids with pressure-sensitive matrices", *International journal of solids and structures*, vol. 39, no. 5, pp. 1385–1403, 2002.

[21] C. C. Roth and D. Mohr, "Determining the strain to fracture for simple shear for a wide range of sheet metals", *International Journal of Mechanical Sciences*, vol. 149, pp. 224–240, 2018.

[22] F. Bardi and S Kyriakides, "Plastic buckling of circular tubes under axial compression—part i: Experiments", *International journal of mechanical sciences*, vol. 48, no. 8, pp. 830–841, 2006.

[23] H. Wang and H. B. Chew, "Molecular dynamics simulations of plasticity and cracking in lithiated silicon electrodes", *Extreme Mechanics Letters*, vol. 9, pp. 503–513, 2016.

[24] W. Song, Y. Yu, and Y. Guan, "Role of void shape on shock responses of nanoporous metallic glasses via molecular dynamics simulation", *International Journal of Mechanical Sciences*, vol. 218, p. 107 076, 2022.

[25] Q. Shao, L. Bouhala, A. Younes, P. Núñez, A. Makradi, and S. Belouettar, "An xfem model for cracked porous media: Effects of fluid flow and heat transfer", *International Journal of Fracture*, vol. 185, pp. 155–169, 2014.

[26] E. Mikaeili and P. Liu, "Numerical modeling of shear band propagation in porous plastic dilatant materials by xfem", *Theoretical and Applied Fracture Mechanics*, vol. 95, pp. 164–176, 2018.

[27] B. E. Hachi, A. E. Benkhechiba, M. R. Kired, D. Hachi, and M. Haboussi, "Some investigations on 3d homogenization of nano-composite/nano-porous materials with surface effect by fem/xfem methods combined with level-set technique", *Computer Methods in Applied Mechanics and Engineering*, vol. 371, p. 113 319, 2020.

[28] N. Noii, A. Khodadadian, and F. Aldakheel, "Probabilistic failure mechanisms via monte carlo simulations of complex microstructures", *Computer Methods in Applied Mechanics and Engineering*, vol. 399, p. 115 358, 2022.

[29] O. Karpenko, S. Oterkus, and E. Oterkus, "Peridynamic analysis to investigate the influence of microstructure and porosity on fatigue crack propagation in additively manufactured ti6al4v", *Engineering Fracture Mechanics*, vol. 261, p. 108 212, 2022.

[30] Y. Pan, P. Wu, S. Fan, X. Peng, and Z. Chen, "Peridynamic simulation of fatigue crack growth in porous materials", *Engineering Fracture Mechanics*, vol. 300, p. 109 984, 2024.

[31] C. Miehe, L.-M. Schänzel, and H. Ulmer, "Phase field modeling of fracture in multi-physics problems. part i. balance of crack surface and failure criteria for brittle crack propagation in thermo-elastic solids", *Computational Methods in Applied Mechanics and Engineering*, vol. 294, pp. 449–485, 2015.

[32] C. Miehe, M. Hofacker, L.-M. Schänzel, and F. Aldakheel, "Phase field modeling of fracture in multi-physics problems. part ii. coupled brittle-to-ductile failure criteria and crack propagation in thermo-elastic–plastic solids", *Computational Methods in Applied Mechanics and Engineering*, vol. 294, pp. 486–522, 2015.

[33] E. Martínez-Pañeda, A. Golahmar, and C. F. Niordson, "A phase field formulation for hydrogen assisted cracking", *Computer Methods in Applied Mechanics and Engineering*, vol. 342, pp. 742–761, 2018.

[34] Y. Su *et al.*, "Thermo-elasto-plastic phase-field modelling of mechanical behaviours of sintered nano-silver with randomly distributed micro-pores", *Computer Methods in Applied Mechanics and Engineering*, vol. 378, p. 113 729, 2021.

[35] Y. Su, J. Zhu, X. Long, L. Zhao, C. Chen, and C. Liu, "Statistical effects of pore features on mechanical properties and fracture behaviors of heterogeneous random porous materials by phase-field modeling", *International Journal of Solids and Structures*, vol. 264, p. 112 098, 2023.

[36] Y. Su, Z. Shen, X. Long, C. Chen, L. Qi, and X. Chao, "Gaussian filtering method of evaluating the elastic/elasto-plastic properties of sintered nanocomposites with quasi-continuous volume distribution", *Materials Science and Engineering: A*, vol. 872, p. 145 001, 2023.

[37] X. Liu *et al.*, "Microstructural evolution, fracture behavior and bonding mechanisms study of copper sintering on bare dbc substrate for sic power electronics packaging", *Journal of Materials Research and Technology*, vol. 19, pp. 1407–1421, 2022.

[38] A. Kurdi, S. Alshihri, T. Tabbakh, N. B. Darwish, J. B. Saedon, and A. K. Basak, "Compressive strength and deformation behavior of the hybrid s phase layer under micro-pillar compression", *Materials Science and Engineering: A*, vol. 861, p. 144 380, 2022.

[39] G. J. Schaffar, D. Tscharnuter, and V. Maier-Kiener, "Exploring the high-temperature deformation behavior of monocrystalline silicon–an advanced nanoindentation study", *Materials & Design*, vol. 233, p. 112 198, 2023.

[40] J. Kappacher, O Renk, D. Kiener, H. Clemens, and V. Maier-Kiener, "How grain boundary characteristics influence plasticity close to and above the critical temperature of ultra-fine grained bcc ta2. 5w", *Acta materialia*, vol. 216, p. 117 110, 2021.

[41] J. Wheeler and J Michler, "Elevated temperature, nano-mechanical testing in situ in the scanning electron microscope", *Review of Scientific Instruments*, vol. 84, no. 4, 2013.

[42] W. C. Oliver and G. M. Pharr, "An improved technique for determining hardness and elastic modulus using load and displacement sensing indentation experiments", *Journal of materials research*, vol. 7, no. 6, pp. 1564–1583, 1992.

[43] S. B. Brown, K. H. Kim, and L. Anand, "An internal variable constitutive model for hot working of metals", *International Journal of Plasticity*, vol. 5, pp. 95–130, 1989.

[44] L. Anand, "Constitutive equations for the rate-dependent deformation of metals at elevated temperatures", *Journal of Engineering Materials and Technology*, vol. 104, pp. 12–17, 1982.

[45] M. Neumann *et al.*, "On a pluri-gaussian model for three-phase microstructures, with applications to 3d image data of gas-diffusion electrodes", *Computational Materials Science*, vol. 156, pp. 325–331, 2019.

[46] X. Long *et al.*, "Phase field fracture modeling of mechanical degradation and crack propagation in random porous sintered nano-silver with thermal and strain-rate effects", *Engineering Fracture Mechanics*, p. 110 753, 2024.

[47] A. A. Griffith, "Vi. the phenomena of rupture and flow in solids", *Philosophical transactions of the royal society of london. Series A, containing papers of a mathematical or physical character*, vol. 221, no. 582-593, pp. 163–198, 1921.

[48] S. Waseem, C. Erdogan, and T. Yalçinkaya, "Phase field modeling of fatigue crack growth retardation under single cycle overloads", *International Journal of Fatigue*, vol. 179, p. 108 064, 2024.

[49] B. Bahrami, H. Ahmadian, M. R. Mehraban, and M. R. Ayatollahi, "Mixed-mode fracture prediction of notched components using phase-field approach", *International Journal of Solids and Structures*, vol. 306, p. 113 113, 2025.

[50] C. Miehe, M. Hofacker, and F. Welschinger, "A phase field model for rate-independent crack propagation: Robust algorithmic implementation based on operator splits", *Computer Methods in Applied Mechanics and Engineering*, vol. 199, no. 45-48, pp. 2765–2778, 2010.

[51] H. Amor, J.-J. Marigo, and C. Maurini, "Regularized formulation of the variational brittle fracture with unilateral contact: Numerical experiments", *Journal of the Mechanics and Physics of Solids*, vol. 57, no. 8, pp. 1209–1229, 2009.

[52] F. Freddi and G. Royer-Carfagni, "Regularized variational theories of fracture: A unified approach", *Journal of the Mechanics and Physics of Solids*, vol. 58, no. 8, pp. 1154–1174, 2010.

[53] F. Freddi and G. Royer-Carfagni, "Variational fracture mechanics to model compressive splitting of masonry-like materials", *Annals of Solid and Structural Mechanics*, vol. 2, pp. 57–67, 2011.

[54] Y.-S. Lo, M. J. Borden, K Ravi-Chandar, and C. M. Landis, "A phase-field model for fatigue crack growth", *Journal of the Mechanics and Physics of Solids*, vol. 132, p. 103 684, 2019.

[55] Y. Navidtehrani, C. Betegon, and E. Martinez-Paneda, "A general framework for decomposing the phase field fracture driving force, particularised to a drucker–prager failure surface", *Theoretical and Applied Fracture Mechanics*, vol. 121, p. 103 555, 2022.

[56] Y. Navidtehrani, C. Betegón, and E. Martínez-Pañeda, "A simple and robust abaqus implementation of the phase field fracture method", *Applications in Engineering Science*, vol. 6, p. 100 050, 2021.

[57] Y. Navidtehrani, C. Betegón, and E. Martínez-Pañeda, "A unified abaqus implementation of the phase field fracture method using only a user material subroutine", *Materials*, vol. 14, no. 8, p. 1913, 2021.

[58] C. G. Dengiz and M. Dorduncu, "A unified phase-field approach for failure prediction in modulus graded adhesively bonded single-lap joints", *Theoretical and Applied Fracture Mechanics*, vol. 127, p. 104 062, 2023.

[59] J. Suryawanshi, G. Singh, S. Msolli, M. H. Jhon, and U. Ramamurty, "Tension-compression asymmetry and shear strength of titanium alloys", *Acta Materialia*, vol. 221, p. 117 392, 2021.

[60] J. Zhao *et al.*, "Strain rate effects on the mechanical behavior of porous titanium with different pore sizes", *Materials Science and Engineering: A*, vol. 821, p. 141 593, 2021.

[61] A Kodam, M. Gundi, Y. Chiu, I. Jones, S. Singh, and J Jain, "A review of challenges and opportunities in micropillar compression studies in mg alloys", *Journal of Magnesium and Alloys*, 2023.

[62] H. Jones, V. Tong, R. Ramachandramoorthy, K. Mingard, J. Michler, and M. Gee, "Micropillar compression of single crystal tungsten carbide, part 1: Temperature and orientation dependence of deformation behaviour", *International Journal of Refractory Metals and Hard Materials*, vol. 102, p. 105 729, 2022.

[63] M. Nasim, Y. Li, and C. Wen, "Length-scale dependent deformation, strengthening, and ductility of fcc/fcc ni/al nanolaminates using micropillar compression testing", *Acta Materialia*, vol. 193, pp. 318–328, 2020.

[64] S Lotfian, M Rodríguez, K. Yazzie, N. Chawla, J Llorca, and J. M. Molina-Aldareguía, "High temperature micropillar compression of al/sic nanolaminates", *Acta Materialia*, vol. 61, no. 12, pp. 4439–4451, 2013.

[65] C. Shih, M. Meyers, and V. Nesterenko, "High-strain-rate deformation of granular silicon carbide", *Acta materialia*, vol. 46, no. 11, pp. 4037–4065, 1998.

[66] M. S. Khorrami, N Saito, Y Miyashita, and M Kondo, "Texture variations and mechanical properties of aluminum during severe plastic deformation and friction stir processing with sic nanoparticles", *Materials Science and Engineering: A*, vol. 744, pp. 349–364, 2019.

[67] Y. Ma, X. Wang, Z. Dong, P. Ni, Z. Li, and H. Liu, "Microstructure and mechanical performance of nickel coating on copper sheet via laser shock processing", *Applied Surface Science*, vol. 592, p. 153 366, 2022.

[68] Y. T. Zhu and T. G. Langdon, "Influence of grain size on deformation mechanisms: An extension to nanocrystalline materials", *Materials Science and Engineering: A*, vol. 409, no. 1-2, pp. 234–242, 2005.

[69] R. Chang, Q. Guo, Z. Ma, R. Ding, C. Liu, and Y. Liu, "Kinetics of voids evolution during diffusion bonding of dissimilar metals on consideration of the realistic surface morphology: Modeling and experiments", *Acta Materialia*, vol. 276, p. 120 121, 2024.

[70] R. Yuan, I. J. Beyerlein, and C. Zhou, "Emergence of grain-size effects in nanocrystalline metals from statistical activation of discrete dislocation sources", *Acta Materialia*, vol. 90, pp. 169–181, 2015.

[71] T Al-Samman and G Gottstein, "Dynamic recrystallization during high temperature deformation of magnesium", *Materials Science and Engineering: A*, vol. 490, no. 1-2, pp. 411–420, 2008.

[72] C. Cui *et al.*, "Dynamic recrystallization and deformation model of β-quenched zr-4 alloy subjected to elevated temperature compression", *Materials Science and Engineering: A*, vol. 849, p. 143 472, 2022.

[73] R. B. Figueiredo, S. Sabbaghianrad, A. Giwa, J. R. Greer, and T. G. Langdon, "Evidence for exceptional low temperature ductility in polycrystalline magnesium processed by severe plastic deformation", *Acta Materialia*, vol. 122, pp. 322–331, 2017.

[74] F. Yan, N. Tao, F Archie, I. Gutiérrez-Urrutia, D. Raabe, and K. Lu, "Deformation mechanisms in an austenitic single-phase duplex microstructured steel with nanotwinned grains", *Acta Materialia*, vol. 81, pp. 487–500, 2014.

[75] C. Chen and K. Suganuma, "Microstructure and mechanical properties of sintered ag particles with flake and spherical shape from nano to micro size", *Materials & Design*, vol. 162, pp. 311–321, 2019.

5

Interface Strength and Crack Propagation Mechanisms in Sintered Copper Nanoparticles

This study investigates the interface strength and fracture behavior of sintered copper (Cu) nanoparticles (NPs) for all-Cu integration in advanced microelectronics packaging. Micro-cantilever bending tests on three configurations (Cu NP-notched, interface-notched and un-notched micro-cantilevers) were analyzed using scanning electron microscopy (SEM), transmission electron microscopy (TEM), transmission Kikuchi diffraction (TKD) and cohesive zone model (CZM). The interface-notched micro-cantilevers demonstrate superior fracture resistance, with a stress intensity factor (K_Q) of 2.88 ± 0.10 MPa·m$^{1/2}$*, compared to* 2.12 ± 0.11 MPa·m$^{1/2}$ *for Cu NP-notched micro-cantilevers. Simulation results, consistent with experimental results, reveal that Cu NP-notched micro-cantilevers exhibit lower fracture resistance due to porosity and stress concentrations, while interface-notched micro-cantilevers show enhanced strength, attributed to robust bonding and reduced void distribution. Un-notched micro-cantilevers display superior load-bearing capacity, with cracks bypassing the interface and propagating through porous regions. Moreover, in un-notched micro-cantilevers, a synergistic deformation mechanism is observed, where crack propagation through the sintered Cu NPs coexists with plastic slip deformation in the Cu substrate. These findings highlight the strong interfacial bonding and effective stress transfer at the Cu substrate-sintered Cu NP interface, validating the feasibility of direct sintering using Cu NPs without additional coatings.*

Parts of this chapter have been published in Acta Materialia, 2025 [1].

5.1. Introduction

All-copper (Cu) integration utilizing Cu nanoparticles (NPs) has emerged as a promising technology for both advanced 3D integration [2–5] and power electronics packaging [6–8]. In 3D integration, direct Cu-to-Cu bonding with sub-10 µm offers superior interconnect density and enhanced electromigration resistance compared to conventional solder-based interconnects [9–11]. However, traditional bulk Cu bonding necessitates high temperatures (>300°C) and and substantial pressures, which pose risks of dielectric layer degradation, particularly in large-scale applications. In contrast, Cu NPs-based bonding enables scalable integration at significantly reduced thermal budgets (160–250°C) and pressures through nanoscale sintering. Recent studies [3, 5] indicate that Cu NPs achieve robust mechanical strength (60 MPa) without requiring costly chemical mechanical polishing (CMP), outperforming conventional thermocompression bonding in process scalability and surpassing solder-based joints in thermal stability. Furthermore, direct sintering using Cu NPs onto a Cu substrate obviate the requirement for silver (Ag) or nickel (Ni) coating layers in power electronics packaging, offering comparable adhesion performance while reducing material costs [12, 13]. Despite these advantages, the large-scale industrial implementation of all-Cu integration using Cu NPs remains limited due to insufficient quantitative data on their interfacial reliability, particularly at the microscale level. This study addresses this critical gap by employing micro-cantilever bending tests to quantitatively assess interface strength, elucidating fracture behaviors that are essential for real-world packaging applications.

Micro-cantilever bending tests have become a widely used technique for evaluating interface strength and fracture toughness at the microscale, providing critical insights into localized deformation and failure mechanisms [14–23]. These tests are particularly effective for probing material interfaces due to their ability to simulate stress states involving both tensile and compressive loading, making them ideal for quantifying interfacial adhesion and mechanical reliability. For example, Matoy et al. [14] applied micro-cantilever bending tests to investigate the fracture behavior of thin-film interfaces, successfully determining energy release rates and critical stress intensities for SiO_2-metal interfaces. Heuer et al. [22] extended this approach to functionally graded materials, demonstrating its applicability for characterizing fracture toughness in heterogeneous systems. Additionally, Armstrong et al. [24] employed micro-cantilever tests to evaluate embrittled grain boundaries in Cu, showcasing its utility in detecting localized failure mechanisms.

Despite these advancements, studies on sintered Cu NPs remain limited. Extensive research has focused on in-situ tensile tests [25, 26], micro-pillar compression tests [27] and micro-cantilever bending tests [28, 29] to investigate the mechanical properties and deformation mechanisms of sintered silver (Ag) and Cu NPs. These studies have provided valuable insights into viscoplasticity, creep behavior and microstructural evolution under loading. However, they have largely overlooked the interface strength of Cu NPs, particularly under bending conditions, leaving a critical gap in the understanding of interfacial fracture mechanisms. Liu et al. [30] examined Cu-Cu joints fabricated via low-temperature sintering of Cu NPs and highlighted the role of metallurgical bonding and sintered neck formation in enhancing mechanical strength. While their work primarily focused on bulk shear strength, quantitative characterization of localized interfacial

fracture properties remains unexplored. This gap in the literature motivates the present study, which aims to provide a detailed understanding of the mechanical reliability and fracture behavior of sintered Cu NPs and their interfaces using micro-cantilever bending tests. These insights are critical for advancing all-Cu integration technologies in microelectronics and structural applications.

Crack propagation in sintered NPs is critically influenced by pore distribution, grain boundaries, and microstructural heterogeneities. Consequently, computational modeling of fracture in such systems necessitates methods capable of resolving complex crack paths while accounting for material stochasticity. To address this challenge, several approaches have been developed, including phase-field fracture model [31–38], extended finite element method (XFEM) [39–43], discrete element method (DEM) [44–47], and the cohesive zone model (CZM) [48–51]. Phase-field fracture model, which represent cracks as diffuse interfaces via energy minimization principles, excel in simulating arbitrary crack nucleation, branching, and coalescence in heterogeneous media—a key feature for sintered NPs with stochastic porosity [52]. However, phase-field model lacks explicit interface elements, limiting their ability to simulate interfacial failure propagation [53, 54]. XFEM supports discrete crack growth without remeshing and incorporates plasticity, making it suitable for ductile fracture analysis [39]. Nonetheless, its reliance on predefined enrichment functions limits its applicability in systems with unpredictable crack paths [55], and it faces difficulties in modeling crack branching and merging due to the need for explicit geometric representation of discontinuities [56]. DEM, ideal for granular fragmentation and flow simulations, struggles with continuum-scale stress field resolution and thermo-elasto-plastic coupling, compounded by prohibitive computational costs for large-scale microstructures [57]. In contrast, CZM are particularly well-suited for simulating interfacial crack propagation in sintered Cu NPs, as they explicitly model decohesion at material interfaces through traction-separation laws [49, 50]. This approach enables precise modeling of interface failure mechanisms, addressing critical gaps in phase-field and XFEM frameworks for heterogeneous systems with complex interfacial interactions.

This study investigates the interface strength and fracture behavior of sintered Cu NPs to assess their potential for all-Cu integration in advanced microelectronic applications. Micro-cantilever bending tests are conducted to evaluate localized deformation and fracture toughness at the interface, highlighting its critical role in ensuring mechanical reliability. Detailed microstructure characterization using scanning electron microscopy (SEM), transmission electron microscopy (TEM) and transmission Kikuchi diffraction (TKD) reveals the influence of sintered neck formation and porosity on stress transfer and crack resistance. Furthermore, CZM is employed to simulate crack propagation and stress distributions, providing insights into damage evolution and interface defects. These findings offer a deeper understanding of the mechanical behavior and reliability of sintered Cu interfaces, supporting the development of all-Cu integration for next-generation microelectronics.

5.2. EXPERIMENTAL AND SIMULATION METHOD

5.2.1. MICRO-CANTILEVER FABRICATION

A die-attach structure, consisting of an aluminum (Al) film, a sintered Cu nanoparticle (NP) layer and a Cu substrate was fabricated using pressure-assisted sintering technology [58]. First, the Cu NP paste was uniformly printed onto a Cu substrate using an automatic screen-printing system and a steel stencil with a thickness of 100 µm (Fig. 5.1a). Then, the printed paste was dried in a nitrogen atmosphere at 120°C for 5 minutes to remove organic solvents. Subsequently, an Al film was applied to the surface of the dried Cu paste to substitute the Cu dummy die, facilitating its removal after the sintering process. Pressure-assisted sintering (Fig. 5.1b) was performed at 250°C under 20 MPa uniaxial stress for 5 minutes in a reducing atmosphere (5% H_2/N_2). After sintering, the samples were cooled to room temperature before removing the Al film and sectioning the samples along the centerline using a diamond saw (Fig. 5.1c). The sintered samples were then prepared for micro-cantilever fabrication.

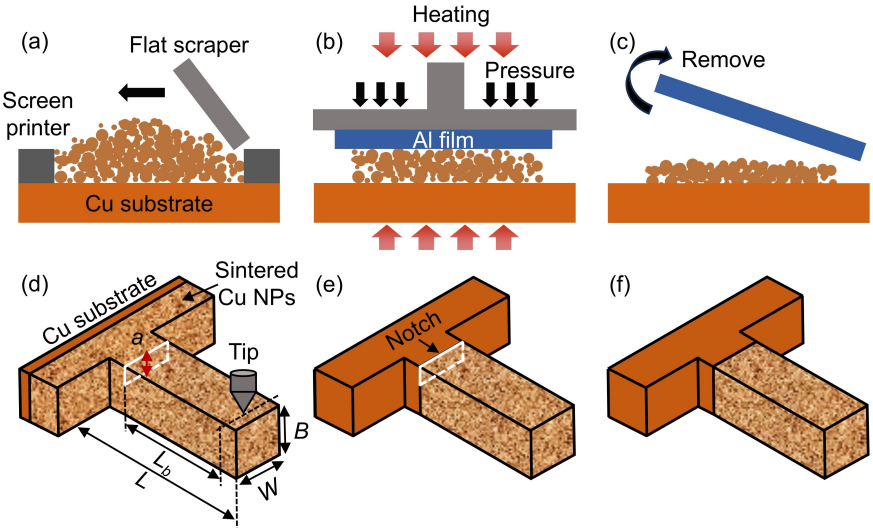


Figure 5.1: Sintering process: (a) screen printing; (b) pressure-assisted sintering; (c) removal of the Al film. Schematic of micro-cantilevers: (d) Cu NP-notched micro-cantilever; (e) interface-notched micro-cantilever; (f) un-notched micro-cantilever.

Micro-cantilever bending tests provide an effective approach for probing the microscale mechanical properties of sintered Cu NPs. Figs. 5.1d-f illustrates the design and fabrication of three types of micro-cantilevers (Cu NP-notched, interface-notched and un-notched) used in this study. These micro-cantilevers were designed to investigate fracture behavior under different conditions, with each configuration targeting specific material interfaces and regions of interest. In Fig. 5.1d, the first micro-cantilever is fabricated entirely within the sintered Cu NP region and includes a notch at the base of the cantilever to assess crack initiation and propagation. The geometric parameters, including length (L), width (W), height (B), and length of notch/interface to nanoindenter (L_b),

along with the notch length (a), were carefully controlled during fabrication to ensure consistency. Fig. 5.1e shows the second configuration, where the micro-cantilever spans the interface between the sintered Cu NPs and the Cu substrate. A notch was introduced at the interface to investigate the interfacial strength and crack propagation behavior. Fig. 5.1f illustrates the third configuration, which also spans the Cu NP–substrate interface but without a notch, enabling the evaluation of intrinsic material deformation and failure mechanisms without pre-existing flaws. The micro-cantilevers were fabricated using a focused ion beam (FIB) milling process. The fabrication steps involved milling U-shaped trenches, tilting and rotating for undercutting, polishing for symmetry, and final cleaning to reduce damage [59].

5.2.2. MICRO-CANTILEVER BENDING TESTS

Micro-cantilever bending tests were conducted at room temperature using an in-situ nanoindenter system (Alemnis AG, Switzerland) integrated into a Zeiss Ultra55 FEG-SEM (Fig. 5.2a)[60]. Representative SEM images of the three micro-cantilevers are presented in Figs. 5.2b–d. Prior to testing, the SEM was employed to precisely align the indenter tip with the fiducial mark located on the top surface of each micro-cantilever. The bending tests were conducted in displacement-controlled mode, maintaining a constant displacement rate of 10 nm s^{-1} for all specimens. The tests proceeded until fracture was observed, ensuring consistent testing conditions. A conospherical diamond tip (radius = 1 µm) was utilized to apply the bending load, as shown. Compared to sharp-tipped indenters, such as the Berkovich indenter, the conical geometry with a spherical tip was selected to minimize stress concentrations and reduce indentation-induced surface damage, thereby improving the accuracy of mechanical property measurements [17]. The nanoindenter system provided high-resolution displacement tracking with drift rates maintained below 10 nm/min, enabling reliable acquisition of load-displacement data. Throughout the experiments, synchronized video recordings and SEM image sequences were captured to continuously monitor the deformation process, facilitating correlation between the applied displacement, measured load and the progression of crack initiation and propagation. This experimental setup ensured precise measurements of mechanical behavior while minimizing artifacts associated with tip geometry and system drift.

5.2.3. 3D RECONSTRUCTION

To investigate the internal microstructure of sintered Cu NPs, FIB-SEM tomography was performed using a dual-beam FEI Helios G4 CX system [61]. Prior to milling, a protective Pt layer (1 µm thick) was deposited over the region of interest (ROI), and fiducial markers were fabricated to ensure precise alignment during sequential milling (Fig. 5.3a). The sample was tilted to 52° to enable perpendicular FIB milling at 30 kV and 40 pA, while SEM imaging was conducted at 10 kV using a secondary electron detector. A U-shaped trench was milled adjacent to the ROI to accommodate redeposited material. Automated slicing and imaging were controlled via Auto Slice and View software, generating 15 nm-thick cross-sectional slices. Approximately 300 high-resolution SEM images were acquired (Fig. 5.3b), and processed using Avizo software for 3D reconstruction [62]. Image alignment and threshold-based segmentation revealed porous regions (highlighted in

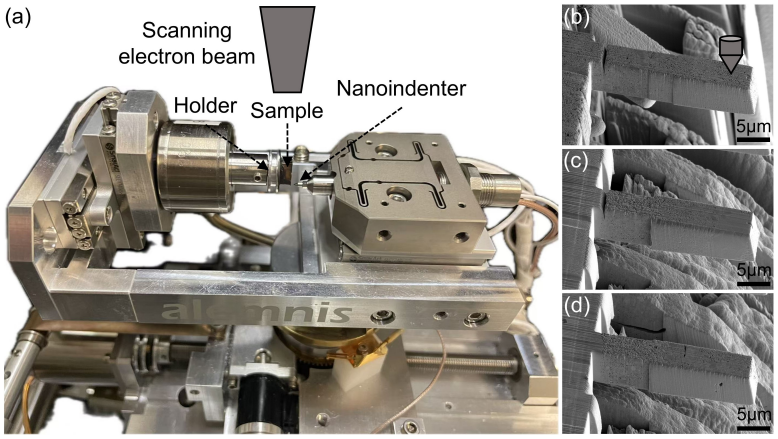


Figure 5.2: (a) In-situ SEM setup with indenter; (b-d) representative SEM images of Cu NP-notched micro-cantilever, interface-notched micro-cantilever, and un-notched micro-cantilever, respectively.

5

blue, Fig. 5.3c), with a calculated porosity of approximately 10.5%. The reconstructed volume of $6 \times 3.5 \times 4$ μm³ (Fig. 5.3d) effectively captured the sintered Cu NP domain and void distribution, demonstrating sufficient representativeness to resolve microstructural features.

5.2.4. TEM AND TKD CHARACTERIZATION

The localized deformation behavior and grain orientation of sintered Cu NPs were characterized using TEM (Cs-corrected Titan Themis) and TKD (Zeiss GeminiSEM 360 and Hitachi Regulus8230). TKD was prioritized over conventional electron backscatter diffraction (EBSD) due to its enhanced spatial resolution (5 nm), sensitivity to weak crystallographic signals, and compatibility with ultrathin specimens—critical advantages for resolving nanocrystalline microstructures [63, 64]. This technique enabled precise mapping of grain orientations and strain distributions in both as-sintered and deformed interfacial regions, providing insights into plasticity mechanisms at the nanoscale.

5.2.5. RANDOM POROUS STRUCTURE MODELING

The porous structures of sintered Cu NPs exhibit inherent randomness in pore size, shape and distribution due to particle rearrangement and coalescence during the sintering process. From a microstructural perspective, sintered Cu NPs can be conceptually represented as a two-phase solid system comprising metallic particles and distributed pores [65]. Accurate modeling of random porous structures is essential for capturing the stochastic characteristics of sintered Cu NPs. To accurately capture this stochastic nature, a Gaussian Random Field (GRF)-based approach was employed to simulate the two-dimensional microstructures [37, 38, 66–68]. The GRF method effectively models spatial heterogeneity by defining a random field $Z(x)$ through a mean function $m(x)$ and a covariance function $C(x_1, x_2)$. In this study, the mean function was set to zero ($m(x) = 0$) to ensure spatial neutrality, while an exponential covariance function con-

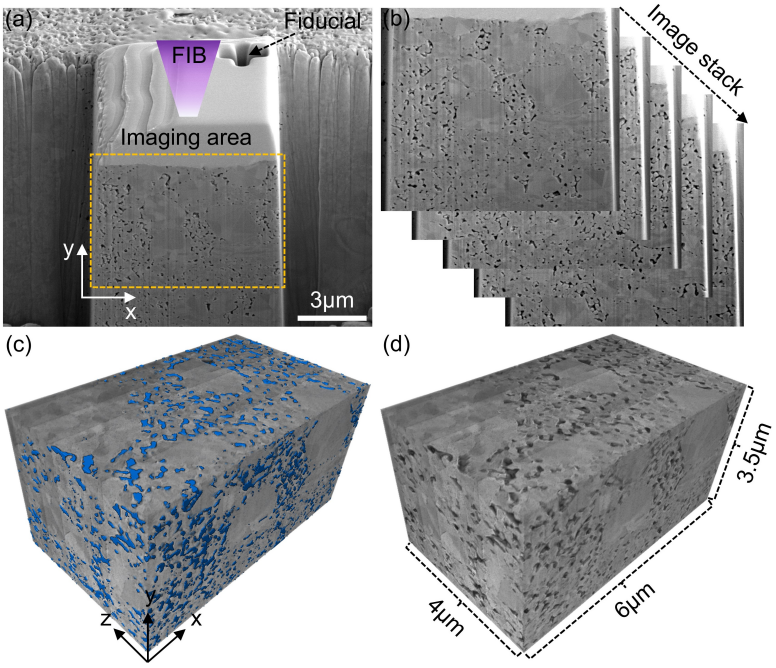


Figure 5.3: (a) FIB milling of the sample with a protective Pt layer deposited; the imaging area is indicated; (b) sequential SEM cross-sections forming an image stack for 3D reconstruction; (c) reconstructed volume highlighting porous regions (blue); (d) sintered Cu NP domain with dimensions.

trolled the spatial correlation of the random field. The covariance function is expressed as:

$$C(x_1, x_2) = \sigma^2 \exp\left(-\frac{\|x_1 - x_2\|}{l}\right), \tag{5.1}$$

where σ^2 represents the variance and l determines the correlation length. A threshold function F_0 was applied to classify the GRF values into solid and pore phases, enabling direct control over porosity. The indicator function $\Psi(x)$ used to separate the phases is given by:

$$\Psi(x) = \begin{cases} 1, & Z(x) \geq F_0, \\ 0, & Z(x) < F_0, \end{cases} \tag{5.2}$$

This probabilistic framework allowed the generation of pore distributions that closely resemble the experimental microstructures observed in SEM and TEM analyses of sintered Cu NPs. The computational implementation of the GRF model was performed on a 2D square domain of size 160×760 with fine grid discretization to ensure spatial accuracy. Initially, random values following a Gaussian distribution were assigned to each grid point. Gaussian smoothing was then applied to introduce spatial correlations, with the kernel width and correlation length calibrated to control pore size distributions. The smoothed field was converted into binary solid and pore regions us-

ing a threshold function, and the resulting structures were meshed to facilitate mechanical simulations (Figs. 5.4b-d). This process enabled precise adjustments to porosity and morphology, matching experimental observations.

5.2.6. COHESIVE ZONE MODEL

In this study, the crack propagation behavior of sintered Cu NPs was simulated using a classical bilinear traction-separation law within the Cohesive Zone Model (CZM) framework [49, 69], as illustrated in Fig. 5.4a. The constitutive relation is characterized by two critical displacement parameters: the critical separation displacement (δ_c), corresponding to the peak traction ($\tau_{\max}$), and the ultimate failure separation displacement (δ_t). The critical fracture energy, equivalent to the area under the traction-separation curve, serves as a fundamental parameter governing material failure. For the pure mode I fracture conditions examined here, the cohesive zone response is defined exclusively by $\tau_{\max}$ and δ_t. This simplification arises from the assumption of a constant tangent stiffness (k_1) during the elastic loading phase prior to damage initiation, ensuring a bilinear constitutive response without additional variables influencing the pre-failure regime. k_1 and k_2 are the interface stiffness which are computed as $k_1 = \tau_{\max}/\delta_c$ and $k_2 = \tau_{\max}/(\delta_t - \delta_c)$.

$$\tau(\delta) = \begin{cases} k_1\delta & 0 \le \delta \le \delta_c \\ k_2(\delta - \delta_t) & \delta_c \le \delta < \delta_t \\ 0 & \delta \ge \delta_t \end{cases} \tag{5.3}$$

As shown in Figs. 5.4b-d, 2D models with randomly distributed pores is used to simulate the mechanical properties and fracture behaviour. The dimension of the model is 4.8 µm × 22.5 µm with quadrilateral elements of 0.03 µm × 0.03 µm. The green regions correspond to the Cu material, while the white regions represent voids, simulating the porosity inherent in the material after sintering. Fig. 5.4b-d shows the three finite element mesh (4 nodes CPS4) structures, namely, Cu NP-notched, interface-notched and un-notched micro-cantilevers. The initial crack length of the notched micro-cantilevers was set as 2 µm. Bend loading was applied along the right edge (denoted by directional arrows) to simulate bending stress conditions. The mechanical properties for our simulations were directly extracted from the experimental stress-strain curves presented in Fig. 5.5b.

5.3. RESULTS AND DISCUSSION

5.3.1. MECHANICAL PROPERTIES

Fig. 5.5a presents the load–displacement curves for the micro-cantilevers. The experimentally recorded loading and displacement data of un-notched micro-cantilevers can be transformed into bending stress and bending strain, respectively, through the following equations [70–72]:

$$\sigma = \frac{4 \cdot F \cdot L_b}{W \cdot B^2} \tag{5.4}$$

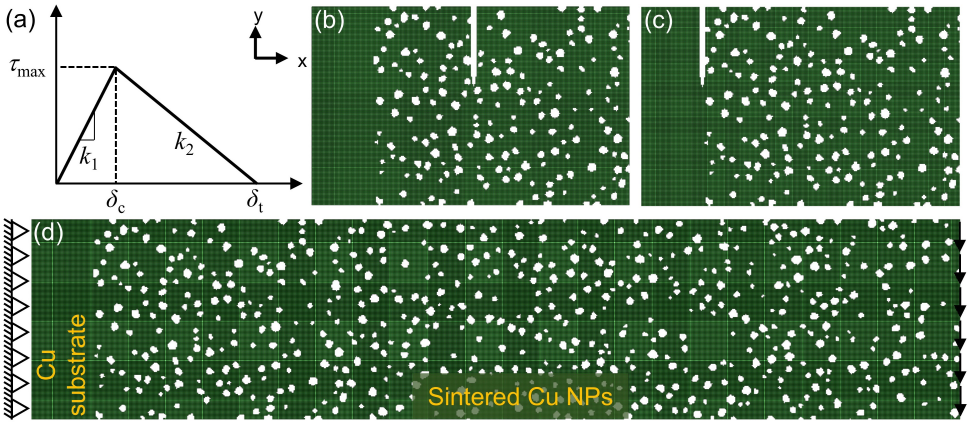


Figure 5.4: (a) Typical bilinear law of CZM; (b) Cu NP-notched model; (c) interface-notched model; (d) un-notched model with boundary conditions.

5

$$\varepsilon = \frac{3 \cdot B \cdot u}{2 \cdot L_b^2} \tag{5.5}$$

where F, L_b, W and B denote the applied force, moment arm, beam width and thickness, respectively. The corresponding stress–strain curves are shown in Fig. 5.5b. The measured elastic modulus of approximately 54 ± 2.4 GPa is consistent with values reported for sintered NPs [29] but lower than those observed in Cu thin films and single-crystal Cu micro-cantilevers [73, 74]. Similarly, the yield stress, determined via the 0.2% offset criterion [71] to be 639 ± 29 MPa, agrees well with prior micro-cantilever bending studies on sintered Cu NPs [29]. In contrast, this value exceeds reported yield strengths for bulk Cu—derived from micro-cantilever bending [75], compression [76], and shear tests [77], which typically range from 180 to 350 MPa, depending on grain size and crystallographic orientation.

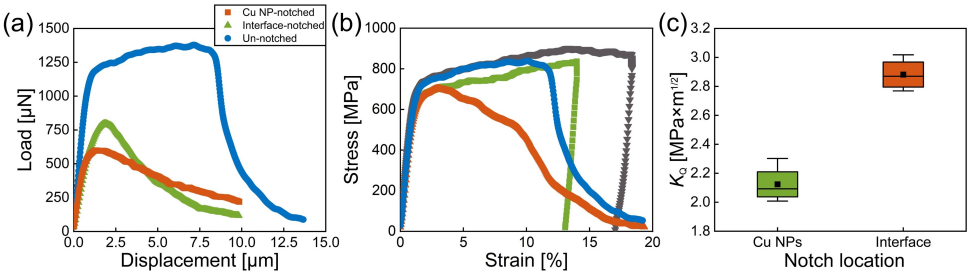


Figure 5.5: (a) Load-displacement curves; (b) stress-strain curves of un-notched micro-cantilevers; (c) stress intensity factors.

As illustrated in Fig. 5.5a, interface-notched micro-cantilevers exhibit superior mechanical performance to those NP-notched micro-cantilevers, suggesting enhanced interfacial integrity and crack propagation resistance at the interface. To quantitatively

evaluate the fracture resistance, the stress intensity factor K_Q (conditional fracture toughness) was computed based on linear elastic fracture mechanics (LEFM) in mode I [28, 78].

$$K_Q = \frac{FL_b}{W \cdot B^{3/2}} \cdot f\left(\frac{a}{B}\right) \tag{5.6}$$

The geometry factor f was derived as a function of crack length and micro-cantilever height, utilizing finite element (FE) modeling data provided by Iqbal et al. [79]. This analysis standardizes the load-displacement data, enabling direct comparison of fracture behavior across different micro-cantilever configurations. As shown in Fig. 5.5f, the stress intensity factor for NP-notched micro-cantilevers is approximately 2.12 ± 0.11 MPa·m$^{1/2}$, which is notably lower than the 2.88 ± 0.10 MPa·m$^{1/2}$ measured for interface-notched micro-cantilevers.

The disparity in K_Q values highlights the superior crack resistance at the Cu substrate-Cu NP interface, which serves as a more effective barrier to crack propagation compared to the sintered Cu NPs. These findings strongly support the feasibility of all-Cu integration, as the superior interface strength ensures improved mechanical reliability. To investigate the strengthening mechanisms underlying the interfacial fracture toughness of the sintered Cu NPs, crack propagation and localized deformation mechanism were systematically analyzed in next parts.

5.3.2. FRACTURE ANALYSIS

Fig. 5.6 delineates the fracture mechanisms of the three micro-cantilever configurations subjected to bending. In notched specimens (Figs. 5.6a, b, d and e), crack propagation preferentially follows the sintered Cu NPs, evidenced by elongated sintering necks—a hallmark of ductile fracture. Notably, interface-notched micro-cantilevers exhibit a higher critical stress intensity factor (2.88 ± 0.10 MPa·m$^{1/2}$) than those NP-notched micro-cantilevers (2.12 ± 0.11 MPa·m$^{1/2}$). This disparity stems from microstructural heterogeneity: NP-notched micro-cantilevers (Figs. 5.6a, d) display elevated porosity distribution near the notch tip than interface-notched micro-cantilevers. Increased porosity amplifies localized stress concentrations, reducing fracture resistance and accelerating crack propagation through the porous NP matrix.

Un-notched micro-cantilevers (Figs. 5.6c, f) further validate this mechanism. Crack paths deviate from the Cu-substrate interface, instead propagating through the sintered Cu NPs. This deflection underscores the dominance of stress concentrations within the porous NP layer over interfacial adhesion, confirming the sintered NPs' lower cohesive strength compared to the monolithic Cu substrate. Complementary schematics (Figs. 5.6g–i) illustrate how porosity governs crack initiation and growth, with stress concentrations nucleating at high-porosity regions and propagation modulated by the sintered network's tortuosity. These findings emphasize the critical role of microstructural defects in dictating fracture resistance in hierarchical systems.

Figs. 5.7a and b reveals a synergistic deformation mechanism in un-notched micro-cantilevers, where crack propagation through the sintered Cu NPs coexists with plastic slip deformation in the Cu substrate. The substrate (Fig. 5.7a) exhibits distinct slip bands, indicative of dislocation glide under tensile bending stresses. Concurrently, the

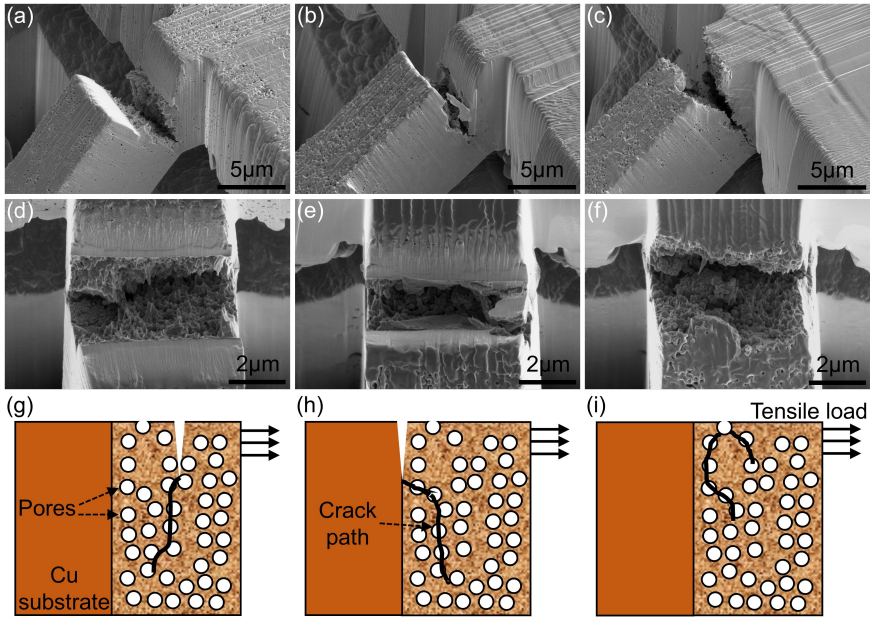


Figure 5.6: Fracture morphology and crack propagation in sintered Cu NP micro-cantilevers: (a, d) NP-notched; (b, e) interface-notched; (c, f) un-notched specimens. (g-i) Schematics of corresponding crack propagation mechanisms.

NP layer (Fig. 5.7b) undergoes crack propagation preceded by localized plastic deformation, evidenced by elongated sintering necks. This dual behavior highlights mechanical compatibility: the substrate accommodates strain via crystallographic slip, while the NP layer redistributes stress through ductile neck elongation prior to fracture.

The absence of interfacial delamination confirms robust bonding between the NPs and substrate. However, fracture localization within the NP layer demonstrates that residual porosity and microstructural heterogeneities (e.g., incomplete sintering necks) act as preferential stress concentrators, overriding the interfacial adhesion strength. This underscores the sintered Cu NPs' role as the performance-limiting phase, constrained by their inherent porosity. The coexistence of substrate plasticity and NP-layer cracking further suggests that sintering parameters must be optimized to enhance neck connectivity, thereby improving load-transfer efficiency without compromising interfacial integrity.

5.3.3. INTERFACIAL DEFORMATION MECHANISMS

To elucidate the microstructural and interfacial deformation mechanisms in sintered Cu NP systems, a correlative analysis was conducted using TEM and TKD. Investigations were focused on two representative regions: an undeformed interface, and a deformed interface located at the root of a bent micro-cantilever (Figs. 5.7c, d). TKD mapping of the undeformed region (Figs. 5.8a, b) revealed a randomized grain orientation distribution within the sintered Cu NPs, indicative of the absence of preferential crystallographic alignment. This structural randomness, coupled with a minimal presence of interfacial

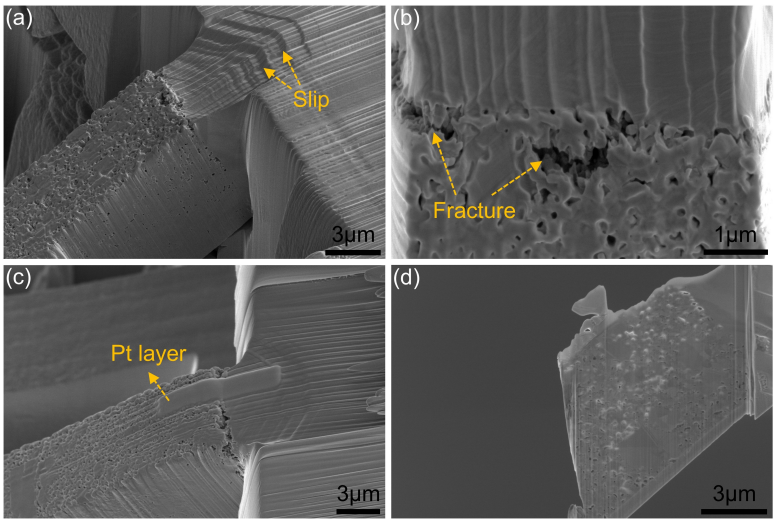


Figure 5.7: Deformation behavior of un-notched micro-cantilevers: (a, b) Crack propagation through sintered Cu NPs with concurrent slip deformation in Cu substrate; (c) TEM sample preparation location; (d) fabricated TEM sample.

voids or discontinuities, suggests the formation of robust metallurgical bonding between the sintered NPs and the underlying Cu substrate.

Post-deformation analyses of the interfacial region (Figs. 5.8c, d) reveal substantial microstructural reorganization within the NP layer. Bright-field TEM imaging (Fig. 5.8c) confirms the occurrence of localized plastic deformation, manifested by the elongation of sintering necks. This morphological evolution is attributed to stress concentrations facilitated by the intrinsic porosity of the sintered network. Simultaneously, the appearance of slip bands within the Cu substrate (Fig. 5.8c) reflects the activation of dislocation glide, a primary plastic deformation mechanism in face-centered cubic (FCC) metals subjected to tensile stress [80, 81]. The corresponding TKD map (Fig. 5.8d) illustrates a heterogeneous grain structure, characterized by a mixture of equiaxed and elongated nanograins, along with deformation-induced lattice distortions that adversely affect diffraction pattern quality. These distortions—likely stemming from dislocation tangles and residual stress accumulation—complicate orientation indexing and highlight the intrinsic difficulty of characterizing highly strained microstructures.

Importantly, deformation twinning was observed in the substrate (Figs. 5.8c, d), signifying the activation of secondary plastic deformation mechanisms under bending stress. Despite the evident plasticity and microstructural evolution within the sintered NP layer, the integrity of the particle–substrate interface remained preserved. These results emphasize the necessity of optimizing sintering parameters—such as the application of external pressure during processing—to reduce porosity, enhance interparticle neck growth, and ultimately improve the mechanical load-bearing performance of the sintered NP layer without compromising interfacial cohesion.

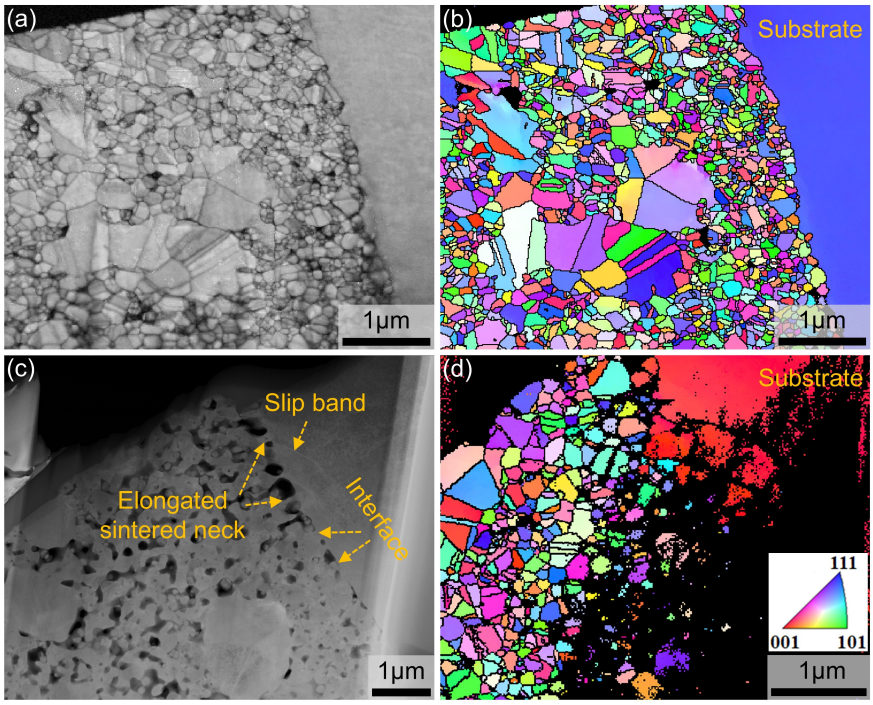


Figure 5.8: Grain orientation analysis of sintered Cu NPs at the interface: (a) TKD band contrast map showing pattern quality; (b) initial grain orientation map; (c) bright-field TEM image of deformed region with slip bands and elongated sintered necks; (d) post-deformation grain orientation map.

5.3.4. NUMERICAL SIMULATION OF CRACK PROPAGATION

Fig. 5.9 illustrates the load-displacement responses obtained from the simulation, highlighting the influence of notch location. For Cu NP-notched micro-cantilevers, the load-displacement curve demonstrates a significantly lower peak value. In contrast, interface-notched micro-cantilevers exhibits higher strength due to fewer voids, indicating that interface bonding plays a crucial role in mechanical integrity. The un-notched micro-cantilevers achieve the highest load values. These findings align well with experimental results presented in Fig. 5.5, confirming the influence of void distribution and notch location on strength.

Fig. 5.10 provides a detailed view of crack propagation path and von Mises stress distribution, revealing localized stress concentrations that act as precursors to crack initiation. The subfigures in Fig. 5.10 corresponds to the points on the load-displacement curves shown in Fig. 5.9. The results underscore the significant role of voids in crack propagation, consistent with findings on sintered Ag NPs [28], where porosity governs fracture paths and reduces structural stability. Similar to observations by Su et al. [37] and Chen et al. [28], the porous distribution in sintered Cu NPs creates stress hot spots that accelerate failure. The observed stress localization emphasizes the need to optimize sintering parameters, such as pressure and temperature, to minimize porosity, improve

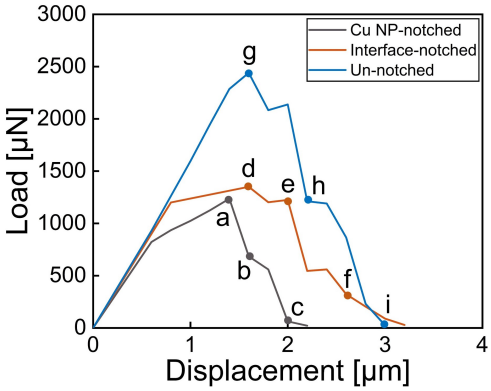


Figure 5.9: Load-displacement curves.

sintering neck formation and enhance mechanical uniformity.

The agreement between CZM and experimental results (Fig. 5.6 and Fig. 5.7) further validates these observations. Fracture morphologies in Fig. 5.6 depict crack propagation through porous regions and weakened sintering necks, paralleling the CZM predictions. Additionally, the elongated sintered Cu NPs and localized deformation near stress concentrators observed in Fig. 5.7 align with the stress patterns in Fig. 5.10. However, the presence of porosity in the sintered Cu NPs introduces stress concentrators, reducing overall structural stability. In conclusion, this analysis highlights the robust bonding and effective stress transfer at the Cu substrate interface, reinforcing the feasibility of directly sintering Cu NPs onto a Cu substrate without additional coatings. This approach ensures mechanically reliable, all-Cu integration, making it highly promising for advanced electronic packaging applications.

5.4. CONCLUSION

In this study, the interface strength and fracture behavior of sintered Cu NPs were systematically investigated using micro-cantilever bending tests, SEM, TEM, TKD and CZM. This integrated experimental and computational approach enabled a comprehensive analysis of crack initiation and propagation mechanisms of sintered Cu NPs. The main conclusions are as follows:

1. The Cu substrate-sintered Cu NP interface exhibits higher fracture resistance than the sintered Cu NPs, with a stress intensity factor K_Q of approximately 2.88 ± 0.10 MPa·m$^{1/2}$ compared to 2.12 ± 0.11 MPa·m$^{1/2}$ for cracks propagating within the sintered Cu NPs. This highlights the robust bonding and effective stress transfer at the interface, supporting the feasibility of direct sintering of Cu NPs to a Cu substrate without the need for other coating.

2. Fracture surface analyses reveal that in both types of notched micro-cantilevers, crack propagation preferentially follows the sintered Cu NPs, evidenced by elongated sintering necks. For un-notched micro-canitlevers, interestingly, synergistic deformation mechanism in un-notched micro-cantilevers, where crack propagation through the

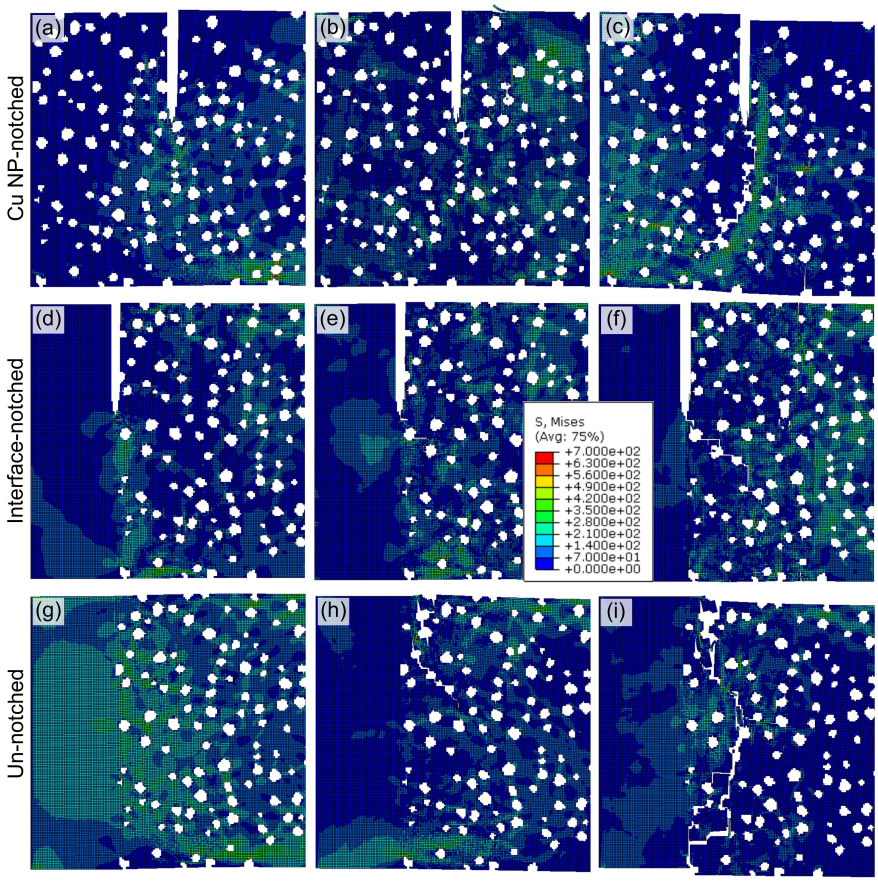


Figure 5.10: Crack propagation path and distributions of von Mises stress: (a-c) Cu NP-notched micro-cantilever (a, 0-728 MPa; b, 0-601 MPa; c, 0-696 MPa); (d-f) interface-notched micro-cantilever (d, 0-569 MPa; e, 0-598 MPa; f, 0-650 MPa); (g-i) un-notched micro-cantielver (g, 0-725 MPa; h, 0-678 MPa; i, 0-735 MPa).

sintered Cu NPs coexists with plastic slip deformation in the Cu substrate.

3. TKD analysis demonstrates that the sintered Cu NPs exhibit random crystallographic orientations, while the negligible interfacial void density indicates robust metallurgical bonding with the underlying Cu substrate. Complementary TEM and TKD characterization reveals substrate plastic deformation through both slip band formation and sintering neck elongation at the interface.

4. CZM results demonstrate that notch location significantly impacts mechanical properties. Cu NP-notched micro-cantilevers exhibit lower fracture resistance due to increased porosity and stress concentrations, while interface-notched micro-cantilevers show higher strength, attributed to robust bonding and reduced void distribution. Cracks predominantly bypass the interface, propagating through porous regions in the sintered Cu NPs, demonstrating the interface's ability to effectively transfer stress and resist fracture. This performance underscores the potential of direct sintering of Cu NPs

onto Cu substrates as a reliable and efficient method for all-Cu integration, without requiring additional coatings, for advanced applications in microelectronics and packaging technologies.

REFERENCES

[1] L. Du *et al.*, "Interface strength and crack propagation mechanisms in sintered copper nanoparticles", *Acta Materialia*, vol. 296, no. 12118, p. 7, 2025.

[2] L. Del Carro, J. Zürcher, U. Drechsler, I. E. Clark, G. Ramos, and T. Brunschwiler, "Low-temperature dip-based all-copper interconnects formed by pressure-assisted sintering of copper nanoparticles", *IEEE Transactions on Components, Packaging and Manufacturing Technology*, vol. 9, no. 8, pp. 1613–1622, 2019.

[3] S. Wang, G. Zou, Y. Wu, Z. Deng, R. Du, and L. Liu, "Patterned Cu nanoparticle film for all-Cu interconnection without chemical mechanical polishing pretreatment", *IEEE Transactions on Components, Packaging and Manufacturing Technology*, vol. 13, no. 5, pp. 604–614, 2023.

[4] X. Ji, L. Du, H. Van Zeijl, G. Zhang, J. Derakhshandeh, and E. Beyne, "20 μm pitch cu-to-cu flip-chip interconnects through cu nanoparticles sintering", in *2024 IEEE 74th Electronic Components and Technology Conference (ECTC)*, IEEE, 2024, pp. 1891–1895.

[5] S. Wang, G. Zou, R. Du, and L. Liu, "Transferring fine-pitch Cu nanoparticle bumps for low-temperature Cu-Cu bonding in chip-scale integration", *IEEE Transactions on Components, Packaging and Manufacturing Technology*, 2025.

[6] B. H. Lee, M. Z. Ng, A. A. Zinn, and C. L. Gan, "Application of copper nanoparticles as die attachment for high power led", in *2015 IEEE 17th Electronics Packaging and Technology Conference (EPTC)*, IEEE, 2015, pp. 1–5.

[7] H.-J. Huang, X. Wu, M.-B. Zhou, and X.-P. Zhang, "A highly reliable die bonding approach for high power devices by low temperature pressureless sintering using a novel Cu nanoparticle paste", in *2020 IEEE 70th Electronic Components and Technology Conference (ECTC)*, IEEE, 2020, pp. 1697–1702.

[8] D. Dai *et al.*, "A rapid-sintering cu-cu joints with ultrahigh shear strength and super reliability for power electronics package", *Materials Science in Semiconductor Processing*, vol. 178, p. 108 405, 2024.

[9] T.-C. Chou *et al.*, "Investigation of pillar–concave structure for low-temperature Cu–Cu direct bonding in 3-D/2.5-D heterogeneous integration", *IEEE Transactions on Components, Packaging and Manufacturing Technology*, vol. 10, no. 8, pp. 1296–1303, 2020.

[10] D. Liu *et al.*, "Investigation of low-temperature Cu–Cu direct bonding with pt passivation layer in 3-D integration", *IEEE Transactions on Components, Packaging and Manufacturing Technology*, vol. 11, no. 4, pp. 573–578, 2021.

[11] C. He *et al.*, "Nanocrystalline copper for direct copper-to-copper bonding with improved cross-interface formation at low thermal budget", *Nature Communications*, vol. 15, no. 1, p. 7095, 2024.

[12] C.-J. Du, X. Li, Y.-H. Mei, and G.-Q. Lu, "An explanation of sintered silver bonding formation on bare copper substrate in air", *Applied Surface Science*, vol. 490, pp. 403–410, 2019.

[13] D. Yamagiwa *et al.*, "Pressureless sinter joining of bare Cu substrates under forming gas atmosphere by surface-oxidized submicron Cu particles", *Journal of Materials Science: Materials in Electronics*, vol. 32, no. 14, pp. 19 031–19 041, 2021.

[14] K. Matoy, T. Detzel, M. Müller, C. Motz, and G. Dehm, "Interface fracture properties of thin films studied by using the micro-cantilever deflection technique", *Surface and Coatings Technology*, vol. 204, no. 6-7, pp. 878–881, 2009.

[15] G. Otieno *et al.*, "Stiffness, strength and interwall sliding in aligned and continuous multi-walled carbon nanotube/glass composite microcantilevers", *Acta Materialia*, vol. 100, pp. 118–125, 2015.

[16] S Massl, W Thomma, J. Keckes, and R. Pippan, "Investigation of fracture properties of magnetron-sputtered tin films by means of a fib-based cantilever bending technique", *Acta materialia*, vol. 57, no. 6, pp. 1768–1776, 2009.

[17] G. Dehm, B. N. Jaya, R. Raghavan, and C. Kirchlechner, "Overview on micro-and nanomechanical testing: New insights in interface plasticity and fracture at small length scales", *Acta Materialia*, vol. 142, pp. 248–282, 2018.

[18] R. Daniel *et al.*, "Grain boundary design of thin films: Using tilted brittle interfaces for multiple crack deflection toughening", *Acta materialia*, vol. 122, pp. 130–137, 2017.

[19] J. Tatami, Y. Imoto, T. Yahagi, T. Takahashi, and M. Iijima, "Relationship between bending strength of bulk porous silicon carbide ceramics and grain boundary strength measured using microcantilever beam specimens", *Journal of the European Ceramic Society*, vol. 40, no. 7, pp. 2634–2641, 2020.

[20] R. Henry, H. Saad, A. Doitrand, S. Deville, and S. Meille, "Interface failure in nacre-like alumina", *Journal of the European Ceramic Society*, vol. 40, no. 13, pp. 4694–4699, 2020.

[21] J. Ast, M. Ghidelli, K. Durst, M. Göken, M. Sebastiani, and A. M. Korsunsky, "A review of experimental approaches to fracture toughness evaluation at the microscale", *Materials & Design*, vol. 173, p. 107 762, 2019.

[22] S Heuer, B.-S. Li, D. Armstrong, Y Zayachuk, and C. Linsmeier, "Microstructural and micromechanical assessment of aged ultra-fast sintered functionally graded iron/tungsten composites", *Materials & Design*, vol. 191, p. 108 652, 2020.

[23] A. H. Iyer, P. Gupta, P. Gudmundson, and A. Kulachenko, "Measuring microscale mechanical properties of pvdf binder phase and the binder-particle interface using micromechanical testing", *Materials Science and Engineering: A*, vol. 881, p. 145 352, 2023.

[24] D. Armstrong, A. Wilkinson, and S. Roberts, "Micro-mechanical measurements of fracture toughness of bismuth embrittled copper grain boundaries", *Philosophical Magazine Letters*, vol. 91, no. 6, pp. 394–400, 2011.

[25] D. Hu *et al.*, "High temperature viscoplastic deformation behavior of sintered nanocopper paste used in power electronics packaging: Insights from constitutive and multi-scale modelling", *Journal of Materials Research and Technology*, vol. 26, pp. 3183–3200, 2023.

[26] K. Wakamoto, D. Yasugi, T. Otsuka, K. Nakahara, and T. Namazu, "Fracture mechanism of sintered silver film revealed by in-situ sem uniaxial tensile loading", *IEEE Transactions on Components, Packaging and Manufacturing Technology*, 2024.

[27] C. Chen and K. Suganuma, "Microstructure and mechanical properties of sintered ag particles with flake and spherical shape from nano to micro size", *Materials & Design*, vol. 162, pp. 311–321, 2019.

[28] C. Chen *et al.*, "Macroscale and microscale fracture toughness of microporous sintered ag for applications in power electronic devices", *Acta Materialia*, vol. 129, pp. 41–51, 2017.

[29] D. Hu, L. Du, M. Alfreider, J. Fan, D. Kiener, and G. Zhang, "Microscopic fracture toughness of notched porous sintered cu micro-cantilevers for power electronics packaging", *Materials Science and Engineering: A*, vol. 897, p. 146 316, 2024.

[30] J. Liu, H. Chen, H. Ji, and M. Li, "Highly conductive cu–cu joint formation by low-temperature sintering of formic acid-treated cu nanoparticles", *ACS applied materials & interfaces*, vol. 8, no. 48, pp. 33 289–33 298, 2016.

[31] E. Martínez-Pañeda, A. Golahmar, and C. F. Niordson, "A phase field formulation for hydrogen assisted cracking", *Computer Methods in Applied Mechanics and Engineering*, vol. 342, pp. 742–761, 2018.

[32] M. Dittmann *et al.*, "Phase-field modeling of porous-ductile fracture in non-linear thermo-elasto-plastic solids", *Computational Methods in Applied Mechanics and Engineering*, vol. 361, p. 112 730, 2020.

[33] B. He, L. Schuler, and P. Newell, "A numerical-homogenization based phase-field fracture modeling of linear elastic heterogeneous porous media", *Computational Materials Science*, vol. 176, p. 109 519, 2020.

[34] B. He, T. Vo, and P. Newell, "Investigation of fracture in porous materials: A phase-field fracture study informed by reaxff", *Engineering with Computers*, vol. 38, pp. 5617–5633, 2022.

[35] H. Hu, L. Qi, and X. Chao, "Physics-informed neural networks (PINN) for computational solid mechanics: Numerical frameworks and applications", *Thin-Walled Structures*, p. 112 495, 2024.

[36] Y. Su *et al.*, "Thermo-elasto-plastic phase-field modelling of mechanical behaviours of sintered nano-silver with randomly distributed micro-pores", *Computer Methods in Applied Mechanics and Engineering*, vol. 378, p. 113 729, 2021.

[37] Y. Su, J. Zhu, X. Long, L. Zhao, C. Chen, and C. Liu, "Statistical effects of pore features on mechanical properties and fracture behaviors of heterogeneous random porous materials by phase-field modeling", *International Journal of Solids and Structures*, vol. 264, p. 112 098, 2023.

[38] Y. Su, Z. Shen, X. Long, C. Chen, L. Qi, and X. Chao, "Gaussian filtering method of evaluating the elastic/elasto-plastic properties of sintered nanocomposites with quasi-continuous volume distribution", *Materials Science and Engineering: A*, vol. 872, p. 145 001, 2023.

[39] N. Moës, J. Dolbow, and T. Belytschko, "A finite element method for crack growth without remeshing", *International journal for numerical methods in engineering*, vol. 46, no. 1, pp. 131–150, 1999.

[40] F. Xu, H. Hajibeygi, and L. J. Sluys, "Multiscale extended finite element method for deformable fractured porous media", *Journal of Computational Physics*, vol. 436, p. 110 287, 2021.

[41] A. R. Khoei, M Vahab, E Haghighat, and S Moallemi, "A mesh-independent finite element formulation for modeling crack growth in saturated porous media based on an enriched-FEM technique", *International Journal of Fracture*, vol. 188, pp. 79–108, 2014.

[42] R. Verma, P. Kumar, R Jayaganthan, and H. Pathak, "Extended finite element simulation on tensile, fracture toughness and fatigue crack growth behaviour of additively manufactured Ti6Al4V alloy", *Theoretical and Applied Fracture Mechanics*, vol. 117, p. 103 163, 2022.

[43] A. Muixí, O. Marco, A. Rodríguez-Ferran, and S. Fernández-Méndez, "A combined XFEM phase-field computational model for crack growth without remeshing", *Computational Mechanics*, vol. 67, pp. 231–249, 2021.

[44] M. Nikolić, "Discrete element model for the failure analysis of partially saturated porous media with propagating cracks represented with embedded strong discontinuities", *Computer methods in applied mechanics and engineering*, vol. 390, p. 114 482, 2022.

[45] Z. Wang, L. Yang, S. Zhu, W.-L. Song, and H.-S. Chen, "Exploring mechanical failure of porous electrode meso structure using the discrete element method", *Extreme Mechanics Letters*, vol. 46, p. 101 252, 2021.

[46] R. H. Moghaddam and A. Golshani, "Fatigue behavior investigation of artificial rock under cyclic loading by using discrete element method", *Engineering Failure Analysis*, vol. 160, p. 108 105, 2024.

[47] J. Zhang, Y. Chen, R. Du, X. Zhao, and J. Wu, "Macroscopic and microscopic mechanical characteristics and crack propagation behavior of sandstone-like samples with single cracks under freeze–thaw cycles: Experimental and numerical simulation", *Theoretical and Applied Fracture Mechanics*, vol. 129, p. 104 201, 2024.

[48] S. Zhao *et al.*, "On mode ii fracture toughness of sintered silver based on end-notch flexure (enf) test considering various sintering parameters", *Materials Science and Engineering: A*, vol. 823, p. 141 729, 2021.

[49] J. Wei, Y. Dai, and F. Qin, "Inverse identification of cohesive zone parameters for sintered nano-silver joints based on dynamic convolution neural network", *Engineering Fracture Mechanics*, vol. 292, p. 109 651, 2023.

[50] Y. Dai, Y. Li, Z. Zan, and F. Qin, "Bondline thickness effect on fracture and cohesive zone model of sintered nano silver adhesive joints under end notched flexure tests", *Fatigue & Fracture of Engineering Materials & Structures*, vol. 46, no. 6, pp. 2062–2079, 2023.

[51] Y. Dai, Z. Zan, S. Zhao, and F. Qin, "Mode II cohesive zone law of porous sintered silver joints with nickel coated multiwall carbon nanotube additive under ENF test", *Theoretical and Applied Fracture Mechanics*, vol. 121, p. 103 498, 2022.

[52] Y. Wang and J. Li, "Phase field modeling of defects and deformation", *Acta Materialia*, vol. 58, no. 4, pp. 1212–1235, 2010.

[53] T.-T. Nguyen, J. Yvonnet, D. Waldmann, and Q.-C. He, "Phase field modeling of interfacial damage in heterogeneous media with stiff and soft interphases", *Engineering Fracture Mechanics*, vol. 218, p. 106 574, 2019.

[54] J Zambrano, S Toro, P. Sánchez, F. Duda, C. Méndez, and A. Huespe, "Interaction analysis between a propagating crack and an interface: Phase field and cohesive surface models", *International Journal of Plasticity*, vol. 156, p. 103 341, 2022.

[55] C. A. Duarte and D.-J. Kim, "Analysis and applications of a generalized finite element method with global–local enrichment functions", *Computer methods in applied mechanics and engineering*, vol. 197, no. 6-8, pp. 487–504, 2008.

[56] D. Xu, Z. Liu, X. Liu, Q. Zeng, and Z. Zhuang, "Modeling of dynamic crack branching by enhanced extended finite element method", *Computational Mechanics*, vol. 54, pp. 489–502, 2014.

[57] J. E. Andrade and U. Mital, "Multiscale and multiphysics modeling of soils", *Geotechnical fundamentals for addressing new world challenges*, pp. 141–168, 2019.

[58] W. Chen *et al.*, "Unraveling the hydrogen sulfide aging mechanism on electrical-thermal–mechanical property degradation of sintered nanocopper interconnects used in power electronics packaging", *Materials & Design*, vol. 238, p. 112 702, 2024.

[59] J. Ast, M. N. Polyakov, G. Mohanty, J. Michler, and X. Maeder, "Interplay of stresses, plasticity at crack tips and small sample dimensions revealed by in-situ microcantilever tests in tungsten", *Materials Science and Engineering: A*, vol. 710, pp. 400–412, 2018.

[60] A. H. Iyer, K. Stiller, and M. H. Colliander, "Room temperature plasticity in thermally grown sub-micron oxide scales revealed by micro-cantilever bending", *Scripta Materialia*, vol. 144, pp. 9–12, 2018.

[61] L. Du *et al.*, "Microstructural and mechanical anisotropy in pressure-assisted sintered copper nanoparticles", *Acta Materialia*, vol. 287, p. 120 772, 2025.

[62] R. Zhu, G. Niu, Z. Qu, P. Wang, R. Zhang, and D. Fang, "In-situ quantitative tracking of micro-crack evolution behavior inside CMCs under load at high temperature: A deep learning method", *Acta Materialia*, vol. 255, p. 119 073, 2023.

[63] S. N. Kumaran, S. K. Sahoo, C. Haase, L. A. Barrales-Mora, and L. S. Toth, "Nanostructuring of a high entropy alloy by severe plastic deformation: Experiments and crystal plasticity simulations", *Acta Materialia*, vol. 250, p. 118 814, 2023.

[64] S. Park, J. G. Kim, J. B. Seol, H. Sung, *et al.*, "Ultrastrong and stress corrosion cracking-resistant martensitic steels", *Acta Materialia*, vol. 239, p. 118 291, 2022.

[65] X. Chao, W. Tian, F. Xu, and D. Shou, "A fractal model of effective mechanical properties of porous composites", *Composites Science and Technology*, vol. 213, p. 108 957, 2021.

[66] M. Neumann *et al.*, "On a pluri-gaussian model for three-phase microstructures, with applications to 3d image data of gas-diffusion electrodes", *Computational Materials Science*, vol. 156, pp. 325–331, 2019.

[67] Y. Gao, Y. Jiao, and Y. Liu, "Ultra-efficient reconstruction of 3d microstructure and distribution of properties of random heterogeneous materials containing multiple phases", *Acta Materialia*, vol. 204, p. 116 526, 2021.

[68] X. Long *et al.*, "Phase field fracture modeling of mechanical degradation and crack propagation in random porous sintered nano-silver with thermal and strain-rate effects", *Engineering Fracture Mechanics*, p. 110 753, 2024.

[69] S. T. Mousavi, N. Richart, C. Wolff, and J.-F. Molinari, "Dynamic crack propagation in a heterogeneous ceramic microstructure, insights from a cohesive model", *Acta Materialia*, vol. 88, pp. 136–146, 2015.

[70] C. Motz, T. Schöberl, and R. Pippan, "Mechanical properties of micro-sized copper bending beams machined by the focused ion beam technique", *Acta materialia*, vol. 53, no. 15, pp. 4269–4279, 2005.

[71] E. Demir, D. Raabe, and F. Roters, "The mechanical size effect as a mean-field breakdown phenomenon: Example of microscale single crystal beam bending", *Acta Materialia*, vol. 58, no. 5, pp. 1876–1886, 2010.

[72] M. Wurmshuber *et al.*, "Tuning mechanical properties of ultrafine-grained tungsten by manipulating grain boundary chemistry", *Acta materialia*, vol. 232, p. 117 939, 2022.

[73] S.-H. Hong, K. Kim, Y.-M. Kim, J.-H. Hahn, C.-S. Lee, and J.-H. Park, "Characterization of elastic moduli of cu thin films using nanoindentation technique", *Composites science and technology*, vol. 65, no. 9, pp. 1401–1408, 2005.

[74] D. E. Armstrong, A. J. Wilkinson, and S. G. Roberts, "Measuring anisotropy in young's modulus of copper using microcantilever testing", *Journal of materials research*, vol. 24, pp. 3268–3276, 2009.

[75] C Howard, R. Fritz, M. Alfreider, D. Kiener, and P Hosemann, "The influence of microstructure on the cyclic deformation and damage of copper and an oxide dispersion strengthened steel studied via in-situ micro-beam bending", *Materials Science and Engineering: A*, vol. 687, pp. 313–322, 2017.

[76] M. Mutoh, T. Nagoshi, T.-F. M. Chang, T. Sato, and M. Sone, "Micro-compression test using non-tapered micro-pillar of electrodeposited cu", *Microelectronic engineering*, vol. 111, pp. 118–121, 2013.

[77] J. G. Gigax, J. K. Baldwin, C. J. Sheehan, S. A. Maloy, and N. Li, "Microscale shear specimens for evaluating the shear deformation in single-crystal and nanocrystalline cu and at cu–si interfaces", *Journal of Materials Research*, vol. 34, no. 9, pp. 1574–1583, 2019.

[78] R. O. Ritchie and D. Liu, *Introduction to fracture mechanics*. Elsevier, 2021.

[79] F Iqbal, J Ast, M Göken, and K Durst, "In situ micro-cantilever tests to study fracture properties of nial single crystals", *Acta Materialia*, vol. 60, no. 3, pp. 1193–1200, 2012.

[80] A. S. Khan and J. Liu, "A deformation mechanism based crystal plasticity model of ultrafine-grained/nanocrystalline FCC polycrystals", *International Journal of Plasticity*, vol. 86, pp. 56–69, 2016.

[81] F. Wang *et al.*, "Topology and evolution of dislocation structures mediated by glissile reactions in face-centered cubic metals", *Acta Materialia*, vol. 268, p. 119 748, 2024.

6

Particle Morphology-dependent Fracture Toughness in Sintered Copper Particles

This study investigates the influence of copper (Cu) particle morphology on the fracture toughness and elucidates the pronounced size-dependent effects using micro-cantilever bending tests. Three particle configurations—monomodal, bimodal, and flake-shaped—were examined, revealing strong correlations between morphology, densification behavior, and crack resistance. Bimodal Cu, characterized by hierarchical particle packing, demonstrated superior fracture toughness due to enhanced neck formation and energy dissipation mechanisms such as crack deflection and ligament bridging. In contrast, flake-shaped Cu exhibited brittle fracture behavior, attributed to anisotropic porosity and weak interlamellar bonding. A clear size effect was observed: smaller micro-cantilevers consistently exhibited higher apparent fracture toughness across all morphologies, reflecting increased plasticity and localized energy absorption at reduced dimensions.

6.1. INTRODUCTION

DISTINCT morphologies of copper (Cu) particles—namely monomodal, bimodal, and flake-shaped—lead to significant variations in the resulting sintered microstructures, thereby influencing mechanical performance. While prior studies have extensively explored the mechanical behavior of sintered Cu [1–3], the specific role of particle morphology in governing fracture toughness remains insufficiently understood. This gap is critical, as the fracture resistance of sintered interconnects directly impacts the reliability and durability of next-generation power electronic devices. To address this, the present study systematically investigates the fracture behavior of sintered Cu derived from different particle morphologies, aiming to elucidate the underlying structure–property relationships that dictate toughness and deformation mechanisms.

In parallel, the influence of specimen size on mechanical properties has been well documented for dense metallic systems, particularly at the micro- and nanoscale [4–6], where yield strength and flow stress exhibit pronounced size effects. For instance, nanometer-thick metallic Cu films demonstrate increased fracture toughness with growing sample thickness [7, 8], attributed to transitions in deformation modes and fracture morphology near the crack tip. However, such size effects may manifest differently in sintered materials due to their intrinsic porosity and heterogeneous microstructure [9–11]. Unlike fully dense metals, sintered Cu particles exhibit mechanical behavior dominated by pore distribution and neck growth between particles. Thus, to capture the interplay between sample size and fracture resistance in porous systems, this study also considers size-dependent effects by fabricating micro-cantilevers of three distinct dimensions.

6.2. METHODS

6.2.1. MATERIALS FABRICATION

The sintering process (Fig. 6.1a) and parameters have been described in detail in Chapter 3. In this study, three distinct Cu particle morphologies were investigated: monomodal (uniform spherical NPs), bimodal (mixed spherical NPs), and flake-shaped particles. The initial morphologies of these particles, characterized by scanning electron microscopy (SEM), was shwon in (Figs. 6.1b–d). Cross-sectional analysis after sintering (Figs. 6.1e–g) highlights the influence of particle morphology on densification behavior and the resulting microstructure, with bimodal particles showing reduced porosity attributed to their higher initial packing density [12]. Bimodal Cu particle assemblies exhibit superior packing density compared to both monomodal and flake-shaped particles [13–15], as shown in Fig. 6.2. This is primarily attributed to the presence of smaller particles that effectively occupy the interstitial voids between larger particles, thereby enhancing the overall packing efficiency. In contrast, monomodal particles—comprising uniformly sized spheres—lack this hierarchical size distribution, resulting in increased pore volume and reduced contact area between adjacent particles. Flake-shaped particles, due to their anisotropic geometry and tendency to align during packing, introduce significant interlayer voids and hinder uniform densification [16, 17]. These morphological limitations reduce the packing density and restrict efficient sintering. Consequently, the bimodal particle system is expected to achieve enhanced densification and reduced

residual porosity after sintering, which are critical for improving the mechanical performance and reliability of the sintered Cu structures.

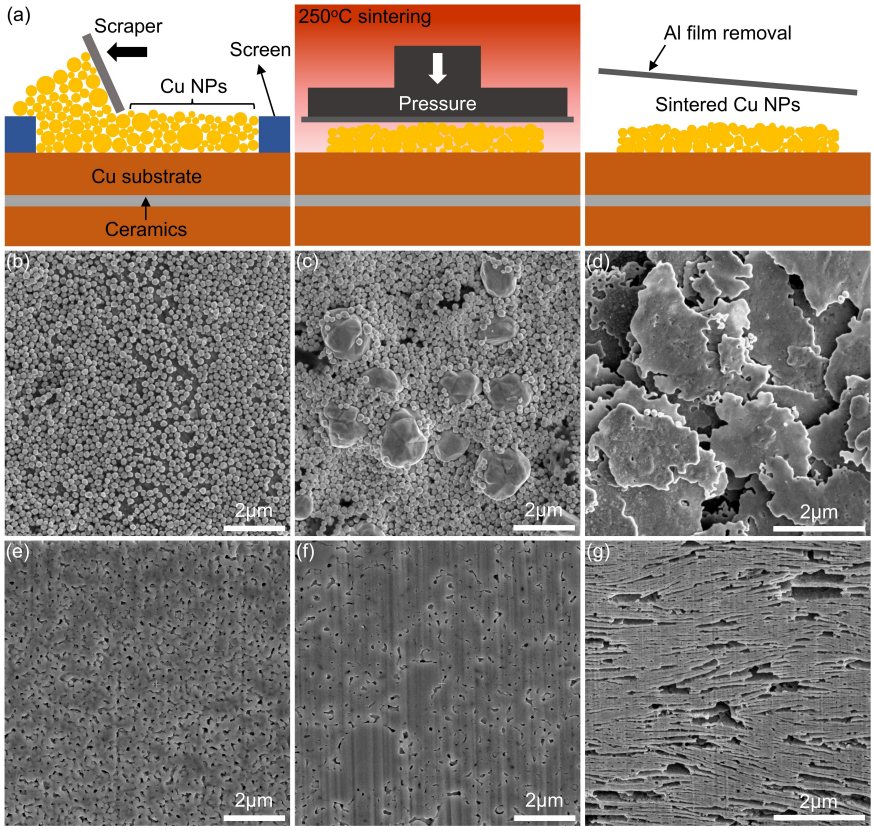


Figure 6.1: (a) Schematic of sintering process; (b–d) initial morphologies: monomodal, bimodal, and flake particles; (e–g) corresponding sintered microstructures.

To investigate the three-dimensional (3D) internal architecture of sintered Cu particles, serial sectioning combined with volumetric reconstruction was performed using a dual-beam focused ion beam scanning electron microscope (FIB-SEM). The detailed 3D reconstruction methodology is provided in Chapter 2. For monomodal and bimodal Cu NP samples, a slice thickness of 15 nm was employed to achieve high-resolution imaging, while a coarser thickness of 50 nm was used for flake-shaped Cu NPs to account for their higher porosity and larger structural features. Each dataset consisted of 200 to 500 sequential slices, generating a grayscale image stack representative of the milled volume. Reconstruction of the 3D tomographic models was conducted using Avizo software (Thermo Fisher Scientific), incorporating automated slice alignment, noise filtering, and adaptive thresholding techniques for accurate phase segmentation and visualization of the porous microstructure [18].

To evaluate the size-dependent fracture toughness of sintered Cu particles, micro-

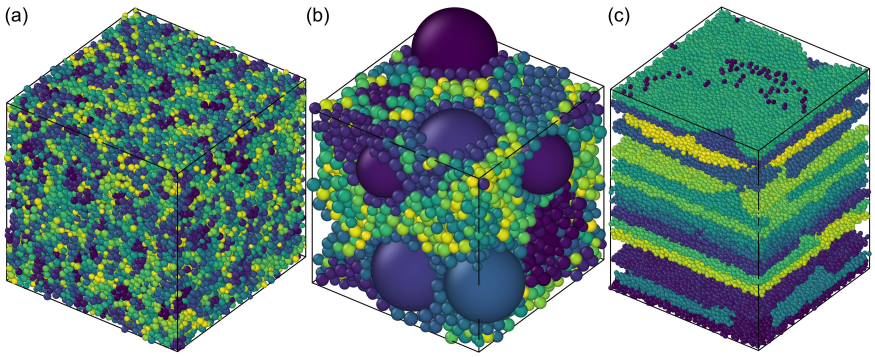


Figure 6.2: Initial packing configurations of Cu particles: (a) monomodal, (b) bimodal, and (c) flake-like distributions, illustrating particle arrangement and heterogeneity prior to sintering.

cantilevers with three distinct widths (5 µm, 10 µm, and 20 µm) were fabricated, as illustrated in Fig. 6.3. The fabrication process, based on FIB milling, is schematically depicted in Fig. 6.3a. Representative SEM images of the resulting cantilevers with varying dimensions are shown in Figs. 6.3b–d, respectively, highlighting the geometric consistency and surface quality achieved across all sizes.

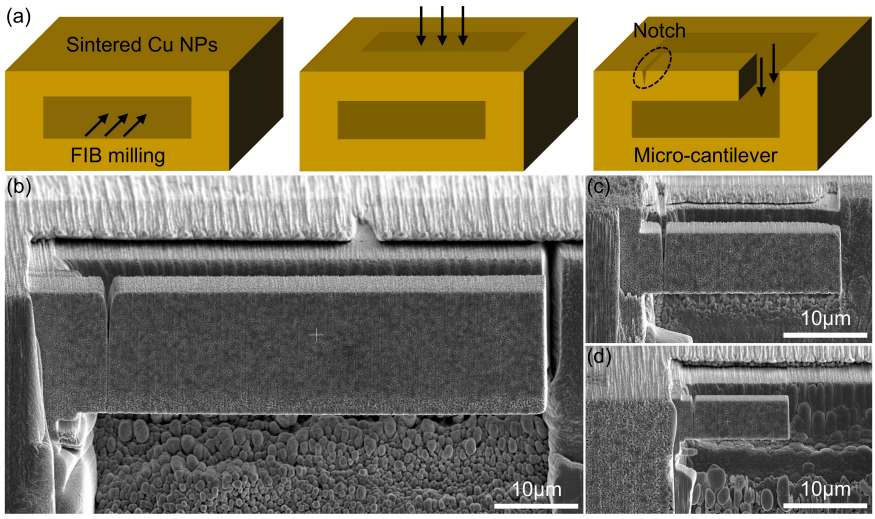


Figure 6.3: (a) FIB milling process for micro-cantilever fabrication; (b–d) SEM images of micro-cantilevers with varying sizes and well-defined notches.

6.2.2. NANOINDENTATION TEST

Nanoindentation tests were performed using a KLA Nanoindenter G200, employing the continuous stiffness measurement (CSM) method to evaluate hardness, Young's modulus (E), and stress-strain behavior based on the analytical framework first proposed by

Oliver and Pharr [19]. A superimposed sinusoidal signal of 2 nm amplitude and 45 Hz frequency was applied, with a constant indentation strain rate of $\dot{\varepsilon} = 0.05\,\mathrm{s}^{-1}$. Mechanical properties were assessed at a maximum indentation depth of 2500 nm, with six indentations performed per condition to ensure statistical reliability. In this study, spherical nanoindenter tips were employed to ensure consistent mechanical characterization and to mitigate the effects of microstructural heterogeneity inherent in porous sintered Cu structures. The use of spherical indenters enables a more stable contact geometry and progressive engagement with the material [20, 21], allowing for the capture of both elastic and plastic deformation behaviors over a broader range of penetration depths. This approach reduces the influence of local porosity variations and surface irregularities, thereby providing a more representative assessment of the intrinsic mechanical properties of the sintered microstructure.

6.2.3. MICRO-CANTILEVER BENDING TEST

All micro-cantilever bending tests were conducted using a Hysitron PI85 picoindenter (Bruker Corporation, Billerica, USA) equipped with a nanoDMA III upgrade for continuous stiffness measurement (CSM), integrated within a SEM (Leo 1540XB, Carl Zeiss AG, Oberkochen, Germany). A constant loading rate of 10 µN/s was applied, accompanied by a superimposed sinusoidal signal of 80 Hz and an amplitude of 5 µN to facilitate continuous stiffness measurements [22, 23]. Throughout the tests, force-displacement data and in situ SEM micrographs were recorded simultaneously at a rate of 2 images per second, enabling detailed post-processing and correlation of mechanical behavior with microstructural observations.

The fracture toughness of sintered Cu particles was evaluated using the J-integral approach, which adheres to the iterative methodology prescribed by elastic-plastic fracture mechanics (EPFM) in accordance with ASTM E1820 [23, 24]. Specifically, the J-integral for elasto-plastic materials was determined by summing the elastic and plastic contributions, as expressed in Eq. 6.1:

$$J(a) = J^{\mathrm{el}}(a) + J^{\mathrm{pl}}(a) \tag{6.1}$$

$$J_n^{\mathrm{el}} = \frac{K_{q,n}^2(1-\nu^2)}{E} \tag{6.2}$$

$$J_n^{\mathrm{pl}} = \left\{ J_{n-1}^{\mathrm{pl}} + \frac{\eta_n}{W-a_n}\frac{A_n^{\mathrm{pl}} - A_{n-1}^{\mathrm{pl}}}{B} \right\} \left\{ 1 - \gamma_n \frac{a_n - a_{n-1}}{W-a_n} \right\} \tag{6.3}$$

Here, $J^{\mathrm{el}}(a)$ and $J^{\mathrm{pl}}(a)$ represent the elastic and plastic components of the J-integral, respectively, evaluated at a given crack length a, while n denotes the iteration step number. B and W represents the specimen thickness and width, respectively. ν is the Poisson's ratio and E represents the Young's modulus of the material. The elastic contribution, $J^{\mathrm{el}}(a)$, is derived from linear elastic fracture mechanics (LEFM), where $K_{q,n}$ denotes the plane-strain stress intensity factor, as expressed in Eq. 6.4:

$$K_{q,n} = \frac{6F_nL}{BW^2}\sqrt{\pi a_n} f\left(\frac{a_n}{W}\right) \tag{6.4}$$

where L denotes the bending length, measured from the notch to the point of force application. F_n denotes the applied force at iteration step n, while $f\left(\frac{a_n}{W}\right)$ represents a geometry-dependent factor for the micro-cantilevers, which is calculated according to Eq. 6.5.

$$f\left(\frac{a}{W}\right) = \sqrt{\frac{2w}{\pi a}\tan\left(\frac{\pi a}{2w}\right)}\frac{0.923 + 0.199\left(1-\sin\left(\frac{\pi a}{2w}\right)\right)^4}{\cos\left(\frac{\pi a}{2w}\right)} \tag{6.5}$$

The plastic contribution to the J-integral ($J^{\mathrm{pl}}(a)$) was determined using geometry-independent prefactors, $\eta = 1.9$ and $\gamma = 0.9$. These values were selected based on the analogous loading behavior observed between single-edge notched bending (SENB) configurations and cantilever-shaped microbeams [23, 24], both of which exhibit similar stress intensity evolution under bending-dominated fracture conditions. The plastic work, A^{pl}, representing the energy dissipated through irreversible deformation, was calculated at each loading increment n as the area enclosed between the load–displacement curve and its elastic component. This computation was carried out in accordance with Eq. 6.6, enabling a quantitative assessment of plastic energy contributions to the overall fracture process.

$$A_n^{\mathrm{pl}} = A_n - A_n^{\mathrm{el}} = \int_0^{u_n} F\,du - \frac{F_n^2}{2k_n} \tag{6.6}$$

Here, u_n, F_n, and k_n represent the displacement, applied load, and stiffness, respectively.

6.3. RESULTS AND DISCUSSION

6.3.1. POROSITY ANALYSIS

The 3D internal architectures of sintered Cu particles were reconstructed using FIB-SEM tomography, as illustrated in Figs. 6.4a–c. The reconstructed volumes reveal distinct porosity distributions for monomodal, bimodal, and flake-shaped Cu NPs, with the blue and gray regions representing porosity and the Cu matrix, respectively. Notably, bimodal Cu NPs exhibit a more homogeneous and reduced porosity network (Fig. 6.4b), whereas flake-shaped particles display large, interconnected porous domains (Fig. 6.4c), reflecting their anisotropic morphology and inefficient packing. Quantitative porosity analysis was performed on the 3D reconstructions using Avizo software, with results summarized in Figs. 6.4d–g. The volume porosity (V_p) values were determined as 13.2% for monomodal, 6.7% for bimodal, and 17.8% for flake-shaped Cu NPs, highlighting the superior densification efficiency of bimodal particles due to their optimized size distribution and enhanced particle rearrangement during sintering. Areal porosity measurements along the X, Y, and Z directions further corroborate these trends: monomodal and bimodal Cu NPs exhibit nearly isotropic porosity distributions (Figs. 6.4d, e), consistent with their spherical particle geometry. In contrast, flake-shaped Cu NPs demonstrate significant anisotropy, with markedly higher areal porosity in the XY plane (Fig. 6.4f), a direct consequence of their platelet-like morphology and preferential alignment during sintering. The pronounced porosity fluctuations observed in flake-shaped Cu NPs (Fig. 6.4g) can be attributed to their nonuniform packing and the formation of large,

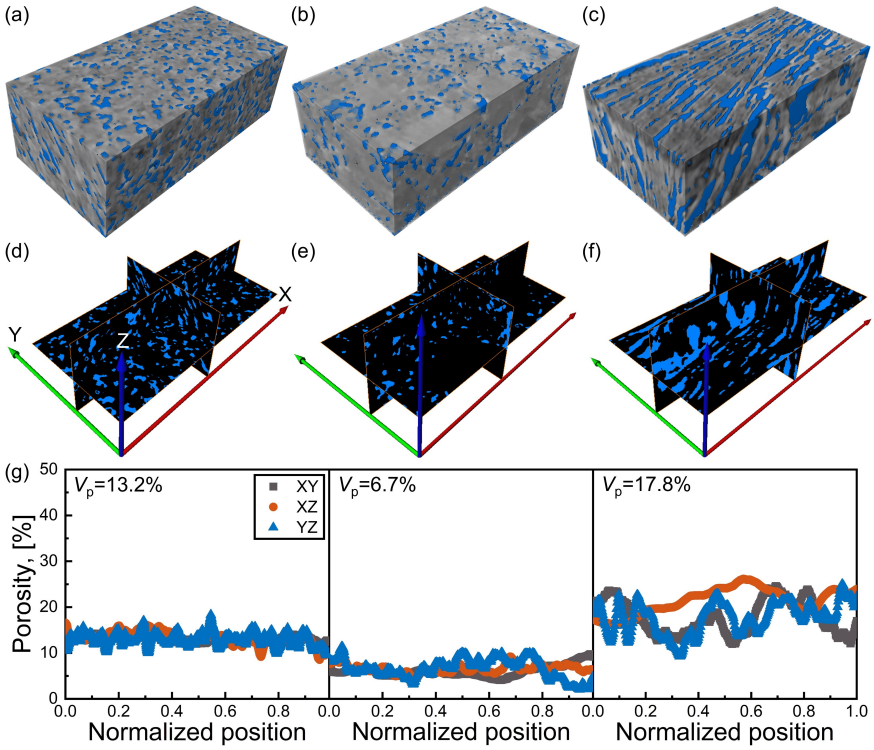


Figure 6.4: 3D reconstruction of sintered Cu structures showing pore morphology and distribution: volumetric renderings (a–c), orthogonal cross-sections (d–f), and porosity profiles along normalized positions in XY, XZ, and YZ planes (g).

irregular voids between adjacent flakes. This anisotropy not only compromises mechanical integrity but also influences thermal and electrical conductivity. Conversely, the reduced and isotropic porosity of bimodal Cu NPs underscores their potential for applications requiring high density and uniform properties, such as power electronics packaging and thermal interface materials.

6.3.2. STRESS-STRAIN CURVES

To evaluate the mechanical behavior of sintered Cu with different particle morphologies (monomodal, bimodal, and flake-based), nanoindentation tests were conducted, as shown in Fig. 6.5. A spherical indenter (Fig. 6.5a) was employed to assess the load–penetration response, and a representative SEM image of the indentation imprint is shown in Fig. 6.5b. The extracted elastic modulus and yield strength are summarized in Fig. 6.5c, revealing that bimodal sintered Cu exhibits the highest stiffness, attributed to its enhanced packing density and well-developed necking. In contrast, monomodal Cu shows moderate performance, while the flake-based structure demonstrates the weakest mechanical properties due to lamellar porosity and poor interparticle bonding.

The load–displacement curves (Fig. 6.5d) confirm the superior load-bearing capac-

ity of the monomodal structure and the early failure tendency of the flake-based sample. Corresponding modulus–depth profiles (Fig. 6.5e) show stable mechanical responses, with the bimodal Cu maintaining the highest modulus throughout, indicative of robust interconnectivity. Stress–strain curves (Fig. 6.5f) further reinforce these trends, with the monomodal and bimodal structures showing the higher stress tolerance and strain hardening, while the flake-based system displays limited plasticity. Overall, these results highlight the critical influence of particle morphology on the mechanical integrity of sintered Cu.

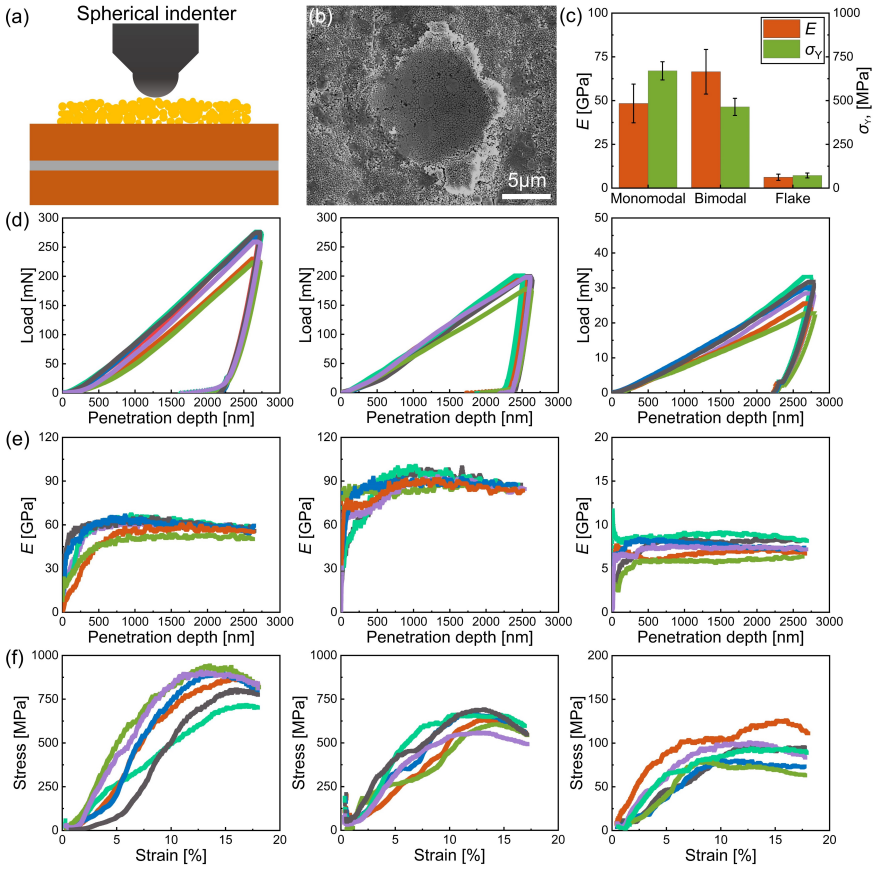


Figure 6.5: (a) Schematic of nanoindentation setup; (b) SEM image of the indentation imprint; (c) comparison of elastic modulus (E) and yield strength for monomodal, bimodal, and flake Cu particles; (d) load–displacement curves; (e) modulus–depth profiles; (f) corresponding stress–strain responses.

6.3.3. FRACTURE TOUGHNESS

The J-integral resistance curves (J-Δa) presented in Fig. 6.6 provide a quantitative assessment of fracture toughness evolution for the three types of sintered Cu microstructures under different micro-cantilever sizes. The large micro-cantilevers exhibit a dis-

tinct trend in which the bimodal sintered Cu demonstrates the highest J-integral values, indicating superior resistance to crack propagation. This behavior is attributed to the enhanced interparticle bonding and load transfer efficiency facilitated by the presence of larger particles within the bimodal structure. In contrast, the monomodal Cu shows lower J-integral values due to its relatively homogeneous microstructure and limited sintered neck formation, which results in earlier crack initiation and propagation. The flake Cu samples, characterized by anisotropic porosity and weak interlamellar bonding, exhibit the lowest fracture resistance across all cantilever sizes, highlighting their vulnerability to interfacial failure mechanisms. The observed J-integral trends align with existing studies on microscale fracture toughness assessment, where the fracture resistance increases with improved sintering-induced interfacial bonding. The distinction between stable crack growth in the bimodal and monomodal Cu, compared to unstable fracture in the flake Cu, highlights the crucial role of sintering morphology in defining energy dissipation during crack propagation. The presence of distinct crack deflection and bridging mechanisms in the bimodal Cu further contributes to its superior fracture toughness. Additionally, the comparison of in-plane and out-of-plane cantilever orientations in the flake Cu structure reveals significant anisotropy, with higher fracture resistance observed in the in-plane configuration, likely due to the orientation of sintered interfaces relative to the applied stress. These findings provide a comprehensive understanding of fracture behavior in sintered Cu, demonstrating the interplay between microstructure, crack propagation resistance, and specimen size effects.

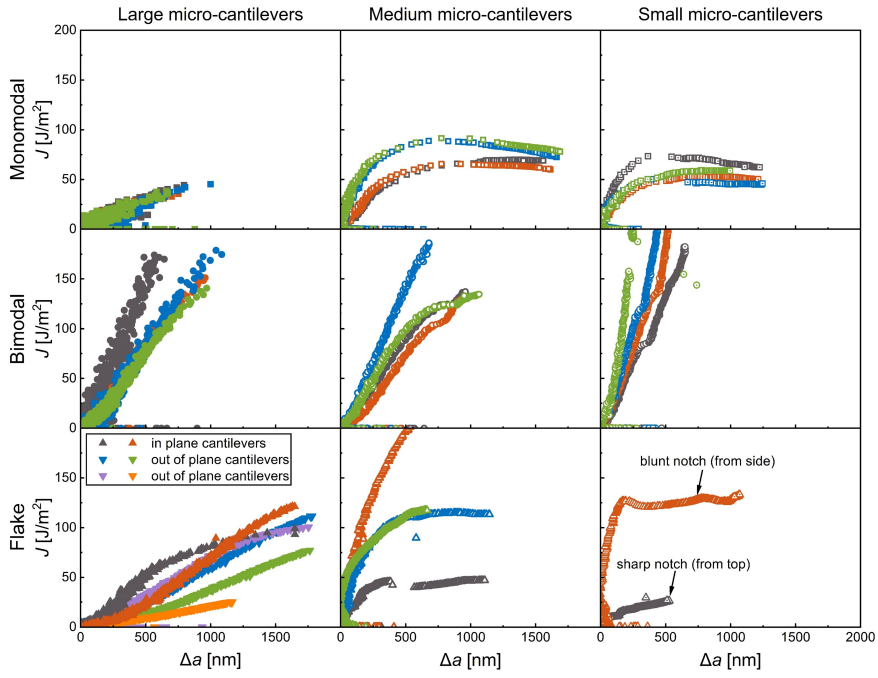


Figure 6.6: J-Δa curves of monomodal, bimodal and flake sintered Cu particles.

The fracture toughness results presented in Fig. 6.7 provide a comparative evaluation of the mechanical resistance to crack propagation in monomodal, bimodal, and flake sintered Cu across different micro-cantilever sizes. The four evaluated fracture toughness metrics—K_{LEFM}, $K_{\mathrm{CTOD},J}$, $K_{Q,J}$, and $K_{\mathrm{Fracture},J}$—highlight distinct differences in crack resistance based on microstructural characteristics. Overall, the bimodal sintered Cu consistently exhibits the highest fracture toughness (around 3 MPa·m$^{1/2}$) across all cantilever sizes, indicating superior crack resistance due to its optimized microstructural densification and stronger sintering necks. The monomodal sintered Cu demonstrates moderate fracture toughness (around 1.8 MPa·m$^{1/2}$), which can be attributed to its relatively uniform microstructure but with higher residual porosity. In contrast, the flake sintered Cu presents the lowest fracture toughness values (around 0.4 MPa·m$^{1/2}$), particularly in the small and medium micro-cantilevers, where the weak interlamellar bonding and anisotropic porosity significantly reduce crack propagation resistance. A pronounced size-dependent trend is evident in the values of $K_{\mathrm{CTOD},J}$ across all sintered Cu variants, wherein micro-cantilevers with smaller dimensions consistently exhibit elevated apparent fracture toughness relative to their medium- and large-sized counterparts. This behavior is primarily ascribed to enhanced plastic deformation mechanisms operative in the smaller specimens, which facilitate increased energy dissipation at the crack tip prior to the onset of fracture. The observed size effect underscores the critical role of plasticity-dominated toughening in microscale fracture processes.

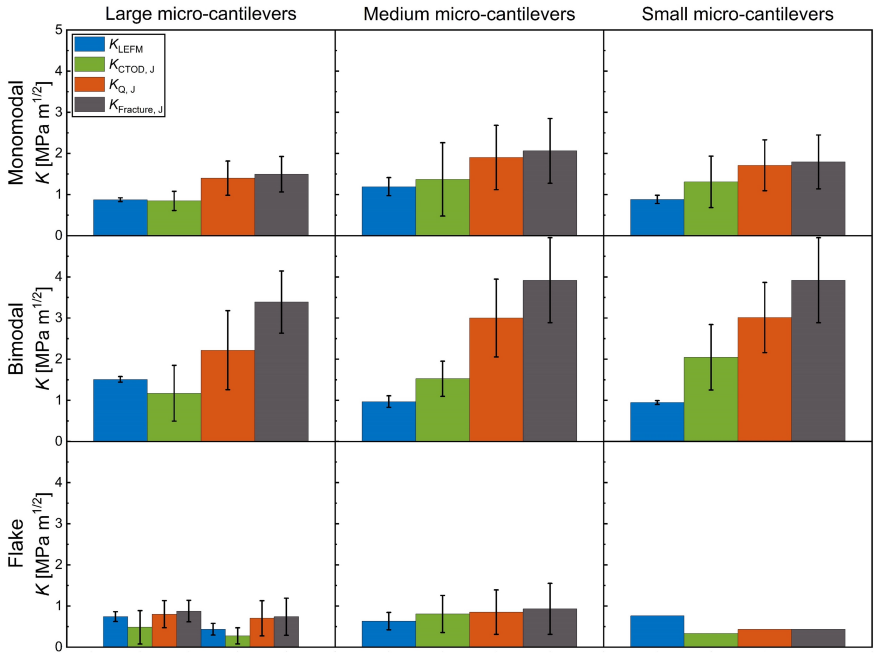


Figure 6.7: Fracture toughness of monomodal, bimodal and flake sintered Cu particles.

The differences between the fracture toughness evaluation methods suggest that the plastic deformation contribution varies across different sintered Cu types. The bimodal

Cu exhibits a significant increase in $K_{\text{Fracture},J}$ compared to K_{LEFM}, indicating substantial energy dissipation due to enhanced interparticle bonding. In contrast, the flake Cu maintains relatively low values across all methods, reaffirming its brittle failure mode. These findings align with previous studies on the fracture behavior of sintered structures, where the degree of sintering and interparticle connectivity play crucial roles in determining fracture toughness. This study reinforces that bimodal sintered Cu offers the most effective combination of toughness and microstructural stability, making it a strong candidate for applications requiring enhanced mechanical reliability in electronic packaging and high-temperature environments.

6.3.4. FRACTURE MORPHOLOGY

The fracture processes of the three types of sintered Cu micro-cantilevers, as illustrated in Fig. 6.8, reveal distinct crack initiation and propagation behaviors, reflecting the influence of microstructural characteristics on failure mechanisms. In the monomodal sintered Cu, shown in Figs. 6.8a–c, crack initiation occurs at the notch, followed by stable crack propagation with limited crack deflection. The relatively homogeneous microstructure of monomodal sintered Cu results in a straightforward fracture path, with failure predominantly governed by localized plastic deformation and void nucleation at grain boundaries. The presence of fine pores throughout the microstructure slightly influences crack propagation, but the crack growth remains relatively uniform. As the crack advances, microscale bridging mechanisms are minimal, leading to a relatively lower fracture toughness compared to bimodal structures.

In contrast, the bimodal sintered Cu micro-cantilevers (Figs. 6.8d–f) demonstrate enhanced fracture resistance due to more effective crack deflection and bridging mechanisms. The presence of larger particles in the bimodal microstructure facilitates energy dissipation during crack propagation, as cracks are forced to deviate from a straight path, promoting increased crack resistance. The sequential images illustrate a more gradual failure process, with evident crack blunting and ductile ligament bridging, contributing to a higher fracture toughness. This behavior aligns with the mechanical response observed in Fig. 6.7, where bimodal sintered Cu exhibits superior toughness compared to monomodal and flake-based structures. In contrast, the flake sintered Cu micro-cantilevers (Figs. 6.8g–i) exhibit a brittle fracture response with rapid crack propagation along the weak interlamellar interfaces. The fracture path in these samples is characterized by delamination and interfacial failure, with minimal resistance to crack extension. The anisotropic porosity in the flake structure creates preferential fracture paths, significantly reducing the energy required for crack propagation and leading to the lowest fracture toughness among the three Cu sintering types.

Further insights into the fracture mechanisms are provided in Figs. 6.8j–m, which highlight the fracture surfaces and crack morphology. The monomodal Cu (Fig. 6.8j) exhibits a relatively uniform fracture surface with some ductile features, indicating localized plastic deformation. The bimodal Cu (Figs. 6.8k, l) shows evidence of microvoid coalescence and ductile tearing, confirming its improved fracture resistance due to enhanced interparticle bonding and heterogeneous grain distribution. In contrast, the flake Cu (Fig. 6.8m) exhibits a highly brittle fracture surface with distinct interlamellar separation, reinforcing its susceptibility to interfacial failure. These observations are

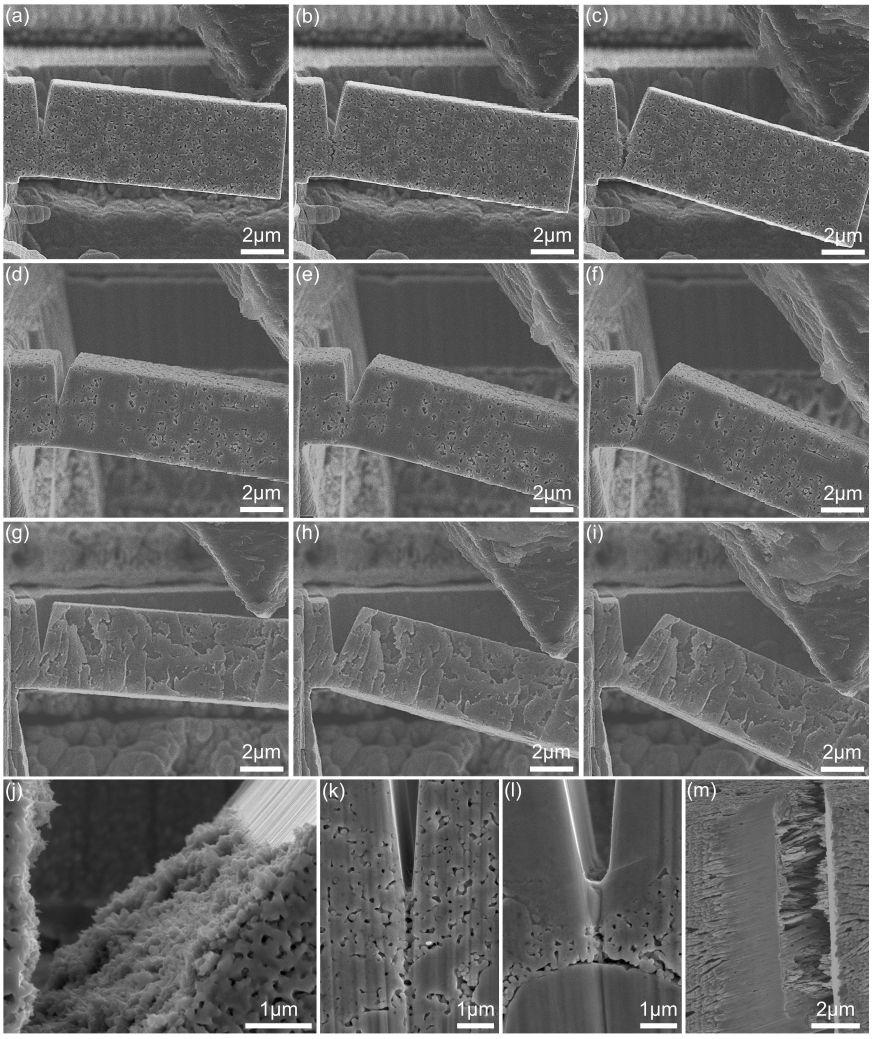


Figure 6.8: Fracture morphologies of sintered Cu with varying particle types: (a–c) monomodal, (d–f) bimodal, and (g–i) flake. Detailed views of crack features: (j) fracture surface (monomodal), (k–l) crack tips (bimodal), and (m) crack path morphology (flake).

consistent with prior studies on sintered structures, where microstructural heterogeneity and sintering quality significantly influence fracture behavior. The findings provide a comprehensive understanding of the failure mechanisms in sintered Cu, underscoring the importance of optimizing microstructure to achieve superior mechanical performance in applications such as microelectronics and high-temperature interconnects.

6.4. CONCLUSION

The main conclusions are as follows:

1. 3D FIB-SEM reconstructions revealed that bimodal Cu particles achieve the most homogeneous and densified microstructure, with significantly reduced porosity and improved interparticle neck formation compared to monomodal and flake-shaped counterparts. In contrast, flake-shaped Cu exhibited highly anisotropic and interconnected porous networks, severely compromising structural integrity.

2. Fracture toughness is strongly dependent on particle morphology. Bimodal sintered Cu consistently showed the highest resistance to crack propagation due to effective crack deflection and bridging mechanisms. Monomodal Cu exhibited moderate toughness, while flake-shaped Cu demonstrated the lowest fracture resistance, primarily due to weak interlamellar bonding and anisotropic porosity.

3. A pronounced size effect was observed across all sintered Cu types: smaller microcantilever specimens consistently exhibited higher apparent fracture toughness. This is attributed to enhanced plasticity at reduced dimensions, which promotes localized energy dissipation and delays crack initiation.

REFERENCES

[1] S. Yang, W. Kim, and M. Cho, "Molecular dynamics study on the coalescence kinetics and mechanical behavior of nanoporous structure formed by thermal sintering of cu nanoparticles", *International Journal of Engineering Science*, vol. 123, pp. 1–19, 2018.

[2] M. Maneshian and A Simchi, "Solid state and liquid phase sintering of mechanically activated w–20 wt.% cu powder mixture", *Journal of Alloys and Compounds*, vol. 463, no. 1-2, pp. 153–159, 2008.

[3] Y. Zuo, S. Carter-Searjeant, M. Green, L. Mills, and S. H. Mannan, "High bond strength cu joints fabricated by rapid and pressureless in situ reduction-sintering of cu nanoparticles", *Materials Letters*, vol. 276, p. 128 260, 2020.

[4] Y. Wang *et al.*, "Fracture behavior and deformation mechanisms in nanolaminated crystalline/amorphous micro-cantilevers", *Acta Materialia*, vol. 180, pp. 73–83, 2019.

[5] J. Luksch, A. Lambai, G. Mohanty, F. Schaefer, and C. Motz, "Bridging macro to micro-scale fatigue crack growth by advanced fracture mechanical testing on the meso-scale", *Materials Science and Engineering: A*, vol. 884, p. 145 452, 2023.

[6] Y. Huang *et al.*, "Harvesting superior intrinsic plasticity in nitride ceramics with negative stacking fault energy", *Acta Materialia*, p. 120 774, 2025.

[7] J.-H. Choi, H. Kim, J.-Y. Kim, K.-H. Lim, B.-C. Lee, and G.-D. Sim, "Micro-cantilever bending tests for understanding size effect in gradient elasticity", *Materials & Design*, vol. 214, p. 110 398, 2022.

[8] R. Henry *et al.*, "Local fracture toughness measurements in polycrystalline cubic zirconia using micro-cantilever bending tests", *Mechanics of Materials*, vol. 136, p. 103 086, 2019.

[9] D. Hu, L. Du, M. Alfreider, J. Fan, D. Kiener, and G. Zhang, "Microscopic fracture toughness of notched porous sintered cu micro-cantilevers for power electronics packaging", *Materials Science and Engineering: A*, vol. 897, p. 146 316, 2024.

[10] L. Du, D. Hu, R. Poelm, W. Van Driel, and K. Zhang, "Micro-cantilever bending test of sintered cu nanoparticles for power electronic devices", in *2023 24th International Conference on Thermal, Mechanical and Multi-Physics Simulation and Experiments in Microelectronics and Microsystems (EuroSimE)*, IEEE, 2023, pp. 1–4.

[11] C. A. Isaza M, Y Cardona-Maya, J. Rudas, C. Carreño-Gallardo, J. Meza, and J. Herrera-Ramírez, *Tem in-situ deformation study of magnesium reinforced with carbon nanotubes by bending test*, 2023.

[12] S.-J. Zhou *et al.*, "Enhanced densification of ultrafine ti (c, n)-based cermets based on grain-growth induced liquid-phase pore filling mechanism", *Journal of Alloys and Compounds*, vol. 986, p. 174 141, 2024.

[13] L. Ma *et al.*, "Sintering mechanism of bimodal-sized cu nanoparticle paste for power electronics packaging", *Journal of Electronic Materials*, vol. 53, no. 6, pp. 2988–2998, 2024.

[14] L. Zou *et al.*, "3d morphology of bimodal porous copper with nano-sized and micron-sized pores to enhance transport properties for functional applications", *ACS Applied Nano Materials*, vol. 3, no. 8, pp. 7524–7534, 2020.

[15] A. Zareei *et al.*, "Highly conductive copper–silver bimodal paste for low-cost printed electronics", *ACS Applied Electronic Materials*, vol. 3, no. 8, pp. 3352–3364, 2021.

[16] T. Pereira, C. L. P. Leme, S. Marschner, and S. Rusinkiewicz, "Printing anisotropic appearance with magnetic flakes", *ACM Transactions on Graphics (TOG)*, vol. 36, no. 4, pp. 1–10, 2017.

[17] C. Chen and K. Suganuma, "Microstructure and mechanical properties of sintered ag particles with flake and spherical shape from nano to micro size", *Materials & Design*, vol. 162, pp. 311–321, 2019.

[18] T. I. Anderson, B. Vega, J. McKinzie, S. A. Aryana, and A. R. Kovscek, "2d-to-3d image translation of complex nanoporous volumes using generative networks", *Scientific Reports*, vol. 11, no. 1, p. 20 768, 2021.

[19] W. C. Oliver and G. M. Pharr, "An improved technique for determining hardness and elastic modulus using load and displacement sensing indentation experiments", *Journal of materials research*, vol. 7, no. 6, pp. 1564–1583, 1992.

[20] J. Liu, F. Zhao, Z. Xiao, Y. Wang, Z. Liu, and H. Zheng, "The establishment of the normal contact force model for a one-dimensional sphere chain subjected to impact load", *International Journal of Mechanical System Dynamics*, vol. 2, no. 1, pp. 131–142, 2022.

[21] X. Li, X. Luo, P. Li, Y. Huang, J. Yang, and Q. Zhou, "Size effect and indenter shape dependence of indentation and scratching behavior for laser melting deposited ti-6al-4v alloy", *Materials Science and Technology*, vol. 41, no. 6, pp. 443–456, 2025.

[22] M. Wurmshuber, M. Alfreider, S. Wurster, M. Burtscher, R. Pippan, and D. Kiener, "Small-scale fracture mechanical investigations on grain boundary doped ultrafine-grained tungsten", *Acta Materialia*, vol. 250, p. 118 878, 2023.

[23] M. Alfreider, D. Kozic, O. Kolednik, and D. Kiener, "In-situ elastic-plastic fracture mechanics on the microscale by means of continuous dynamical testing", *Materials & Design*, vol. 148, pp. 177–187, 2018.

[24] M. Alfreider, R. Bodlos, L. Romaner, and D. Kiener, "The influence of chemistry on the interface toughness in a wti-cu system", *Acta Materialia*, vol. 230, p. 117 813, 2022.

7

Mode-Dependent Fracture Behavior of Sintered Copper Nanoparticles

This study introduces a comprehensive methodology for evaluating the fracture toughness of sintered copper (Cu) nanoparticles (NPs) under mode I (tensile), mode II (in-plane shear), and mode III (out-of-plane shear) loading conditions using micromechanical tests. By systematically designing three fracture configurations, we quantify the critical stress intensity factors K_I, K_{II}, and K_{III}, revealing the anisotropic fracture behavior of the porous Cu system. To further explore deformation mechanisms, atomic layer deposition (ALD) of Al_2O_3 was applied in 20 nm and 50 nm thicknesses. While all coatings enhanced fracture resistance, the mode-dependent response varied: mode I fractures retained ductile tearing; mode II promoted shear-induced particle interlocking; and mode III exhibited complex stress triaxiality with increased crack stability. Al_2O_3 coatings constrained surface deformation and delayed crack initiation without altering the core fracture mode, offering tunable toughness through interface engineering. These findings provide a novel framework for fracture testing and design of mechanically robust sintered interconnects.

7.1. INTRODUCTION

UNDERSTANDING the fracture behavior of materials under different loading conditions is essential for predicting their mechanical performance in practical applications. While mode I (tensile) fracture toughness has been extensively studied, the fracture resistance of materials under mode II (in-plane shear) and mode III (out-of-plane shear) loading remains less explored, particularly at the microscale [1–4]. This work investigates the fracture toughness of sintered copper (Cu) nanoparticles (NPs) under all three loading modes to provide a comprehensive assessment of their mechanical reliability. By employing novel microscale testing techniques, we determine the critical stress intensity factors (K_I, K_{II}, and K_{III}) and analyze the fracture mechanisms governing crack propagation under each condition. The results shed light on the anisotropic fracture behavior of sintered Cu NPs, offering insights into their suitability for applications requiring resistance to complex stress states.

Atomic layer deposition (ALD) has emerged as a promising strategy to enhance the mechanical properties of porous metals [5–8], particularly for applications requiring high reliability under thermal and mechanical stress. In power electronics, sintered Cu NPs are widely used due to their excellent electrical and thermal conductivity, but their porous structure often leads to mechanical instability and crack propagation under operational stresses. Previous studies have demonstrated that thin ceramic coatings, such as Al_2O_3, can significantly strengthen metal nanoparticle-based structures by reinforcing pore walls and inhibiting crack formation [9–12]. This study systematically investigates the effect of Al_2O_3 coatings with thicknesses of 20 nm and 50 nm on the fracture behavior of sintered Cu NPs. By elucidating the relationship between coating thickness, crack propagation resistance, and mechanical stability, our work provides critical insights into how ALD-engineered ceramic layers can improve the durability and performance of sintered Cu NPs, paving the way for more robust power electronics systems.

7.2. METHODS

7.2.1. SAMPLE PREPARATION

Fig. 7.1 illustrates the sintering and fabrication process of the Cu NPs. The detailed sintering process has been reported in Chapter 2. Microstructural evolution is examined via SEM imaging (Figs. 7.1b and c). The unsintered Cu NPs exhibit a densely packed, monomodal distribution with high uniformity (Fig. 7.1b). After sintering, particle fusion yields a porous yet continuous network, confirming effective neck growth and partial densification (Fig. 7.1c). A three-dimensional reconstruction (5 µm × 4 µm × 3 µm) of the sintered structure (Fig. 7.1d) quantifies the spatial distribution of the sintered Cu phase (gray) and residual porosity (blue), revealing an interconnected porous network with a measured porosity of 13.2%.

Fig. 7.2 illustrates the finite element (FE) simulation models and corresponding stress distribution results used to validate the specimen designs for mode II and mode III fracture tests. The simulations were conducted using the commercial FE software Ansys. As shown in Figs. 7.2a and c, the geometrical configurations of the test specimens for both mode II and mode III loading are presented. In each case, the specimen contains a notched region where the stress is expected to concentrate, thereby promoting crack ini-

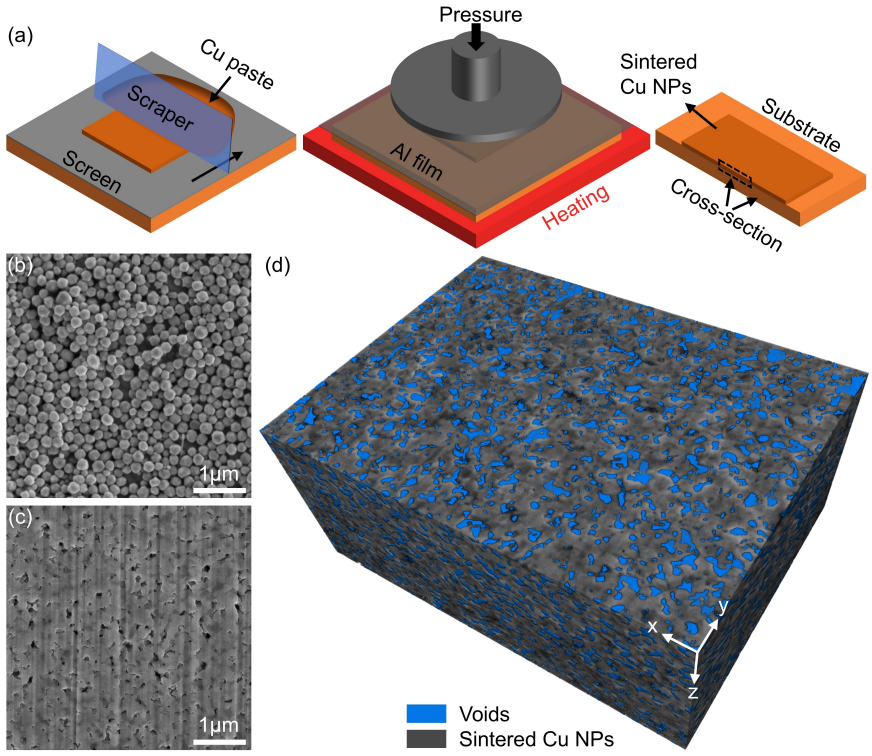


Figure 7.1: (a) Sintering process; (b) initial particle morphology; (c) SEM image of sintered Cu NPs; (d) 3D reconstruction.

tiation and propagation under shear loading conditions. To reduce computational cost and exploit geometrical symmetry, only one half of the specimen was explicitly modeled, with appropriate symmetry boundary conditions applied along the mid-plane. A flat punch indenter was incorporated into the simulation as a rigid body and was assumed to be in hard, frictionless contact with the specimen surface. The results of the simulated stress fields are shown in Figs. 7.2b and d for mode II and mode III loading, respectively. In both loading modes, the peak stress localizes at the crack tip, validating the efficacy of the specimen geometry in driving fracture behavior predominantly under the intended shear modes.

7.2.2. ALD COATING

ALD was employed to deposit Al_2O_3 coatings on the fabricated specimens corresponding to mode I, II and III loading conditions. Two nominal coating thicknesses (20 nm, 50 nm) were investigated to assess the influence of surface passivation on mechanical performance. ALD is a vapor-phase thin-film deposition technique renowned for its atomic-level precision and uniformity, achieved through sequential, self-limiting surface reactions [13, 14]. In this study, the deposition process consisted of alternating exposures

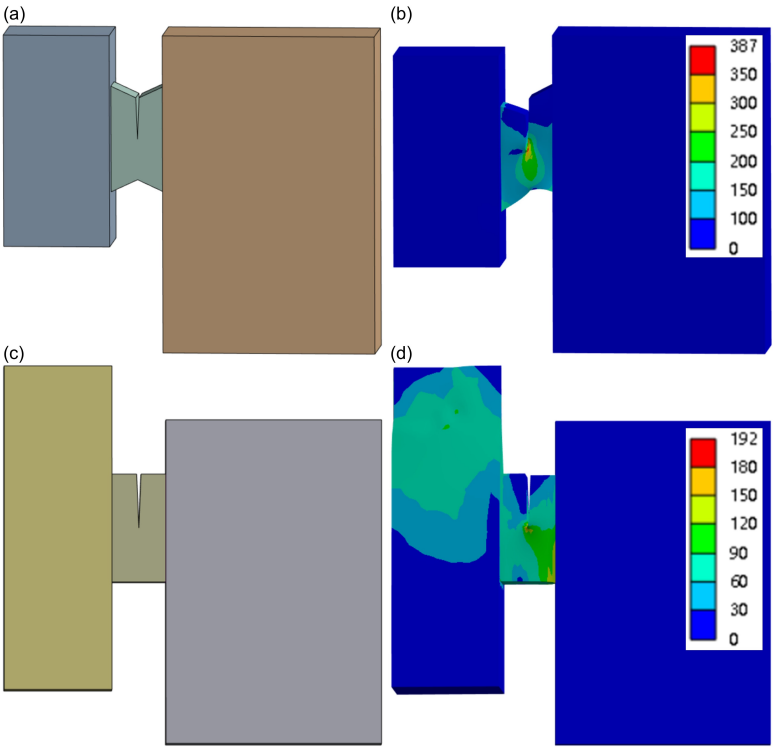


Figure 7.2: Finite element simulations of specimen geometries under (a, b) mode II and (c, d) mode III loading: (a, c) model geometry; (b, d) stress distribution.

to trimethylaluminum (TMA) and water (H_2O) vapor precursors, enabling controlled growth of Al_2O_3 with sub-nanometer precision per cycle. The total film thickness was accurately tuned by varying the number of ALD cycles. Due to the inherently conformal nature of ALD, the resulting Al_2O_3 layers uniformly coated the entire micro-cantilever surfaces, including complex features such as notches and sharp edges, thereby eliminating pinholes and minimizing surface irregularities. This conformal coating not only serves as an effective passivation layer but also contributes to the mechanical integrity of the structures by reducing surface energy heterogeneities and stabilizing crack propagation paths. Consequently, ALD-enabled Al_2O_3 coatings are expected to enhance the reliability and consistency of fracture toughness measurements by mitigating surface-induced variability.

7.2.3. MICRO-MECHANICAL TEST

Samples for fracture toughness testing were fabricated using a dual-beam scanning electron microscope (SEM) integrated with a focused ion beam (FIB) system (FEI Helios G4CX) at an accelerating voltage of 30 kV. To ensure high precision, the fabrication process followed a systematic approach. Initially, a cleaning cut was performed along the specimen edge to remove surface irregularities and establish a defect-free region for

milling. Coarse shaping was then carried out using high ion currents (65 nA to 2.5 nA) to rapidly define the cantilever geometry. However, due to localized heating effects, surface fusion occurred at high ion currents. To eliminate this fused layer and refine the structure, fine milling was conducted at a reduced ion current of 1.1 nA. Throughout the milling process, the sample was rotated by 90° to ensure uniform polishing of all cantilever faces. Notches were introduced prior to fine milling using an ion current of 1.1 nA to maintain a consistent depth across the cantilever width. This step was crucial as surface notches often exceed the intended depth due to ion penetration effects. The notch depth-to-thickness ratio was maintained between 0.45 and 0.55 to ensure reliable fracture toughness measurements.

As shown in Fig. 7.3, three distinct designs were fabricated to evaluate different fracture modes. The first design (Fig. 7.3a) was used for mode I (opening mode), where the notch was placed perpendicular to the loading direction to promote tensile crack propagation [15]. For mode II (in-plane shear), a modified cantilever with an inclined notch was fabricated to facilitate crack propagation parallel to the shear plane [16], ensuring dominant mode II loading (Fig. 7.3b). The third design (Fig. 7.3c) was tailored for mode III (out-of-plane shear) [2, 3], where the notch was positioned to induce torsional loading and crack propagation under shear-dominated conditions [17]. These precisely milled micro-cantilevers provided a robust experimental platform for assessing fracture toughness across different loading modes while maintaining geometric consistency across specimens.

Micromechanical tests were performed using a Hysitron PI85 picoindenter (Bruker Corporation, Billerica, USA) equipped with a nanoDMA III module for continuous stiffness measurement (CSM) [18]. The system was integrated within a scanning electron microscope (SEM) (Leo 1540XB, Carl Zeiss AG, Oberkochen, Germany) to enable in situ mechanical testing. A constant loading rate of 10 µN/s was applied, while a sinusoidal oscillation of 80 Hz with a 5 µN amplitude was superimposed to continuously monitor stiffness variations. During testing, both force-displacement curves and real-time SEM images were captured at a rate of two frames per second, ensuring precise tracking of deformation and crack propagation. This setup allowed for detailed post-analysis of mechanical responses in correlation with the evolving microstructural features.

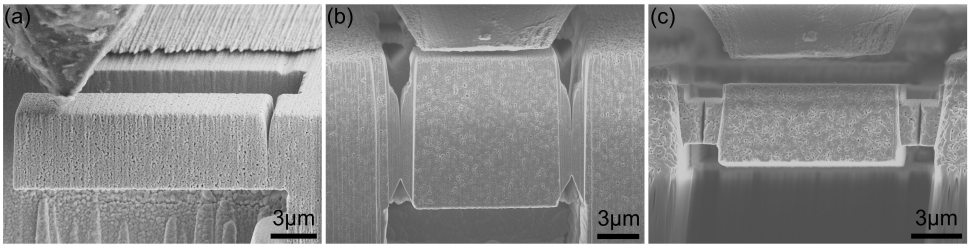


Figure 7.3: SEM images of specimen morphologies under (a) mode I, (b) mode II, and (c) mode III loading.

7.3. RESULTS AND DISCUSSION

7.3.1. LOAD-DISPLACEMENT CURVES

Fig. 7.4 presents the load–displacement responses of specimens designed for mode I (tensile), mode II (in-plane shear), and mode III (out-of-plane shear) fracture tests, with Al_2O_3 coatings of varying thicknesses (0, 20, and 50 nm). The mechanical response under each loading condition reveals distinct failure mechanisms governed by coating thickness and interfacial mechanics. Under mode I loading, which is dominated by normal tensile stresses, a modest yet consistent increase in peak load is observed with increasing Al_2O_3 thickness—from 234 ± 8 μN (uncoated) to 303 ± 3 μN (50 nm). This strengthening effect can be attributed to the suppression of surface flaws and crack initiation by the conformal Al_2O_3 layer, although the overall fracture mode remains tensile-driven with limited plasticity. In contrast, mode II specimens exhibit the highest peak loads across all configurations, with the 50 nm coating achieving a significant increase to 7997 ± 661 μN from 5110 ± 121 μN in the uncoated case. This enhancement is indicative of effective interfacial shear reinforcement, whereby the coating constrains plastic deformation and promotes stress redistribution. However, the presence of sharp load drops—particularly in the 50 nm case—suggests a transition toward brittle failure, likely driven by unstable crack propagation facilitated by elevated interfacial stresses.

The most pronounced influence of the Al_2O_3 coating is observed in mode III specimens, where complex mixed-mode loading activates both shear and tensile components. Here, the peak load increases dramatically—by approximately 277%—from 1735 ± 812 μN (uncoated) to 6536 ± 283 μN (50 nm coating). Despite the substantial gain in load capacity and apparent stiffness, the corresponding load–displacement curves exhibit severe instability and abrupt load drops, reflecting compromised damage tolerance. This behavior suggests that while the coating enhances the apparent strength, it simultaneously introduces stress intensification at material interfaces and notch roots, exacerbating crack nucleation under triaxial stress states. The divergent response across fracture modes underscores the importance of stress state in modulating coating effectiveness. In mode I, reinforcement is limited by tensile decohesion at the interface, whereas in mode II, shear loading enables greater load transfer but at the expense of brittle failure risk. Under mode III conditions, the interplay between normal and shear stresses further amplifies local stress concentrations, making the system highly sensitive to interfacial defects. Therefore, although Al_2O_3 coatings universally improve nominal strength, their influence on fracture resistance is strongly mode-dependent—ranging from modest suppression of tensile cracking to significant yet brittle-prone reinforcement under shear and mixed-mode loading.

7.3.2. FRACTURE TOUGHENSS

To quantitatively assess the fracture resistance of specimens subjected to Mode I loading, the stress intensity factor K_I—representing the conditional fracture toughness—was determined within the framework of linear elastic fracture mechanics (LEFM). The computational approach and experimental methodology for evaluating K_I have been comprehensively described in Chapter 5. In a similar manner, the fracture parameters for mode II and mode III loading conditions were characterized using the corresponding

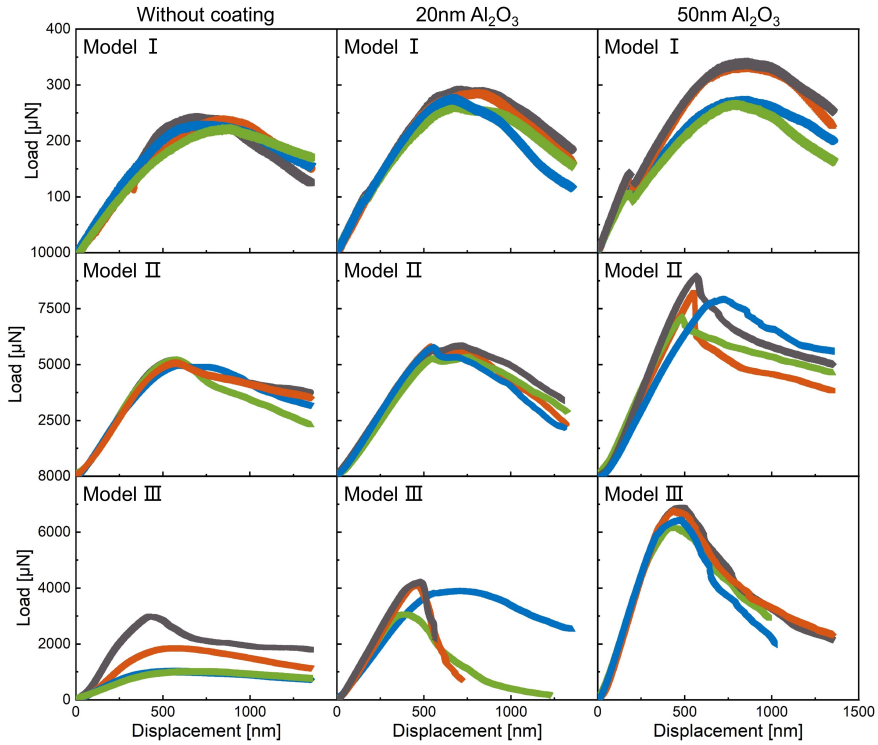


Figure 7.4: Load–displacement curves under mode I, II, and III loading for specimens with varying Al_2O_3 coatings (0 nm, 20 nm, and 50 nm).

stress intensity factors, K_{II} and K_{III}, respectively. These parameters capture the crack-driving forces under in-plane shear (mode II) and out-of-plane or tearing shear (mode III) conditions. The formulations and procedures used to evaluate K_{II} and K_{III} are detailed below [2].

$$K_{II} = \frac{F}{2W\sqrt{B}} f_{KII}\left(\frac{a}{B}\right) \tag{7.1}$$

$$f_{KII}\left(\frac{a}{B}\right) = 0.434 + 2.068\frac{a}{B} \tag{7.2}$$

$$K_{III} = \frac{F}{2W\sqrt{B}} f_{KIII}\left(\frac{a}{B}\right) \tag{7.3}$$

$$f_{KIII}\left(\frac{a}{B}\right) = 0.575 + 2.064\frac{a}{B} \tag{7.4}$$

where F, a, W and B denote the applied force, crack depth, beam width and thickness, respectively.

Fig. 7.5 presents the quantified fracture toughness values of specimens subjected to mode I, II, and III loading, each with Al_2O_3 coatings of 0 nm, 20 nm, and 50 nm. A consistent enhancement in fracture resistance is observed with increasing coating thickness across all loading modes. Under mode I loading, the fracture toughness increases from 0.68 ± 0.033 MPa·m$^{1/2}$ (uncoated) to 0.78 ± 0.024 MPa·m$^{1/2}$ with 20 nm coating, and further to 0.86 ± 0.089 MPa·m$^{1/2}$ with 50 nm. Mode II specimens show a more pronounced improvement, with toughness values rising from 0.75 ± 0.053 MPa·m$^{1/2}$ (uncoated) to 0.89 ± 0.040 MPa·m$^{1/2}$ (20 nm) and 1.16 ± 0.073 MPa·m$^{1/2}$ (50 nm), indicating the coating's strong efficacy in enhancing interfacial shear resistance. The most significant gain is observed in mode III, where the fracture toughness escalates from 0.27 ± 0.140 MPa·m$^{1/2}$ (uncoated) to 0.62 ± 0.061 MPa·m$^{1/2}$ (20 nm) and peaks at 1.06 ± 0.079 MPa·m$^{1/2}$ for 50 nm coatings. These results underscore the substantial role of Al_2O_3 passivation layers in improving fracture resistance, particularly under complex stress states.

The variation in fracture toughness across loading modes reflects the distinct mechanical responses induced by each stress condition. Mode I loading, governed by tensile opening stresses, primarily activates interfacial decohesion and is less sensitive to coating thickness due to the limited contribution of shear resistance. In contrast, mode II loading involves in-plane shear, where the Al_2O_3 coating can more effectively impede crack propagation through enhanced interfacial friction and constraint of plastic deformation. Mode III loading, characterized by a combination of shear and tensile stresses, induces elevated stress triaxiality and localized strain concentration, which amplifies the effect of coating in delaying crack growth. However, this mixed-mode condition also imposes higher demands on coating integrity and adhesion. Thus, while Al_2O_3 coatings consistently improve nominal fracture resistance, their strengthening efficacy is most pronounced in shear-dominated and mixed-mode configurations, where complex stress states are more effectively mitigated by the coating's mechanical barrier function.

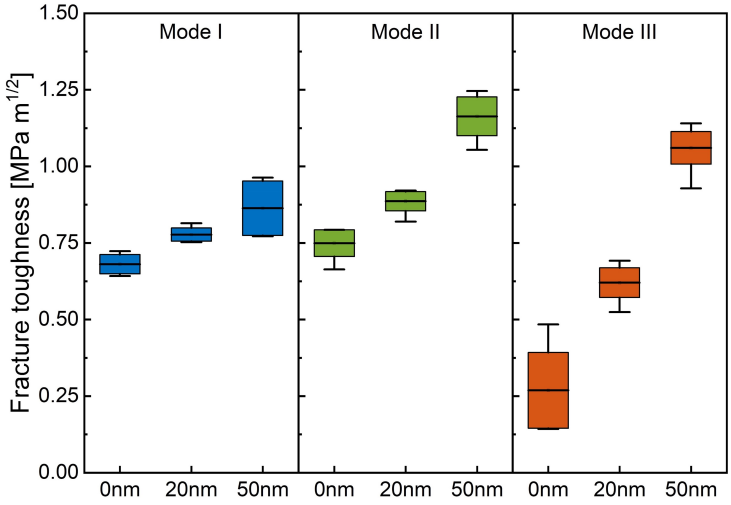


Figure 7.5: Fracture toughness under mode I, II, and III loading as a function of Al_2O_3 coating thickness (0 nm, 20 nm, and 50 nm).

7.3.3. FRACTURE MORPHOLOGY

Fig. 7.6 presents SEM images of mode I fracture surfaces for specimens coated with varying Al_2O_3 thicknesses: 0 nm (Figs. 7.6a, b), 20 nm (Figs. 7.6c, d), and 50 nm (Figs. 7.6e, f). Across all specimens, the fracture surfaces exhibit characteristic ductile features, with notably elongated and necked Cu particles indicating significant plastic deformation during crack propagation. In the uncoated specimen (0 nm, Figs. 7.6a, b), severe particle elongation and interparticle tearing are evident near the fracture tip, suggesting that crack growth proceeded through a ductile rupture mechanism dominated by void coalescence and ligament failure within the sintered Cu matrix. The introduction of a 20 nm Al_2O_3 coating (Figs. 7.6c, d) does not substantially alter the overall fracture morphology. However, closer inspection reveals the presence of adhered coating fragments along the crack flanks, particularly at the interface between the coating and underlying Cu particles. This suggests that the ALD-grown Al_2O_3 film imposes additional surface constraint, increasing interfacial resistance and enhancing crack tip confinement. In the 50 nm coated specimen (Figs. 7.6e, f), the coating is even more prominently retained on the fracture surface, forming a partially intact interfacial layer and reinforcing particle boundaries. Despite this surface strengthening effect, the underlying Cu matrix still undergoes ductile fracture, as indicated by similar particle elongation patterns observed in all three cases. This consistent morphology suggests that the Al_2O_3 coating improves mode I fracture toughness primarily by constraining surface deformation and suppressing early crack opening, rather than by fundamentally altering the fracture mechanism. Thus, the enhanced toughness with increasing coating thickness—rising from 0.68 ± 0.033 MPa·m$^{1/2}$ (uncoated) to 0.86 ± 0.089 MPa·m$^{1/2}$ (50 nm)—is attributed to surface passivation and interfacial strengthening, while bulk fracture remains governed by ductile tearing of sintered Cu ligaments.

Fig. 7.7 presents SEM images of fracture surfaces from specimens subjected to mode II loading, with Al_2O_3 coating thicknesses of 0 nm (Figs. 7.7a, b), 20 nm (Figs. 7.7c, d), and 50 nm (Figs. 7.7e, f). All specimens exhibit pronounced shear deformation features significant interparticle interlocking [19, 20]. In the uncoated specimen (0 nm), the fracture surface reveals uneven topography with elongated Cu ligaments and extensive particle bridging, indicative of shear-driven ductile failure. However, the absence of a surface constraint permits localized debonding and particle pull-out, limiting the overall fracture toughness to 0.75 ± 0.053 MPa·m$^{1/2}$. With the introduction of a 20 nm Al_2O_3 coating, the fracture morphology remains similarly ductile, but coating fragments are intermittently retained along the shear plane. These fragments suggest improved interfacial cohesion and suppression of early interparticle debonding, contributing to an increase in fracture toughness to 0.89 ± 0.040 MPa·m$^{1/2}$. The 50 nm coated specimens display more prominent and continuous Al_2O_3 adhesion at the fracture interface, while still preserving evidence of particle deformation and interlocking. The thickened coating effectively constrains surface deformation and promotes more uniform stress transfer across the fracture plane, which corresponds with the highest measured mode II toughness of 1.16 ± 0.073 MPa·m$^{1/2}$. These observations confirm that shear-induced particle interlocking governs mode II fracture, while Al_2O_3 coatings enhance mechanical integrity by strengthening interfacial resistance and delaying crack propagation.

Fig. 7.8 displays SEM images of mode III fracture surfaces—characterized by mixed-

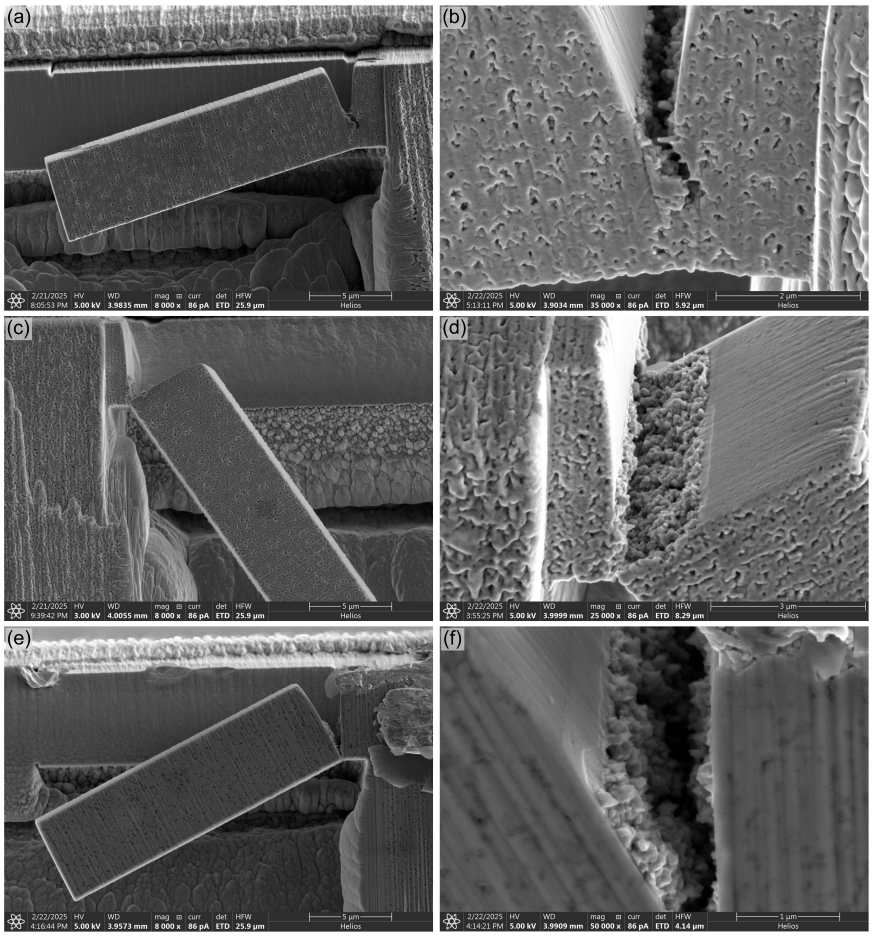


Figure 7.6: SEM images of specimens under mode I loading with Al_2O_3 coating thicknesses of (a, b) 0 nm, (c, d) 20 nm, and (e, f) 50 nm.

mode loading involving both tensile and out-of-plane shear—across specimens with Al_2O_3 coatings of 0 nm (Figs. 7.8a, b), 20 nm (Figs. 7.8c, d), and 50 nm (Figs. 7.8e, f). In the uncoated specimens, the fracture surface appears rough and irregular, with extensive out-of-plane displacement and ductile tearing features such as necked particles and crack blunting. The lack of constraint under mixed-mode stress allows for premature crack deflection and unstable propagation, reflected in the low fracture toughness value of 0.27 ± 0.140 MPa·m$^{1/2}$. Upon applying a 20 nm Al_2O_3 coating, the fracture surface reveals improved structural cohesion and partial retention of the coating along the fracture interface. Although the Cu matrix still shows ductile elongation, the coating helps stabilize crack advancement under complex triaxial stresses, leading to a significant increase in fracture toughness to 0.89 ± 0.040 MPa·m$^{1/2}$. In the 50 nm coated specimen, continuous coating adhesion and smoother fracture flanks suggest enhanced surface passiva-

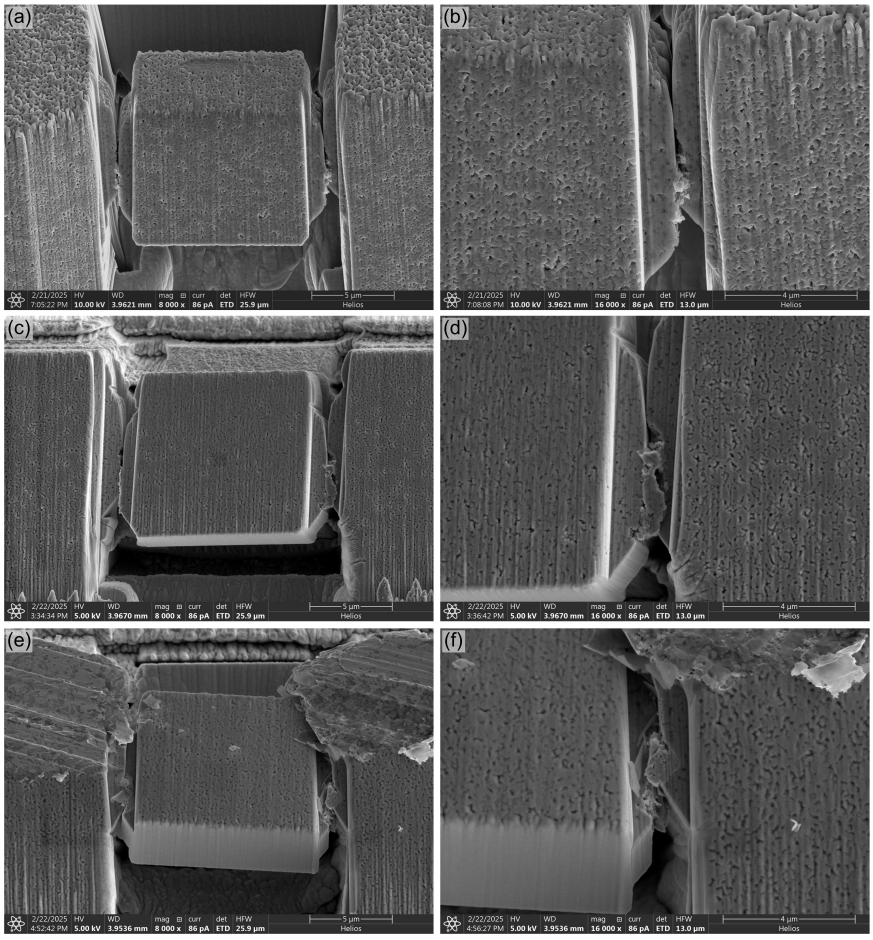


Figure 7.7: SEM images of specimens under mode II loading with Al_2O_3 coating thicknesses of (a, b) 0 nm, (c, d) 20 nm, and (e, f) 50 nm.

tion. Nevertheless, localized brittle features near the coating layer coexist with ductile tearing of the underlying Cu, indicating a mixed fracture mechanism. The increased interfacial constraint delays crack initiation and suppresses unstable opening under shear-tensile coupling, resulting in the highest toughness of 1.06 ± 0.079 MPa·m$^{1/2}$. Thus, under mode III loading, the Al_2O_3 coating enhances fracture resistance by constraining crack evolution across multiple stress components, despite not fundamentally altering the ductile failure mechanism of the Cu matrix.

7.4. CONCLUSION

The main conclusions are as follows:

1. The fracture toughness of sintered Cu NPs exhibits a strong dependence on the

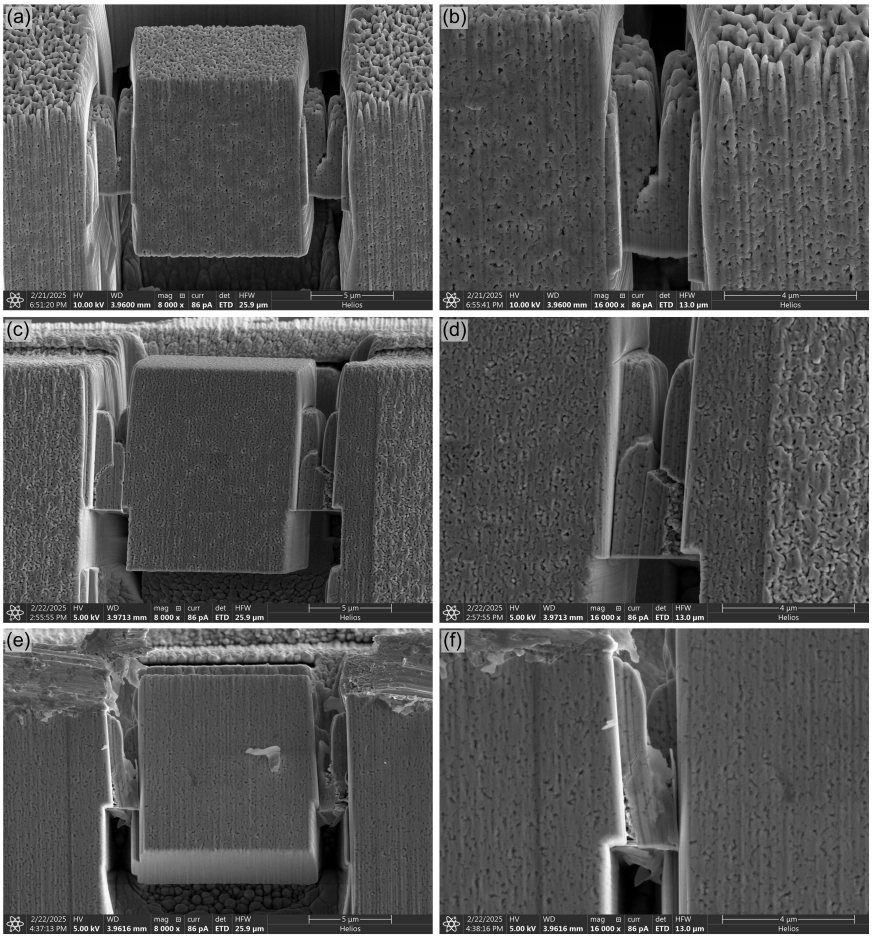


Figure 7.8: SEM images of specimens under mode III loading with Al_2O_3 coating thicknesses of (a, b) 0 nm, (c, d) 20 nm, and (e, f) 50 nm.

applied loading mode. Mode II (in-plane shear) shows the highest toughness due to shear-induced particle interlocking, followed by mode I (tensile) characterized by ductile tearing, and mode III (out-of-plane shear) which displays the lowest toughness due to complex triaxial stress states and unstable crack propagation. These results confirm the anisotropic fracture resistance of the porous Cu network under different mechanical loading conditions.

2. Deformation mechanisms vary significantly across loading modes. Mode I loading is governed by tensile stress, promoting ductile failure through void coalescence and ligament rupture. In contrast, mode II fracture is dominated by interfacial shear, where extensive particle interlocking and bridging contribute to enhanced energy dissipation. Mode III exhibits mixed-mode behavior involving both tensile and shear stresses, leading to combined ductile tearing and out-of-plane crack deflection.

3. The Al_2O_3 coating enhances fracture toughness across all loading modes, with the most pronounced improvement observed under shear-dominated and mixed-mode conditions. The coating constrains surface deformation, delays crack initiation, and reinforces interparticle boundaries without altering the underlying ductile fracture mechanism.

REFERENCES

[1] J.-H. Yan, M. A. Sutton, X. Deng, and C.-S. Cheng, "Mixed-mode fracture of ductile thin-sheet materials under combined in-plane and out-of-plane loading", *International Journal of Fracture*, vol. 144, no. 4, pp. 297–321, 2007.

[2] J. Ast *et al.*, "Interfacial fracture behavior and adhesive strength in tensile and shear loading of sic-pyc-sic composites by micro-scale specimens", *Acta Materialia*, vol. 259, p. 119 273, 2023.

[3] J. Luksch, A. Lambai, G. Mohanty, F. Schaefer, and C. Motz, "Bridging macro to micro-scale fatigue crack growth by advanced fracture mechanical testing on the meso-scale", *Materials Science and Engineering: A*, vol. 884, p. 145 452, 2023.

[4] H. Wafai, A. Yudhanto, G. Lubineau, R Yaldiz, and N Verghese, "An experimental approach that assesses in-situ micro-scale damage mechanisms and fracture toughness in thermoplastic laminates under out-of-plane loading", *Composite Structures*, vol. 207, pp. 546–559, 2019.

[5] M. M. Biener *et al.*, "Ald functionalized nanoporous gold: Thermal stability, mechanical properties, and catalytic activity", *Nano letters*, vol. 11, no. 8, pp. 3085–3090, 2011.

[6] L. Zhang, J. H. Prosser, G. Feng, and D. Lee, "Mechanical properties of atomic layer deposition-reinforced nanoparticle thin films", *Nanoscale*, vol. 4, no. 20, pp. 6543–6552, 2012.

[7] E. Almog, A. Sharma, Y. Qi, J. Zimmerman, and E. Rabkin, "Hybrid hierarchical nanolattices with porous platinum coating", *Acta Materialia*, vol. 225, p. 117 552, 2022.

[8] J. J. do Rosário, Y. Häntsch, G. A. Schneider, and E. T. Lilleodden, "A combined compression and indentation study of mechanical metamaterials based on inverse opal coatings", *Acta materialia*, vol. 195, pp. 98–108, 2020.

[9] Z. Yin, S. Tao, X. Zhou, and C. Ding, "Microstructure and mechanical properties of al2o3–al composite coatings deposited by plasma spraying", *Applied Surface Science*, vol. 254, no. 6, pp. 1636–1643, 2008.

[10] J. Jia, B. Zhang, D. Liu, S. Liu, G. Ji, and R. Ji, "Effects of al2o3 coating induced structural and mechanical changes of c/c composites", *Journal of Alloys and Compounds*, vol. 818, p. 152 847, 2020.

[11] K Spencer, D. Fabijanic, and M.-X. Zhang, "The influence of al2o3 reinforcement on the properties of stainless steel cold spray coatings", *Surface and Coatings Technology*, vol. 206, no. 14, pp. 3275–3282, 2012.

[12] A. M. Alkalbani and G. T. Chala, "A comprehensive review of nanotechnology applications in oil and gas well drilling operations", *Energies*, vol. 17, no. 4, p. 798, 2024.

[13] B. Gupta *et al.*, "Recent advances in materials design using atomic layer deposition for energy applications", *Advanced Functional Materials*, vol. 32, no. 3, p. 2 109 105, 2022.

[14] S. Yasmeen, S. W. Ryu, S.-H. Lee, and H.-B.-R. Lee, "Atomic layer deposition beyond thin film deposition technology", *Advanced Materials Technologies*, vol. 8, no. 20, p. 2 200 876, 2023.

[15] M. Hammouda, H. Osman, and H. Sallam, "Mode i notch fatigue crack growth behaviour under constant amplitude loading and due to the application of a single tensile overload", *International journal of fatigue*, vol. 26, no. 2, pp. 183–192, 2004.

[16] S. Xu, H. W. Reinhardt, and M. Gappoev, "Mode ii fracture testing method for highly orthotropic materials like wood", *International Journal of Fracture*, vol. 75, no. 3, pp. 185–214, 1996.

[17] C Santus *et al.*, "Torsional-loaded notched specimen fatigue strength prediction based on mode i and mode iii critical distances and fracture surface investigations with a 3d optical profilometer", *International Journal of Fatigue*, vol. 161, p. 106 913, 2022.

[18] M. Alfreider, R. Bodlos, L. Romaner, and D. Kiener, "The influence of chemistry on the interface toughness in a wti-cu system", *Acta Materialia*, vol. 230, p. 117 813, 2022.

[19] L. Scholtès and F.-V. Donzé, "A dem model for soft and hard rocks: Role of grain interlocking on strength", *Journal of the Mechanics and Physics of Solids*, vol. 61, no. 2, pp. 352–369, 2013.

[20] Y. Chen, Q. Qi, R. Lai, Y. Zhu, J. Duan, and Z. Nie, "Influence mechanism of particle shapes and gradations on vibration-induced deformation of coarse-grained soils: A multi-scaled insight", *Powder Technology*, p. 121 356, 2025.

8

CONCLUSION AND FUTURE PERSPECTIVE

8.1. CONCLUSIONS

THIS thesis presents a comprehensive investigation into the microstructure evolution and mechanical properties of sintered copper (Cu) nanoparticles (NPs) through the integration of multiscale simulations and micro-mechanical tests. The key contributions of this thesis are summarized as follows:

Anisotropic Properties: Uniaxial sintering pressure induces significant anisotropy in sintered Cu NPs. MD simulations reveal that sintered necks preferentially align in the direction of applied stress, enhancing mechanical strength along this axis. Micro-cantilever bending and tensile simulations confirm that fracture toughness in the sintering direction is 41% higher in experiments and 108% higher in simulations compared to perpendicular directions.

Deformation Mechanisms: Sintered Cu NPs combine high strength with low elastic modulus, making them ideal for electronic packaging. Their deformation follows a two-stage mechanism: initial compressive loading compacts voids and forms dense interparticle contacts, followed by intragranular slip-driven plasticity. The interplay of particle size, crystallographic orientation, and porosity promotes energy dissipation, improves load transfer, suppresses strain localization, and hinders crack propagation through multiple active deformation pathways.

Viscoplastic Deformation: Higher strain rates enhance yield strength due to strain-rate hardening, while elevated temperatures (175°C to 350°C) induce thermal softening, reducing mechanical stability. Phase-field fracture modeling reveals that porosity distribution critically influences crack initiation and propagation, with smaller voids leading to higher stiffness and delayed failure.

Interface Strength: Sintered Cu-Cu substrate interfaces exhibit superior fracture resistance ($K_Q = 2.88 \pm 0.10$ MPa·m$^{1/2}$) compared to cracks within sintered Cu NPs ($K_Q = 2.12 \pm 0.11$ MPa·m$^{1/2}$). CZM modeling confirms that crack paths predominantly prop-

agate through porous regions rather than the interface, highlighting strong interfacial bonding and effective stress transfer at the Cu-Cu interface.

Particle Morphology: Bimodal sintered Cu exhibits higher fracture toughness than monomodal and flake-shape Cu due to enhanced sintering neck formation and effective crack deflection mechanisms. Flake-shape Cu demonstrates weak interlamellar bonding and anisotropic porosity, resulting in lower fracture resistance and a higher tendency for brittle failure.

Loading modes: Fracture toughness in sintered Cu NPs is strongly mode-dependent. Mode II (in-plane shear) demonstrates the highest toughness due to particle interlocking, followed by mode I (tensile) with ductile tearing, and mode III (out-of-plane shear), which exhibits the lowest toughness owing to triaxial stress and unstable crack propagation. These results underscore the anisotropic fracture resistance of the porous Cu network.

ALD Coatings: ALD coatings profoundly influence the fracture response of sintered Cu NPs by constraining surface deformation, retarding crack initiation, and enhancing interparticle boundary integrity. Notably, these modifications occur without disrupting the fundamental ductile fracture mechanisms intrinsic to the porous Cu network, indicating that the coatings act primarily as mechanical stabilizers rather than altering the material's intrinsic plasticity.

8.2. FUTURE PERSPECTIVE

The research presented in this thesis advances the fundamental understanding of sintered Cu NPs for high-performance electronic packaging and interconnect applications. Building upon the insights gained, several promising directions for future investigation are proposed:

Oxidation issue: Given the high chemical reactivity of Cu, surface oxidation remains a critical challenge that may compromise mechanical integrity and long-term reliability. Future studies should systematically assess the influence of oxide layers on fracture behavior, interfacial bonding, and environmental degradation to enable robust performance under service conditions.

Size effect: While this study has addressed the mechanical behavior of sintered Cu NPs, the influence of particle diameter across nano- to microscale ranges remains inadequately understood. Systematic investigation of particle and grain size scaling is essential to uncover size-dependent deformation and fracture mechanisms, enabling controlled microstructural design for optimized mechanical performance.

Stiffness mismatch: Compared to Ag, Cu exhibits a higher elastic modulus, which may lead to increased stress concentrations and earlier crack initiation under mechanical loading. Elucidating the role of stiffness mismatch in crack propagation and mechanical failure is crucial for optimizing the structural reliability of Cu-based interconnects.

Metamaterial design: The unique combination of low elastic modulus and high yield strength in sintered Cu suggests potential for metamaterial-inspired design. Future research could explore architected Cu structures that leverage these mechanical characteristics for enhanced energy absorption, compliance, or damage tolerance. Additionally, developing direct-sintered metamaterial architectures may offer novel pathways for integrating structural functionality with electrical performance.

ACKNOWLEDGEMENTS

To all who have walked this path with me, I offer my deepest gratitude.

First and foremost, I express my sincere gratitude to my promotor, Prof. Guoqi Zhang. It was under his guidance that I embarked on this academic journey, and his unwavering support, insightful mentorship, and high expectations have been instrumental in shaping my development as a researcher. He has always emphasized the importance of aiming high, encouraging me to look beyond the low-hanging fruit and seek research that is both impactful and innovative. Whether I faced uncertainties in project management, struggled with experimental setbacks, or felt complacent about progress, his wisdom, professionalism, and relentless passion for research continuously motivated me to strive for excellence. I am deeply honored to be his student.

I am also deeply grateful to Prof. Willem Dirk van Driel, Dr. René H. Poelma, Prof. Xuejun Fan, and Prof. Jiajie Fan for their invaluable guidance and support. Their expertise was instrumental in shaping my research direction, broadening my scientific perspective, and significantly improving the quality of my academic writing.

I extend my sincere gratitude to Prof. Daniel Kiener, Prof. Verena Maier-Kiener, Dr. Markus Alfreider, and Dr. Gerald Schaffar for their invaluable support during my research visits to Austria. I am also grateful to Prof. Magnus Hörnqvist Colliander and Dr. Olof Bäcke at Chalmers University of Technology for their essential contributions to our collaborative experiments. Furthermore, I thank Dr. Jaber Derakhshandeh and Dr. Eric Beyne at IMEC, for the opportunity to undertake a short-term internship, which provided valuable training in advanced packaging technologies. Their expertise, commitment, and generous support were instrumental to the advancement of my research.

I am grateful to Dr. Susan Zhao from Signify for her valuable insights and experimental support in solder fatigue studies. I also thank Caroline Beelen-Hendrikx, Jizhe Yin, Dr. Corinne Bestory, Owen Law, and Inse Bonne from Nexperia for their sustained technical support and constructive input on electromigration projects. Our regular meetings significantly advanced my research and contributed to the development of my project management skills.

I must also express my heartfelt gratitude to my outstanding colleagues: Dr. Xinrui Ji, Dr. Shanliang Deng, Dr. Ru Li, Dr. Chunjian Tan, Dr. Shaogang Wang, Dr. Zhen Cui, Dr. Yue Sun, Dr. Henk van Zeijl, Dr. Joost Romijn, Dr. Hesheng Lin, Dr. Baoyun Sun, Dr. Nick Liu, Dr. Dong Hu, Dr. Henry Antony Martin, Chenshan Gao, Kai Liu, Weiping Jiao, Zihan Zhang, Lai Wei, Heng Ma, Zhoubang Du, Xiao Hu, Zichuan Li, Jiarui Mo, Yaqian Zhang, Ping Sun, Tianyi Jin, Nikhil Gupta, Adwait Inamdar, Nikki de Ruijter, Filip Simjanoski, Alireza Mehrabi, Ole Bergmann, Amir Ghorbani, Sjoerd de Jong, and many others.

Finally, I express my deepest gratitude to my parents and my beloved partner. Their unwavering support, patience, and encouragement have been my strongest pillar of strength throughout this journey. Without them, this achievement would not have been possible.

Curriculum Vitæ

Leiming Du

05-07-1996 Born in Shandong, China.

Education

2021–2025 Ph.D. in Microelectronics
Delft University of Technology, Delft, the Netherlands
Thesis: Sintering Fundamentals of Nano-Metallic Particle Interconnects
Promotor: Prof. dr. G.Q. Zhang, Prof. dr. ir. W.D. van Driel
Copromotor: Dr. ir. R.H. Poelma

2018–2021 Master of Engineering in Mechanics
Harbin Institute of Technology, Shenzhen, Guangdong, China

2014–2018 Bachelor of Engineering Mechanics
China University of Mining and Technology, Jiangsu, China

Research Experience

2023–2024 Internship
Interuniversity Microelectronics Centre (IMEC)
Leuven, Belgium

2019–2021 Internship
Institute of Mechanics, Chinese Academy of Sciences
Beijing, China

Awards

2025 IEEE EPS PhD Fellowship

List of Publications

Journal Papers

1. **L. Du**, G. Schaffar, W. Jiao, K. Liu, R. H. Poelma, V. Maier-Kiener, J. Fan, D. Kiener, W. D. van Driel, X. Fan, G. Zhang, *Tailoring Microstructure and Mechanical Properties of Sintered Cu Nanoparticles*, Acta Materialia. (Under Review)

2. **L. Du**, G. Schaffar, W. Jiao, R. H. Poelma, V. Maier-Kiener, J. Fan, D. Kiener, W. D. van Driel, X. Fan, G. Zhang, *Strain rate and temperature dependent viscoplasticity of sintered Cu nanoparticles*, Materials & Design (2025): 114319.

3. **L. Du**, W. Jiao, O. Bäcke, M. H. Colliander, R. H. Poelma, J. Fan, W. D. van Driel, X. Fan, G. Zhang, *Interface strength and crack propagation mechanisms in sintered copper nanoparticles*, Acta Materialia (2025): 121187.

4. **L. Du**, K. Liu, D. Hu, O. Bäcke, X. Hu, X. Ji, J. Fan, R. H. Poelma, M. H. Colliander, G. Zhang, *Microstructural and mechanical anisotropy in pressure-assisted sintered copper nanoparticles*, Acta Materialia (2025): 120772.

5. X. Yan, **L. Du**, C. Gu, T. Tian, C. Gao, G. Zhang, J. Fan, *Microscale Mechanical Properties in Sintered Copper Nanoparticles*, Materials Science and Engineering: A (2025): 148684

6. S. Feng, **L. Du**, Z. Cui, X. Zhu, X. Fan, G. Zhang, J. Fan, *Evaluating the electromigration effect on mechanical performance degradation of aluminum interconnection wires: A nanoindentation test with molecular dynamics simulation study*, Applied Surface Science (2024): 160992.

7. D. Hu, **L. Du**, M. Alfreider, J. Fan, D. Kiener, G. Zhang, *Microscopic fracture toughness of notched porous sintered Cu micro-cantilevers for power electronics packaging*, Materials Science and Engineering: A (2024): 146316.

8. Y. Zhang, **L. Du**, O. Bäcke, S. Kalbfleisch, G. Zhang, S. Vollebregt, M. H. Colliander, *Measuring residual stresses in individual on-chip interconnects using synchrotron nanodiffraction*, Applied Physics Letters (2024): 083501.

9. X. Ji, **L. Du**, S. He, H. van Zeijl, G. Zhang, *Microstructural and micromechanical characterization of sintered nano-copper bump for flip-chip heterogeneous integration*, Microelectronics Reliability (2023): 115180.

10. D. Hu, C. Qian, X. Liu, **L. Du**, Z. Sun, X. Fan, G. Zhang, J. Fan, *High temperature viscoplastic deformation behavior of sintered nanocopper paste used in power electronics packaging: Insights from constitutive and multi-scale modelling*, Journal of Materials Research and Technology (2023): 3183-3200.

11. X. Long, K. Chong, Y. Su, **L. Du**, G. Zhang, *Connecting the macroscopic and mesoscopic properties of sintered silver nanoparticles by crystal plasticity finite element method*, Engineering Fracture Mechanics (2023): 109137.

CONFERENCE PAPERS

1. **L. Du**, W. Jiao, J. Fan, G. Zhang, *Tailoring sintering pressure to optimize nanoparticle connectivity and mechanical strength in Cu-based interconnects*, IEEE 75rd Electronic Components and Technology Conference (ECTC) (2025).
2. **L. Du**, X. Ji, K. Liu, J. Fan, G. Zhang, *Investigating coalescence kinetics in Cu nanoparticle by molecular dynamics and 3D reconstruction*, 25th International Conference on Electronic Packaging Technology (ICEPT) (2024).
3. **L. Du**, S. Deng, Z. Cui, R. Poelma, C. Beelen-Hendrikx, G. Zhang, *Multi-parameters optimization for electromigration in WLCSP solder bumps*, 25th International Conference on Thermal, Mechanical and Multi-Physics Simulation and Experiments in Microelectronics and Microsystems (EuroSimE) (2024).
4. **L. Du**, X. Zhao, R. Poelma, W. D. van Driel, G. Zhang, *High-temperature creep properties of a novel solder material and its thermal fatigue properties under potting material*, IEEE 73rd Electronic Components and Technology Conference (ECTC) (2023).
5. **L. Du**, D. Hu, R. Poelma, W. D. van Driel, G. Zhang, *Micro-cantilever bending test of sintered Cu nanoparticles for power electronic devices*, 24th International Conference on Thermal, Mechanical and Multi-Physics Simulation and Experiments in Microelectronics and Microsystems (EuroSimE) (2023).
6. **L. Du**, X. Zhao, P. Watté, R. Poelma, W. D. van Driel, G. Zhang, *Investigation of potting compounds on thermal-fatigue properties of solder interconnects*, IECON 2022 – 48th Annual Conference of the IEEE Industrial Electronics Society (2022).
7. Z. Du, **L. Du**, G. Zhang, *Electromigration simulation of copper-pillar bump in 3D integration*, 26th International Conference on Thermal, Mechanical and Multi-Physics Simulation and Experiments in Microelectronics and Microsystems (EuroSimE) (2025).
8. X. Ji, **L. Du**, H. van Zeijl, G. Zhang, J. Derakhshandeh, E. Beyne, *20 μm pitch Cu-to-Cu flip-chip interconnects through Cu nanoparticles sintering*, IEEE 74th Electronic Components and Technology Conference (ECTC) (2024).
9. J. Mo, G. J. K. Schaffar, **L. Du**, V. Maier-Kiener, D. Kiener, S. Vollebregt, G. Zhang, *Investigating mechanical properties of silicon carbide coated carbon nanotube composite at elevated temperatures*, IEEE 37th International Conference on Micro Electro Mechanical Systems (MEMS) (2024).
10. X. Ji, H. van Zeijl, W. Jiao, S. He, **L. Du**, G. Zhang, *Low temperature fine pitch all-copper interconnects combining photopatternable underfill films*, IEEE 73th Electronic Components and Technology Conference (ECTC) (2023).